FIRST ASSESSMENT OF THE MAGNETIC-HYDROSTATIC MAIN BEARING PROPOSED FOR THE DUCK WAVE-ENERGY CONVERTER

Colin G Anderson

A Thesis Submitted for the
Degree of Doctor of Philosophy

University of Edinburgh
November 1985

ABSTRACT

A preliminary assessment is made of the novel large-scale bearing proposed for the 'duck' wave energy converter. The bearing is designed to work by combining the principles of self-pressurised fluid lubrication, and passive permanent magnet repulsion, and these two topics are dealt with in approximately equal measure.

Following a description of the specification and design of the bearing, a performance analysis is made, based on standard lubrication theory assumptions. Although over-simplified, this predicts favourable characteristics, including high load capacity, low fluid pressures, and low friction. The analytical assumptions are then reassessed, and those characteristics of bearing performance not predicted from lubrication theory, namely turbulence and fluid inertia, are examined. Both are found to enhance load capacity, with the most significant effect arising as an indirect consequence of fluid inertia. The indirect influence of fluid inertia is described, and experimental evidence presented of its magnitude, and its asymmetric characteristic: the experimental model used is that of converging/diverging radial flow between plane parallel discs.

The permanent magnet repulsion system, and the topic of magnet geometry optimisation are discussed. After examining the correct analytical models and optimisation procedures, several mathematical analyses are detailed. The results of these include theoretical results for the maximum force, force/unit volume, and stiffness/unit volume which can be exerted by two-dimensional rectangular magnets, and the maximum force and force/unit volume for three-dimensional magnets. Experimental results are included which verify the theoretical predictions.

The thesis concludes with a short discussion on the overall feasibility of the proposed bearing.

DECLARATION

Unless otherwise acknowledged, the work, and opinions, contained in this thesis are my own.

Colin G Anderson
Edinburgh Wave Power Project
Department of Mechanical Engineering
University of Edinburgh
November 1985

CONTENTS

		Page
Abstract		ii
Declaration		iii
Contents		iv
CHAPTER 1 - INTRODUCTION		
1.1	Preface	1
1.2	Topics of Study: Chapter Breakdown	1
CHAPTER 2 - LITERATURE REVIEW		
2.1	Introduction	6
2.2	Bearing Specification and Design	6
2.3	Performance Analysis	7
2.4	Axisymmetric Radial Fluid Flow	8
2.5	Permanent Magnet Principles	11
2.6	Magnet Geometry Optimisation	12
CHAPTER 3 - THE PROPOSED BEARING: SPECIFICATION AND DESIGN		
3.1	Chapter Summary	14
3.2	Wavepower, and the Edinburgh Duck	14
3.3	The Bearing Specification	16
3.4	The Choice of Bearing Mechanism	17
3.5	The Proposed Bearing	22
3.6	Operating Principles	24
3.7	Design Details, and a Precedent	26
3.8	Designing for 25-Year Life	28
3.9	Magnet Axial Alignment	29
3.10	Conclusions	31
CHAPTER 4 - PERFORMANCE ANALYSIS		
4.1	Chapter Summary	32
4.2	Analytical Model	32

Page

4.3 Stiffness Characteristics (Static Loading) 35
4.4 Damping Characteristics (Dynamic Loading) 35
4.5 Frequency Response 38
4.6 The Two-Dimensional Approximation 42
4.7 Nonlinear Stiffness 42
4.8 The Magnet Sheet 44
4.9 Limitations of Lubrication Theory 44
4.10 Power Dissipation and Temperature Rise 45
4.11 Maximum Pressure, and Pressure Gradient 47
4.12 The Need for Asymmetric Bearing Response 48
4.13 Conclusions 50

CHAPTER 5 - BEARING LUBRICATION IN MORE DETAIL

5.1 Chapter Summary 52
5.2 Flow Regimes 52
5.3 Turbulent Lubrication 54
5.4 Turbulent Power Loss 58
5.5 The Influence of Fluid Inertia 59
5.6 Fluid Inertia: Pressure Drop Across the Magnet Sheet 61
5.7 Convergent Radial Flow 65
5.8 The Importance of the Inertial Pressure Imbalance 66
5.9 The Complete Flow Field 69
5.10 Conclusions 70

CHAPTER 6 - RADIAL FLOW EXPERIMENTS

6.1 Chapter Summary 72
6.2 Experimental Apparatus 72
6.3 Pressure and Flow Measurement 79
6.4 Experimental Results 81
6.5 Quantitative Results Analysis 86
6.6 Conclusions 93

Page

CHAPTER 7 - THE PERMANENT MAGNET REPULSION SYSTEM

7.1 Chapter Summary 94
7.2 Introduction 94
7.3 Magnetic Material Selection 95
7.4 Analytical Models for Permanent Magnets 96
7.5 Optimising the Magnet Geometry 98
7.6 Optimisation Procedures 100
7.7 Related Work 103
7.8 Conclusions 104

CHAPTER 8 - PERMANENT MAGNET OPTIMISATION

8.1 Chapter Summary 106
8.2 Magnetic Forces 106
8.3 Magnetic Stiffness 111
8.4 The Scaling Laws for Force and Stiffness 112
8.5 Geometry Optimisation (1): Constrained Force/Length 114
8.6 Geometry Optimisation (2): ..... Stiffness/Length 122
8.7 Optimisation: Applying the Results 127
8.8 Optimisation (3): Unconstrained Force/Volume 129
8.9 Optimisation (4): ..... Stiffness/Volume 133
8.10 Multiple-Pair Magnet Arrangements 137
8.11 Three-Dimensional Optimisation (1): Constrained 142
8.12 Three-Dimensional Optimisation (2): Unconstrained 144
8.13 Conclusions 146

CHAPTER 9 - PERMANENT MAGNET ANALYSIS: EXPERIMENTAL RESULTS

9.1 Chapter Summary 149
9.2 Experimental Objectives 149
9.3 Experimental Apparatus (1): Magnet Levitation-Bed 150
9.4 Experimental Apparatus (2): The Magnets 156
9.5 Verifying the Two-Dimensional Geometry 159
9.6 Force Measurements 163
9.7 Magnetic Stiffness 167

Page

9.8 Demonstration of Non-Uniform Magnetisation 169
9.9 Optimum Geometries (1): Constrained Force/Length 172
9.10 Optimum Geometries (2): ..... Stiffness/Length 175
9.11 Optimum Geometries (3): Unconstrained Force/Volume 178
9.12 Optimum Geometries (4): ..... Stiffness/Volume 184
9.13 Conclusions 187

CHAPTER 10 - SUMMARY AND CONCLUSIONS

10.1 Performance Characteristics of the Proposed Bearing 188
10.2 The Magnetic Repulsion System 189
10.3 Bearing Feasibility 190
10.4 Suggestions for Further Work 191

References 193
Acknowledgements 201

CHAPTER 1
INTRODUCTION

1.1 Preface

The work described in this thesis represents a preliminary examination of the large scale bearing proposed for the Salter 'duck' wave-energy converter.

No prototype of the bearing has yet been constructed. Because of its dimensions, and the hitherto untried combination of features which it embodies, it has been considered of paramount importance first to develop a sound theoretical understanding of the likely operating characteristics of the bearing. Also, because the economic viability of the bearing is governed by the volume of permanent magnet material which is used to provide a part of its load capacity, optimisation of the magnetic repulsion system for minimum magnet volume has been identified as a fundamental requirement.

Following from the above, this thesis concentrates on those topics judged to be of most importance at this early stage of the bearing's development. In some cases these are examined to an extent exceeding that required in the context of the bearing design. Similarly, certain of the experimental techniques described may be of interest only in their own right, or in terms of very different applications to that of the bearing. In both these respects, it is hoped that this does no more than reflect the nature of fundamental research.

1.2 Topics of Study: Chapter Breakdown

In chapter 2, a review is made of relevant literature. Descriptions are included of previous work, although these are necessarily brief: more detailed aspects of prior research are included within the appropriate chapters.

Chapter 3 begins with a brief description of the duck wave energy converter, followed by the specification for its main bearing. Some previous design solutions, and their limitations, are described. There then follows a description of the currently proposed bearing design, which operates on the combined principles of self-pressurised fluid lubrication, and passive permanent magnet repulsion. The bearing's operating characteristics are explained, and some details given of its construction.

In chapter 4, a preliminary analysis is made of the bearing's operating characteristics. This is based on lubrication theory assumptions, and a simplified, two-dimensional, analytical model. The results include mathematical expressions for stiffness, damping, fluid pressure, load capacity, and power dissipation; numerical values are then assigned to these quantities on the basis of provisional bearing dimensions. The various analytical assumptions are subsequently examined, and two topics which emerge as worthy of further investigation are turbulent fluid lubrication, and the influence of fluid inertia. The importance of both lies in their being potentially load-enhancing.

Chapter 5 contains a more detailed examination of the bearing's lubrication characteristics, centring on the topics noted above, ie. turbulent lubrication, and fluid inertia. The likelihood of the former occurring is estimated on the basis of a film Reynolds number criterion. An order-of-magnitude estimate of load capacity is then made assuming turbulent lubrication, and a Reynolds number-dependent 'equivalent viscosity'. This calculation, suggested by a previous analysis, is based on a 'turbulent Poiseuille flow' model. The influence of fluid inertia is then examined, and its importance found to reside in an 'indirect' effect, which, although fortuitous, may

be exploited to significantly enhance the load capacity of the bearing, and also endow it with a favourably asymmetric response.

A simplified fluid flow model is proposed to quantify the indirect effect of fluid inertia: the model is that of axisymmetric radial flow between plane parallel discs, with the fluid either diverging from, or converging towards, a central orifice. The quantity of most interest is identified as the pressure drop which, in a diverging flow, accompanies the establishment of a fully-developed velocity profile in the radial film from initial stagnation conditions upstream of the orifice. Some previous estimates of this quantity are cited, and its importance discussed in terms of the performance of the bearing. Chapter 5 concludes with a brief consideration of the overall flow pattern in the bearing lubricating film, and a suggested method for a more detailed analysis.

Chapter 6 is a record of experimental work undertaken to confirm the appropriate law governing the orifice pressure drop in axisymmetric, diverging radial flow between plane parallel discs, and also to make qualitative comparisons between the two cases of diverging, and converging flow. The influence of orifice geometry in the former case is also examined, paying particular respect to the phenomenon of flow separation. The experimental apparatus is described in some detail, as it includes certain features thought to be novel, eg. the hydrostatic load-cell, and hydrostatic calibrated-pressure source.

Chapter 7 introduces the subject of the permanent-magnet repulsion system proposed for the bearing, and lists the criteria for magnetic material selection, detailing the advantageous properties of 'hard' permanent magnets. The topic of magnet geometry optimisation is raised, where the aim of the optimisation procedures is to be able to specify any combination

of magnet pole-separation and bearing radial force or stiffness, and then find the minimum quantity of magnetic material required to achieve it. Emphasis is placed on the important difference between constrained and unconstrained optimisation procedures; previous analyses have in general been of the latter kind, which is not useful in the present application. Both procedures are nonetheless described, with respect to an isolated, two-dimensional, symmetric magnet pair: this, for reasons given, is the appropriate analytical geometry in the present case. The correct analytical models for hard magnets are then described in non-mathematical terms.

Chapter 8 contains six theoretical geometry-optimisation analyses for hard permanent magnets. The two of most importance with regard to the duck bearing are the area-constrained optimisations for maximum force and stiffness per unit length of an isolated, symmetric, two-dimensional magnet-pair. Included for more academic interest are two unconstrained optimisations of the same two-dimensional geometry for maximum force and stiffness/unit volume. The final two analyses deal briefly with a symmetric, three-dimensional magnet pair, which is optimised for maximum force, and maximum force/unit volume.

The geometry optimisation schemes differ from those previously published in several respects. Firstly, they are all based on rigorous analytical and computer-numerical methods: while prior analyses have relied on graphical estimates of function maxima, the present work invokes numerical estimates, found by seeking the zero values of analytic function derivatives. Secondly, constrained optimisation analyses of the two geometries noted above do not appear to have been carried out previously. Thirdly, the four optimisation schemes dealing with two-dimensional magnet-pairs take into account the possibility of horizontal misalignment of the opposing pole faces: the situation where the poles are perfectly aligned (previously considered in some unconstrained optimisations) thus represents

a special, rather than the general, case. The results in this chapter include estimates of the maximum force which can ever be exerted by a two-dimensional, and also by a three-dimensional, rectangular magnet pair.

In chapter 9, experiments are described which were carried out to verify the theoretical results of chapter 8. Only two-dimensional magnet geometries were investigated, and magnetic force and stiffness measurements were made using a specially designed magnetic 'levitation-bed'. This is fully described, and its ability to simulate true two-dimensional characteristics is illustrated. To interpret, and display, the experimental results, important use is made of the scaling laws for magnetic force and stiffness. These are described in chapter 8, together with the appropriate procedures for normalisisng results. Chapter 9 also includes a short discussion of the non-ideal character exhibited by experimental magnets, with a demonstration of the phenomenon of non-uniform magnetisation. The possible limitations of ideal-magnet theory in the context of the overall bearing design are noted.

Chapter 10 is a summary of the thesis, including a discussion of the overall viability of the proposed bearing, and some suggestions for further work.

CHAPTER 2
LITERATURE REVIEW

2.1 Introduction

In this chapter, a general review is made of previously published work. The review is divided into sections, roughly corresponding to the various topics examined in the thesis. More specific details of prior analyses, experimental results, etc. appear in those chapters where context justifies their inclusion.

2.2 Bearing Specification and Design (Chapter 3)

The current bearing design was first proposed by Salter (1981a) in a review of the problems facing large-scale wave energy devices in general, and the duck in particular. The 1985 reference design for the duck is described in UK Department of Energy publication ETSU R26 (ETSU, 1985a). Of the many wave energy devices originally proposed in the wake of the oil crisis of the early nineteen seventies - a good review of them is given by Shaw (1982) - the duck is one of the few still under active consideration. The characteristic duck shape was established at an early stage (Salter, 1974) to maximise energy extraction from the waves. The current specification for its main bearing is based on scale tank-tests performed using a model duck mounted on a rigid axis (Jeffrey et al, 1978), with the maximum non-reversing load in a calm sea estimated on the basis of tidal current data for a likely offshore site (Lee, 1981). In practice, active spine 'compliance' would greatly reduce the full-scale bearing loads (Salter, 1980) but the fixed-axis force figures quoted in chapter 3 are nonetheless retained as conservative design objectives.

Previous bearing design proposals have included a compound roller-cage/plain bearing (Salter, 1978), and the 'slubber'

bearing (Salter, 1980). Although both designs lacked the essentially contactless load capability of the current proposal, the slubber bearing exploited wave action to provide a self-pressurised fluid lubrication capability. This feature has been retained in the current design (Salter, 1981a) to support the large reversing wave loads, while a permanent-magnet repulsion system, acting in parallel, has been proposed to sustain the much lower non-reversing wave loads. The overall system is a magnetic-repulsion enhanced, compliant, self-acting, low pressure hydrostatic bearing. The benefits of compliance in hydrostatic thrust bearings have been demonstrated by Dowson and Taylor (1967) and Castelli et al (1967) using high-pressure oil as the lubricant, and by Levy and Coogan (1968) using low-pressure air. The closest analogue to the proposed design, however, appears to be the 'weeping' bearing, which occurs in nature, in the skeletal joints of large mammals. The mechanism of weeping lubrication has been proposed, and experimentally demonstrated, by McCutchen (1959).

Although detailed design is not the purpose of the present work, certain of the problems facing successful operation of the bearing are confronted: these include marine fouling, the proposed solution to which is based on biocidal fouling control experiments carried out by Picken et al (1981) and invokes the use of on-board electrolysis of seawater, as recommended by Hudson et al (1982); the problem of magnet axial misalignment is likewise addressed, this being threatened by the inherent instability of passive magnetic repulsion, first predicted in the classic theorem of Earnshaw (1839).

2.3 Performance Analysis (Chapters 4 and 5)

The simplified lubrication-theory analysis is an adaptation of that of Archibald (1956) who considered several squeeze-film problems, among them the dynamic loading of a two-dimensional full journal bearing, without rotation. Although his analysis is closely followed, a different integration constant to

Archibald's is assumed when deriving the bearing pressure distribution; the constant used is that determined by Kuzma (1970), who derived it from short bearing theory, in the limit of an L/D ratio tending to infinity.

The general characteristics of bearings operating in a turbulent lubrication regime have been documented by Constantinescu (1962), and include increases in both load capacity and friction, with turbulence identified as a potential advantage in water-lubricated plastic bearings. A linearised turbulent lubrication theory was developed by Ng and Pan (1965) based on the 'law of the wall', in which the derived governing equation of fluid motion was similar in form to that in the laminar flow case. The theory is applicable to systems involving shear (Couette) flow, and was found to account well for prior experimental results (Smith and Fuller, 1956, Orcutt, 1965) in terms of both overall load/displacement behaviour, and fluid pressure distribution. In a subsequent analysis of thrust-bearing performance under superlaminar conditions, Wilcock (1977) defined a Reynolds number dependent viscosity, based on an empirical fit to the theoretical results of Ng and Pan (above); he then exploited the similarities between the turbulent and laminar theories, and proceeded to make standard lubrication-theory (laminar flow) calculations, in which an effective 'turbulent viscosity' replaced the usual constant viscosity term.

2.4 Axisymmetric Radial Fluid Flow (Chapters 5 and 6)

The 'indirect' influence of fluid inertia, which is predicted to enhance the load capacity of the proposed duck bearing, was investigated in this study using the model of diverging/converging axisymmetric radial fluid flow, between plane parallel discs (see section 1.2). The radial pressure distribution in such flows was first predicted by Rayleigh (1917) on the basis of lubrication theory, ie. neglecting fluid inertia, and assuming viscous, laminar flow. The logarithmic

pressure distribution which he proposed is still universally used in those cases where inertial effects may be ignored. Of the earliest attempts to take account of fluid inertia in axisymmetric laminar radial flows, that of McGinn (1955) is outstanding: in a comprehensive theoretical and experimental study, this author proposed the radial pressure distribution to be a linear combination of Rayleigh's viscous solution, and an ideal (frictionless) fluid term including a scalar kinetic energy correction factor, to correct for the parabolic velocity profile.

More rigorous analyses than McGinn's have been made, in general invoking boundary-layer theory to derive the radial pressure distribution. Livesey (1959) and Moller (1963) used the momentum-integral method, Jackson and Symmons (1965a) employed an iterative method in which inertial effects are treated as a perturbation to viscous flow, while Peube (1963), Savage (1964), and Patrat (1975) favoured various methods of series expansion. Milne (1965) explains the basis of the various methods. Notably, the resulting expressions for pressure distribution in the last four of the above analyses reduce, in the first approximation, to that proposed by McGinn. There seems little to be gained in the present investigation by preferentially employing the results of these boundary-layer analyses: none is strictly valid at small radii (Wilson, 1972), which is the region of interest in the present study, and none includes entry conditions appropriate to the situation being modelled. One further radial-flow investigation worthy of mention is that of Raal (1978), who performed a sophisticated computer-numerical analysis. This however dealt with very low Reynolds number flows, and again employed simplified entry conditions.

Various estimates have been forwarded for the static pressure drop which corresponds to the establishment of a fully-developed parabolic velocity profile in diverging, laminar, radial flows of the kind described above. In a comprehensive review of the

effects of inertia in fluid lubrication, Milne (1965) proposed a pressure correction corresponding to the kinetic energy required to establish a parabolic profile from initial stagnation conditions. This assumption was used by Kawashima in his studies on flat-disc valves (1976, 1978), in which an additional head loss observed at the film entry was suppressed by subsequent use of a rounded inlet profile. A slightly lower estimate (see chapter 5) for the entry pressure drop was suggested by Mori and Yabe (1966, 1967) in their analyses of hydrostatic thrust bearings with multiple supply holes. These authors used a momentum-theory calculation to find the increased momentum of a parabolic, over a uniform, velocity profile, then equated the overall pressure loss to the sum of the latter's momentum contribution plus the calculated increase. A slightly different technique was used by Vohr (1969), who integrated the momentum across the width of the parabolic profile (a boundary-layer technique); this gave a lower value still for the pressure loss (see chapter 5), although agreement with experimental data was found to be good.

The phenomenon of flow separation at the entry to a diverging radial film was experimentally observed, and indeed photographed, by McGinn (1955). Moller (1963) found that a rounded inlet profile prevented formation of the separation 'bubble', a similar observation to that of Kawashima (1978). Vohr (1969) and Jackson and Symmons (1965b) noted a severe pressure drop immediately downstream of the film entry, explaining it in terms of flow separation; the latter authors also suggested that reattachment of the separation 'bubble' ocurred much further downstream, and was responsible for asymmetry in the observed radial pressure distribution. The onset of flow separation was predicted in the theoretical analyses of Ishizawa (1965, 1966) and Raal (1978), although only the latter treatment is considered strictly correct, as Ishizawa's analyses invoke an untenable flow-development model (Wilson, 1972).

A turbulent diverging flow will inevitably undergo reverse transition to laminar conditions once the reduced-Reynolds number Re^X (see chapter 6) falls below a certain critical value. Theoretical predictions of this value range from 10 (Livesey, 1959) down to 4 (Patrat, 1975). The experimental observations of Chen and Peube (1964) and Kreith (1965) tend to support the latter figure, with critical Re^X values of 4.71 and 4.06, respectively.

2.5 Permanent Magnet Principles (Chapter 7)

For an overall review of the theoretical principles and practical applications of permanent magnets, the 1977 text of McCaig is highly recommended (ref). The same author performed some of the earliest rigorous experiments using 'hard' permanent magnets (1961), and consistently advocated the correct analytical methods to use when dealing with systems comprising this type of magnet (1968).

The appropriate mathematical models to use in analyses of all-hard magnet systems (containing no 'soft' iron) are by no means new, and can be traced to the work of Maxwell (1873). A hard permanent magnet is commonly treated as either an air-cored solenoid, or as a pair of pole-faces of uniform charge-density. The two models yield identical results, and their relative merits have been compared in a comprehensive review by Craik and Harrison (1974), with special regard to cylindrically symmetric magnets. For rectangular magnets (the relevant geometry in this thesis) the external and internal field strengths can be found using analytic expressions derived by Craik (1966, 1967) on the basis of the pole model; these are given in full by McCaig (1977).

The way in which mutual forces between rectangular magnets may be calculated is well described by Tsui et al (1972) in a thorough theoretical and experimental investigation, which includes a worked example, that of repulsion between two

cube-shaped magnets. Solenoid mathematics are used, following the precedent of Borcherts (1971), and the experimental results well support the theory, although - importantly - only in cases where opposing magnets of the same material are used. Full analytic expressions for the forces of interaction between two-dimensional rectangular magnets, the geometry appropriate to many bearing analyses (including the present one), are given by Yonnet (1980). This author has published a large body of work on the topic of permanent magnetic bearings, and has pointed out the important stiffness relationships for these systems (1978a), which, according to the theorem first proposed by Earnshaw (1839), must always possess at least one direction of instability. Yonnet's publications include two excellent reviews of all-permanent magnetic bearings, covering aspects such as orientation of the magnetic vectors (1978b) and the advantages of different fundamental bearing configurations (1981a).

2.6 Magnet Geometry Optimisation (Chapters 8 and 9)

The optimisation procedures in this study all deal with isolated, symmetric, magnet pairs. Previous analyses of such configurations have relied on first deriving an appropriate objective function such as force/unit volume, or stiffness/unit volume, plotting this against the magnet dimensions, and hence finding graphically both the function maximum, and optimum magnet geometry.

Coffey et al (1972) performed analyses of the kind described above, to find the maximum force/unit volume available from two- and three-dimensional rectangular magnet pairs for a given pole separation. Minnich (1971) performed an essentially similar analysis of the two-dimensional geometry, recording identical results (see section 8.8). Cooper et al (1973) examined the case of a three-dimensional cylindrical magnet pair, finding the maximum possible force/unit volume, at a given clearance, to exceed by about 4% that available from rectangular magnets.

Yonnet (1981b) optimised the two-dimensional rectangular geometry for maximum stiffness/unit volume, and also derived an implicit analytic expression for the magnet pole-width which maximises stiffness in this configuration, given a specified pole-height and clearance. All the above optimisation analyses were unconstrained, in the sense that only pole-separation was specified, the optimum magnet dimensions then being sought without prior restriction placed on their ultimate values. The analyses all assumed full alignment of opposing magnetic poles.

One of the most thorough optimisation schemes to have been undertaken was that of Henning (1973), who sought to minimise the volume of track magnet required for a proposed permanent-magnet levitated ground vehicle. His analysis employed computer-numerical methods to find the objective function (in this case force/unit volume) maxima, by seeking the zero-values of its appropriate first derivative. Although its solutions were specific to preselected vehicle payload configurations, the analysis is noteworthy both for its rigorous mathematical nature, and because it took into account cross-interactions between the parallel rows of magnets in the track/vehicle system. Henning's analysis was soundly based on the prior work of Baran, who first described the basis of the optimisation procedure used (1971), and reported its preliminary results in a review (1972).

Indeed, a review of permanent magnet analyses, particularly of repulsion systems, would be incomplete without mention of Baran, who may be regarded as a pioneer in the field. On the basis of the pole-surface magnetic model, this author was perhaps the first to formulate analytical force expressions for two-dimensional rectangular magnet pairs (Baran, 1962), and in subsequent experiments with small permanent magnets, he employed the elegant technique of using soft iron to simulate closely spaced opposing pole-faces, thereby finding "satisfactory" agreement with theoretical force predictions (1964).

CHAPTER 3
THE PROPOSED BEARING: SPECIFICATION AND DESIGN

3.1 Chapter Summary

A brief description of the 'duck' wave-energy converter is followed by the specification for its main bearing. The limitations of conventional bearing designs in this application are noted, and two previous design proposals are described. A description of the currently proposed bearing then follows, together with an explanation of its operating principles, in which the distinct roles of fluid lubrication and passive magnetic repulsion are emphasised. Certain similarities are pointed out between the fluid lubrication characteristics of the new bearing and those which exist in a naturally occurring system. Some design features necessary to ensure a 25-year operating life in a marine environment are suggested. Finally, a mechanism is suggested to overcome the problem of magnet axial instability.

3.2 Wavepower, and the Edinburgh Duck

The duck wave energy converter was originally conceived in response to the cutback in world oil production of the early nineteen-seventies, and the current reference design is the result of a ten-year evolution process. At one time, several different wavepower devices were under active consideration by the United Kingdom Department of Energy (see Shaw, 1982), but current UK policy is unfavourable to their deployment (ETSU, 1985b). The resource nonetheless remains, and with it the continuing development of the duck.

The reference two-gigawatt wave-energy station consists of 896 ducks attached to cylindrical 'spines', moored in 80-100 metres water depth, and stationed 35km off the Scottish coast (ETSU, 1985a). Figure 3.1 shows the individual duck/spine unit.

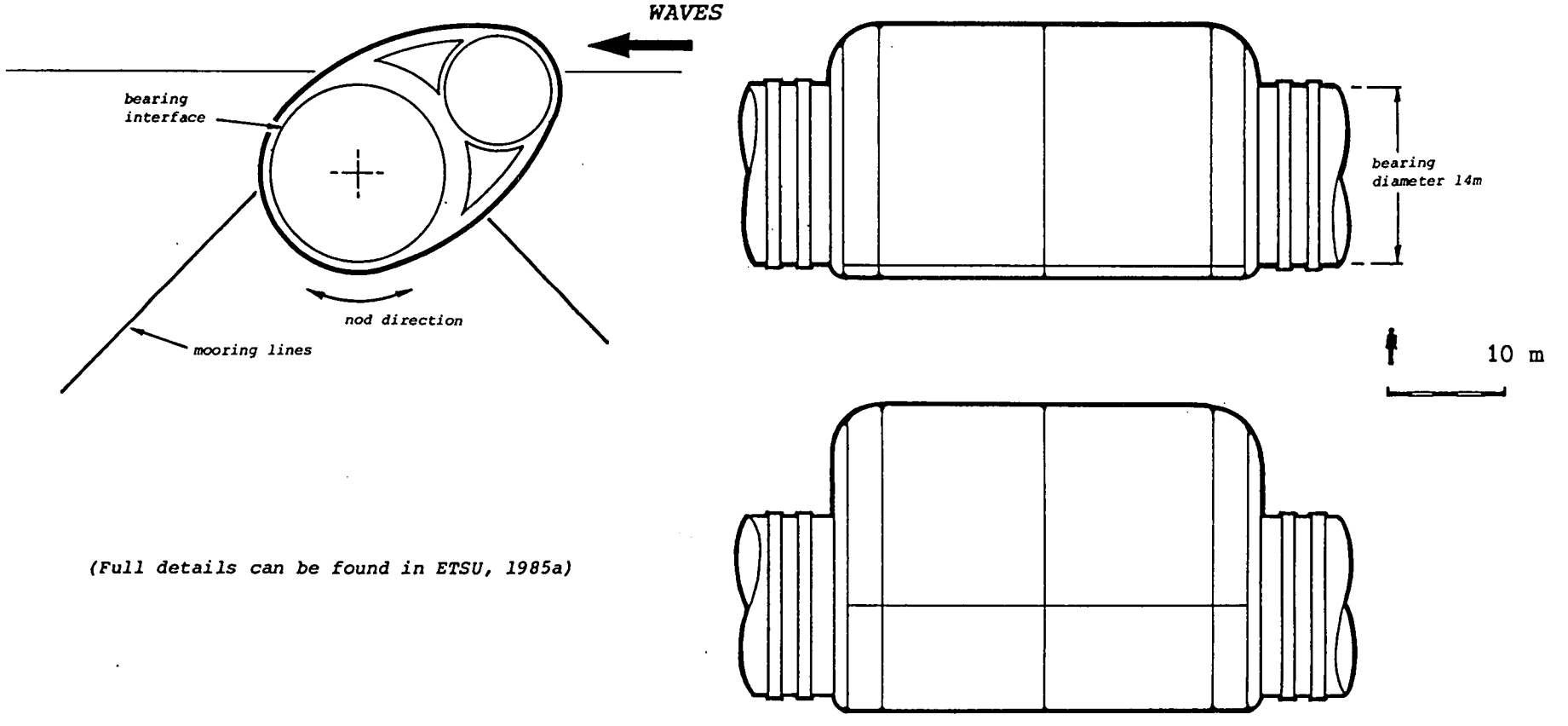

(Full details can be found in ETSU, 1985a)

FIGURE 3.1
The Duck Wave-Energy Converter

The maximum rated output of a single duck is 2.25 MW. Incident waves cause the duck to rotate, or 'nod', about its spine, and by damping this motion, energy is extracted. The cross-sectional profile of the duck has been developed to maximise the transfer of energy from the waves, and minimise the generation of new waves on the leeward side (Salter, 1974). Although the hydrodynamic principle on which the duck operates has remained unchanged since its conception, the detailed design has been subject to continuous development. One feature to have stimulated considerable thought is the main bearing between the duck and its spine. The bearing is 37m long with a diameter of 14m, and requires to meet the following specification.

3.3 The Bearing Specification

(1) The target-life for the bearing, in line with that of the overall device, is 25 years; during this period no significant degradation of performance should occur.

(2) Wave action imposes unsteady loads, which are comprised of reversing (cyclic) and non-reversing components. The peak values of the cyclic loads are estimated as 100 kN per metre of bearing length at rated output working, and 1000 kN per metre under 'freakwave' loading. The maximum period for full load reversal under the conditions of greatest continuous loading is approximately 7 seconds. The non-reversing component of wave load under rated output conditions is 10 kN per metre. These figures are based on scale-model tests of a duck mounted on a non-compliant axis (Jeffrey et al, 1978), and therefore represent conservative estimates.

(3) Non-reversing loads, due to tidal currents, can exist even in the absence of waves. The maximum load, calculated using data for a typical Hebridean wave-field with current velocity of approximately 0.5 m/s (Lee, 1981), is 60 kN per duck (1.6 kN per metre).

(4) Civil, rather than mechanical, engineering tolerances must be accomodated in the construction of the bearing. Furthermore, under the stresses imposed by wave loading the spine will bend, and remain neither truly straight nor round.

(5) A low friction bearing is required. Bearing friction will squander incident wave-energy, and reduce the efficiency of the duck. In sea conditions where maximum energy capture is required, the fractional loss of power can be taken as approximately twice the bearing's coefficient of friction (Salter, 1981a). Friction also causes wear (see requirement no.1).

(6) The bearing must operate in a marine environment, with its attendant hazards of corrosion, and marine-growth fouling. The possibility of excluding seawater from the duck-to-spine clearance is considered both unrealistic and undesirable.

(7) The bearing mechanism must be radially thin. This is to allow, for reasons of strength, the greatest possible spine diameter.

(8) The bearing surface (shear) velocity is cyclic, with a peak value of 5 m/s in the highest waves (Jeffrey et al, 1978); the bearing must be load-sustaining throughout the cycle, including periods of zero velocity.

3.4 The Choice of Bearing Mechanism

The suitability, and limitations, of 'conventional' bearing mechanisms in regard to the above specification can best be seen by examining four of the commonest types, namely plain, rolling element, fluid lubricated, and magnetic.

Plain bearings rely on solid-to-solid contact between opposing surfaces. The lowest obtainable coefficients of friction, typically 0.04 - 0.12, are probably those achieved using PTFE on

one or both bearing surfaces (Rabinowicz, 1968), but even assuming the lowest figure, a plain bearing would still dissipate 8% of the duck's incident power (see requirement 5 of the specification). More seriously, the corresponding wear would severely limit the bearing's life.

Rolling element bearings can give friction coefficients two orders of magnitude lower than the best plain designs. At one stage the roller-cage design shown in figure 3.2 was proposed (Salter, 1978): the rolling tyres are made of rubber, with the cage running at half the bearing shear velocity. In heavy sea conditions, the wave loads cause the tyres to compress, and the cage to default to behaving as a plain bearing element: in this way, the power loss is significant only in conditions when power is abundant. Despite its ability to greatly reduce frictional losses, the design still required large bearing loads to be taken by solid-to-solid contact, with the inevitable consequence of wear. This characteristic ultimately precluded all rolling element designs.

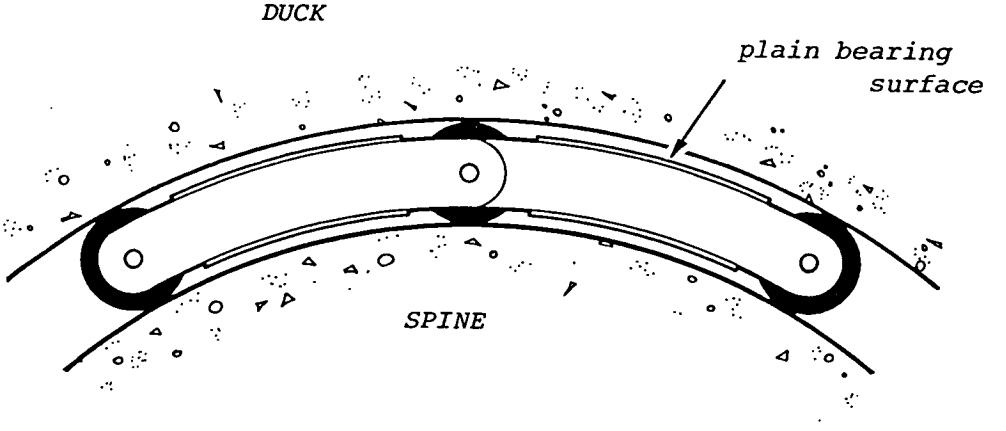

FIGURE 3.2
An Early Bearing Proposal (Salter, 1978)

Fluid-lubricated bearings offer lower friction still, and furthermore, the losses in a correctly-operating fluid bearing do not result in surface wear. Of the three basic types which can be considered: hydrodynamic, squeeze-film, and hydrostatic, the first must be discounted. Hydrodynamic bearings can support no load without relative movement of the opposing surfaces, and are therefore unsuitable in the present application (see specification part 8).

In a pure squeeze-film bearing, the load capacity is generated by surface approach velocity. Although the annular space between the duck and spine cannot be directly used as a squeeze-film bearing (which would require too fine, and too accurate, a clearance), the cyclic loading regime is ideal for self-pressurised lubrication of a similar kind; this, indeed, is the basis of the current bearing design (see section 3.5).

In a hydrostatic bearing, coefficients of friction as low as 10^{-6} can be achieved. Conventionally, such bearings require high-pressure oil supplies, very fine clearances, and metal surfaces which have been machined to very fine tolerances. A bearing of this sort is clearly ill-suited to the duck's imprecise geometry and harsh working environment. However, the hydrostatic principle can be applied under very different conditions. The presence of at least one compliant surface has been demonstrated to increase load capacity (Dowson and Taylor, 1967, Castelli et al, 1967) and the only constraint on lubricant pressure is that it be sufficient to support a given load: Levy and Coogan (1968) have successfully demonstrated a compliant-surface, hydrostatic thrust-bearing using low-pressure air as the lubricant.

The characteristics of a low-pressure, compliant hydrostatic bearing, ie. the ability to support large loads in an evenly-distributed fashion, operate with very low friction, and incur no wear, were at an early stage identified as ideal for the present application. The original design to exploit them was the 'slubber' bearing, essentially a self-pressurising, compliant hydrostatic bearing (Salter, 1980). The slubber bearing incorporated many of the principles of the present design, and can be regarded as its immediate predecessor. Its operating characteristics are explained by referring to figure 3.3.

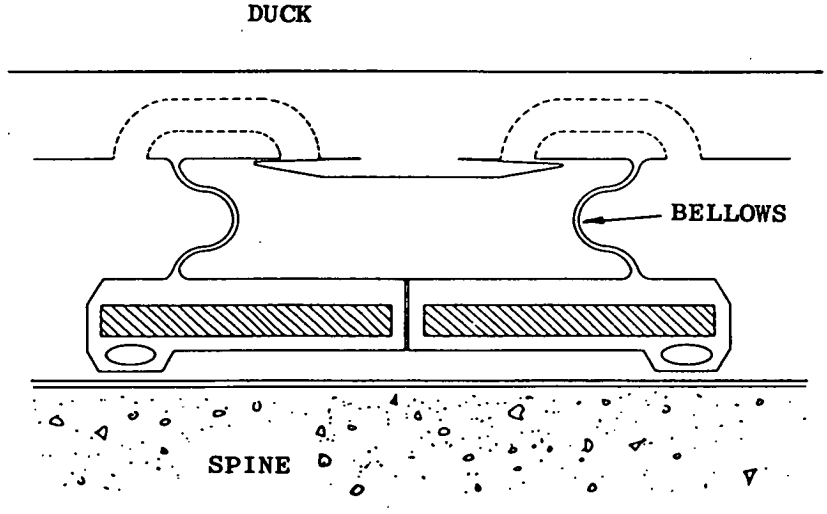

FIGURE 3.3
The 'Slubber' Bearing (Salter, 1980)

The inner surface of the duck is covered with a large number of pads of the type shown. Because of the pad geometry, a positive load causes the water pressure in the flexible bellows-chamber to rise above that outside in the duck/spine gap; water flows via a restriction to the pocket below, from where it leaks out between the land and the spine surface. The two never make

contact. The pad acts exactly like a circular thrust bearing when positively loaded, and non-return valves allow its bellows chamber to recharge during the negative half of the load-cycle. In this way the slubber bearing exploits to advantage the seemingly harshest features of its operating environment. The necessity of a seawater-filled clearance is used to provide the bearing with a lubricant, while the cyclic nature of the major wave loads supplies a natural pumping action, operating in perfect phase with the applied load.

Unfortunately, despite the ideal cyclic-load characteristics of the proposed slubber bearing, it suffered from the inability to support non-reversing loads, however small, without some measure of solid-to-solid contact. The current design overcomes this problem, by including a parallel load element which is able to sustain the relatively modest non-reversing loads, using passive permanent magnet repulsion (see section 3.5).

There are two major types of magnetic bearing, active and passive. Active bearings are deemed unsuitable for the present application on the grounds of too-high power consumption, potentially requiring several hundred watts of power per tonne of load (Salter, 1981a). Passive magnetic bearings employ permanent magnets arranged either in attraction or repulsion, and require no power. The maximum load capacity depends on the magnet material used, and the bearing geometry. Although the strongest permanent magnets available today can exert maximum pressures of up to 500 kPa (73 psi), these are little more than exotic laboratory specimens; the corresponding best which can be achieved using more conventional magnets is about 36 kPa (5.2 psi). Although this would be insufficient to support large alternating wave-loads, it is of a suitable order to support the smaller non-reversing loads. Passive magnetic bearings operate as contactless mechanisms, and this feature, allied to their zero power requirement, makes them ideal in the present context.

3.5 The Proposed Bearing

The current bearing design was first proposed by Salter (1981a); figure 3.4 shows a cross-section taken parallel to the spine axis. The clearance between the 'hard' surfaces of the duck and spine is relatively large (provisionally 150 mm), but is mostly taken up by a compressible sponge-like lining, attached to the inner surface of the duck. This lining is completely filled with seawater, and has the characteristic that, when compressed,

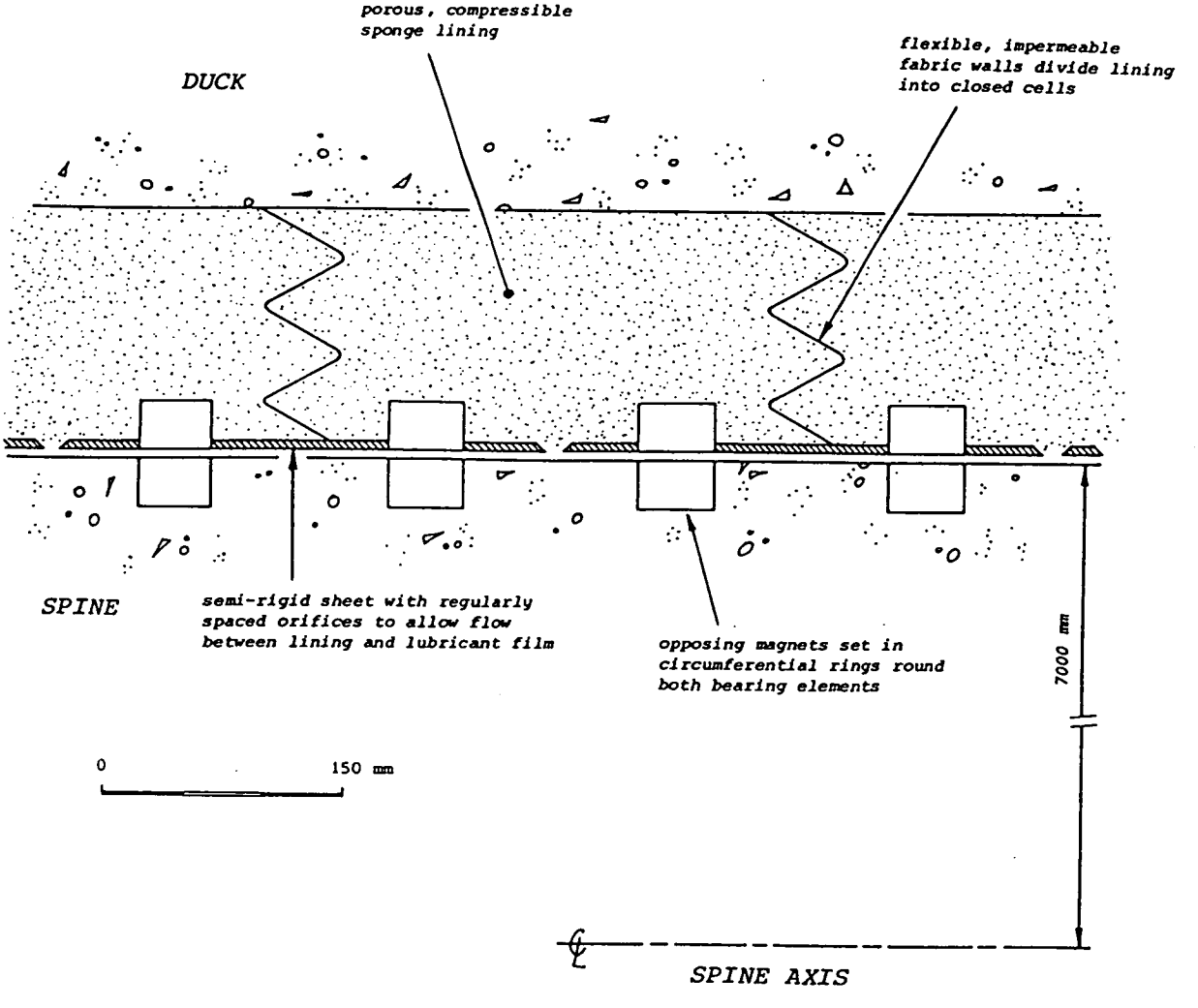

FIGURE 3.4: Cross Section of the Proposed Bearing

it allows water to be squeezed out only into the narrow clearance between its base and the surface of the spine. The function of this narrow clearance is to entrain a lubricating film. Lateral flow within the lining is prevented by a combination of its own impedance, and the presence of flexible, impermeable fabric walls, which effectively divide the lining into closed rectangular (or other shaped) 'cells'.

The base of the lining is bonded to a semi-rigid sheet with regularly-spaced orifices in it, these representing the only route by which water can pass between the lining and the narrow clearance. Fixed to the sheet are permanent magnets: these take the form of rectangular blocks laid end-to-end, forming parallel closed rings round the circumference of the bearing. Opposite the magnets in the sheet, and oriented in mutual repulsion with them, are similar rings inlaid in the surface of the spine. Both the compressible lining and the repelling magnets have spring characteristics, and when an external force acts to close down the duck-to-spine hard clearance, the lining thickness and the magnets' pole separation decrease in inverse proportion to their relative stiffnesses.

Assuming lateral fluid pressure gradients to be small, it is the ratio of magnetic to lining stiffness which alone dictates the dimensions of the thin lubricating film. The magnetic stiffness is much the greater, provisionally by up to 50 times, so that a force which causes a large lining compression gives rise to a much smaller decrease in pole clearance. In this way, the lubricating film can potentially be maintained despite large relative excursions of the duck and spine. Although the film equilibrium thickness, provisionally 2-3 mm, is very large by normal lubrication standards, the ratio of film thickness to flow path-length is of the order of 10^{-4}, similar to that of a small scale squeeze-film bearing.

3.6 Operating Principles

Consider now, the effect of a wave load acting on the duck, and tending to close down the bearing 'hard' clearance. As the two hard surfaces approach, the compliant lining compresses, causing water to be squeezed out of the lining into the narrow-clearance, where it is then free to flow axially to the ends of the bearing, or circumferentially round to the other side, according to the local pressure gradients. Flexible impedances incorporated at the extreme ends of the bearing can be used to encourage flow preferentially round its circumference. No lateral flow of water takes place within the flexible lining, which discharges the water it contains via the orifices in the magnet-sheet, into the lubricating film: the sheet effectively behaves as a compliant hydrostatic thrust pad with multiple supply holes.

With a favourably high film thickness ratio (ie. an escape path several thousand times the thickness), significant increases in fluid pressure, and hence load capacity, can potentially be sustained. However, the bearing dimensions should ensure that the fluid pressures and pressure gradients will, in absolute terms, be very low. The pressure gradient across the width of the hard clearance will largely be that associated with the orifice discharge of water from the lining, and to a first approximation, the film thickness will be independent of local water pressure (it is explained in section 5.5 how the orifice pressure drop should actually enhance load capacity). The duration for which the bearing can sustain a wave load will be determined by the time it takes to completely discharge the lining, and is potentially many times greater than the reversal time of the longest wave-loads.

While the squeezing action on the loaded side of the bearing discharges water from the lining, the lining on the other side recharges. This not only results in the bearing being ideally suited to a cyclic load regime, but also has the important

consequence that both 'loaded' and 'unloaded' sides of the bearing contribute to the overall load capacity (and should strictly be referred to as positively and negatively loaded). The recharging lining draws water back through a clearance almost as narrow as that on the positively loaded side, and a negative pressure gradient will therefore exist in the lubricant film, corresponding to a positive contribution to the overall load-capacity. The net effect is an even spreading of the load round the entire bearing circumference.

In this way, the large cyclic loads are resisted by hydrostatic pressure, self-generated in the bearing. The non-reversing loads can create no such pressure, and are instead supported by permanent-magnet repulsion. The magnet arrangement is essentially that of a stacked multi-element radial bearing, where each element consists of two concentric rings of rectangular section (the inner ring being that on the spine surface). Precompression of the compliant lining during bearing assembly is proposed to establish the equilibrium magnetic pole clearance.

The magnets and compliant-lining represent a pair of springs connected in series; the relative displacement of duck to spine under a non-reversing load will therefore be dictated by the weaker spring, ie. the lining. The essential lubricating film thickness should be maintained despite significant non-uniformities in the spine geometry: the semi-rigid sheet in which the magnets are mounted is designed to be rigid locally, but with sufficient compliance to conform to large-scale deviations of the spine surface, and this characteristic ought to be enhanced by a high value of magnetic repulsion stiffness.

The key features of the proposed design are an ability to withstand low non-reversing loads indefinitely, and large alternating loads for periods greatly in excess of those which ever occur in practice, in both cases without the load-carrying

surfaces ever touching: the bearing has thus been designed for zero wear. This does not imply zero friction, but means that any frictional energy losses will take place entirely within the lubricating water.

3.7 Design Details, and a Precedent

The same pressure gradients which dictate the flow in the lubricating film also exist in the compliant lining directly above it. Because the pressure gradients will be low, however, the lining need have only modest resistance to lateral fluid flow. A natural or synthetic foam rubber is the most probable material for the lining; the flexible cell walls can be made from fabric-reinforced rubber. For the semi-rigid sheet in which the magnets are embedded, a material is required which has the characteristics of thin plywood, or glass-reinforced plastic. One suggestion is for a rubber sheet stiffened with wire mesh (Salter, 1981a). The nature of the magnets themselves is discussed in greater detail in chapter 7, but it can briefly be noted that the magnetic blocks will be made of anisotropic barium or strontium ferrite, which materials combine the favourable properties of good magnetic strength and stability in repulsion applications, total resistance to corrosion, and relatively low cost.

The proposed design has been called a 'magnetically enhanced squeeze-film bearing', but this is a misnomer. In a true squeeze-film bearing, the fluid-flow in which the load-capacity is developed is bounded by two converging bearing surfaces; in the duck bearing, the lubricating film-width stays approximately constant during a load cycle, with relative movement of the two surfaces contributing very little to load pressure. A strict description of the bearing would be 'magnetic-repulsion enhanced, self-pressurising, compliant-hydrostatic'. Although this combination of features is perhaps novel, it may be observed that the design actually comprises a parallel arrangement of two well-established components. The first of

these is a passive permanent-magnet repulsion bearing. The second has been called a 'weeping', or 'sponge-hydrostatic', bearing, and exists in nature, in the articular joints of various species of large land mammal.

The mechanism of weeping lubrication was first proposed by McCutchen (1959) to explain the ability of skeletal joints to support very high loads - up to one ton per square inch - with minimal friction, notably in cases where the relative velocity of the 'bearing' surfaces is negligibly low. Figure 3.5 shows a typical skeletal joint.

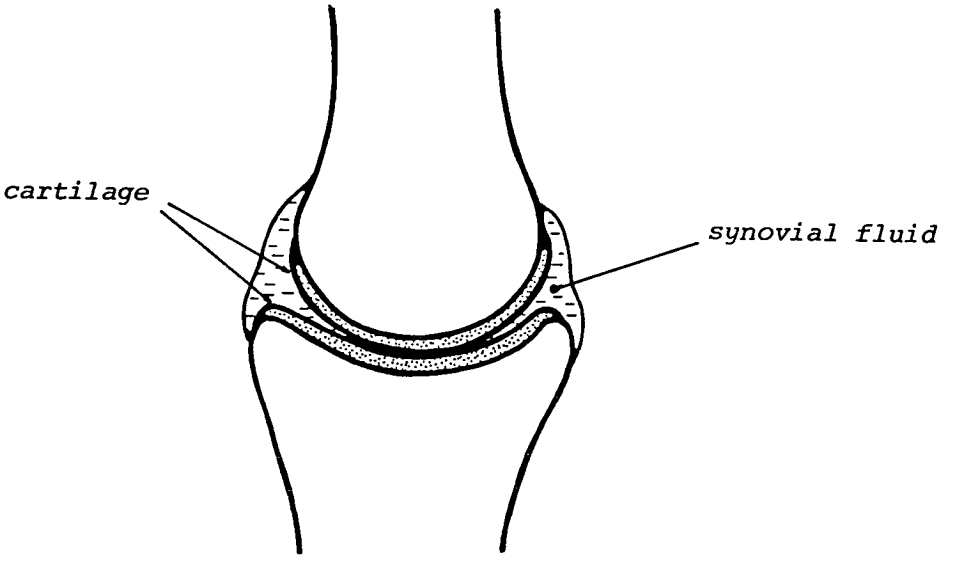

FIGURE 3.5
The Skeletal Joint - a 'Weeping' Bearing (after McCutchen, 1967)

The opposing surfaces are each covered with a layer of articular cartilage, resembling a microporous sponge, which is filled with a liquid lubricant (the synovial fluid). An applied load causes the cartilage to compress, and 'weep' fluid into a tiny clearance between the surfaces, from where it has a long escape-path to the edges of the joint. Fluid pressure thus builds up sufficient to support the load; the cartilage acts in parallel, but only experiences the small compression force dictated by its own stiffness. For the joint to operate in this manner, the cartilage characteristics must be very similar to those of the proposed lining for the duck bearing: indeed, in one experimental simulation, McCutchen used a layer of closed-cell sponge with pinhole perforations in it to direct the flow - an arrangement very similar to that shown in figure 3.4. His experiments proved the mechanism to work, but highlighted that a positive load capacity can only be sustained for a finite time, after which the compressed surfaces have to recharge with fluid.

The articular joint is not a perfect analogue of the duck bearing, however, as it does not rely entirely on weeping lubrication (McCutchen, 1967; Dowson, 1967) and some degree of surface-to-surface contact occurs. In the duck bearing, natural 'running repairs' will not be possible, and for this reason the permanent-magnet system is included to ensure zero surface contact. Nonetheless, the operating principle of the weeping bearing is obviously sound, and it can be argued that it has been more thoroughly developed and tested than that of any other.

3.8 Designing for 25-Year Life

Two major threats to the specified design life of the bearing are corrosion, and marine fouling - the disadvantages of an open bearing which uses seawater as a lubricant. To prevent corrosion, non-metals will be used almost exclusively in construction, eg., plastics, natural and synthetic rubber, and

glass-reinforced plastic. Ferrite magnets do not corrode by virtue of their chemical composition, which is very similar to that of the iron oxide in rust.

To prevent marine fouling, and in particular the potential growth of hard-shelled species on the bearing surfaces, treatment of the bearing water with a biocide is proposed. Although dependent on the level of wave action, the time taken for complete exchange of the water in the bearing will be long (provisionally 24 hours), thus maximising the efficiency of any toxic agent released into the clearance. One of the most effective methods of fouling prevention is continuous low-level chlorination. The concentration of this toxin is of less importance than the length of time for which it is administered (Picken, 1981), and the presence of 0.02 - 0.05 ppm of chlorine continuously active in the bearing would be enough to deter the settlement and growth of hard fouling species which could resist much higher intermittent doses of the biocide. Chlorine generation by on-board electrolysis of seawater is possible, and has been recommended as particularly suitable for wave-energy converters, due to the ready availability of electricity, the absence of ecological side-effects, and the safety of installation and operation (Hudson et al, 1982).

3.9 Magnet Axial Alignment

The bearing has so far been described as a pure non-contact design. There is, however, a fundamental reason why this can never be entirely true in practice, and that is the inherent instability of passive magnetic repulsion. This instability applies equally to attractive systems, and was first identified by Samuel Earnshaw in his classic theorem of 1839 (ref). The theory shows that completely free levitation using passive permanent magnets can never be stably achieved, and that there must always exist at least one direction in which movement will be unstable. For the magnets in the bearing, this direction is parallel to the spine axis. In another form, Earnshaw's theorem

shows that for a bearing of this kind, the stiffer the magnetic repulsion is radially, the greater will be the axial instability (see section 8.3).

It is therefore necessary to provide some mechanical means to restrict the relative axial movement of the magnetic rings, and keep their opposing pole-faces aligned. One method suggested for doing this is illustrated in figure 3.6.

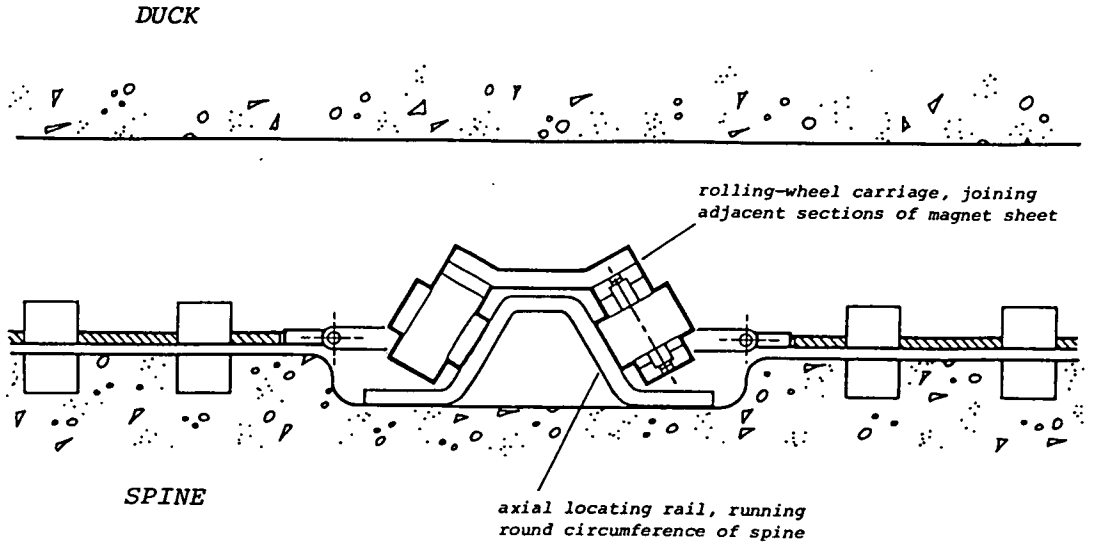

FIGURE 3.6: A Possible Magnet Axial-Alignment Mechanism

The sheets in which the outer (duck) magnetic rings are mounted are connected together at their edges by a number of rolling-wheel carriages, which run on circumferential locating rails set in the spine surface. As the duck rotates, the mechanism ensures that the magnets on the two opposing surfaces remain axially aligned. The system is designed to be tolerant to large shear movements of the compliant lining. The radial forces which keep the wheels on the rails are very low and

practically constant, being dependent only on the lining stiffness, and not the fluid pressure. With the magnets in perfect alignment, the axial forces are theoretically zero, and so the nearer this condition can be met, the less will be the wear of the rolling wheels. The angled section of the rails shown in figure 3.6 is designed to ensure that, assuming equal wear of the wheels on either side, no misalignment will result.

3.10 Conclusions

The bearing specification has been detailed, on the basis of scale-model experiments. To meet the specification, the current bearing proposal combines the principles of self-pressurising, compliant, hydrostatic lubrication, and permanent-magnet repulsion. The bearing uses treated seawater as its lubricant, and exploits the large scale of the duck in its operation, with a lubricating film thickness ratio comparable to that of a small scale squeeze-film bearing. The large cyclic loads imposed by wave action will be supported almost entirely by fluid pressure, and the lower non-reversing loads by magnetic repulsion. The design is contactless, save for the necessary magnet axial alignment mechanism: this, however, is subject to only small and uniform loads. Load distribution over the bearing area will be even, with fluid pressures and pressure gradients low as a result. To ensure its longevity, the bearing will be constructed from non-corroding materials, and the seawater lubricant will be electro-chlorinated to prevent fouling.

CHAPTER 4
PERFORMANCE ANALYSIS

4.1 Chapter Summary

In this chapter, a preliminary analysis is made of the bearing's performance characteristics. Both static and dynamic loading are considered, in the latter case using a simplified two-dimensional model and 'classical' lubrication theory assumptions. The results include expressions for bearing stiffness and damping which are subsequently incorporated in an equation of motion, in order to estimate the bearing's response to cyclic loading. On the basis of provisional bearing dimensions, performance characteristics are calculated including maximum eccentricity, maximum power dissipation, temperature rise, friction coefficient, and maximum fluid pressure. The assumptions made in the analysis are examined, and the desirability of an asymmetric response to cyclic loading is explained.

4.2 Analytical Model

In order to make useful predictions of the bearing's performance characteristics without invoking a prematurely high level of mathematics, a simplified model of the system is proposed. With reference to figure 4.1, the following assumptions are made:

(1) The bearing is assumed to be two-dimensional, with all fluid flow taking place in the plane of figure 4.1. End leakage is therefore neglected.

(2) The compliant lining is represented as a porous, isoelastic layer attached to the inner surface of the duck, and occupying most of the duck-to-spine hard clearance. The lining is absorbent, in the manner of a sponge, but possesses anisotropic flow characteristics. Water can flow only radially in or out of it, according to whether it is being recharged or discharged,

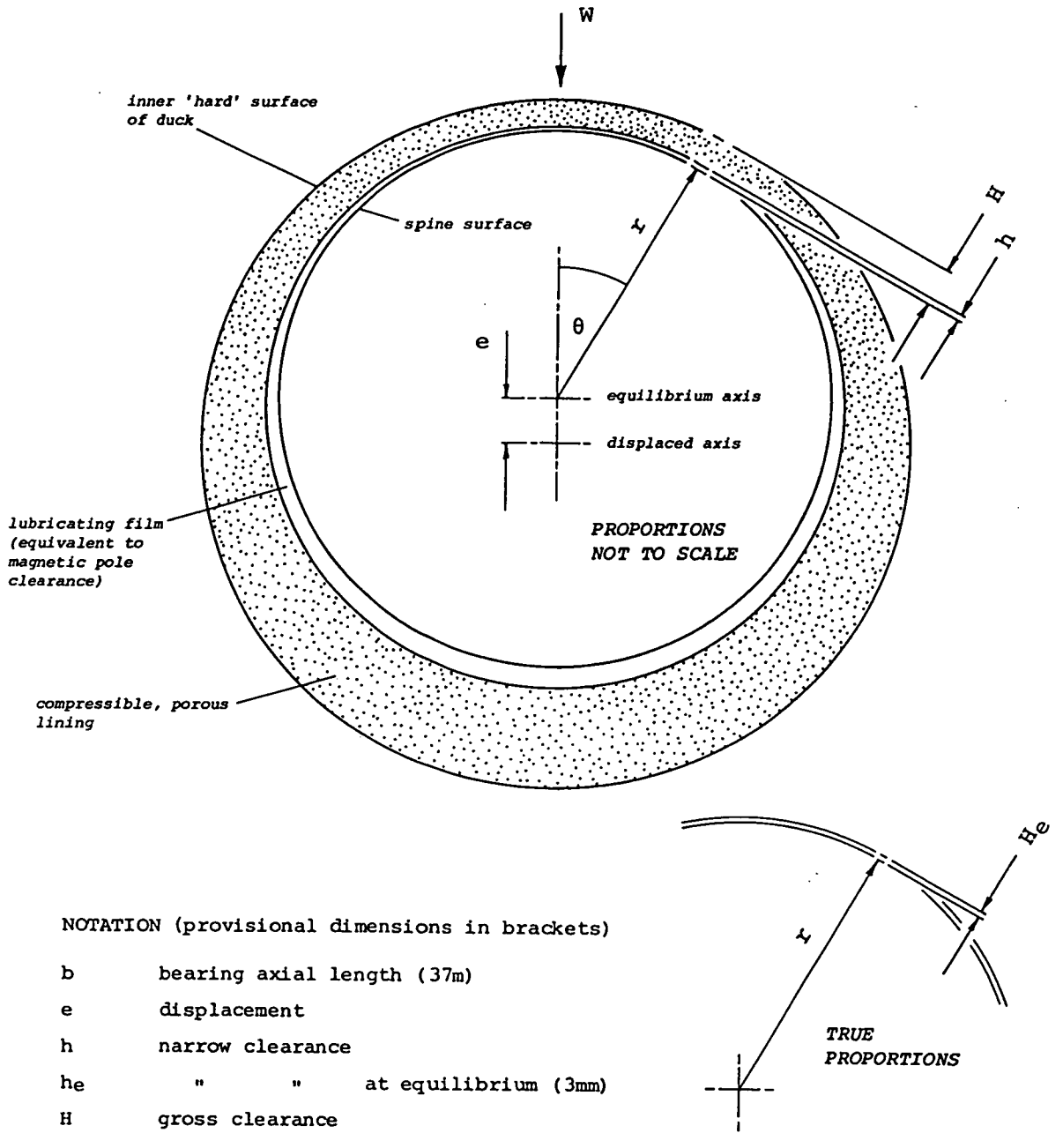

NOTATION (provisional dimensions in brackets)

b	bearing axial length (37m)
e	displacement
h	narrow clearance
h_e	" " at equilibrium (3mm)
H	gross clearance
H_e	" " at equilibrium (0.15m)
r	spine radius (7m)
W	applied load

NON-DIMENSIONAL PARAMETERS

E	eccentricity = e/H_e
m	gross clearance ratio = H_e/r (0.021)
λ	lining thickness ratio = h/H (0.020)

FIGURE 4.1
Bearing Cross Section: Diagrammatic

respectively, and no lateral flow takes place within it. In this way, a given section of the lining can communicate water only into or out of the narrow clearance bounded by its base, and the surface of the spine. No losses are assumed in the flow in or out of the lining, and hence, pressure gradients across the hard clearance are neglected, with the pressure in the lubricating film taken to be the same as that in the adjacent lining.

(3) The semi-rigid sheet which forms an inner skin to the lining, and on which the duck magnets are fixed, is ignored. Although water flows in and out of the lining only through the orifices in this sheet, these are disregarded, and flow across the lining inner surface is assumed to occur uniformly over its area. The magnetic rings are not considered as rigid elements; bending and shear forces in the magnet sheet are neglected, and its mass and thickness are also disregarded.

(4) The radial stiffnesses of both the lining and the repulsion magnet system are taken to be constant. Both elements could be mechanically represented by annular nests of radially-directed springs. In the case of the lining, both axial and circumferential strain are neglected. Similar assumptions have been made in analyses of compliant-surface thrust bearings with elastomeric surfaces (see Castelli et al, 1969): in the present case, however, the compliant lining is both compressible and porous, unlike an elastomer.

(5) 'Classical' lubrication theory assumptions are made: flow in the lubricating film is assumed to be viscous-dominated and laminar, with fluid inertia neglected.

In due course several of the above assumptions, not least those pertaining to lubrication theory, are placed under scrutiny.

4.3 Stiffness Characteristics (Static Loading)

Under a static displacement e from equilibrium, the gross (hard-surface) bearing clearance H is given approximately by:

$$H = H_e - e\cos\theta \tag{4.1}$$

The compliant lining thickness is approximately equal to the entire gross clearance. Hence if the lining compressibility constant, with units of pressure per unit radial deflection, is k_s, then the local spring pressure P_s exerted on the inside of the duck at angle θ to the load-line is found from:

$$P_s = P_s(\text{equiln.}) + k_s e\cos\theta \tag{4.2}$$

The applied static load W_s is resisted by this pressure according to:

$$W_s = 2\int_0^{\pi} P_s br\cos\theta\, d\theta \tag{4.3}$$

And hence, using the non-dimensional notation given in figure 4.1,

$$W_s = k_s b\pi m r^2 E \tag{4.4}$$

Thus the static deflection obeys a linear spring law. The lining compressibility constant k_s would be chosen to match a desired maximum static eccentricity E to a particular static load W_s. The other terms in equation 4.4 are determined by the bearing dimensions.

4.4 Damping Characteristics (Dynamic Loading)

The following analysis is an adaptation of that of Archibald (1956), who considered the case of a two-dimensional full-journal bearing, subject to dynamic loading, but without rotation (one of a number of squeeze-film analyses carried out by this author). In his analysis, Archibald first derived an

expression for the circumferential pressure gradient in a dynamically loaded journal, by equating two expressions for lubricant flowrate. One of these was based on geometric considerations, and the other on the lubrication-theory expression for the one-dimensional flow of a viscous fluid between plane parallel walls (see eg. Barwell, 1979). Expressions for pressure distribution and load were subsequently found by integration. In the present case, Archibald's analysis is adapted to take account of the compliant lining in the duck bearing (whose simplified properties are noted above).

Consider a constant load W_d acting on the outer bearing element, causing time-dependent displacement e and velocity $\dot{e}$. At an angle Θ to the load-line, the volume flowrate through the narrow clearance h is found from geometric considerations by:

$$q = br \sin\Theta \, de/dt \qquad \textit{(displacement flow)} \tag{4.5}$$

in which all the fluid squeezed out of the compliant lining is assumed to flow through the narrow clearance maintained by magnetic repulsion. From lubrication theory, the flowrate is also given by:

$$q = \frac{-bh^3}{12\mu r} \, dP/d\Theta \qquad \textit{(viscous flow)} \tag{4.6}$$

Equating these gives the circumferential pressure gradient:

$$dP/d\Theta = \frac{-12\mu r^2 \sin\Theta}{h^3} \, de/dt \tag{4.7}$$

Assuming negligible pressure gradients across the gross clearance, the narrow clearance h is determined only by the balance of spring forces on the two sides of the magnet sheet. If these are selected to obey a linear relationship, with:

$$h = \lambda H \tag{4.8}$$

then the pressure gradient is given by:

$$dP/d\theta = \frac{-12\mu \sin\theta \; dE/dt}{m^2 \lambda^3 \; (1 - E \cos\theta)^3} \qquad (4.9)$$

in which non-dimensional notation is again used (see figure 4.1). The pressure distribution round the circumference is found by integrating equation 4.9, hence:

$$P(\theta) = \frac{6\mu \; dE/dt}{m^2 \lambda^3 E} \left\{ \frac{1}{(1 - E \cos\theta)^2} + C_i \right\} \qquad (4.10)$$

in which C_i is a constant of integration, whose value is taken as that determined by Kuzma (1970) for a two-dimensional full journal bearing, ie.:

$$C_i = \frac{-2}{(2 + 3E^2)} \qquad \text{(Kuzma, 1970)} \qquad (4.11)$$

In Kuzma's analysis, the constant is derived from short-bearing theory, in the limit of an L/D ratio tending to infinity; the author explains why only this approach is strictly correct. The value of C_i does not however influence total dynamic load W_d, which is found by integrating incremental pressure loading round the bearing circumference (cf. equation 4.3). Doing this in the present case, the load is found from:

$$W_d = \frac{12\pi\mu br \; dE/dt}{m^2 \lambda^3 (1 - E^2)^{3/2}} \qquad (4.12)$$

The above result invites comparison with the two cases of:

(1) A conventional journal bearing of the same length and diameter, and clearance equal to the present gross clearance H.

(2) A journal bearing of again the same dimensions, but clearance equal to the narrow (lubricating film) clearance h.

In the first of these, the load is found from equation 4.12 using $\lambda = 1$, with the resultant load value then λ^3 times that

for the proposed bearing. In the second case, the load will be λ times that of the new bearing. The constant λ, which represents the lubricating film thickness to gross clearance ratio, is provisionally 0.02: the proposed design is thus predicted to have 125,000 times the load capacity of a similarly sized journal-bearing, and, perhaps surprisingly, 50 times the load capacity of a bearing with one-fiftieth the hard-surface clearance. To explain the latter finding, the new design could be compared to a journal bearing with narrow clearance h, and a replenishable lubricant supply which increased its load-supporting time by a factor of $1/\lambda$.

4.5 Frequency Response

Consider, now, the outer bearing element to be subject to a unidirectional alternating load $F_0 \sin\omega t$, representing the component of wave load causing relative movement of the duck and its spine (as opposed to simultaneous acceleration of both components). If the effective mass of the duck, including added hydrodynamic inertia terms, is M, then the equation for the relative motion will be:

$$M \, d^2e/dt^2 = F_0 \sin\omega t - \sum \text{bearing forces} \qquad (4.13)$$

The bearing forces are given by equations 4.4 and 4.12, and hence:

$$M\ddot{E} + C\dot{E} + KE = (F_0 / mr) \sin\omega t \qquad (4.14)$$

where:

$$C = \frac{12\pi\mu b}{m^3 \lambda^3 (1 - E^2)^{3/2}}$$

$$K = k_s b \pi r$$

It can be seen that the damping coefficient C is nonlinear, increasing with eccentricity E - however, if E is small, then:

$$C = \frac{12\pi\mu b}{m^3 \lambda^3} \qquad (4.15)$$

and under these conditions the equation of motion may be treated as linear. If the provisional dimensions given in figure 4.1 are now used to assign numerical values to the above coefficients, and assuming a lining compressibility constant k_s of 9190 N/m^2 per metre deflection, the following values are found:

$$C = 1.77 \times 10^{10} \ kgs^{-1}$$

$$K = 7.48 \times 10^{6} \ kgs^{-2} \qquad (4.16)$$

Because of its added inertia, the duck's effective mass M is dependent on wave-frequency, but will be of the same order as the 'dry' mass of 3400 tonnes (3.4×10^6 kg). Using these figures it may be seen that damping very strongly dominates the equation of relative motion (equation 4.14), with a ratio of actual to critical damping in excess of 1000. Forced resonance poses no apparent threat to the bearing. The dimensionless response of the bearing to the forcing function can then be found from the approximate formula:

$$E = E_{max} \sin(2\pi ft - \pi/2) \qquad (4.17)$$

where:

$$E_{max} = \frac{F_0}{2\pi fmrC}$$

The maximum hard-surface approach velocity is given in dimensional, and non-dimensional, forms respectively by:

$$\dot{e}_{max} = \frac{F_0}{C} \tag{4.18}$$

$$\dot{E}_{max} = \frac{F_0}{mrC} \tag{4.19}$$

Figure 4.2 is a plot of E_{max} against wave frequency, assuming the maximum-ever (freakwave) force amplitude F_0 of 37 MN. In practice, wave loads of this size would not occur cyclically, but as isolated and random events: use of this figure is therefore conservative. In general, little power is found in waves outside a band with period 5-25 s (Silvester, 1974), and from figure 4.2 the highest value of E_{max} in this range is approximately 0.06, corresponding to 6% maximum eccentricity. Such a small value of E_{max} can be used to justify the original assumption of constant damping C (see equation 4.14).

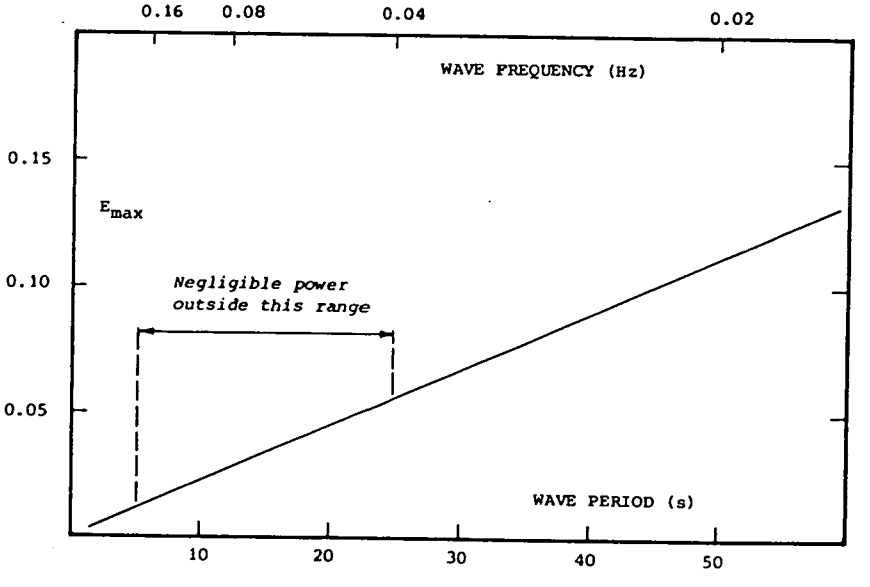

FIGURE 4.2: Bearing Frequency Response. Maximum eccentricity vs wave period, assuming a freakwave force amplitude F_0 of 37MN.

The response of the bearing to real, irregular wave loads can be investigated on the basis of the linearised equation of motion, and experimental wave force records. Figure 4.3 shows time-records of the two orthogonal components of wave force in a typical 'mixed' sea.

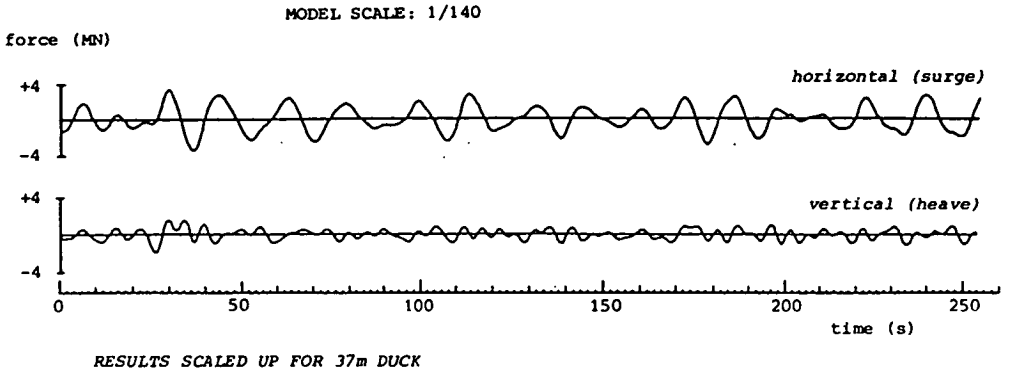

FIGURE 4.3: Experimental Wave Force Records

The measurements are scaled up from model test results. The bearing response to these may be predicted either by first using a Fourier analysis to convert the force records to a set of component frequencies, and then summing the individual responses to these, or more directly by examining an integrated force record, the instantaneous value of which is approximately proportional to bearing displacement. Although neither analysis is included here, the bearing response is predicted to be 'safe' due to the continually reversing nature of the loads shown in figure 4.3, and the comparatively small magnitude of the non-reversing components (see section 3.3).

On the basis of the analysis so far, the operating characteristics of the bearing are predicted to be favourable. It is therefore important to now examine in more detail some of the assumptions underlying the simplified analytical model.

4.6 The Two-Dimensional Approximation

For plain journal bearings, the assumption of no axial flow is usually deemed reasonable for L/D (length/diameter) ratios greater than about four (see eg. Massey, 1979). Although the duck bearing has an L/D ratio of 2.64, it can incorporate flexible impedances at its ends to minimise axial leakage and increase its 'effective L/D ratio'. However, even assuming end leakage to halve the minimum damping coefficient C, the result would still be only 12% maximum eccentricity under freakwave loading.

Skew loading must also be considered. Because incident waves are not in general parallel to the bearing axis, phase differences will exist between the forces experienced along its length. The instantaneous difference in the force exerted at the two ends of the bearing can be roughly estimated using theoretical correlation coefficients for multidirectional wave spectra (Salter, 1981b): these reflect the similarity of the instantaneous forces at different distances along the length of the duck. Assuming the most severe conditions, the difference in force is predicted to be about 30% of the mean value. The precise effects of skew loading require more detailed analysis, but no catastrophic implications seem obvious at this stage.

4.7 Nonlinear Stiffness

So far, constant stiffness has been assumed in both the compliant lining and the repulsion magnet system. In practice, however, magnetic stiffness increases strongly with decreasing pole separation (see section 8.3). A comparison of the relationships between narrow and gross clearances (h and H respectively) for the two cases of constant and nonlinear magnetic stiffness is seen in figure 4.4. The nonlinearity depicted is arbitrary, but chosen to represent a case where the equilibrium film thickness h_e is the same in the two cases.

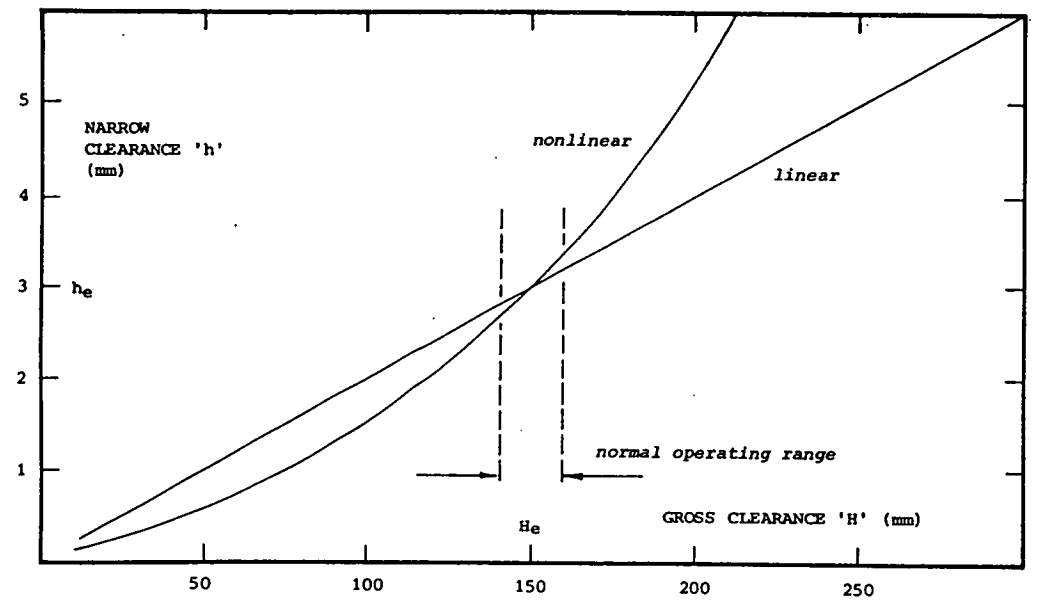

FIGURE 4.4: Clearance Relationships. Correspondence between the 'hard surface' clearance H and the lubricating film thickness h, for the two cases of constant and nonlinear magnetic stiffness.

The bearing response was predicted in section 4.5 to give a maximum of 6% variation in gross clearance H, and over this range nonlinear stiffness may be represented as constant; for the case illustrated, it then corresponds to a slightly lower value than the equivalent constant rate shown. Load capacity should be little affected. If the effective magnetic stiffness is significantly lower than the equivalent constant rate, then an increase in dynamic load capacity will accrue, at the expense of a smaller minimum film thickness. This may be a desirable feature.

Another case of interest is of a magnetic repulsion stiffness so much greater than that of the lining that the film thickness is effectively constant: the result is a strictly constant damping coefficient (as in equation 4.15). Such an arrangement would require more magnetic material, but would provide the greatest insurance against surface to surface contact.

4.8 The Magnet Sheet

Bending moments and shear forces in the compliant magnet sheet have been neglected. In operation, the deviation of the sheet from its equilibrium annular shape will correspond to a diameter variation of no more than 0.05%. Allied to the required compliance of the material, this appears to justify the initial assumption. Similarly, the mass, and hence inertia, of the sheet are neglected on the grounds that its radial velocity and acceleration are insignificant. Its physical dimensions can be incorporated into the definition of the gross clearance H, and do not affect the analysis.

4.9 Limitations of Lubrication Theory

The lubrication-theory assumptions detailed in section 4.2 require to be revised. In particular, the possibility of turbulence in the lubricating film, and the influence of fluid inertia, cannot be ignored. These important topics are further investigated starting in the next chapter.

The assumption of negligible pressure drop across the bearing hard clearance is not correct. A difference in pressure will exist across the magnet-sheet orifices where the compliant lining is discharging water into the narrow clearance, and any section of the sheet through which water is being squeezed will therefore experience net fluid loading. This loading will tend to reduce the magnets' clearance until the accompanying increase in repulsion cancels it out: the lubricant film thickness is therefore not determined solely by the balance of magnetic and lining stiffnesses, but also by the local fluid flow characteristics. The implications of this are important, as a potentially greater load capacity can accrue. This topic is further discussed in chapter 5.

4.10 Power Dissipation and Temperature Rise

The bearing dissipates power as heat due to viscous damping of (a) the relative radial motion of duck and spine, and (b) the duck's angular (nod) rotation. Only rotation damping will result in loss of useful power from the duck, but both effects contribute to raising the temperature of the bearing water.

The power dissipated in the first case can be calculated as the product of load and approach velocity, thus:

$$\text{Maximum Power Dissipation} \quad P_{max} = F_0 \dot{e}_{max} \tag{4.20}$$

where $\dot{e}_{max}$ can be substituted using equation 4.18, giving:

$$\text{Maximum Power} = \frac{F_0^2}{C} \tag{4.21}$$

The damping coefficient C was provisionally evaluated in equation 4.16. The appropriate value of F_0 in this case is the load at maximum rated output, rather than the maximum isolated (freakwave) load which must be withstood, hence for a 37 metre bearing, F_0 = 3.7 MN (see section 3.3), giving:

$$\text{Maximum Power} \approx 800 \text{ watts} \tag{4.22}$$

The damping of the duck's rotation is calculated as a shear loss, from:

$$P_{shear} = \frac{\mu A v^2}{h} \tag{4.23}$$

where the bearing surface area A = 1627 m^2, the limiting rms surface velocity v = 0.61 m/s (Jeffrey et al, 1978), and using

a mean film thickness h = 3 mm, and $\mu = 1.3 \times 10^{-3}$ Ns/m^2 (the viscosity of water at 10°C), then:

$$P_{shear(max)} = 260 \text{ watts} \qquad (4.24)$$

This figure represents only about 0.01% of the duck's rated output of 2.25 MW, and is considered a negligible loss. An equivalent coefficient of friction f is found as the ratio of shear force to applied load, giving:

$$\text{Coefft. of friction 'f'} = 9 \times 10^{-5} \qquad (4.25)$$

which is comparable to that of a good hydrostatic bearing.

The rate of temperature rise in the bearing water is influenced by the thermal conductivity of the solid surfaces, and by the rate of water exchange with the outside sea; a limiting figure is calculated assuming both effects to be negligible, hence:

$$\Delta T \text{ / unit time} = \frac{\text{Total Power Dissipation}}{C_m \times m} \qquad (4.26)$$

where C_m = 4190 Jkg^{-1}deg^{-1}, and the total mass m of water in the bearing, including the compliant lining, is 244 tonnes, giving:

$$\Delta T \text{ / unit time} \simeq 0.08\,C° \text{ per day} \qquad (4.27)$$

The water in the lining acts as a heat-sink, limiting the temperature rise in the bearing. If the last calculation is repeated taking m to be the mass of water in the narrow clearance only, a temperature rise of over 4C° per day results. The time required for complete water exchange has been provisionally set at 24 hours to maximise the efficiency of the antifouling chlorination treatment: in this respect, the temperature rise in equation 4.27 is negligible, though this might not be the case without the heat-sink characteristic.

It must be pointed out at this stage that the preceding calculations are likely to underpredict both the bearing losses and the temperature rise. Despite the 'classical' lubrication assumptions, the bearing is certain to operate in a mixed laminar/turbulent regime; however, it is estimated (see chapter 5) that turbulent lubrication will not increase the power loss, friction coefficient, or temperature rise sufficiently to warrant concern.

4.11 Maximum Pressure, and Pressure Gradient

Maximum fluid pressure exists on the axis of applied load, where $\Theta = 0$, and hence from equations 4.10 and 4.11, its maximum value P_{max} is given by:

$$P_{max} = \frac{6\mu\dot{E}}{m^2\lambda^3}\left\{\frac{1}{E(1-E)^2} - \frac{1}{E(2+3E^2)}\right\} \qquad (4.28)$$

Substituting for $\dot{E}$ using equation 4.19, and subsequently for damping coefficient C using equation 4.15, leads to the following expression for the maximum fluid pressure P_{max}:

$$P_{max} \approx \frac{18\mu F_0}{m^3\lambda^3 rC} \qquad (4.29)$$

The freakwave maximum force F_0 is 37 MN, and under these conditions a maximum eccentricity E of 0.06 can be taken, according to figure 4.2. Evaluating equation 4.29, then:

$$P_{max} = 52 \text{ kPa} \qquad (4.30)$$

Maximum pressure under rated-output loading is approximately one-tenth as great, ie. 5.2 kPa (about 0.75 psi). In conventional bearing terms, these are very low pressures.

It is important also to determine the maximum likely pressure gradient, as this dictates the necessary strength of the flexible walls in the compliant lining, which must resist lateral fluid flow within the lining (see figure 3.4). From

equation 4.9 an - again conservative - estimate is given by:

$$(dP/d\theta)_{max} \simeq \frac{-12\mu\dot{E}_{max}}{m^2\lambda^3(1-E_{max})^3} \qquad (4.31)$$

giving, under freakwave conditions:

$$(dP/d\theta)_{max} \simeq 67 \text{ kPa per radian} \qquad (4.32)$$

If the lining's impedance to lateral flow is assumed to be entirely due to its flexible cell walls, and the circumferential pitch of these is taken as 0.15 m, then from equation 4.32 the maximum water pressure they must resist is is calculated as 1600 Pa (0.23 psi), which corresponds to a fabric strength requirement for the cell walls of 240 N/m; this should be easily met in practice.

Some regions of the bearing on the 'recharging' side will experience lower-than-ambient water pressures, and the possibiity of cavitation should therefore not be overlooked. On the basis of the present analysis, however, no problem is foreseen: the maximum negative pressure will be always numerically smaller than the maximum positive (pressure distribution is geometrically nonsymmetric about a diametric line at 90° to the load), and using equation 4.30 as a worst estimate for the P_{max} (positive), the minimum absolute pressure at the uppermost point of the bearing is predicted to always exceed 0.5 bar (noting that at the deepest point of the bearing the ambient still-water pressure is 1.3 bar). Although no threat of cavitation is envisaged, the problem must be kept in mind each time a more detailed fluid-flow model is advanced.

4.12 The Need for Asymmetric Bearing Response

The form of the damping coefficient C (equation 4.14), which dominates the bearing's equation of motion, predicts that for any eccentricity E, the instantaneous force resisting motion of the bearing in one direction with velocity $\dot{E}$ is exactly the

reverse of the force resisting motion in the opposite direction with velocity $-\dot{E}$, ie. the instantaneous response is symmetric. This is closely analogous to the conventional squeeze-film situation in which, for the same clearance, the force needed to push two lubricated plane surfaces together is the same as that needed to pull them apart. In consequence, a loading regime which combines a reversing and a non-reversing component will apparently cause the duck to oscillate about a mean position displaced from equilibrium by an amount dictated by the compliant lining stiffness and the magnitude of the non-reversing load (the displacement can be calculated from equation 4.4).

This is not a desirable characteristic. Although the non-reversing component of wave force is an order of magnitude less than the cyclic component (see section 3.3), it is nonetheless large enough to require a high lining stiffness in order to avoid large displacements from equilibrium. The provision of a high lining stiffness in itself presents no problem: the difficulty lies in the need to have a magnetic stiffness perhaps 20-50 times as high, and hence the greater the lining stiffness, the more magnetic material will be required. The bearing apparently has a characteristic of suffering large static deflections under small non-reversing loads, while being able to withstand the largest imaginable cyclic loads for almost negligible deflection. This is not anomalous: for example, without solid-to-solid contact, a conventional non-rotating journal bearing has no static load capacity at all.

However, an answer to the problem seems to lie in the 'indirect' influence of fluid inertia. It is shown in the next chapter how this can give rise to a non-symmetric bearing response, such that the static displacement from equilibrium under cyclic loading may be potentially much less than the above simple theory predicts. As a result, the lining stiffness can then be selected on the basis of the maximum non-reversing load

encountered in the absence of wave action; this is estimated as only 60 kN per duck (see section 3.3), in contrast to the non-reversing component of a rated-output wave regime, which is over six times as large (370 kN). Although the influence of inertia is in the above respect fortuitous, it can potentially be exploited at the design stage to greatly minimise the magnet requirement, as the volume of magnet material is, roughly speaking, proportional to the maximum non-reversing load.

4.13 Conclusions

The simplified analysis in this chapter predicts the bearing compliant lining to have a linear spring characteristic, which will dictate the non-reversing load response. Under dynamic loading, however, damping strongly dominates, with a ratio of actual-to-critical damping in excess of 1000. Under maximum-ever (freakwave) loading, the maximum eccentricity is estimated to be of the order of 6%.

Bearing power dissipation and temperature rise are estimated to be of a negligible order, the former representing approximately 0.01% of the rated power output of the device. An equivalent friction coefficient of less than 10^{-4} is predicted. The maximum-ever fluid pressure is estimated to be low, approximately 52 kPa, and cavitation is not foreseen as a problem. The flexible walls of the compliant lining would require little strength to resist lateral fluid flow.

The analysis predicts symmetric bearing response to dynamic loading, in the sense that the derived damping coefficient, although nonlinear, is a function only of eccentricity, and not direction of relative surface motion. An asymmetric response is, however, seen as necessary to prevent unduly large static offsets caused by the non-reversing components of wave force. The exploitation, in the design of the bearing, of a fortuitous 'indirect' effect of fluid inertia (described in the next chapter) is proposed to provide the required asymmetric

response. The performance figures calculated in this chapter require some measure of revision, as all are based on simplified analytical assumptions. Of these assumptions, those of two-dimensional flow, linear stiffness, and negligible magnet-sheet internal forces are all thought to be reasonable. However, the lubrication-theory assumption of viscous-dominated laminar flow with negligible inertia must be revised, and the pressure drop across the sheet cannot be neglected. The probability of a turbulent lubricating film in the bearing, and the important influence of fluid inertia, require further examination. This is begun in the next chapter.

CHAPTER 5
BEARING LUBRICATION IN MORE DETAIL

5.1 Chapter Summary

In this chapter, a more realistic assessment is made than that in chapter 4 of the fluid lubricating regimes likely to be encountered in practice. The effects of a turbulent lubricating film are considered, and an order-of-magnitude estimate made for load capacity, on the basis of a 'turbulent Poiseuille flow' model.

Fluid inertia is discussed in terms of both its 'direct' and 'indirect' influences, with the latter potentially offering a favourably asymmetric bearing response. The indirect effect of fluid inertia is associated with a drop in static pressure across those orifices in the magnet-sheet which are discharging fluid into the lubricating film. A simple model, that of axisymmetric radial flow between plane parallel discs, is used to estimate the magnitude of the effect, and its influence on the overall load capacity of the bearing.

Based on previous research, an alternative to the lubrication-theory analysis in chapter 4 is suggested, which might better predict the pressure and flow characteristics of the lubricating film.

5.2 Flow Regimes

At a given moment, the water flowing in the bearing lubricating film has a range of velocities, depending on its position relative to the load-line. As a result, different regions of the bearing are simultaneously subject to different fluid lubrication regimes, varying from predominantly viscous flow, both laminar and turbulent, to flow with significant inertial character and, in some regions, flow separation. In addition, the flow is everywhere unsteady (time-dependent). The overall

picture is thus seen to be highly complex. To get some idea of the likely flow regimes, the value of local film Reynolds number Re_f is examined. This is defined in the same way as for one-dimensional flow between infinitely wide parallel plates (bearing axial flow being neglected), hence:

$$Re_f = \frac{\rho h U}{\mu} \tag{5.1}$$

where h is the film thickness, and U the mean fluid velocity, given by:

$$U = \frac{r \sin\theta \dot{e}}{h} \tag{5.2}$$

Combining (5.1) and (5.2), and using the previous non-dimensional notation:

$$Re_f = \frac{\rho m r^2 \dot{E} \sin\theta}{\mu} \tag{5.3}$$

Note that Re_f is independent of film thickness, but varies with position θ and velocity $\dot{E}$. Hence Re_f equals zero at all times on the load-line, and takes its maximum value where $\theta = \pi/2$, giving:

$$Re_f\,(max) = \frac{\rho m r^2 \dot{E}}{\mu} \tag{5.4}$$

Using the same provisional bearing dimensions as in chapter 4, the values of $\dot{E}_{max}$ corresponding to rated-output and freakwave loading are found from equation 4.19, respectively, as 0.0014 and 0.014, giving $Re_f(max)$ = 1460 and 14600. For steady flow between parallel plates, a critical value of Re_f of 2000 applies (Davies and White, 1928) and hence, although the first of the above film Reynolds numbers suggests flow in the laminar/turbulent transition region under steady conditions, with unsteady flow, turbulence is to be expected. The higher Reynolds number certainly indicates turbulence. Near the load axis (Re_f = 0) the flow is predicted to be laminar; this is

however based on the simplified model, which takes no account of the local flow patterns in the vicinity of the holes in the magnet-sheet. Here, more than one type of flow is to be expected, and the effect on local fluid pressure of the flow through the sheet orifices can be made to exert a strong influence on the overall bearing load capacity (see sections 5.5 to 5.8).

5.3 Turbulent Lubrication

The effects of a turbulent lubricating film on bearing performance in general are well documented: increases in both load capacity and bearing friction are to be expected (Constantinescu, 1962). Turbulence is expected in the present case because of the combination of a lubricant of low kinematic viscosity (water) and relatively high fluid velocities. This is not unusual in bearing technology. Commonly, however, these conditions are caused by high surface shear rates in rotating bearings, while in the present case surface velocities are practically zero, and flow is due to externally impressed pressure gradients; the term Poiseuille flow can be used, although it perhaps more strictly applies to fully developed laminar conditions. Bearings which operate in a turbulent Poiseuille flow regime do not appear to be common.

A theoretical method for calculating bearing performance under turbulent Couette (surface-shear) flow conditions has been suggested by Ng and Pan (1965), based on the 'law of the wall' for flows of this type. The model has found good agreement with experimental data for journal bearings operating in a superlaminar regime (Smith and Fuller, 1956), and for partial arc pads under similar conditions (Orcutt, 1965). Practical application of the theory has more recently been made by Wilcock (1977). This author adapted a conventional laminar-flow analysis to include an effective 'turbulent viscosity', which is

dependent on Reynolds number, and given by:

$$\mu_t = \mu \times 0.0219\ (Re)^{0.657} \qquad (5.5)$$

where equation 5.5 is an empirical fit to the theoretical data of Ng and Pan, with which it agrees to within 6% for Re in the range 1500 to 50,000.

Because of the different natures of the two flow regimes, the above expression can not be applied in the present case. The technique does however suggest that a similar analysis might be made if an equivalent expression to equation 5.5 could be derived for turbulent Poiseuille flow. This is done below. It should be pointed out that the treatment has not been experimentally verified, and is intended only to give an order of magnitude estimate for the bearing power dissipation under turbulent conditions.

For fully-developed, steady one-dimensional flow with mean velocity U, between two infinitely wide parallel plates a distance h apart, the pressure gradient in the direction of flow is given by the following two expressions. The first is based on lubrication theory, and assumes the flow to be viscous dominated and laminar:

$$dP/dx = \frac{-12\mu U}{h^2} \qquad \text{LAMINAR} \qquad (5.6)$$

The second derives from pipe-flow theory (see Ward-Smith, 1980, p.183), and assumes fully-developed turbulent flow:

$$dP/dx = \frac{-\rho f U^2}{h} \qquad \text{TURBULENT} \qquad (5.7)$$

where f in equation 5.7 is a Reynolds number dependent friction factor. It is now assumed that the two expressions can be simultaneously valid, if an effective 'turbulent viscosity' μ_t is first defined, and substituted for viscosity μ in

equation 5.6. The two expressions are then equated, and the following relationship is found:

$$\mu_t = \frac{\mu f(Re)}{12} \qquad (5.8)$$

In which Re is defined as in equation 5.1. For turbulent flow between smooth surfaces, Ward-Smith gives the following implicit relationship between f and Re:

$$f^{-\frac{1}{2}} = 1.768 \log_e \{ f^{\frac{1}{2}}(Re) \} + 0.29 \qquad (5.9)$$

In order to evaluate equation 5.8 for a given Reynolds number, equation 5.9 must first be solved numerically. This is straightforward, and values of effective viscosity μ_t can thus be tabulated over the appropriate range of Re. Figure 5.1 shows a plot of μ_t/μ (the factor by which true viscosity must be multiplied to account for turbulence) against Reynolds number in the range 1000-20,000.

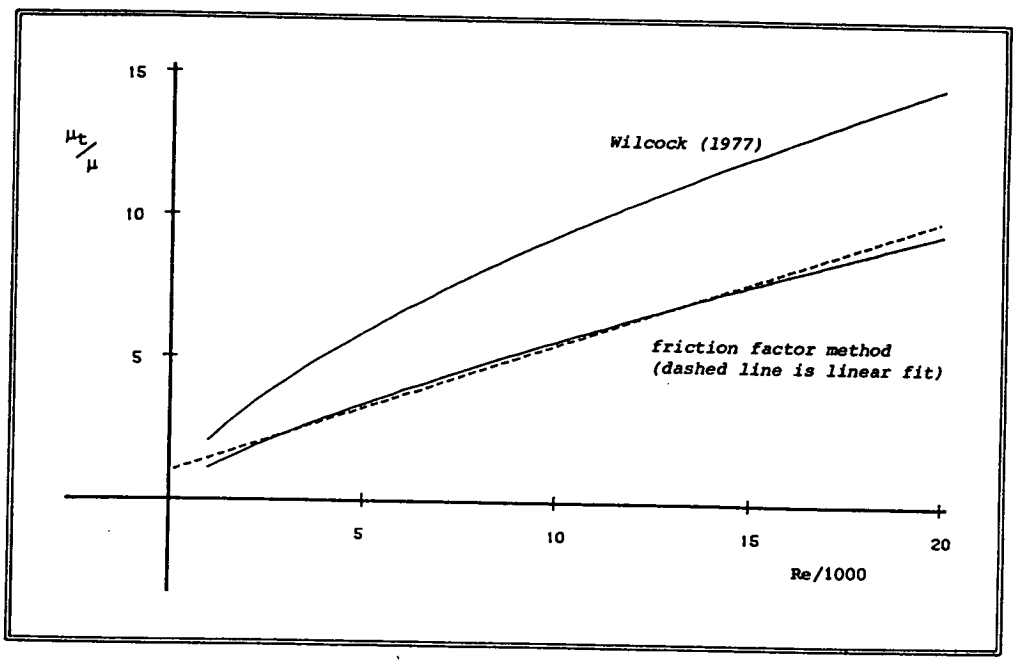

FIGURE 5.1: Turbulent Viscosity Correction Factors. The ratio of turbulent to true viscosity as a function of Reynolds number.

Also shown in figure 5.1 is a curve corresponding to Wilcock's correction factor which, for the reasons given above, is included for order of magnitude comparisons only. To simplify the analysis, a linear fit is now made to the curve in figure 5.1 (see dashed line) such that:

$$\mu_t = \mu(1 + \alpha Re) \qquad (5.10)$$

where:

$$\alpha = 4.5 \times 10^{-4}$$

This linear relationship has the desirable characteristic that at Reynolds number zero, μ_t is equal to μ. This is important, as regions of the lubricating film have zero Re at all times: a relationship such as equation 5.5 would not take account of this condition. Expression 5.10 is now used to substitute for μ in the lubrication-theory governing equation (equation 4.7), and the damping analysis of section 4.4 then proceeds, otherwise as before.

A new expression for the damping coefficient, C (turbulent), is thus obtained, which is related to the lubrication theory value C (laminar) according to:

$$C\,(\text{turbulent}) = C\,(\text{laminar}) + \eta\dot{E} \qquad (5.11)$$

where:

$$\eta = \frac{32\alpha\rho br^2}{m^2\lambda^3}$$

and, assuming the same provisional bearing dimensions as so far used:

$$\eta = 7.11 \times 10^{12} \quad kg \qquad (5.12)$$

The second term in equation 5.11, ie. that arising from turbulent considerations, will be of the same order as C (laminar) when dimensionless velocity $\dot{E}$ equals C (laminar)/η. Using equation 4.16 for C (laminar), this then corresponds to velocity $\dot{E} = 0.0025$, which lies between the two values predicted for $\dot{E}_{max}$ under rated-output loading (0.0014) and freakwave loading (0.014), though significantly closer to the first.

Because of the assumptions involved - equations 5.6 and 5.7 refer to steady, fully developed flow between plane parallel surfaces, besides which the influence of orifice flow is again ignored - and the unproven nature of the analytical precept, the above result is to be treated as an order of magnitude estimate only. However, the approximately similar magnitudes of laminar and turbulent damping terms at a maximum approach velocity near that of rated-output loading, suggest that turbulent lubrication might usefully increase the load capacity of the bearing under these conditions.

5.4 Turbulent Power Loss

The power dissipated by the bearing at rated output working, assuming a turbulent lubricating film, is hard to quantify. In the simple treatment of chapter 4, a shear loss was calculated using constant viscosity (equation 4.23), and assuming laminar conditions. It would be incorrect simply to replace the laminar viscosity term with a turbulent equivalent found from the analysis in section 5.3: there, the 'effective viscosity' was derived for a turbulent Poiseuille flow regime, whereas the bearing power loss actually occurs as the result of surface shear. Similarly, using an effective viscosity based on the model of eg. Wilcock (see section 5.3), neglects the fact that in the present case turbulence does not result from shear. A tentative estimate of power loss is therefore made in the following way. The maximum film Reynolds number (ie. with peak bearing velocity, and evaluated at $\Theta = \pi/2$) under rated output conditions is calculated on the basis of both pressure flow and

shear flow criteria. The former was above noted to be 1460, the latter, based on a mean clearance h = 3 mm, and surface shear velocity v = 5 m/s, has a value of 7500. Using the higher of these, an effective viscosity is then read from the upper curve in figure 5.1 (after Wilcock); the turbulent viscosity is found to be approximately eight times the laminar value. Using equation 4.23 as before, save for the substitution of the turbulent viscosity term, gives a new estimate for power dissipation:

$$\text{Turbulent power loss} = 1.6 \text{ kW} \qquad (5.13)$$

Although nearly an order of magnitude greater than that found assuming lubrication theory, this is still a negligible loss, representing only 0.07% of the duck's output.

Note that in the above example, peak bearing velocities are used to estimate Reynolds number, but rms values inserted in the equation for shear loss. This is intended to give a conservative estimate for the increase in effective viscosity, by accomodating the uncertainties which exist in the analysis (see above).

5.5 The Influence of Fluid Inertia

The influence of fluid inertia on bearing performance can be divided into 'direct' and 'indirect', of which the latter is of much greater importance in enhancing load capacity.

The significance of the direct effect can be roughly estimated by calculating the mean dynamic pressure head of the fluid film as $1/2\ \rho U^2$ at $\Theta = \pi/2$ (where its maximum value occurs) for the two cases of freakwave and rated-output loading. Assuming the mean clearance h = 3 mm, the maximum dynamic pressures in each case are found, respectively, as 12 kPa and 0.12 kPa. These figures represent 23% and 2.3% of the corresponding maximum bearing pressures (as calculated in section 4.11); assuming the

extra force required to accelerate the fluid corresponds to an increase in load capacity, then, while inertial effects might directly enhance bearing performance in the most extreme waves, they appear to be of little significance under normal operating conditions.

The indirect influence of fluid inertia arises because dynamic pressures, although low compared with overall film pressure, can be of the same order as the spring pressures acting on the two sides of the magnet sheet. These in turn determine the bearing's damping characteristics, by controlling the film thickness to hard clearance ratio h/H. A small imbalance in pressure across the sheet, causing the narrow clearance to close down by, say, a millimetre, from an equilibrium value of 3 mm, would increase the local flow impedance by a factor greater than three; this results from the inverse-cube law for lubrication flow. Exactly such a fluid pressure imbalance is caused when the water in the compliant lining is squeezed out through the sheet orifices into the clearance: inside the lining the fluid is at rest, and the increase in its velocity on entering the lubricant film is accompanied by a drop in static pressure, corresponding to the acquisition of its dynamic (inertial) head. The effect is greatest in those areas of the bearing discharging the most water, ie. closest to the effective load application point ($\theta = 0$), and here will be observed the greatest increases in local load capacity.

Not only does this characteristic of fluid inertia potentially increase the overall load capacity of the bearing, it also gives it an asymmetric response, offering a large reduction in the amount of magnetic material required (see section 4.12). An asymmetric response will occur because no pressure imbalance of the kind described above exists on the negatively loaded side of the bearing, where water is being drawn from the lubricating film back into the compliant lining. In this region, the dynamic pressure head of the fast-moving fluid is effectively

lost as it re-enters the lining, and its static pressure remains constant. The local flow impedance does not as a result experience indirect enhancement due to fluid inertia. The overall asymmetric characteristic is due to the combination of the one-sided nature of the dynamic pressure imbalance, and the fact that those parts of the bearing where clearance is smallest contribute most to the damping of motion in either direction (as in the conventional squeeze-film case).

It is thus predicted as an inherent characteristic of the bearing that, at any value of eccentricity except zero, it will require less force to pull the two elements back towards their equilibrium position with a given velocity, than it would to further displace them at the same velocity. By exploiting this characteristic at the design stage, the large cyclic components of wave load could then be allowed to dictate the maximum eccentricity of the bearing in normal operation - where this is predicted to be no more than 6% - with the modest calm sea current loads (see section 4.12) then representing the greatest non-reversing forces able to cause static displacement.

5.6 Fluid Inertia: Pressure Drop Across the Magnet Sheet

To estimate the likely pressure imbalance due to fluid inertia, the simple case is examined of a section of the bearing on, or close to, the load axis. On the positively loaded side of the bearing, the compliant lining is compressed, and water flows outwards through the holes in the magnet-sheet, into the narrow clearance. By disregarding the asymmetry of the discharge due to bearing curvature and axial leakage, the situation reduces to that shown in figure 5.2, ie. axisymmetric, diverging radial flow between two plane parallel discs.

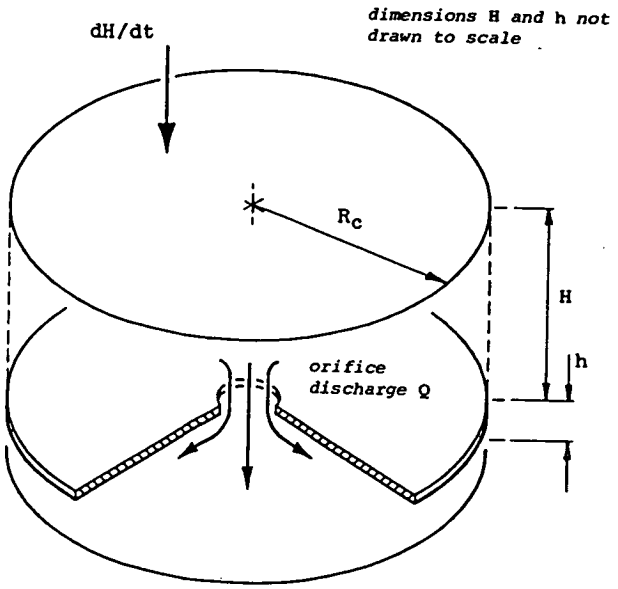

FIGURE 5.2: Bearing 'Equivalent Cell' Discharge. Flow in the lubricating film is approximated by radially diverging flow between plane parallel discs.

Assuming a steady volume discharge Q, the mean radial velocity U(r) of the fluid in the lubricating film at radius r from the orifice centreline is given by:

$$U(r) = \frac{Q}{2\pi rh} \qquad (5.14)$$

from which it is seen that the velocity is at a maximum at the orifice edge, and decreases with radius. If laminar flow is assumed, then the fully developed velocity profile at radius r_1 downstream of the centreline has the parabolic distribution shown in figure 5.3(a); a uniform 'flat' entry profile is assumed at the orifice edge. The dynamic head associated with a parabolic velocity distribution is given (see eg. Massey, 1979) in terms of mean velocity U_1 according to:

$$p_1(\text{dynamic}) = \frac{27}{35}\rho U_1^2 \qquad (5.15)$$

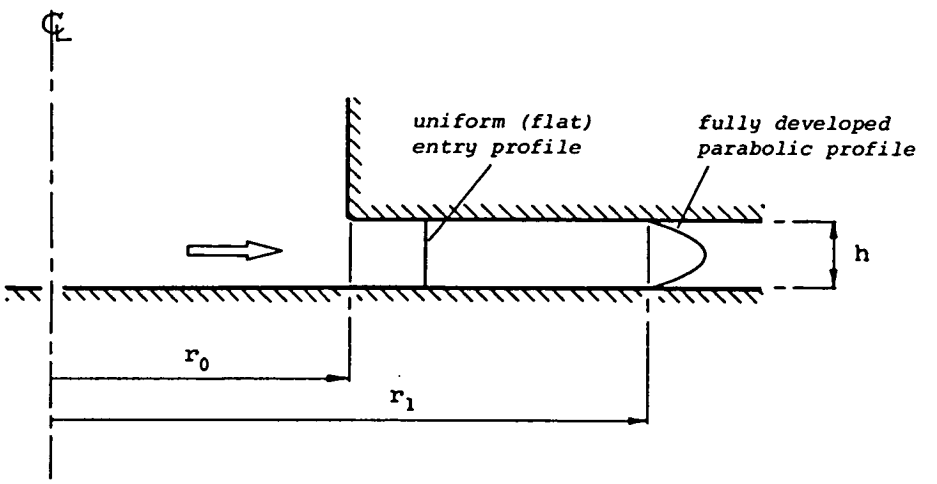

(a) DIVERGING FLOW

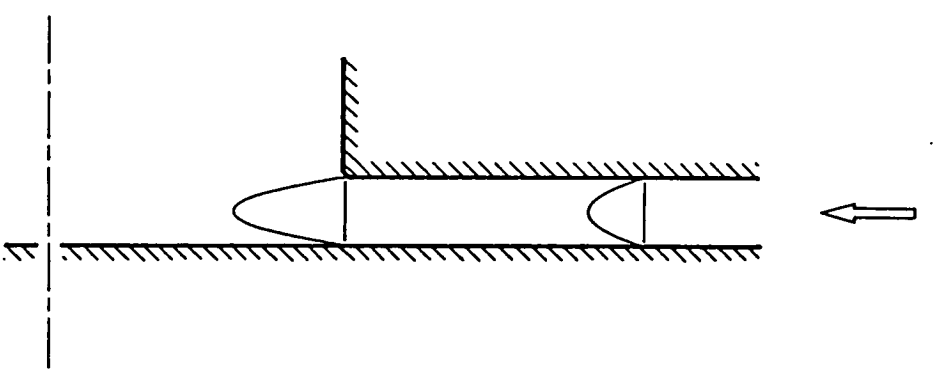

(b) CONVERGING FLOW

FIGURE 5.3: Velocity Profiles. Axisymmetric radial flow between plane parallel discs, with (a) flow diverging outwards from the orifice centreline, and (b) flow converging towards the centreline.

The drop in static pressure between a point inside the lining (where static pressure is taken to equal stagnation pressure) and the fully developed flow at r_1 is then given by:

$$\Delta p = \frac{27}{35}\rho U_1^2 + \Delta p_{0,1}(\text{viscous}) \qquad (5.16)$$

where $\Delta p_{0,1}(\text{viscous})$ occurs between radii r_0 and r_1. If the flow were fully developed, with a parabolic rather than flat, profile at r_0, then:

$$\Delta p_{0,1}(\text{viscous}) = \frac{6\mu Q}{\pi h^3}\log_e\left\{\frac{r_1}{r_0}\right\} \qquad (5.17)$$

which represents the classical lubrication-theory pressure loss for axisymmetric radial flow (Rayleigh, 1917). This underestimates the actual loss, as a uniform entry profile at r_0 entails higher (theoretically infinite) shear stresses at the channel walls. However, if full development of the velocity profile occurs close downstream of the orifice edge without significant viscous loss, the dynamic pressure head, and hence static pressure drop, can be approximated by:

$$p_1(\text{dynamic}) \simeq \frac{27}{35}\rho U_0^2 \qquad (5.18)$$

where U_0 is the mean velocity at the orifice edge. This assumption has previously been employed by Kawashima (1976, 1978) to account for the observed pressure drop in radial-flow hydraulic valves.

A different estimate has been proposed by Mori and Yabe (1966) based on a momentum-theorem calculation, whereby the increased momentum of the parabolic, compared with the uniform, velocity profile is equated with a pressure drop of $1/5\ \rho U_0^2$, giving the net dynamic head on entry as:

$$p_1(\text{dynamic}) = \frac{7}{10}\rho U_0^2 \quad \text{(Mori \& Yabe, 1966)} \qquad (5.19)$$

Another estimate has been made by Vohr (1969), based on integration of the momentum across the width of the parabolic profile, with resulting dynamic head term:

$$p_1(\text{dynamic}) = \frac{3}{5}\rho U_0^2 \quad \text{(Vohr, 1969)} \tag{5.20}$$

Of the three estimates, the first - and highest - appears most strictly correct, as it assumes nothing about the losses incurred in the developing profile between r_0 and r_1.

The magnitude of the orifice static pressure drop in the 'discharging' regions of the proposed bearing is a design parameter of potentially fundamental importance. In the next chapter are presented the results of experiments which were undertaken to confirm the appropriate governing equation for this pressure drop, and to demonstrate how, by a suitable choice of orifice geometry, the phenomenon of flow separation can significantly enhance its magnitude.

5.7 Convergent Radial Flow

Consider now the case where the section of the bearing illustrated in figure 5.2 is negatively loaded: the compliant lining recharges, drawing water in from the lubricating film. Making the same assumptions as in section 5.6, the water in the clearance now flows radially inwards, converging towards the orifice. The subsequent deceleration to stagnation conditions results in turbulent loss of the entire dynamic pressure head, with the static pressure inside the lining equal to that in the radial film at the orifice edge. This phenomenon has been experimentally demonstrated by McGinn (1955) and in the present work (see section 6.4).

Figure 5.3(b) shows the velocity profile of the converging radial flow. With a fully developed parabolic profile at r_0, the loss of dynamic head is strictly that given in equation 5.18. Although there is some experimental evidence of a partial

head recovery on the lower wall at the centreline (see section 6.4), this is purely a boundary effect, and is not reflected in the pressure measured above the orifice.

The asymmetric behaviour of the overall bearing arises because of the 'inertia-paradox' of axisymmetric radial flow: in divergent (outward) radial flows, conservation of total pressure leads to a drop in static pressure across the orifice, while in convergent flows, loss of total pressure results in the conservation of static pressure.

5.8 The Importance of the Inertial Pressure Imbalance

If each orifice in the magnet-sheet discharges/recharges the water contained in a volume of the compliant lining equivalent to a 'cell' of plan area πR_c^2, as shown in figure 5.2, then the volume flowrate through the orifice is given by:

$$Q = \pm \pi R_c^2 \, dH/dt \qquad (5.21)$$

and hence from equation 4.1:

$$Q = \pm \pi R_c^2 \, \dot{e} \cos\theta \qquad (5.22)$$

where $\dot{e}$ is the hard-surface approach velocity. The mean radial fluid velocity at the orifice edge, considering only the flow due to discharge of the particular cell being considered, is then found from equations 5.14 and 5.22 as:

$$U_0 = \pm \frac{R_c^2 \, \dot{e} \cos\theta}{2 r_0 h} \qquad (5.23)$$

The resulting static pressure drop across the orifice in diverging radial flow is then found using this expression to substitute for U_0 in equation 5.18, hence:

$$\Delta p \text{ (dynamic)} = \frac{27}{140} \rho R_c^4 \left\{ \frac{\dot{e} \cos\theta}{r_0 h} \right\}^2 \qquad (5.24)$$

In section 4.5 it was shown that the dominance of fluid damping dictates that velocity $\dot{e}$ is proportional to applied load, with the damping coefficient inversely proportional to the cube of the film thickness h (equation 4.17). Hence, from equation 5.24:

$$\Delta p \text{ (dynamic)} \propto \left\{ \frac{F_0 \cos\theta}{r_0} \right\}^2 (R_c h)^4 \qquad (5.25)$$

Superficially, then, and ignoring all nonlinearities, turbulence, etc., the dynamic pressure imbalance increases with the fourth power of clearance h, in contrast to the overall impedance (hence load capacity) of the bearing, which decreases with h^3. The two effects are in a way opposed: the former causes a narrowing of the clearance on the positively loaded side of the bearing, while the latter resists the approach of the two surfaces.

The fact that these opposing effects are governed by high powers of clearance h, with the first decreasing and the second increasing under positive loading, should be exploited from the outset in the bearing design. Its operating characteristics might then be significantly different from those assumed in the simple analysis in chapter 4. A greater equilibrium clearance would be possible, which on the application of a dynamic load would rapidly close down to a safe minimum working value, as the dominance of inertial pressure imbalance and overall impedance changed hands. As a result of the high-order dependence on h of these two characteristics, the working clearance would be maintained within a very narrow band. Utilising this, the 'indirect' influence of fluid inertia, to maximum effect would largely be a matter of incorporating in the design of the bearing the optimum combination of magnetic and compliant lining stiffnesses, lubricating film thickness, and overall 'hard' clearance.

Although no attempt to obtain the ideal combination has yet been made, the task seems eminently feasible, as small changes in the above parameters yield much larger ones in the desired effect. To demonstrate the available design latitude, the influence of equilibrium film thickness h on the dynamic pressure imbalance can be shown by referring to the 'equivalent cell' in figure 5.2. Assuming an orifice radius r_0 of 5 mm, with cell radius R_c of 100 mm, then under freakwave loading ($\dot{H}$ = 0.002 m/s) the maximum dynamic head is found from equation 5.24, with:

$$\Delta p \text{ (dynamic)} = 375 \text{ Pa} \qquad (5.26)$$

This pressure may be quite low in comparison to the magnetic repulsion pressure against which it is required to act; however, by doubling the equilibrium clearance to 6 mm, the above figure rises sixteen-fold to 6.0 kPa, which may well be too high to allow. The appropriate clearance would then obviously lie between the two figures.

The advantage of a large equilibrium film thickness is to allow the use of less magnetic material, because the greater available change in working clearance then allows a less stiff magnetic repulsion system to be employed to provide the minimum calm-sea static load. A rough guess at the possible magnet reduction assumes the amount required to be inversely proportional to the equilibrium clearance, ie. doubling h in the above example might potentially halve the weight of magnets needed. One characteristic to be avoided, however, is a too-great dynamic pressure imbalance acting on the compliant magnet-sheet, which might lead to localised 'grounding' around the discharging orifices (although the corresponding local increase in flow impedance might prevent this occurrence).

5.9 The Complete Flow Field

The simple radial flow patterns described above might be observed in the region of the load axis, but elsewhere, the overall flow pattern will be a much more complex combination of orifice flow and the main flow of the lubricating film. The ratio of orifice discharge (or recharge) flow to the total flow past a section at angle θ to the load axis is given by:

$$\frac{Q_{orifice}}{Q_{total}} = \frac{\pi R_c}{2r \tan\theta} \qquad (5.27)$$

which decreases to zero at 90° to the axis, there being no lining compression in this region.

A possible model of the complex flow field is suggested by the work of Mori and Yabe (1967), who examined the case of a rectangular thrust bearing with multiple supply holes. In their treatment, the assumptions are made of (a) constant clearance, (b) negligible surface velocity, and (c) constant fluid viscosity: under these conditions, Reynolds equation (which governs the flow of a 'classical' lubricant) reduces to Laplace's equation, ie.:

$$\frac{d^2p}{dx^2} + \frac{d^2p}{dy^2} = 0 \qquad (5.28)$$

which is then solved using complex potential theory. Although the method neglects fluid inertia in the film, a correction is included to allow for the pressure drop at the orifice edges (see equation 5.19) due to development of the dynamic head.

If the above assumptions (a-c) were made for the present bearing, this technique could be applied to obtain a more accurate picture of its pressure/flow characteristics. Indeed, the closed nature of the system may well make it a simpler analytical problem than that of the rectangular bearing. The necessary assumption of constant film thickness defines the net flow in the clearance to be always zero, and entirely accounted

for by real point sources and sinks, in the form of the sheet orifices: in contrast to the rectangular thrust bearing case, no additional sinks need be defined to satisfy the boundary conditions. The necessary pressure-loss correction for discharging orifices is given in equation 5.18, and no correction is needed for recharging orifices: analytic distinction between the two is simple, based on position relative to a diametric line at right angles to the load axis. Total discharge is directly proportional to approach velocity $\dot{e}$. Although no start has yet been made on such an analysis, it is strongly recommended as the next theoretical step.

The most complete analysis of all would have to take account of nonlinear stiffness, non-constant clearance (including compliance), film fluid inertia and turbulence, squeeze-film effects, and unsteady flow. A representative experimental model seems a more attractive proposal.

5.10 Conclusions

The water in the lubricating film will have complex flow characteristics, with both turbulence and fluid inertia influencing overall bearing performance. Turbulent lubrication will give rise to increases in both load capacity and power loss compared with those found from the earlier lubrication theory analysis. However, load enhancement will probably be of significance only in extreme waves, and power loss is still estimated as less than 0.1% of the duck's rated output.

The direct influence of fluid inertia will be load enhancing, but is likely to contribute little under normal working conditions. Its indirect influence, represented by the pressure drop across the discharging magnet-sheet orifices, is of much greater significance: this can potentially give rise to greatly increased load capacity, and also endow the bearing with a favourably asymmetric response. The key to the latter characteristic is the lack of a similar pressure drop across the

recharging orifices. Based on the model of axisymmetric (laminar) radial flow, the static pressure drop across a discharging orifice is estimated as $27/35\rho U_0^2$, where U_0 is the mean radial fluid velocity at the orifice edge. By exploiting the indirect effect of fluid inertia, it is proposed that large reductions can be made in the magnet requirement.

A detailed analysis of the lubricating film flow-field in the bearing's narrow clearance is suggested (though not carried out) on the basis of previously published work: the analysis would take account of the components of flow in the overall lubricating film due to local orifice discharge/recharge, including inertial effects, and might yield a more accurate description of the bearing's performance characteristics.

CHAPTER 6
RADIAL FLOW EXPERIMENTS

6.1 Chapter Summary

Experiments, which were designed to demonstrate the important features of the 'indirect' influence of fluid inertia in the proposed bearing, are described. The experimental model used was that of steady, axisymmetric radial flow between plane parallel discs. To simulate both discharge and recharge of water through the sheet-orifices in the the bearing lining, divergent and convergent radial flows were used. Radial pressure distributions were measured for both cases, over the same range of volume flowrates.

The governing law for the orifice pressure loss in diverging flows is investigated by examining the measured pressure losses, expressed dimensionlessly, as a function of the reduced Reynolds number Re^x, while the asymmetry of the effect is demonstrated in a qualitative comparison of the results for diverging and converging flows. A qualitative investigation of the influence of orifice geometry is also made, paying particular regard to the phenomenon of flow separation. The experimental apparatus, its novel features and operational limitations, are fully described, including a load cell, and a pressure calibration device, both of which operate on the same principle as a hydrostatic bearing.

6.2 Experimental Apparatus

The experiments were designed to give pressure variations of accurately measurable size. Because the orifice discharges in the full scale bearing depend greatly on position relative to the load axis, and on the loading regime, experimental conditions were representative of only a small part of the full range, namely that characterised by low values of reduced Reynolds number Re^x (see section 6.5). The range of Re^x,

measured close downstream of the orifice edge, was approximately 2-20; the corresponding range of Reynolds number Re was 180-1500. Under these conditions, the observed pressure losses may be taken to represent the minimum likely at full scale. The experimental equipment was designed to allow:

(a) Investigation of both diverging and converging flows.

(b) Measurement of radial pressure distributions from the orifice centreline outwards.

(c) Independent measurement of the total load exerted by the radial film, for comparison with integrated pressure profiles.

(d) Experiments with different orifice geometries.

Water was chosen as the working fluid. The central piece of apparatus was that shown in figure 6.1 (see also plate 6.1). In it, a fluid film was entrained between two 80 mm diameter plane circular surfaces, each machined integrally with a disc of larger diameter. These were enclosed in a sealed 'load-tower'. Water was supplied under pressure either to a central orifice in the upper disc, for divergent flow, or to a plenum chamber at the film outer radius, for convergent flow (in which case the central orifice became the outlet). Axisymmetric conditions without swirl were encouraged, in divergent flows by the inclusion of a length of straight pipe above the orifice inlet, and in convergent flows by a baffle between the annular inlet chamber and plenum chamber. Eighteen pressure tappings in the surface of the lower experimental disc were used to measure radial pressure distribution, while another three in its side-walls gave the mean plenum chamber pressure. The surface tappings were arranged in a spiral (a) to compensate for possible non-symmetric pressure distributions, and (b) to accomodate more tappings within the available 40 mm radius; the spiral pattern can be seen in plate 6.1. Three separate upper discs were machined, each with a different orifice geometry - these are shown in figure 6.2.

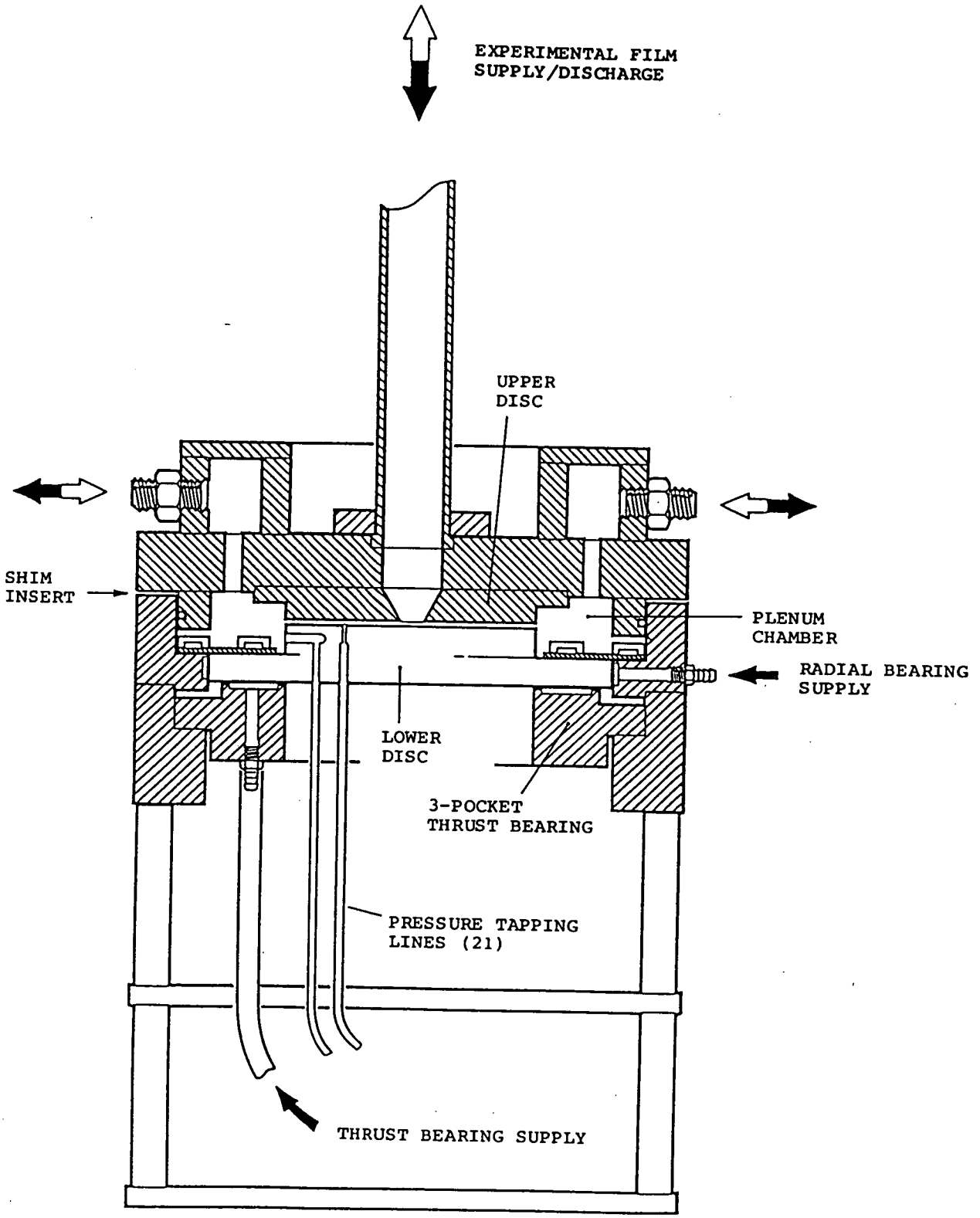

FIGURE 6.1
Radial Flow Apparatus

OVERLEAF

PLATE 6.1
Radial Flow Apparatus. The lower experimental disc (foreground) is supported by a 3-pocket water-fed thrust bearing, or 'hydrostatic load cell', enclosed in the main load-tower apparatus (background). Centralisation of the disc is by a 3-pocket radial bearing. Note the spiral of pressure tappings in the upper surface of the disc.

FOLLOWING PAGE

PLATE 6.2
Hydraulic Impedances. Screw-cut impedances of the kind shown were used to supply both load cell hydrostatic bearings. The parallel-capillary core (foreground) was designed to enable high flowrates of low viscosity lubricant (water) at low Reynolds number, thus avoiding nonlinear characteristics. Each core is enclosed in a shim-reinforced heatshrink sandwich (background).

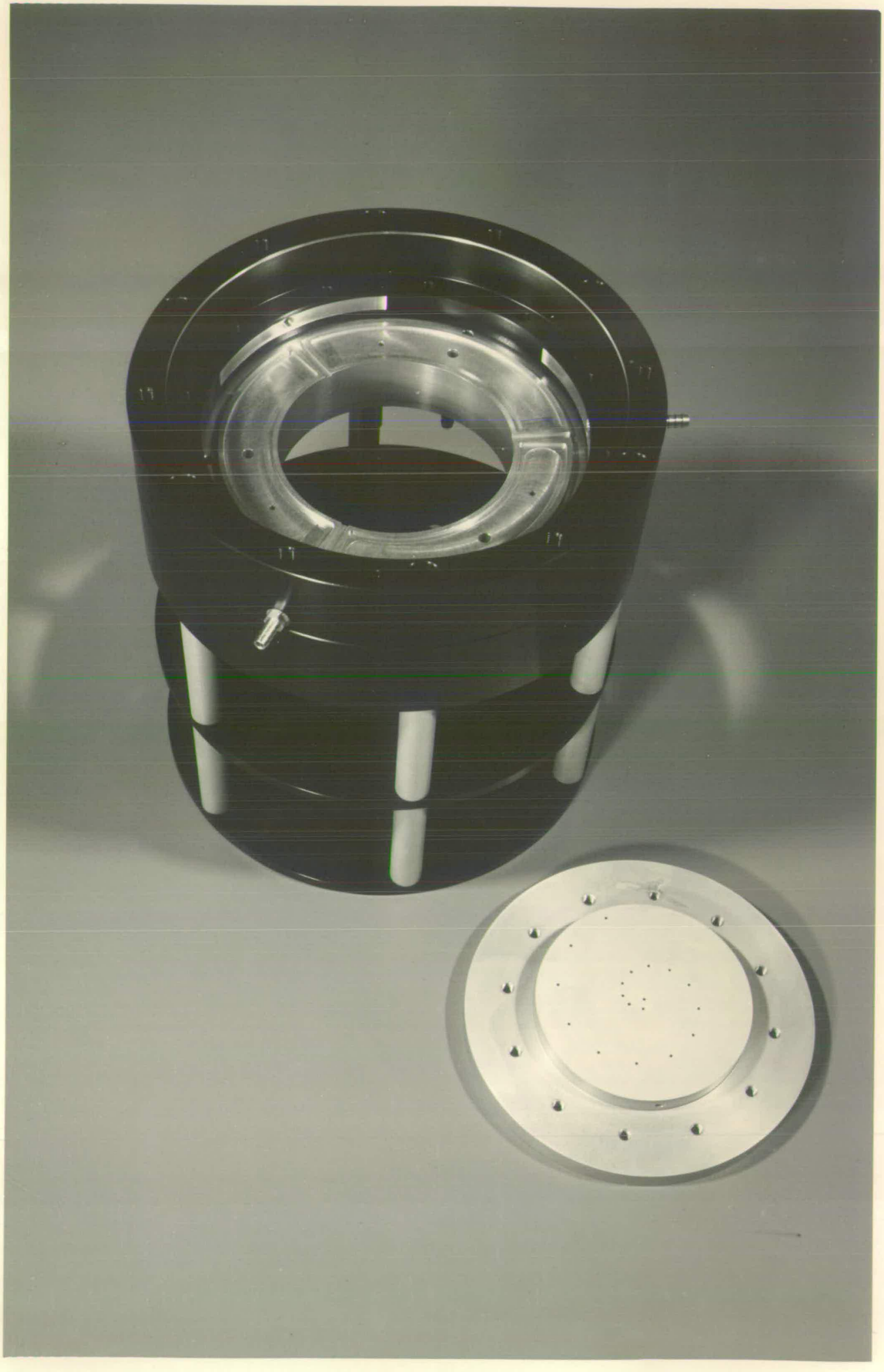

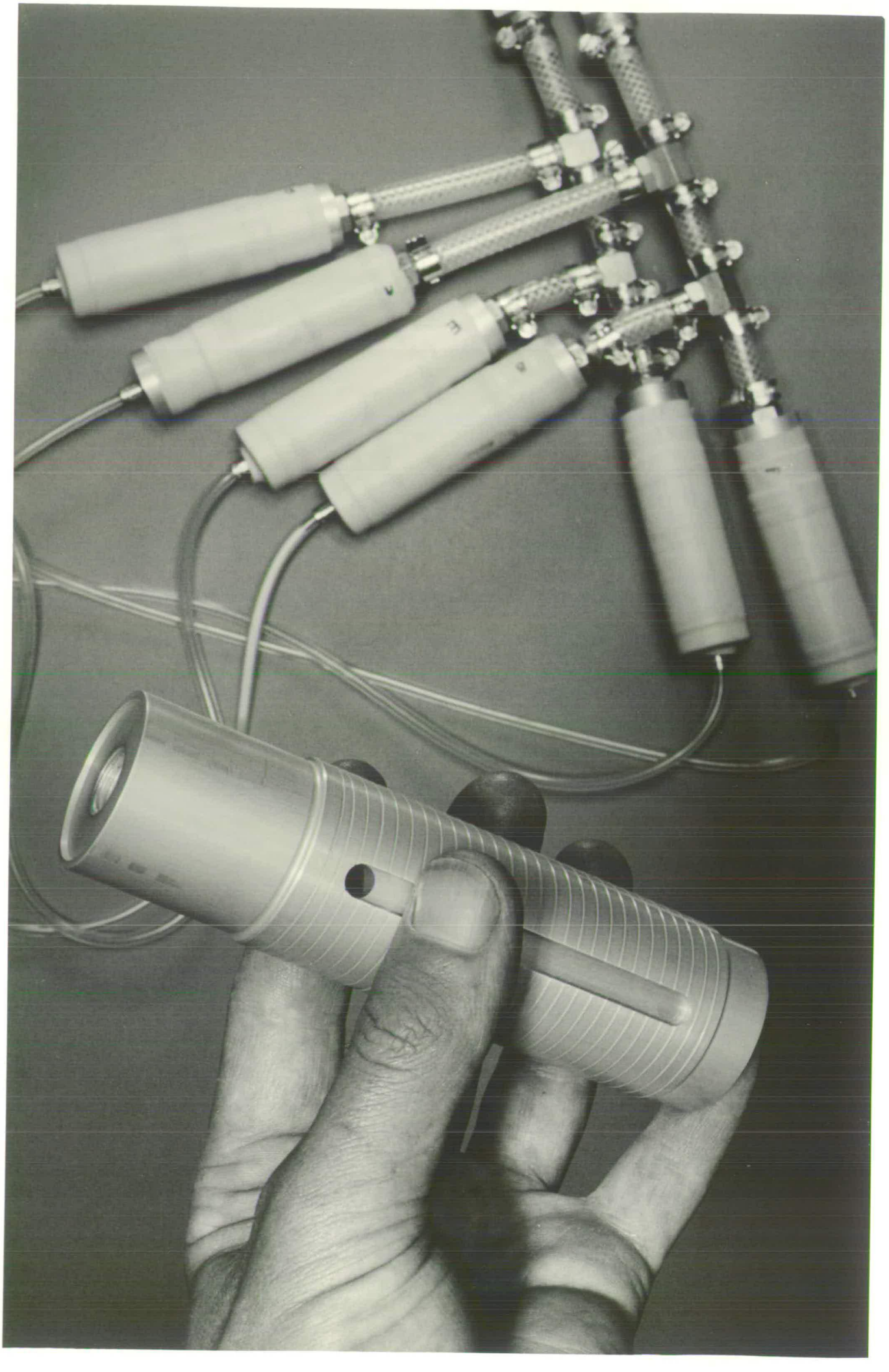

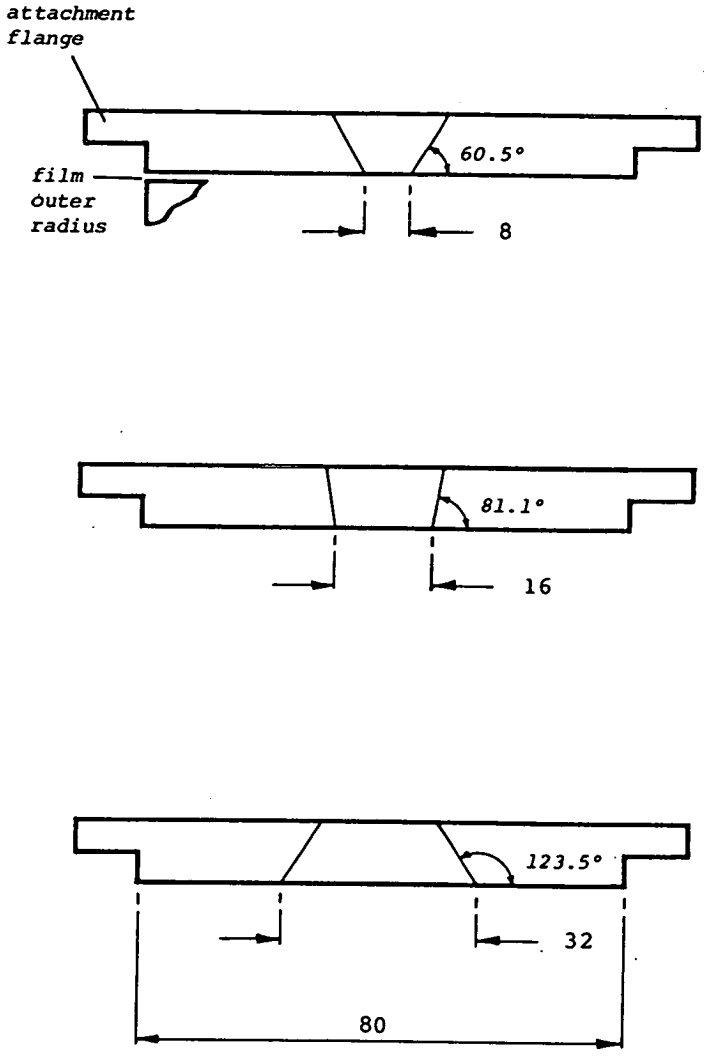

GEOMETRY	r_0/R
O1	0.1
O2	0.2
O4	0.4

DIMENSIONS IN mm

FIGURE 6.2
Experimental Orifice Geometries

In order to measure the total load exerted by the radial film, the lower experimental disc was supported by a three-pocket, water-fed thrust bearing, a 'hydrostatic load cell'. This device operated on the principle that the pocket pressures in a hydrostatic bearing are proportional to the supported load, and that the clearance can be very small, provided that suitable hydraulic impedances are included upstream of the pockets (see eg. Barwell, 1979). By calibrating the thrust bearing's clearance against flowrate and pocket pressure, appropriate corrections to the experimental radial film thickness were tabulated. Tappings were included in each pocket, and total load estimated by averaging pressure measurements taken for the three. To ensure accurate centralisation of the supported disc, without introducing any vertical forces on it which might corrupt load measurement (eg. by friction at the sidewalls), a three-pocket radial hydrostatic bearing was also included; the two bearings can be seen in plate 6.1. Centralisation was better than 0.015 mm, and vertical friction negligible.

Both bearings were supplied with water at approximately 300 kPa, via hydraulic impedances (one per pocket) of the kind shown in plate 6.2; these differed from standard capillary impedances (see eg. Stansfield, 1970) in that a single screw-thread was used to create 48 short parallel capillaries between the inlet and outlet ports. This feature was devised to give the impedances a linear characteristic, by keeping the flow Reynolds number in the capillaries down in the laminar region. The combination of the low viscosity of water and the required high flowrates otherwise threatened turbulent flow. Each impedance core was enclosed in a sandwich of thin brass shim between two layers of heat-shrink tubing.

In practice, the option of load measurement using the thrust bearing was found to be unnecessary, because of the good agreement it showed with loads found from pressure-curve integration (using Simpson's rule); this is shown in figure 6.3,

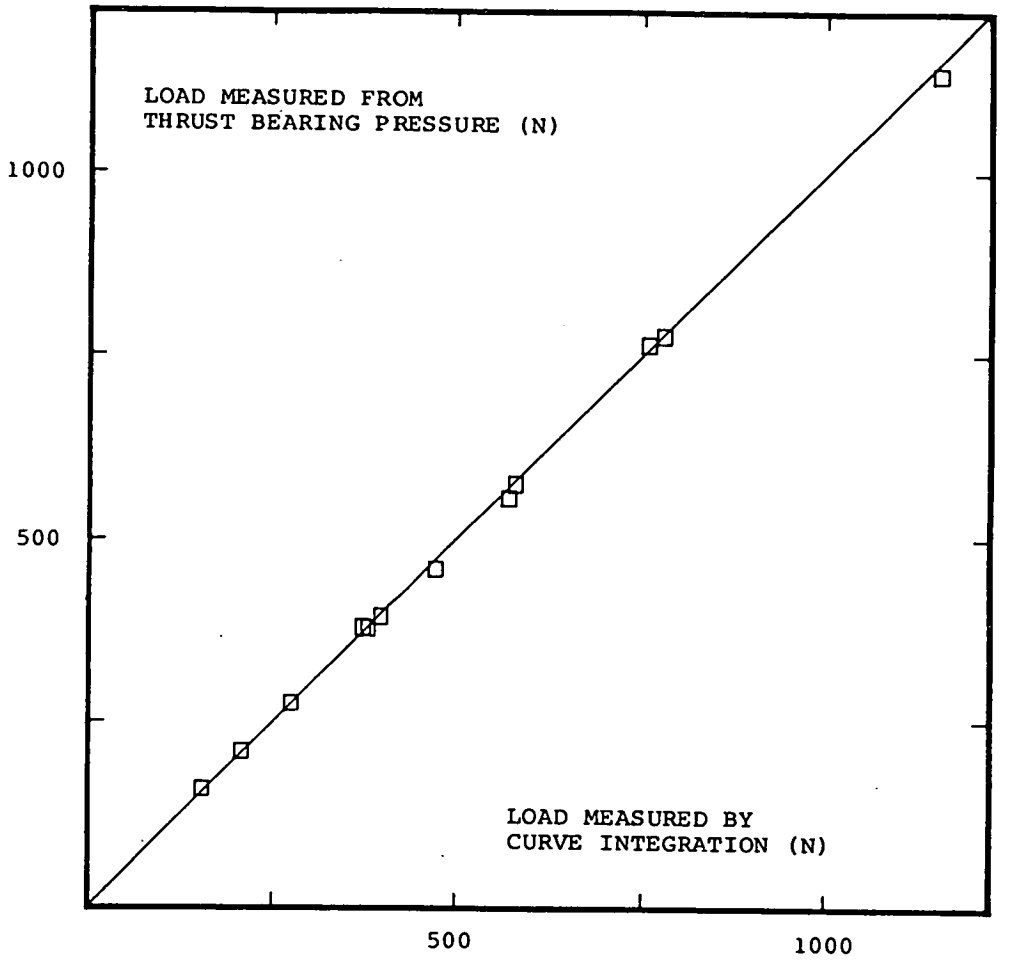

All pressures estimated to be accurate to better than 2% for both load-measurement techniques.

FIGURE 6.3
Characteristics of the Hydrostatic 'Load Cell'

in a comparison of loads measured using the two methods. Agreement to better than 3% is seen over the load range zero to 1150 N. However, because the second method allowed experiments to be made with the thrust bearing grounded, it avoided errors in the experimental film-thickness accumulated from the bearing's flowrate/clearance calibration, and was consquently adopted in preference.

The entire load tower was fabricated from aluminium alloy, with all parts anodised for corrosion protection. Opposing disc and thrust-bearing surfaces were hand-lapped to near optical finish before being anodised. No visible degradation of these surfaces occurred in use.

6.3 Pressure and Flow Measurement

Pressure measurements were made using a solid-state transducer (RS Components Ltd), with nominally linear output in the range 0-30 psi (207 kPa). To achieve maximum accuracy, and also allow operation up to its maximum rating of 60 psi (414 kPa), the transducer was calibrated using the device illustrated in figure 6.4. This again used the hydrostatic bearing principle: a centralised, freely-sliding plunger was levitated by the pressure of water in the pocket below, which was governed by the addition of calibrated weights to the top-plate. The transducer was calibrated over the range 0-372 kPa (54 psi), with the calibration procedure showing repeatability better than 1%. The calibration curve was stored in memory in a CBM 4032 microcomputer, to which the transducer was interfaced via A/D converter (PCI 6300, CIL Microsystems), allowing direct reading and recording of pressures.

All tappings were connected by PVC tubing to a 36-way hydraulic selector switch. This employed a bonded PTFE face seal to connect selectively the required tapping line to the pressure tranducer, while blocking off all the others. Each recorded pressure was the mean of 40 samples taken over a 5-second period, and individual pressure distribution curves were averaged from six nominally identical experiments, each made with the upper disc rotated 60° from its previous position. This procedure was introduced to compensate for non-parallellism of the experimental plates; parallellism was estimated as 3-8 microns, where the latter figure, although small, represented 10% of the film thickness in one experiment.

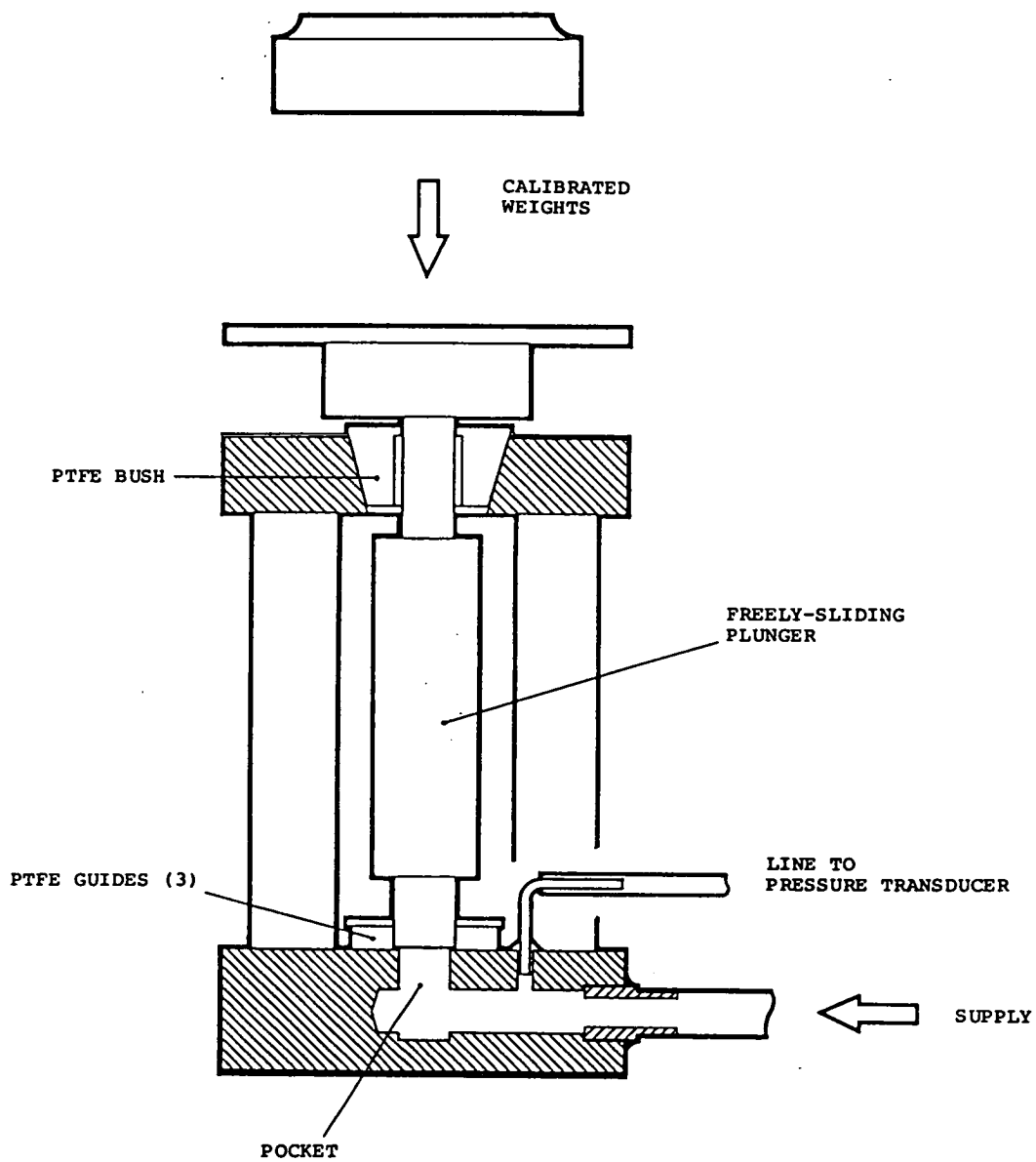

FIGURE 6.4
Hydrostatic Calibrated-Pressure Source

The water supply for all aspects of the apparatus came from a 60 psi (400 kPa) domestic main. Random pressure fluctuations of up to 4% were observed, but by time averaging the measurements (see above) this figure was effectively reduced to less than 1%. The supply was filtered upstream of all experimental apparatus, using a 'Microwynd' 50 μm fibre element, but otherwise was untreated. Flowrates were determined by collection and weighing, with an accuracy of better than 0.25%. Temperature was monitored to within 0.3 C° during each experiment, to correct for viscosity variations.

6.4 Experimental Results

Each experiment involved an averaged measurement (see section 6.3) of the radial pressure distribution in the fluid film, for a given combination of plate separation, inlet pressure, flow direction, and orifice geometry; the three experimental geometries (shown in figure 6.2) had radius ratios r_0/R = 0.1, 0.2, and 0.4. Typical results for these are shown in figures 6.5 - 6.7; note that the points are joined to show the form of each experimental curve: these are not theoretical comparisons.

In all cases, plenum chamber pressure is taken as the datum, and hence the converging flow pressures are depicted as negative. This is purely for convenience: all measured pressures were positive. Note that the true 'zero' pressure for converging flows, corresponding to that measured in the outlet pipe, does not correspond to the reading at zero radius, but to the lowest reading shown in each case (see section 6.5). The values of plate separation h are based on a theoretical fit of equation 6.3 (see section 6.5) to the lowest (diverging) flowrate curve, and differ by up to 10% from nominal estimates made on the basis of the pre-assembled load-cell dimensions. Although the value of h found in each case is thought to be more accurate than nominal (the same technique is used in air-gauging), this applies only to diverging flows.

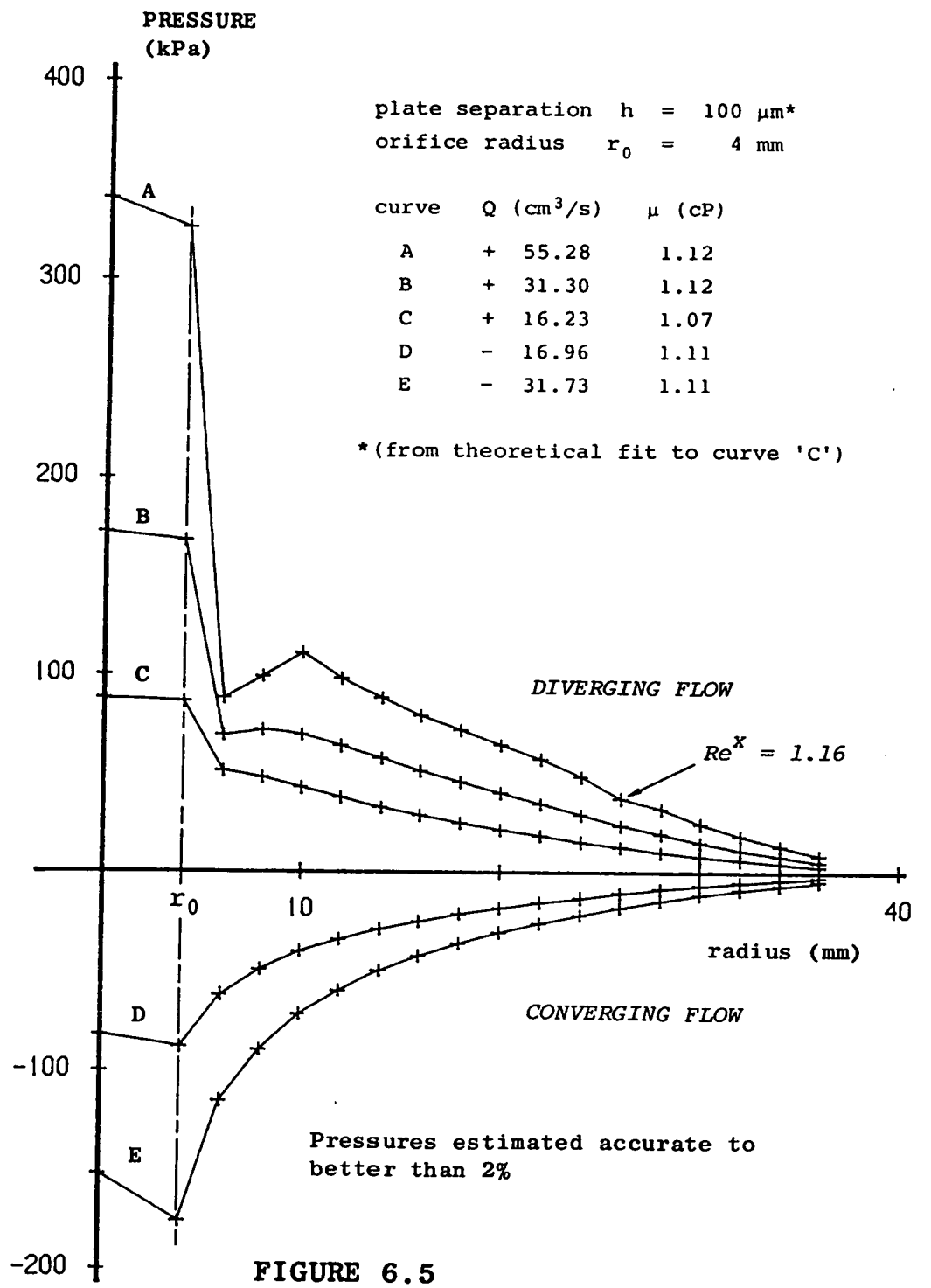

FIGURE 6.5
Radial Flow Results: Orifice 01

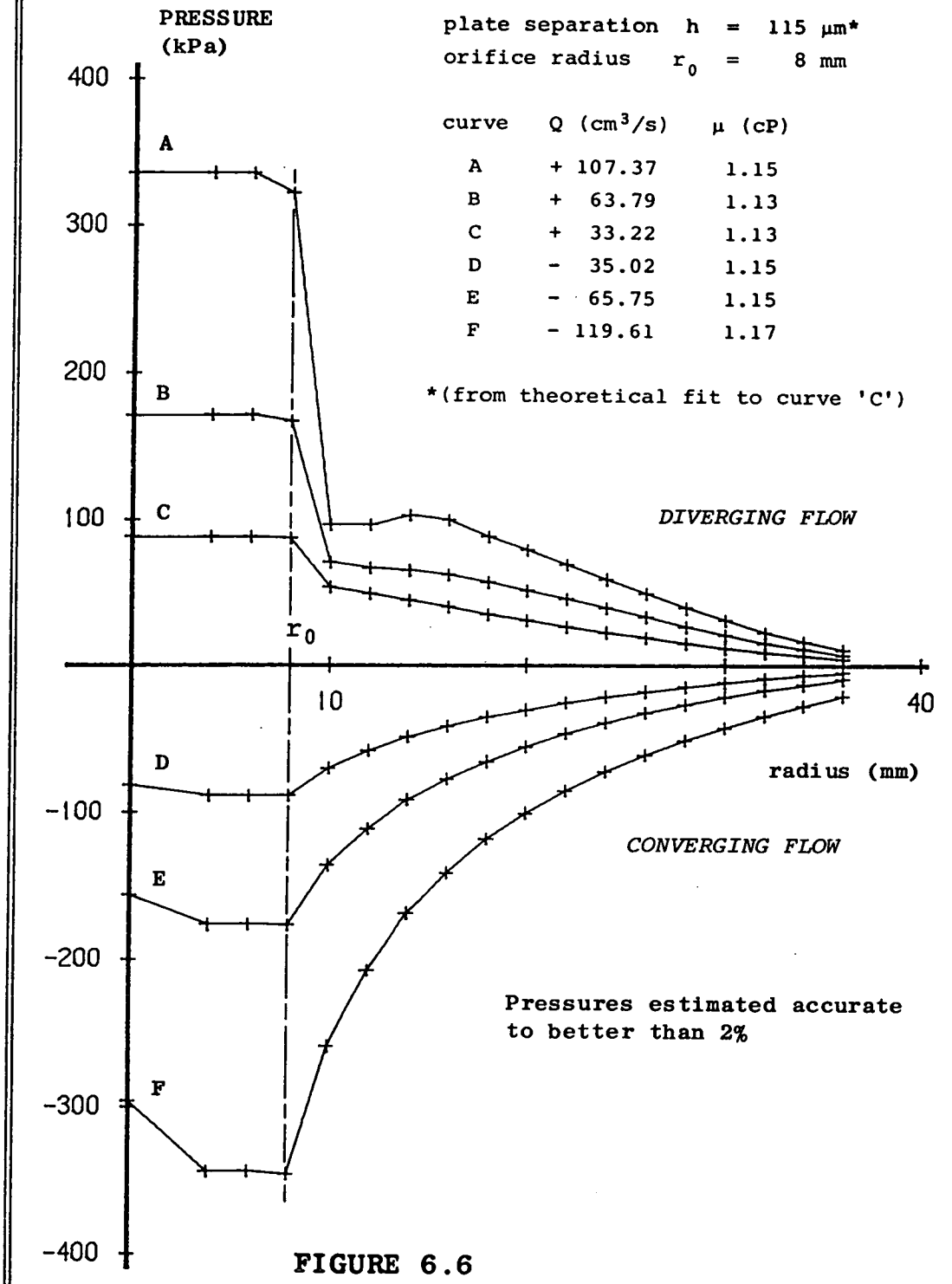

FIGURE 6.6
Radial Flow Results: Orifice O2

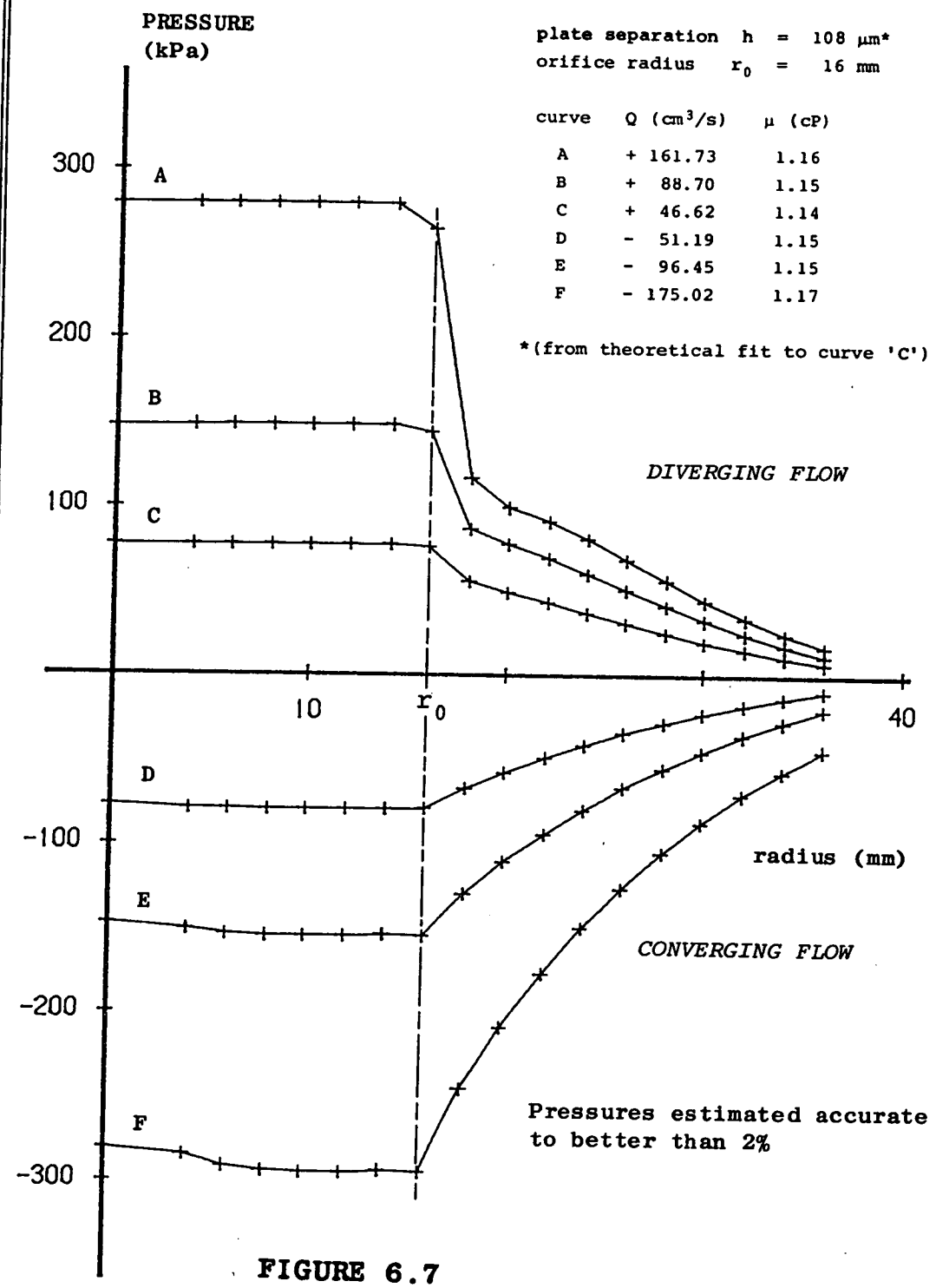

FIGURE 6.7
Radial Flow Results: Orifice O4

Clearance errors were incurred in some converging flow experiments, due to plate deflections caused by high pressure water acting on a much greater internal area of the assembly (see figure 6.1) than in diverging flow experiments. In the worst case, a theoretical curve-fit indicated 25 μm clearance deflection (for a disc thickness of 20 mm): the total fluid load in the experiment was about 4000 N at the time. For the same inlet pressure in diverging flow, a load of only 400 N applied, and deflection was negligible. Despite this, the high-pressure converging flow results are retained, as useful observations can be made from them (see section 6.5, and (2) below).

The main qualitative points to note in figures 6.5 - 6.7 are:

(1) In all cases, the pressure difference from the orifice edge, radius r_0, to the first tapping outwards, radius r_1, is greater in diverging flows than in converging flows of similar flowrate, and the discrepancy increases strongly with flowrate. In converging flows, the pressure drop is accounted for by the sum of the viscous loss and increased dynamic head going from r_1 inwards to r_0. In diverging flows these two effects act in opposition (with theoretical recovery of dynamic head between r_0 and r_1) to produce a smaller contribution to the net pressure drop. However, a large extra loss is incurred due to development of the velocity profile from initial stagnation conditions (see figure 5.3), and this represents the fundamental 'inertial pressure imbalance' described in sections 5.5 - 5.8. It occurs only in diverging flows, and its magnitude is estimated in section 6.5.

(2) In high flowrate converging flows (eg. curve F, figure 6.7) a head loss is seen at the film entry, ie. the disc outer radius (radius = 40 mm). This effect is exactly analogous to that described above, and is associated with development of the velocity profile from the stagnation conditions existing in the plenum chamber.

(3) Diverging flow curves measured at high flowrates tend to be unsmooth, in contrast to similar converging flows. Although viscous/inertial theory predicts non-symmetry for the two cases, in the sense that they would not superimpose if reflected through the axis of zero pressure, the diverging curves might be expected to become smooth at large radii, where viscous effects dominate. A possible explanation is that turbulence and/or flow separation is carried downstream from the region of the orifice edge, where strongly adverse pressure gradients exist (in diverging flows only).

(4) In all converging flow cases, the pressure measured at the orifice centre (radius zero) is seen to be greater than at the orifice edge, demonstrating a partial recovery of dynamic head. However, the pressure measured in the outlet pipe above the orifice was always found to correspond to the lowest film pressure, suggesting that recovery was confined only to the surface of the lower disc.

6.5 Quantitative Results Analysis

To quantify the component of the film entry pressure loss associated with velocity profile development in diverging flows, the measured pressure loss is examined as a function of the reduced Reynolds number Re^x. This is the most useful criterion for dynamic similarity in lubrication analyses where the influence of fluid inertia is important (see eg. Milne, 1965). For axisymmetric radial flow, Re^x is found as the product of Reynolds number Re and the film thickness ratio:

$$Re^x = Re\,(h/r) \qquad (6.1)$$

where r is the radial distance from the radial symmetry axis. Hence:

$$Re^x = \frac{\rho h^2 U}{\mu r} \qquad (6.2)$$

The experimental correlation depends on what theoretical assumption is made of the radial pressure distribution in a diverging flow. In the present case the following expression, first derived by McGinn (1955), is assumed for the static pressure drop between any two radial stations r_1 and r_2:

$$p_1 - p_2 = \frac{6\mu Q}{\pi h^3} \log_e \left\{ \frac{r_2}{r_1} \right\} + \frac{27}{140} \rho \left(\frac{Q}{\pi h} \right)^2 \left\{ \frac{1}{r_2^2} - \frac{1}{r_1^2} \right\} \quad (6.3)$$

Equation 6.3 applies to both diverging and converging flows (with flowrate Q positive in the former) under conditions of steady, fully-developed laminar flow. The expression is a linear combination of two terms: the first of these is the standard lubrication-theory viscous loss, the second the ideal (frictionless fluid) pressure change found between radii r_1 and r_2 by applying Bernoulli's theorem, with a scalar kinetic energy factor (54/35) included to correct for the parabolic velocity profile. The overall expression thus takes account of fluid inertia, but applies only to cases where this is essentially a small correction to the viscous-flow distribution. More rigorous analyses than McGinn's have led to more complex expressions than equation 6.3. There appears, however, little to be gained by using these when dealing with the region of the orifice inlet (see section 2.4).

Consider, now, the measured pressure drop between stagnation conditions at radius zero, and the first tapping downstream of the orifice edge (radius r_1, where $r_1 = r_0 + 2$ mm in all cases). If equation 6.3 is assumed to account for that part of the drop incurred between r_0 and r_1 due to viscous head loss and dynamic head gain, then the overall pressure drop from stagnation to r_1 is given by:

$$\Delta p \text{ (theory)} = \frac{6\mu Q}{\pi h^3} \log_e \left\{ \frac{r_1}{r_0} \right\} + \frac{27}{35} \rho \left\{ \frac{Q}{2\pi r_1 h} \right\}^2 \quad (6.4)$$

in which the second term corresponds to the dynamic head given by equation 5.15, the highest of those noted in section 5.6.

If the pressure drop is now made non-dimensional according to:

$$\Delta p\,(\text{dimensionless}) \;=\; \Delta p \;/\; \left\{ \frac{\mu Q}{2\pi h^3} \right\} \qquad (6.5)$$

then equation 6.4 becomes

$$\Delta p\,(\text{dimensionless}) \;=\; 12 \log_e \left\{ \frac{r_1}{r_0} \right\} \;+\; \frac{27}{35} \left(Re_1^x \right) \qquad (6.6)$$

where Re_1^x is the reduced Reynolds number (see equation 6.2) evaluated at the downstream tapping radius r_1. A plot of measured (dimensionless) pressure drop against Re_1^x in theory then gives a straight line of slope 27/35, ie. the predicted pressure loss coefficient, and intercept 12 x $\log_e\{r_1/r_0\}$, a quantity depending only on the fixed orifice dimensions.

The experimental results are shown in figures 6.8 and 6.9. In all cases the points lie along approximately straight lines, indicating dimensionless pressure drop to increase linearly with Re_1^x. Pressure losses for orifices O1 and O2 are notably higher than predicted at all Re_1^x, but the gradient in both cases agrees quite well with theory; in neither case does it suggest a smaller pressure loss coefficient than that predicted above. With orifice O4 the fit is good, in terms of both gradient and intercept. This is a little surprising, as in this case particularly, a fully developed velocity profile is unlikely to have existed at the downstream tapping. The development-length criterion of Schlichting (1979) can be applied (strictly it refers to non-radial flow, and other reasons exist for using it with caution - see Van Dyke, 1970), giving the following expression for L_d, the distance downstream of the film entry at which full flow development may be assumed:

$$L_d \;\simeq\; 0.04 \times r_1 \times \left(Re_1^x \right) \qquad (6.7)$$

For orifice O4, with Re_1^x of 7.4, the value of L_d is 5.3 mm, whereas the tapping point at r_1 is only 2 mm downstream from

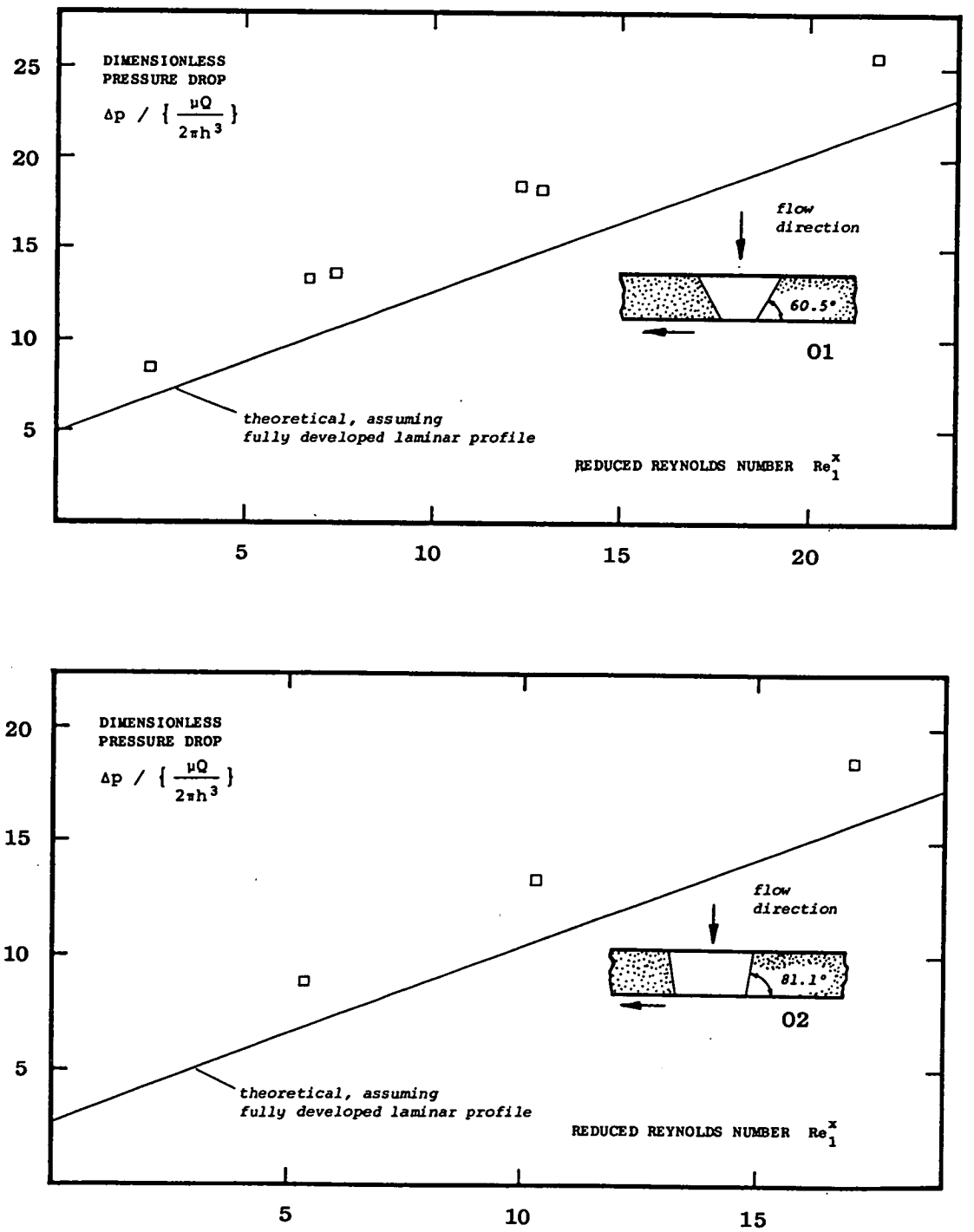

FIGURE 6.8
Experimental Pressure Losses. Results for orifice geometries 01 (top) and 02 (bottom); see figure 6.9 for geometry 04.

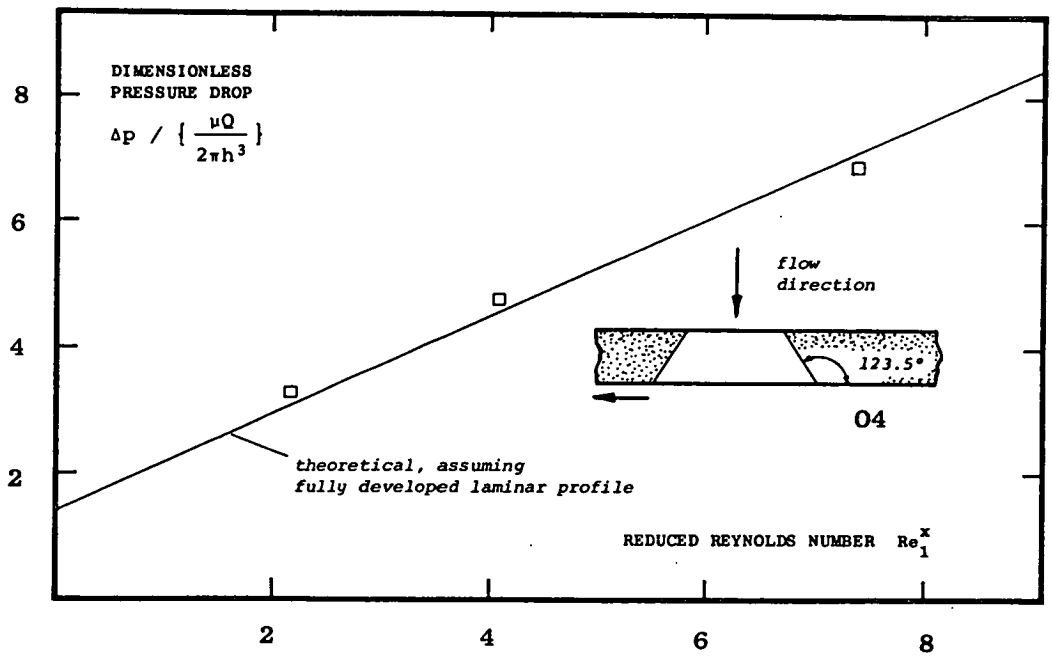

FIGURE 6.9
Experimental Pressure Losses for Orifice 04

the film entrance. An explanation for the nonetheless good agreement with theory, which is in keeping with the other results, is suggested by the possible influence of orifice geometry, and the phenomenon of flow separation. The gentle inlet angle of orifice 04 might encourage significant flow development upstream of r_0, with a parabolic velocity profile well established by r_1, in contrast to the situation predicted assuming a uniform (flat) entry profile. The sharper inlet angles of 01 and 02 are more liable, on the other hand, to give rise to the phenomenon of flow separation, as shown in figure 6.10. The separation 'bubble', which attaches to the inlet channel wall, effectively narrows the clearance, and the increase in local fluid velocity then required to satisfy continuity gives rise to increased viscous losses in

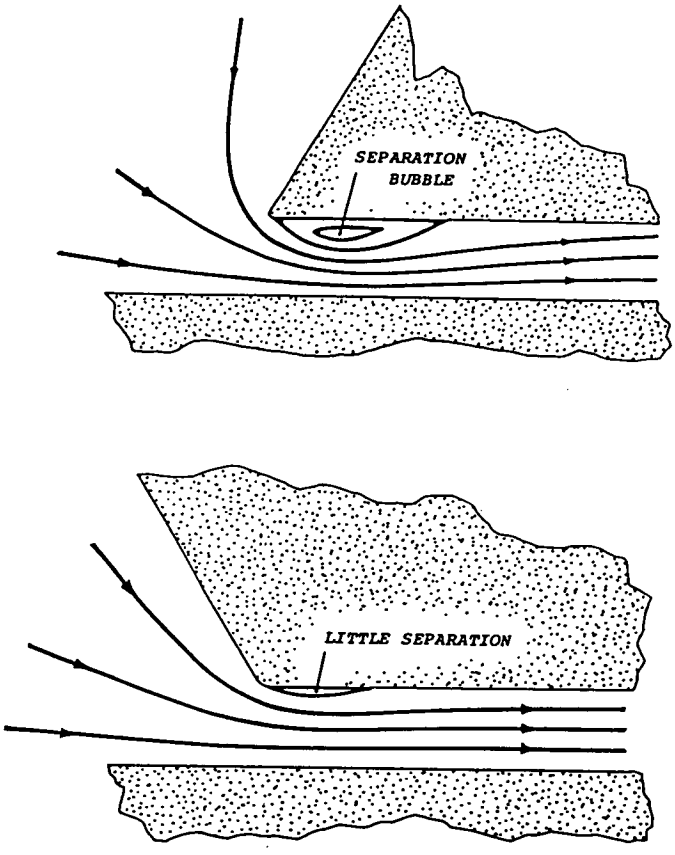

FIGURE 6.10
Flow Separation: The Influence of Orifice Geometry. Sharply curving streamlines (top) give rise to adverse pressure gradients, encouraging flow separation. A smoother inlet profile (bottom) reduces the effect.

this vicinity. Such a mechanism has been proposed by Vohr (1969) and Kawashima (1976) to account for experimental observations; McGinn has photographed the separation bubble at somewhat higher inlet Re^X (115 - 455). Formation of the separation bubble is predicted by Raal (1978) to occur at extremely low Re by the present standards: in a sophisticated numerical analysis (using a simplified and symmetric inlet geometry), he gives the separation criterion, in terms of an

'overall' Reynolds number, by:

$$\frac{\rho Q}{2\pi\mu h} \geqslant 60 \quad \text{(Raal, 1978)} \tag{6.8}$$

while in the present study, experimental measurements were made with this parameter in the range 13,000 - 200,000.

Separation might also account for the non-smooth character of eg. experimental curve A for orifice O1 (figure 6.5). The existence of separated flow far downstream of the inlet has been proposed by Jackson and Symmons (1965b) to explain radial asymmetry at similar Re^X to those of the present study. At the low value of Re^X which applies in the above case (1.16 at r = 28 mm), the alternative explanation of turbulent conditions seems unlikely. The theoretical value of Re^X at which a turbulent, diverging radial flow undergoes reverse transition has been variously estimated as 10 (Livesey), 7.8 (McGinn), 6.89 (Peube) and 4 (Patrat), of which the last is reaffirmed by experimental observations (Chen and Peube, 1964, Re^X_{crit} = 4.71, and Kreith, 1965, Re^X_{crit} = 4.06). Reverse transition to laminar flow should, by this criterion, have occurred in the above case.

The above conclusions must be treated with a certain amount of caution. The good agreement with theory observed for pressure losses with orifice O4, for example, might result from a fortuitous combination of nonideal factors. On one hand, viscous losses at the film entry may exceed those predicted from simple theory, while on the other, incomplete development of the profile at the downstream tapping would result in a lower dynamic head than predicted; the two effects might to some extent cancel. However, the results do suggest that the static pressure drop will always exceed that accounted for by the dynamic head of a parabolic profile, given in equation 5.18, and that deliberate enhancement of the effect can be achieved by using an orifice geometry which encourages flow separation; further investigation is required to find the optimum geometry.

6.6 Conclusions

The experimental results described in this chapter demonstrate the following main points:

(1) Over the range of reduced Reynolds numbers (Re^X) studied, the non-dimensional static pressure drop across a discharging orifice increases in direct proportion to Re^X.

(2) The constant of proportionality, corresponding to the dynamic head pressure coefficient of a fully developed parabolic velocity profile, is given to a good approximation by 27/35 (where the value for a uniform profile is 1/2).

(3) Flow separation increases the pressure loss, and can be encouraged by the use of an appropriate inlet geometry: sharp-angled inlet profiles should be used to maximise the effect in the proposed bearing.

(4) No static pressure drop occurs across a recharging orifice, ie. with converging radial flow. The effect is thus shown to be asymmetric with respect to flow direction, and this should be incorporated as a fundamental design feature in the bearing.

As a footnote with regard to the experimental apparatus: the performance of the 'hydrostatic load cell' was found to be very good, and the method is recommended for general use, though perhaps not in applications where the load supporting film thickness is a critical dimension (depending on the accuracy possible in the pressure/flow/clearance calibration procedure). Furthermore, the overall procedure of experimental design and construction has served as useful experience in dealing with water-lubricated hydrostatic bearings.

CHAPTER 7
THE PERMANENT MAGNET REPULSION SYSTEM

7.1 Chapter Summary

This chapter introduces the subject of the proposed magnetic repulsion system, and begins with a description of the overall aims of the present work on permanent magnets. The material selection criteria for the magnets to be used in the bearing are then listed, and the correct analytical models for 'hard' magnets are described. The topic of magnet geometry optimisation is introduced, and emphasis is placed on the difference between constrained and unconstrained optimisation procedures.

The optimisation procedures appropriate in the present case are described in non-mathematical terms. Previous analyses of permanent magnet systems are noted, and the main differences between these, and those of the present study, are pointed out. The chapter ends with a short review of related work.

7.2 Introduction

The present work on permanent magnets does not represent an attempt to define the repulsion system which would ultimately be used in the duck bearing. In view of the uncertainties which still exist in the bearing's final operating characteristics, this would be a premature exercise.

Instead, the aim is to describe procedures which will allow much more general calculations to be made. The most important of these are geometry-optimisation procedures which will enable easy selection of the optimum magnet dimensions, once the definitive operating characteristics of the bearing are fully known. Optimisation in this respect implies finding the particular magnet geometry which delivers a specified performance, using the minimum amount of magnetic material.

The optimisation analyses are described in chapter 8; in chapter 9 are described experiments which were undertaken to test the theoretical predictions. To understand the basis of the analyses, an outline description of the proposed magnet system, and of permanent magnet theory in general, is first necessary. This follows below.

7.3 Magnetic Material Selection

The magnets to be used in the proposed bearing will be either barium or strontium ferrites. Ferrites have been chosen largely on economic grounds: unprecedented mass production of magnet blocks is expected to make raw material costs the dominant economic factor, and the feedstock is remarkably cheap (£350/ton in 1980: Salter, 1981a). In addition to a low projected cost, and good magnetic characteristics (see below), ferrites offer the considerable advantage of being entirely non-corroding, which is particularly important in the present application.

Ferrites belong to the class of 'hard' magnets, which makes them ideal for repulsion applications. A hard magnet is one whose intrinsic magnetisation (corresponding to its magnetic strength) remains constant in the presence of an adverse magnetic field as strong as that which the magnet can itself exert. Hence, two hard magnets of the same material, operating in mutual repulsion, will experience negligible loss of strength. Ferrites are not the most powerful hard magnets: this distinction belongs to the rare-earth cobalts, with intrinsic magnetisation values of typically 0.8 - 1.0 tesla (T). Although having magnetisation of only 0.2 - 0.4 T (and note that magnetic force goes with magnetisation squared - see section 8.2), the behaviour of ferrites has in at least one case been found to more closely approach that of ideal hard magnets (Tsui et al, 1972).

Both the magnetisation and intrinsic coercivity (the imposed field required to reduce magnetisation to zero) of ferrites vary with temperature; the effects are reversible, however, and for the mean annual temperature range which a submerged seawater bearing will experience off north-west Scotland, ie. 8-14°C (Lee, 1981), reversible changes in magnetisation will represent less than 2% of the nominal strength. Of the two ferrites, barium and strontium, the latter has slightly better magnetic properties, but is more expensive, and difficult to shape during manufacture, giving rise to high scrap losses (30% or more). Both materials yield hard but brittle magnets, which are subject to chipping or cracking under mechanical shock. This does not occur in repulsion applications where a non-contacting mechanism is stipulated, and is not a danger in the present case.

One fortuitous aspect of systems which use only hard magnetic materials is their amenability to fully analytic calculation. With the assumption of constant and uniform magnetisation, mathematical models can be used which date back to the last century (see, eg. Maxwell, 1873), but which only became useful with the advent of hard magnetic materials in the nineteen-fifties. This characteristic is exploited in the present analysis, where a combination of analytic and computer-numerical techniques is used to find optimum magnet geometries to a high degree of accuracy.

7.4 Analytical Models for Permanent Magnets

In an ideal 'hard' permanent magnet, the intrinsic magnetisation is constant and uniform: as a result, the magnet is mathematically equivalent to two pole-surfaces of uniform charge-density, or an air-cored solenoid of uniform current density; the two representations are shown in figure 7.1. Both arise from elementary dipole considerations, and both yield exactly the same results. Their derivation is discussed in most standard texts on electricity and magnetism (eg. Kip, 1969), and McCaig (1977) compares the relative merits of the two methods.

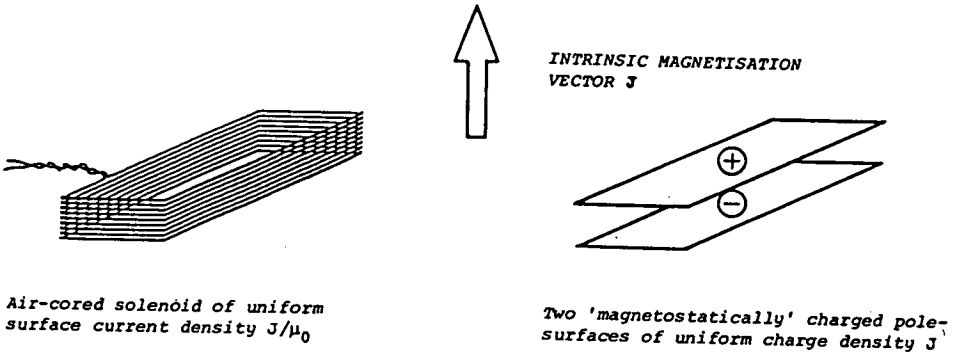

FIGURE 7.1: Analytical Models for Ideal 'Hard' Permanent Magnets

With the charged pole-surface model, fields and forces are found by analogy with electrostatics. The force between two magnets is calculated by integrating the elementary charge interactions, where these obey an inverse-square law (Coulomb's law). Using the solenoid model, overall force is found by integrating the incremental forces acting on one set of current-windings placed in the magnetic field created by another. With rectangular magnet geometries, resultant fields and forces can be expressed analytically; axisymmetric geometries, however, require more complex mathematical treatment (Craik and Harrison, 1974).

Magnetic circuit theory is not in general suitable for calculating forces between magnets, and particulary not in repulsion configurations; McCaig (1977) demonstrates how this can lead to highly erroneous results.

7.5 Optimising the Magnet Geometry

The geometry-optimisation analyses in this thesis are intended to make it possible, having selected a particular bearing characteristic, to find easily the magnet geometry which provides this characteristic, using the minimum volume of magnetic material. The bearing characteristic will ultimately be specified in one of the following two ways:

(1) As the minimum repulsion force required at a specified value of magnet pole separation h (corresponding to the lubricating film thickness), for example the equilibrium separation h_e.

(2) As the minimum stiffness required at a specified clearance.

Note that magnet dimensions optimised for maximum force are not the same as those optimised for maximum stiffness (see section 8.6). In practice, the required repulsion force and stiffness for the bearing will be specified in terms of local radial magnetic pressure, and pressure increase per unit pole deflection, respectively. The values will be local, rather than applying to the bearing as a whole, on account of the compliance of the magnet sheet: the overall stiffness of the bearing would only be an appropriate criterion in a rigid-element design.

The above specification will be subject to one or more constraints, with the result that any optimised geometry will represent a mathematically 'local' rather than 'global' solution. The constraints are of the following forms:

(a) A stipulated minimum magnet cross-sectional size (see figure 3.4). The magnets must be sufficiently large to ensure that an acceptably small loss of repulsion force occurs under the condition of maximum axial offset of opposing pole faces. The possibility of some axial misalignment must be taken into account.

(b) A maximum axial pitch for the magnet rows, chosen with regard to the compliance of the magnet-sheet: too great a pitch might result in bulging of the sheet between rows.

What both the above constraints dictate in practice is that geometry optimisation for maximum force (or stiffness) per unit volume is carried out with the proviso of a certain minimum volume for each opposing magnet pair. In other words, maximum material efficiency is sought not only for a specified pole clearance, but also for a specified magnet volume.

In contrast, the maximum force/unit volume in an unconstrained optimisation is found by specifying only the pole clearance, and placing no initial restriction on the dimensions of the magnets required to achieve it. The required pressure or stiffness in this case is then met by using as many 'globally optimised' magnet pairs as are necessary to provide it, in the knowledge that the material efficiency of each cannot be bettered. However, an unconstrained optimisation, although yielding better material efficiency, is undesirable in the present case. The unconstrained optimum magnet dimensions for either force or stiffness/unit volume are of the same order as the pole clearance (see section 8.9). For an equilibrium clearance of 3 mm, a magnet pair optimised for maximum 'global' force/unit volume has pole width of approximately 6 mm, and height of 4 mm. Opposing magnets of these dimensions would be chronically vulnerable to axial offsets of 2 mm or more. In a structure with the size and constructional tolerances of the duck, this is clearly unacceptable. A certain minimum size of magnet must be stipulated, and hence the correct optimisation procedures are necessarily constrained.

It would be true to say that the economic feasibility of the bearing can be directly linked to the accuracy of magnet axial alignment which can be achieved in practice. If perfect alignment were possible, the magnet geometry could then be

optimised using an unconstrained technique, and blocks of small cross-section (see above) used to make up the opposing rings. Material efficiency would be very high. The greater the maximum-likely misalignment, the larger the magnets need to be, to provide a suitably large safety factor. A sophisticated and expensive axial alignment system might actually result in an overall reduction in bearing cost, by allowing the use of small opposing magnets.

7.6 Optimisation Procedures

The magnet pair cross-sectional dimensions are so much smaller than the bearing radius (by a factor of 100) that bearing curvature may be neglected. Furthermore, the effective length of the equivalent linear magnet array is fixed as the circumference of the bearing, and hence is not a variable. The optimisation thus reduces to a two-dimensional one, in which the quantities to be maximised are force and stiffness per unit length, and these are sought by optimising the cross-sectional dimensions of the magnet pairs. The fixed volume constraint for a magnet pair (see above) reduces to a fixed-area constraint.

Further simplifications are made. By ignoring the 'neighbouring-row' interactions of the parallel rings in the magnet array, only a single pair need be considered. If sufficiently close axial pitching is adopted, neighbouring-row interactions can actually increase total repulsion (see section 8.10): geometry optimisation in neglect of the effect thus yields conservative estimates of required magnet volume. The optimum geometry of an isolated pair can be used as the starting point for more comprehensive (but more specific) analyses taking account of neighbouring-row interactions (see Henning, 1973).

Only symmetric magnet-pairs, ie. with identical dimensions, are considered. It can be mathematically demonstrated (see eg. Coffey et al, 1972) that this is a prerequisite for any optimum configuration, provided that there is no reason to minimise

preferentially the amount of material on one side. In some applications, optimisation is carried out with respect to only one of the components (for example, in permanent magnet 'maglev' railway analyses, optimisation is carried out with the aim of minimising only the track volume, and is achieved at the expense of local material efficiency, measured over the length of the vehicle - see Henning, 1973). Such a constraint does not apply in the present case. The general analytical geometry for a symmetric, two-dimensional magnet pair is shown in figure 7.2.

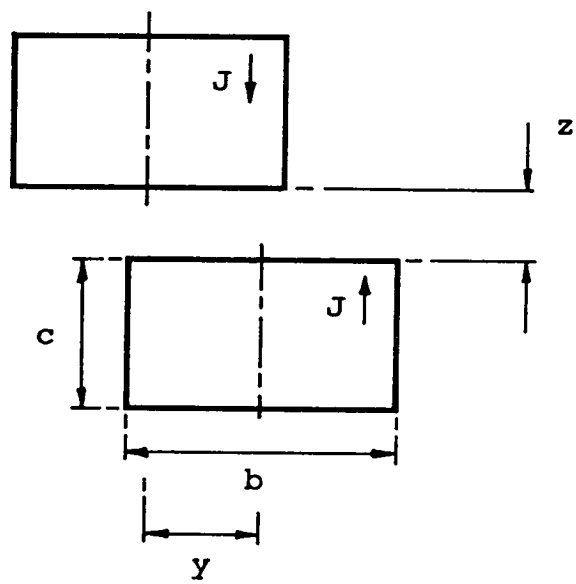

magnet width : b
height : c
pole separation : z
horizontal offset : y
magnetisation : J

NOTE: area A = 2bc

FIGURE 7.2: General Analytic Geometry for a Symmetric, Two-dimensional Magnet Pair

With reference to figure 7.2, the most important optimisation procedures carried out in the present study consist of:

(1) Constrained maximum force/length: the vertical force/unit length for a magnet pair of the given geometry is maximised for a fixed total area A, where A = 2bc, over a range of values of clearance z and lateral offset y. The optimum values of pole-width b and height c are recorded in each case.

(2) Constrained maximum stiffness/length: the vertical stiffness/unit length is maximised in an exactly analogous procedure to (1) above.

(3) Unconstrained maximum force/volume: for a given combination of z and y the global optimum values of b and c are returned which maximise force/volume (as force/unit length divided by area A), with no constraint imposed on the total cross-sectional area.

(4) Unconstrained maximum stiffness/volume: vertical stiffness/unit volume for this geometry is maximised in the analogous procedure to (3) above.

The last two analyses, although of limited usefulness in the present application, are included for completeness' sake: some prior results exist in each case, though only for fully-aligned magnets (y = 0), and based on graphical techniques, in contrast to the present numerical analysis. Minnich (1971) and Coffey et al (1972) both dealt with unconstrained force/volume procedures, while Yonnet (1980) performed an unconstrained stiffness/volume optimisation. The reason for including optimisation of laterally-offset magnet pairs in the present analysis is to allow such a contingency to be included in the bearing's force or stiffness specification, ie. with an allowance for axial misalignment incorporated in the economic optimum geometry.

The important differences between the optimisation analyses described in the present work, and those previously published can be summarised thus:

(1) The present analyses all invoke rigorous analytical and numerical methods. The maxima of objective functions, eg. force/unit volume, are found by numerically seeking zero values of analytic function derivatives. Previous analyses have used graphical estimates of curve maxima.

(2) Constrained optimisation analyses of isolated magnet-pairs do not appear to have been performed previously. The two most important optimisation procedures with regard to the duck bearing are those for maximum force/unit length and stiffness/unit length, using a two-dimensional magnet pair of fixed (constrained) cross-sectional area.

(3) All the two-dimensional magnet optimisation schemes take into account the possibility of horizontal pole-misalignment. The case of fully aligned magnets (which was considered in previous unconstrained optimisations) is thus special, rather than general, in the present study.

Two analyses of a three dimensional rectangular magnet pair, again using rigorous optimisation techniques, are included for interest. All theoretical results are presented in normalised units, to allow them to be easily applied once the final force and stiffness characteristics of the bearing are decided.

7.7 Related Work

The present analyses owe much to studies carried out in several countries over the past twenty-five years, on applications of permanent magnet repulsion as diverse as high-speed vehicle levitation and small-scale frictionless bearings. In the former category, the work of Baran (1962, 1964, 1971, 1972) and Henning (1973) in Germany is especially noteworthy; Baran was one of the

first to perform rigorous performance analyses based on pole-surface mathematics. Also recommended are the reports prepared in the United States by Ford Motors (Borcherts, 1971), the General Electric Company (Minnich, 1971), and Stanford Research Institute (Coffey et al, 1972): the use of solenoid mathematics was invoked in the first two of these. Small-scale magnetic bearings have been comprehensively studied in France by Yonnet (1978a, b, 1980, 1981a, b), who has identified the procedures for optimising bearing geometry to yield maximum stiffness.

For an explanation of the fundamental properties of permanent magnets, and the correct analytical techniques to use in field and force calculations, the reader is encouraged to consult McCaig (1977), whose work consistently emphasises the important practical aspects of permanent magnet systems (1961, 1968). An important experimental study is that of Tsui et al (1972). Other works of related interest include a theoretical force/unit volume optimisation of cylindrical magnets (Cooper et al, 1973), and field calculations for rectangular magnet geometries (Craik, 1966, 1967).

7.8 Conclusions

The characteristics of ferrite magnets make them well suited for use in the proposed bearing. Ferrites offer good magnetic characteristics in repulsion applications, suffer from no corrosion problems, and are relatively cheap.

To calculate magnetic forces and stiffnesses, the magnets may be represented either as charged pole surfaces or air-cored solenoids. With rectangular magnet geometries, fully analytic expressions for fields and forces can be obtained. The magnet-pairs in the duck bearing can be represented as symmetric, two-dimensional rectangular blocks. The important geometry optimisation procedures in this study involve finding the dimensions of an isolated magnet pair which maximise a

desired function, such as force/unit length, or stiffness/unit volume. Two kinds of optimisation procedure are described. In a constrained optimisation, the maximum material efficiency is found assuming a fixed total volume of magnetic material, at a particular pole clearance. In an unconstrained optimisation procedure, only the magnet pole-separation is specified. Because of the problem of magnet axial alignment, constrained optimisation procedures are of more use in the present application.

The analyses described in the present work differ from those previously published, in that:

(a) Computer-numerical methods are used to find function maxima to greater accuracy than with prior graphical methods.

(b) Constrained optimisation procedures are included.

(c) Magnet horizontal offset is included as a variable.

The maximum likely axial offset of the bearing magnets is seen as a fundamental factor in determining the overall cost of the bearing. The better the alignment is, then the smaller, and more material efficient, can be the magnets.

CHAPTER 8
PERMANENT MAGNET OPTIMISATION

8.1 Chapter Summary

This chapter contains all the theoretical permanent-magnet analyses performed in the present study. The expressions for force/unit length and stiffness/unit length for a general two-dimensional magnet pair are first given, after a brief description of their derivation. Some typical theoretical results are shown for magnets of a representative size, and the scaling laws and normalisation procedures for force and stiffness are then listed.

Four optimisation analyses follow, all dealing with an isolated two-dimensional magnet pair. The geometry is first optimised with a constant-area constraint, for maximum force and stiffness/unit length, and then with no constraint, for maximum force and stiffness/unit volume. A worked example is included to demonstrate how the results should be applied in practice. In a discussion of multiple-magnet arrays, the advantages of a heteropolar configuration are explained, and theoretically demonstrated. Finally, two analyses of a three-dimensional magnet pair are described.

8.2 Magnetic Forces

For the general case of a two-dimensional rectangular magnet pair, force/unit length may be calculated using the analytical geometry illustrated in figure 8.1, in which one finite-length rectangular block is levitated above a second of infinite length. Solenoid mathematics are used (see section 7.4), and in figure 8.1 the current windings are shown which are mathematically equivalent to the real permanent magnet blocks. The solenoidal current-density is given by J/μ_0, where J is the magnetisation in tesla, and μ_0 the universal magnetic constant, with value $4\pi \times 10^{-7}$ henrys/metre.

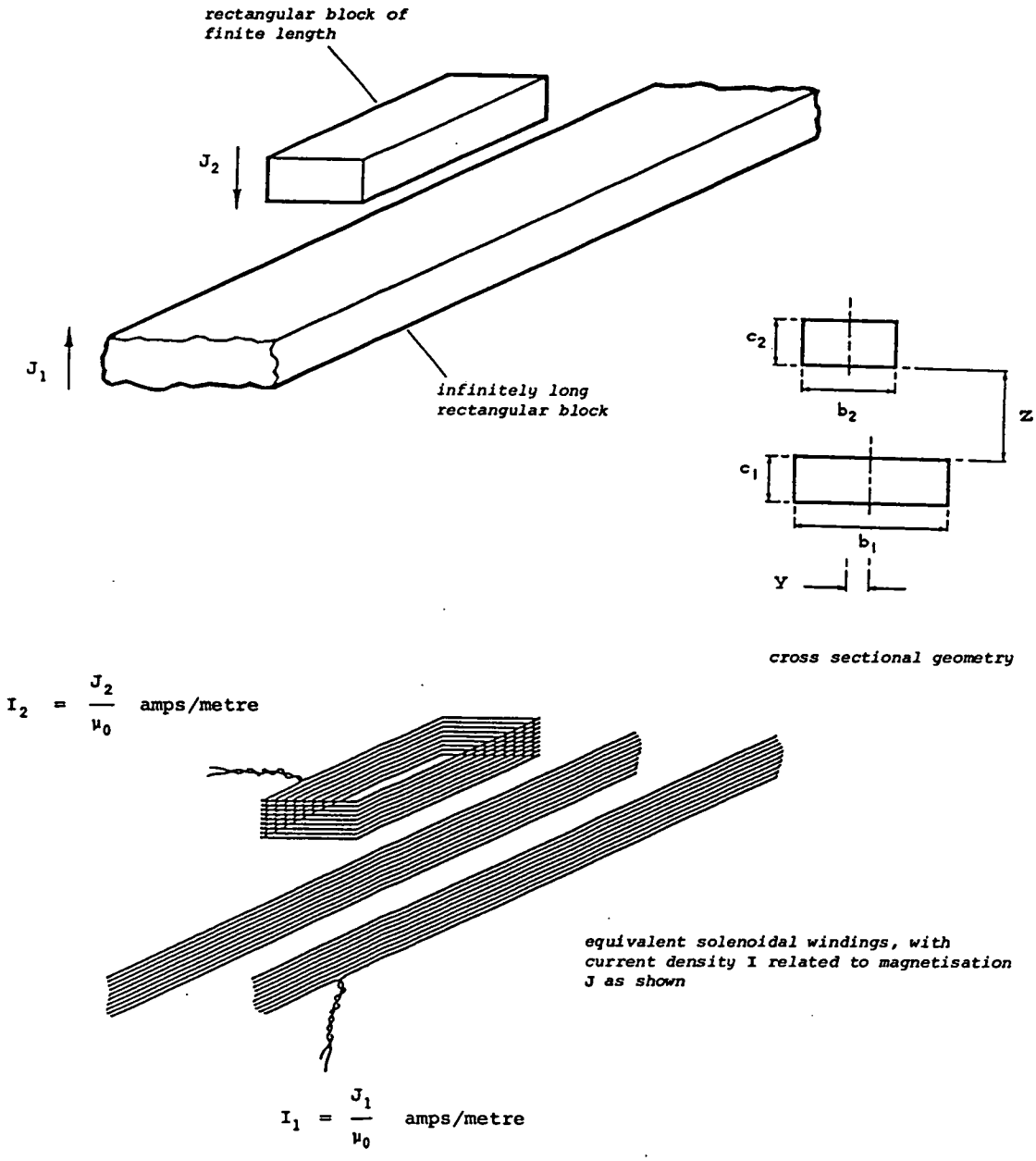

FIGURE 8.1
Two-dimensional Magnet Pair: Analytical Geometry

Beginning with an expression for the force mutually exerted between incremental elements of two conducting loops (see eg. Kip, 1969), the total force of interaction between two rectangular solenoids may be integrated. Two analytic solutions are derived, one for the vertical, and one the horizontal force per unit length; the magnets experience forces identical in magnitude but opposite in direction, according to Newton's third law. Referring to the forces/unit length as F_z and F_y respectively, the two expressions are given by:

$$F_z = \frac{J_1 J_2}{4\pi\mu_0} \sum_{i=1}^{2} \sum_{j=1}^{2} \sum_{k=1}^{4} n_{ij}\, b_{ij}\, p_k \left\{ 2 \tan^{-1}(z_k) + z_k \log_e\{ b_{ij}^2 (1 + z_k^2) \} \right\} \qquad (8.1)$$

$$F_y = \frac{J_1 J_2}{4\pi\mu_0} \sum_{i=1}^{2} \sum_{j=1}^{2} \sum_{k=1}^{4} n_{ij}\, b_{ij}\, p_k \left\{ 2 z_k \tan^{-1}(z_k) - \log_e\{ b_{ij}^2 (1 + z_k^2) \} \right\} \qquad (8.2)$$

in which the geometric nomenclature is that of figure 8.1:

i	j	n_{ij}	b_{ij}	k	p_k	z_k
1	1	1	$y + \frac{1}{2}(b_2 - b_1)$	1	1	$\frac{z}{b_{ij}}$
1	2	-1	$y - \frac{1}{2}(b_2 + b_1)$	2	-1	$\frac{z + c_1}{b_{ij}}$
2	1	-1	$y + \frac{1}{2}(b_2 + b_1)$	3	-1	$\frac{z + c_2}{b_{ij}}$
2	2	1	$y - \frac{1}{2}(b_2 - b_1)$	4	1	$\frac{z + c_1 + c_2}{b_{ij}}$

(8.3)

From equations 8.1 and 8.2 it can be seen that force/unit length is proportional to the magnetisation product J_1J_2, and hence in a system with like-magnets, proportional to J^2. Force/unit volume is found as force/unit length divided by the total cross-sectional area A where, from figure 8.1:

$$A = b_1c_1 + b_2c_2 \qquad (8.4)$$

From equations 8.1 and 8.2, the force/unit length can be found for any two-dimensional magnet-pair. Some typical results are shown in figure 8.2 for magnets with cross-sectional dimensions and magnetic strength appropriate to the duck/spine bearing. The three force-clearance curves correspond to fixed lateral offsets of zero, one-quarter, and one-half pole-width. Note the severe fall-off in vertical repulsion force with increasing offset: at quarter pole-width offset, maximum repulsion force falls to just over half its fully aligned value.

None of the curves behaves asymptotically as clearance tends to zero, and a finite maximum force at pole-contact exists for each. This may seem surprising: equation 8.1 can be derived either from solenoid or coulomb-repulsion arguments (see section 7.4), and in both cases the incremental forces obey an inverse power law, ie. tending to infinity as clearance tends to zero. However, this 'problem' disappears on integration, and the theoretical force at pole-contact is strictly calculable.

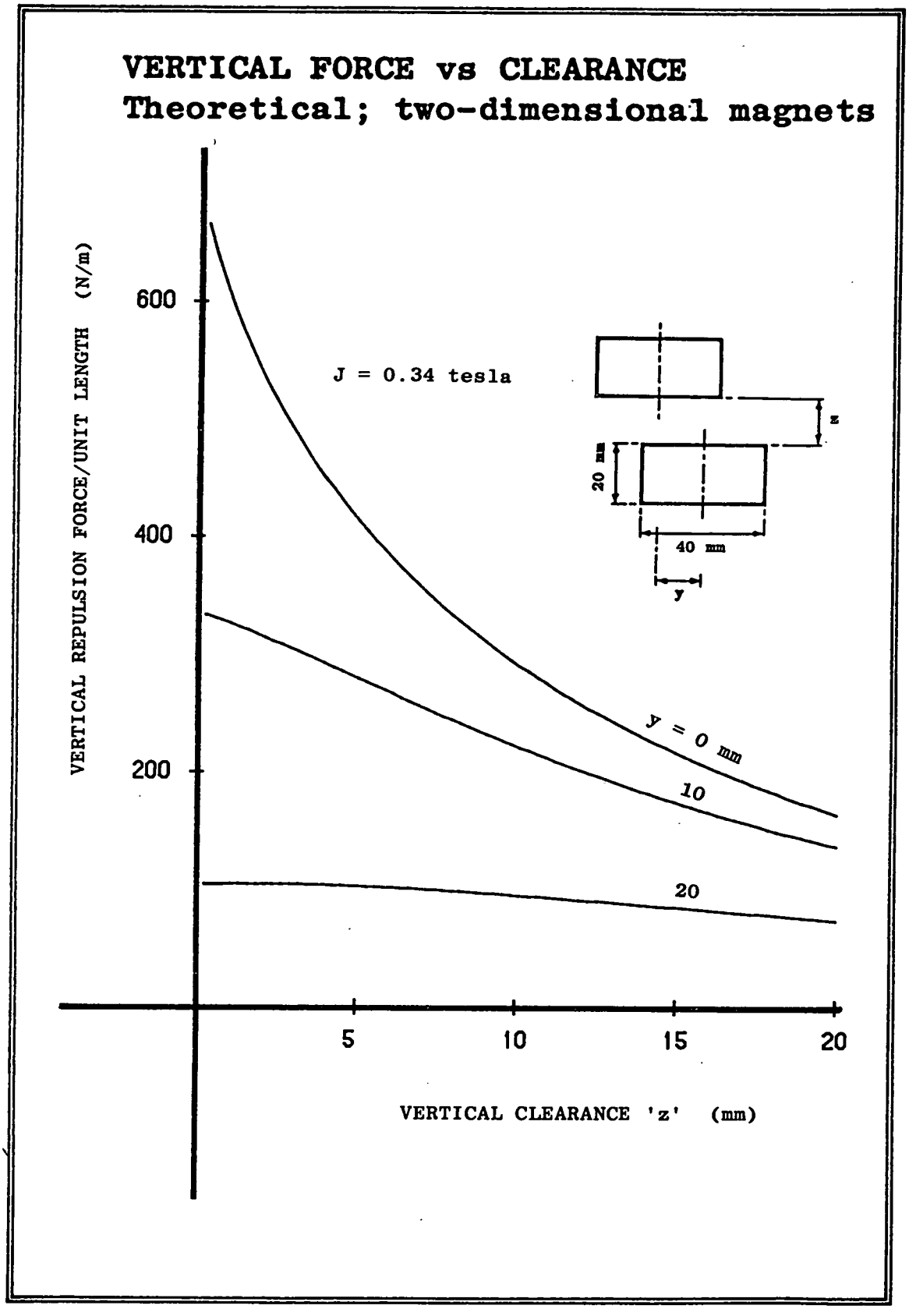
VERTICAL FORCE vs CLEARANCE
Theoretical; two-dimensional magnets
VERTICAL REPULSION FORCE/UNIT LENGTH (N/m)
600
400
200
J = 0.34 tesla
z
20 mm
40 mm
y
y = 0 mm
10
20
5
10
15
20
VERTICAL CLEARANCE 'z' (mm)

FIGURE 8.2

8.3 Magnetic Stiffness

Analytic expressions for vertical and horizontal stiffness/unit length are found by differentiating equations 8.1 and 8.2 with respect to the appropriate displacement terms, hence:

$$K_z = -dF_z/dz \tag{8.5}$$

$$K_y = -dF_y/dy \tag{8.6}$$

where the full expression for K_z is given, using the same notation as above, by:

$$K_z = \frac{J_1 J_2}{4\pi\mu_0} \sum_{i=1}^{2} \sum_{j=1}^{2} \sum_{k=1}^{4} n_{ij} p_k \{ 2 + \log_e \{ b_{ij}^2 (1 + z_k^2) \} \} \tag{8.7}$$

Horizontal stiffness/unit length K_y is easily found, as the components of stiffness in a two-dimensional ideal-magnet system are related according to:

$$K_y = -K_z \tag{8.8}$$

This is in accordance with Earnshaw's theorem (1839), which dictates that stable levitation using permanent magnets is impossible. The instability is implicit in equation 8.8: unless both stiffnesses are zero, one must always be negative, hence unstable. It is for this reason that the bearing requires an axial alignment mechanism of the kind described in section 3.9 (see figure 3.6).

In practice, stiffness/unit length may either be calculated analytically using equation 8.7, or numerically, from force-curve data of the kind graphed in figure 8.2. If the points are sufficiently closely spaced, the latter method gives results indistinguishable from the rigorous calculation.

In figure 8.3 are shown the stiffness characteristics of the same magnet-pair described in section 8.2 (see figure 8.2). Note the highly nonlinear nature of vertical stiffness, and the severe fall-off which occurs with non-zero lateral offset; the effect is much more serious than that observed for force. With zero lateral offset, vertical stiffness tends to infinity at pole contact, in contrast to the behaviour observed for force. This is one situation in which experiment and theory must inevitably disagree.

8.4 The Scaling Laws for Force and Stiffness

The following four rules are general, and apply to all two- or three-dimensional magnet arrangements:

(1) Force is proportional to the square of scale.

(2) Stiffness is directly proportional to scale.

(3) Force/unit volume is inversely proportional to scale.

(4) Stiffness/unit volume is inversely proportional to scale squared.

In addition, the following two rules apply strictly to two-dimensional geometries:

(5) Force/unit length is directly proportional to the scale of the cross-sectional dimensions.

(6) Stiffness/unit length is independent of cross-sectional scale.

These laws are of great use in experimentally validating optimum geometries (see sections 9.9 - 9.12). The importance of observing geometric similarity is emphasised by McCaig (1961), and as a corollary to the scaling laws, the following

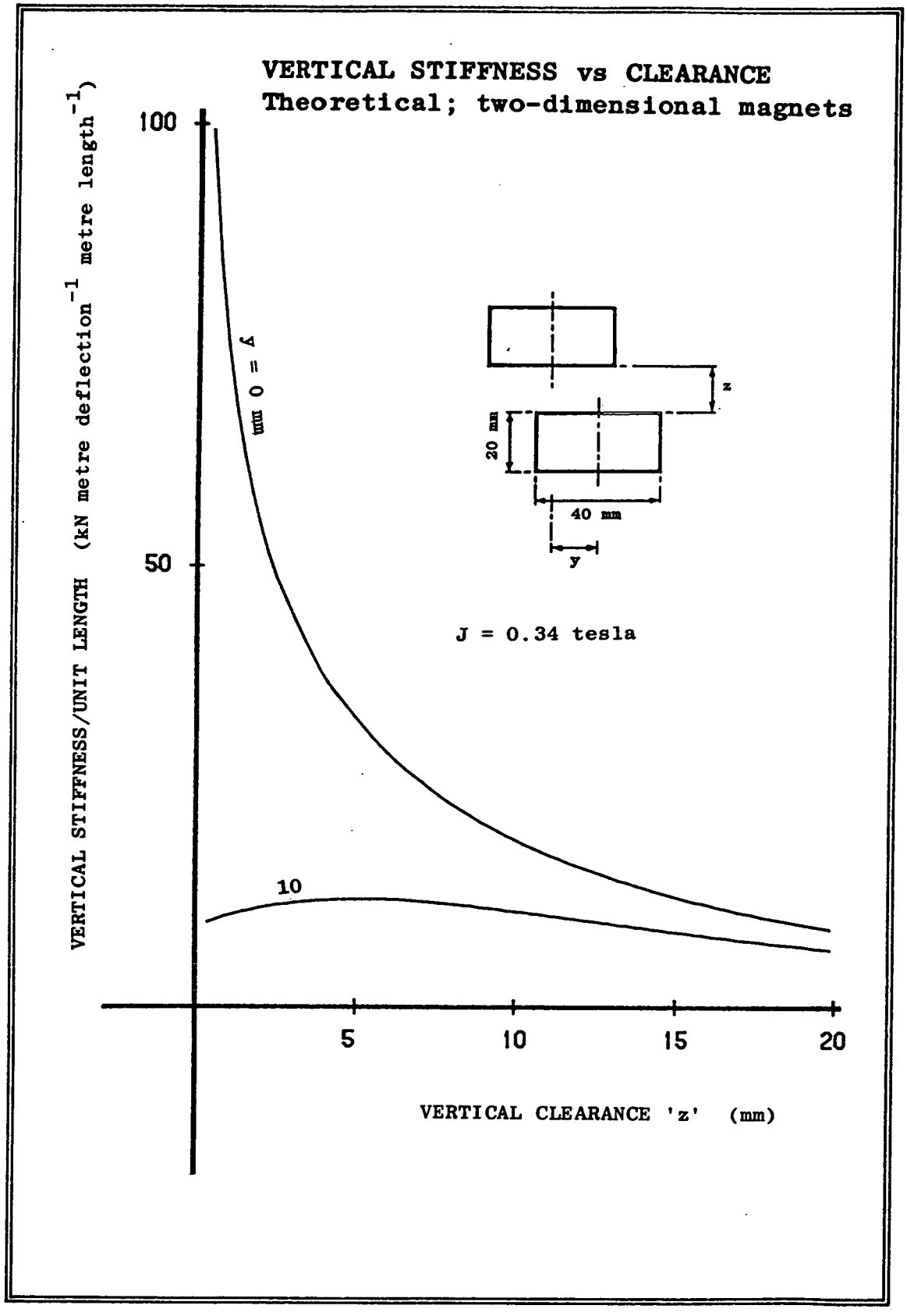
VERTICAL STIFFNESS vs CLEARANCE
Theoretical; two-dimensional magnets
VERTICAL STIFFNESS/UNIT LENGTH (kN metre deflection^{-1} metre length^{-1})
100
50
y = 0 mm
10
z
20 mm
40 mm
y
J = 0.34 tesla
5
10
15
20
VERTICAL CLEARANCE 'z' (mm)

FIGURE 8.3

procedures are noted for converting measured or calculated quantities into scale-independent form, referring specifically to the two-dimensional case:

(a) Force/unit length is divided by a representative cross-sectional dimension.

(b) Force/unit volume is multiplied by a representative cross-sectional dimension.

(c) Stiffness/unit length is automatically scale-independent, and needs no normalising factor.

(d) Stiffness/unit volume is multiplied by the square of a representative cross-sectional dimension.

Normalising is not the same as non-dimensionalising: all the above quantities (a-d) have normalised units of N/m^2, which follows from scaling law no.1. A normalised result is equivalent to that which would accrue if the representative dimension were unity, with all the other dimensions scaled in proportion, according to geometric similarity.

8.5 Geometry Optimisation (1): Constrained Force/Unit Length

The aims of the four most important optimisation procedures were described in section 7.6. In all cases the analytical geometry is that shown in figure 7.2, ie. the two-dimensional case of symmetric magnets with identical magnetisation. In the first analysis, the maximum vertical force/unit length available from a fixed total cross-sectional area A is found over a range of values of pole-clearance z and lateral offset y, with the optimum magnet width b and height c recorded in each case. Although two optimum dimensions are required, there is only one

independent variable, as the constant-area constraint relates b and c according to:

$$c = A/2b \tag{8.9}$$

where A is constant. Arbitrarily choosing b as the independent variable, the maximum of the force/unit length function F_z for a given combination of z and y is found by setting:

$$dF_z/db = 0 \tag{8.10}$$

where:

$$dF_z/db = \partial F_z/\partial b + (\partial F_z/\partial c)\, dc/db$$

From equation 8.9:

$$dc/db = -c/b \tag{8.11}$$

hence, substituting 8.11 into 8.10, the required condition for a maximum of F_z becomes:

$$\partial F_z/\partial b - c/b\,(\partial F_z/\partial c) = 0 \tag{8.12}$$

The partial derivatives $\partial F_z/\partial b$ and $\partial F_z/\partial c$ are found analytically by differentiating equation 8.1 with respect to the appropriate variables.

With a fixed area, the optimum geometry for a given combination of z and y is then found solving equation 8.12, ie. by finding the root of the nonlinear expression on the left hand side. A solution corresponds to the optimum magnet width b_{opt} under the particular conditions stipulated; the corresponding height c_{opt} is then automatically found from equation 8.9.

Because equation 8.10 is equally the condition for a minimum or maximum, a test is necessary to determine to which category a particular solution belongs. A strict analytical test requires calculating the second derivative $d^2 F_z/db^2$. In this analysis, however, the solutions are instead examined directly: the force/unit length available from each optimised geometry is required anyway, and it is a simple matter to check whether it represents a minimum or a maximum.

To solve equation 8.12, an iterative numerical method is necessary. For the present study, a microcomputer was programmed to find solutions using the Newton-Raphson iteration algorithm (see eg. Kreysig, 1983). The method is generally applicable to single-variable functions with multiple real roots, and offers fast convergence. Typical results of the optimisation procedure are shown in figures 8.4 - 8.7.

Figure 8.4 is a plot of the optimum magnet dimensions b and c, and the ratio b/c, for the case of zero lateral offset, at increasing values of pole clearance z. The dimensions are made scale-independent by dividing by the square root of total area, ie. $A^{\frac{1}{2}}$. This linear dimension is chosen to allow easiest interpretation of the results, as both b and c vary with the optimal solution. The points on each curve at given clearance correspond to a single iterated solution of equation 8.12. The vertical force/unit length F_z available from each optimal geometry in figure 8.4 is shown in figure 8.5. Normalisation is achieved by dividing F_z by the product $J^2A^{\frac{1}{2}}$, leaving it independent both of scale and magnetisation (use of b or c as normalising dimension would result in a nonlinear force scale).

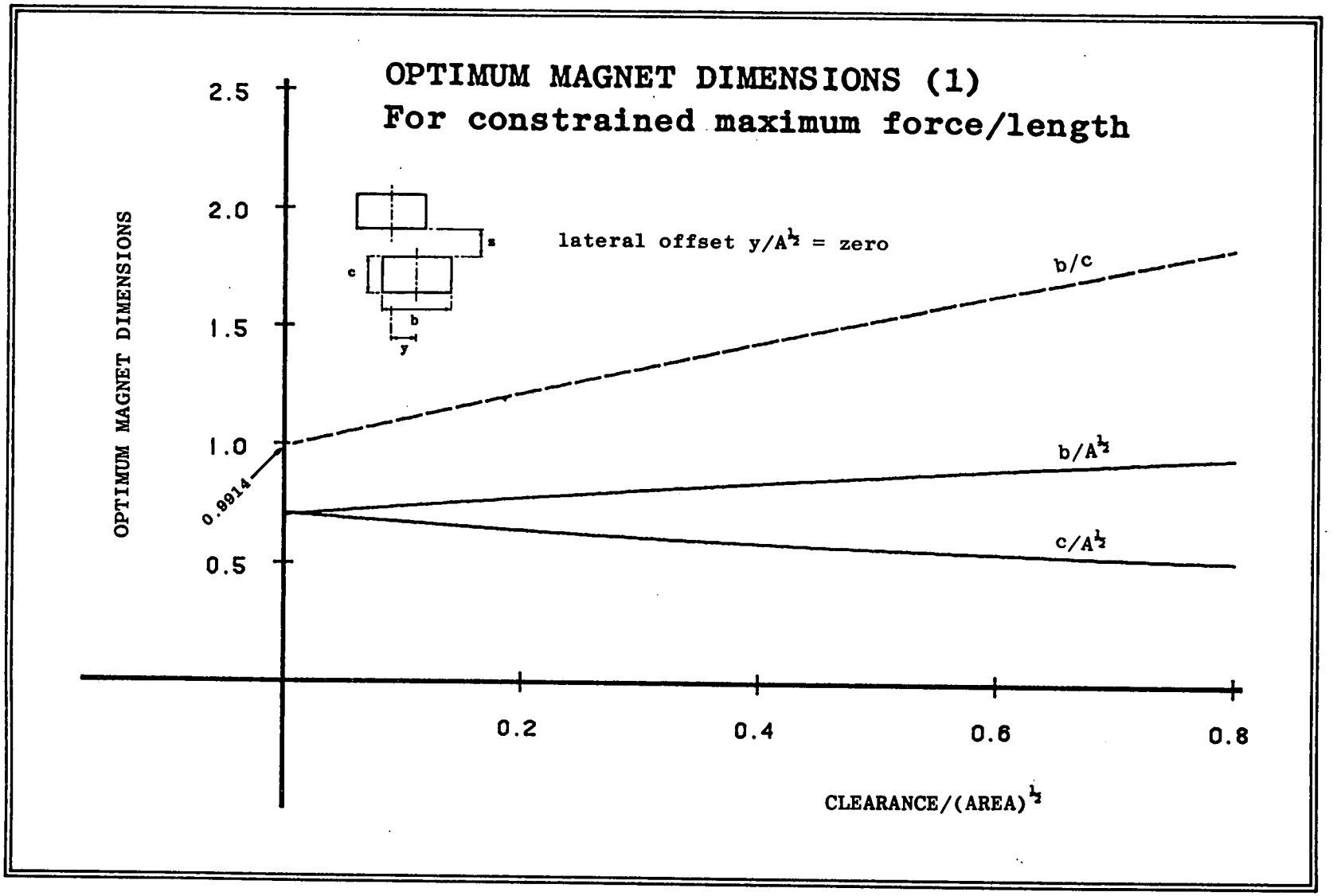
OPTIMUM MAGNET DIMENSIONS (1)
For constrained maximum force/length
OPTIMUM MAGNET DIMENSIONS
2.5
2.0
1.5
1.0
0.5
0.9914
a
c
b
y
lateral offset y/A^½ = zero
b/c
b/A^½
c/A^½
0.2
0.4
0.6
0.8
CLEARANCE/(AREA)^½

FIGURE 8.4

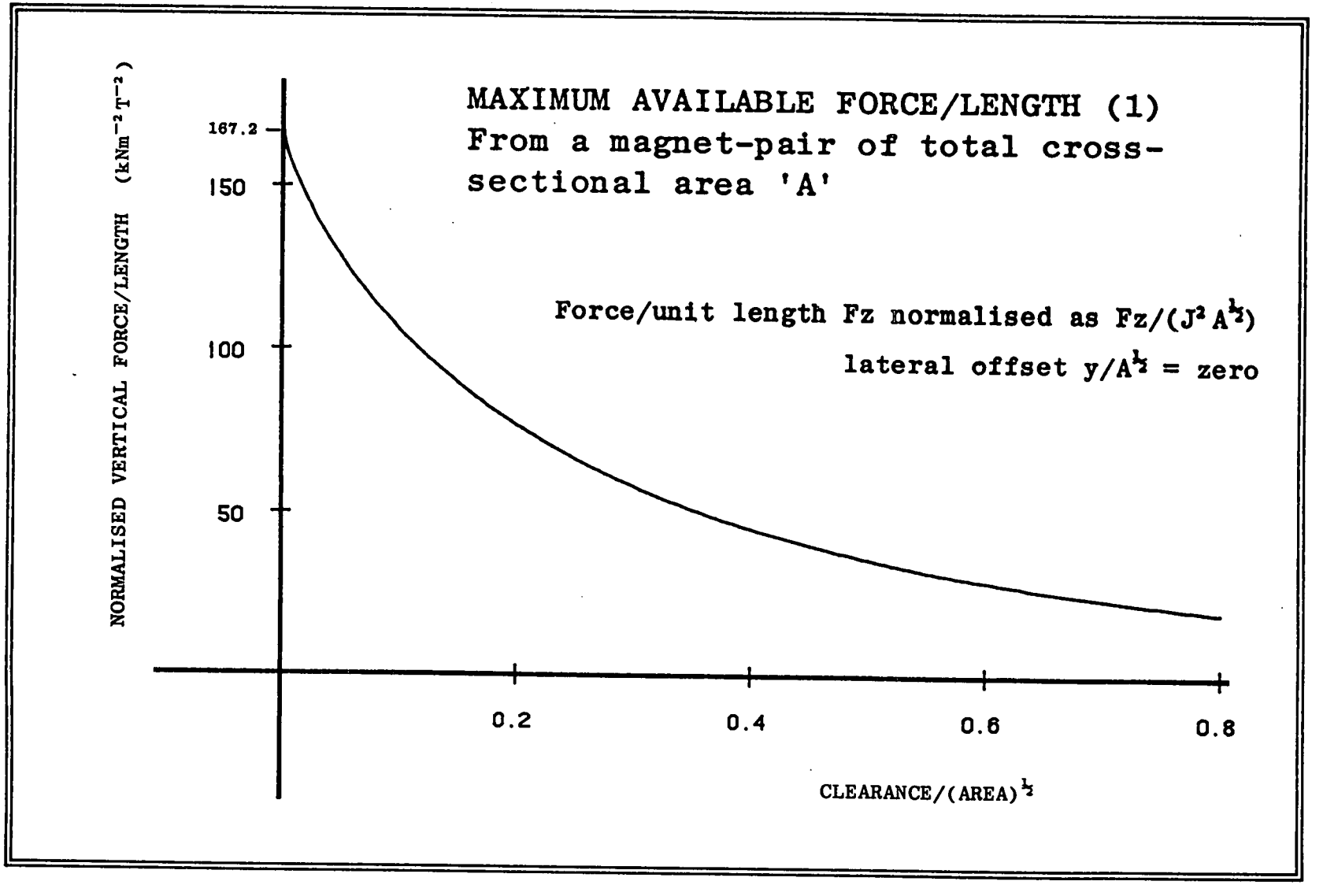
MAXIMUM AVAILABLE FORCE/LENGTH (1)
From a magnet-pair of total cross-sectional area 'A'
Force/unit length Fz normalised as Fz/(J² A½)
lateral offset y/A½ = zero
NORMALISED VERTICAL FORCE/LENGTH (kNm⁻² T⁻²)
167.2
150
100
50
0.2
0.4
0.6
0.8
CLEARANCE/(AREA)½

FIGURE 8.5

Figure 8.4 shows that, with increasing clearance between magnets of fixed cross-sectional area, maximum repulsion force is obtained by increasing the aspect ratio b/c. For two aligned magnets making pole contact, the optimum ratio is given, to four significant figures, by:

$$b/c_{opt} = 0.9914 \qquad (8.13)$$

with the corresponding force/length found by:

$$F_z(opt) = 167.2\ J^2 A^{\frac{1}{2}} \quad kN/m \qquad (8.14)$$

Specific values of $F_z(opt)$ are found using appropriate figures for cross-sectional area A and magnetisation J in equation 8.14.

The above result, for zero clearance and zero offset, is an important special case, as the value of $F_z(opt)$ in equation 8.14 represents the maximum force/unit length which can ever be achieved from a two-dimensional magnet-pair, in attraction or repulsion. From equation 8.13, the optimum aspect ratio for two-dimensional magnets making pole contact is seen to correspond, to within 1%, to a square cross-section (b/c = 1). Although a unity ratio might be more intellectually appealing, the theoretical calculation appears to be correct, with the optimum geometric ratio implicit in the following equation:

$$\tan^{-1}\left\{\frac{2}{R^3 + 3R}\right\} = \frac{1}{R}\log_e\left\{\frac{4R^2 + 4}{R^2 + 4}\right\} \qquad (8.15)$$

where R = b/c, and to which R = 1 is not a solution.

In figures 8.6 and 8.7, the results are shown for an optimisation scheme identical to the above, but with non-zero lateral offset; in this case $y/A^{\frac{1}{2}} = 0.2$. At pole contact, $F_z(opt)$ is now some 23% less than in the fully-aligned case, despite the relatively small offset. The corresponding optimum dimensional ratio b/c is not, however, greatly different.

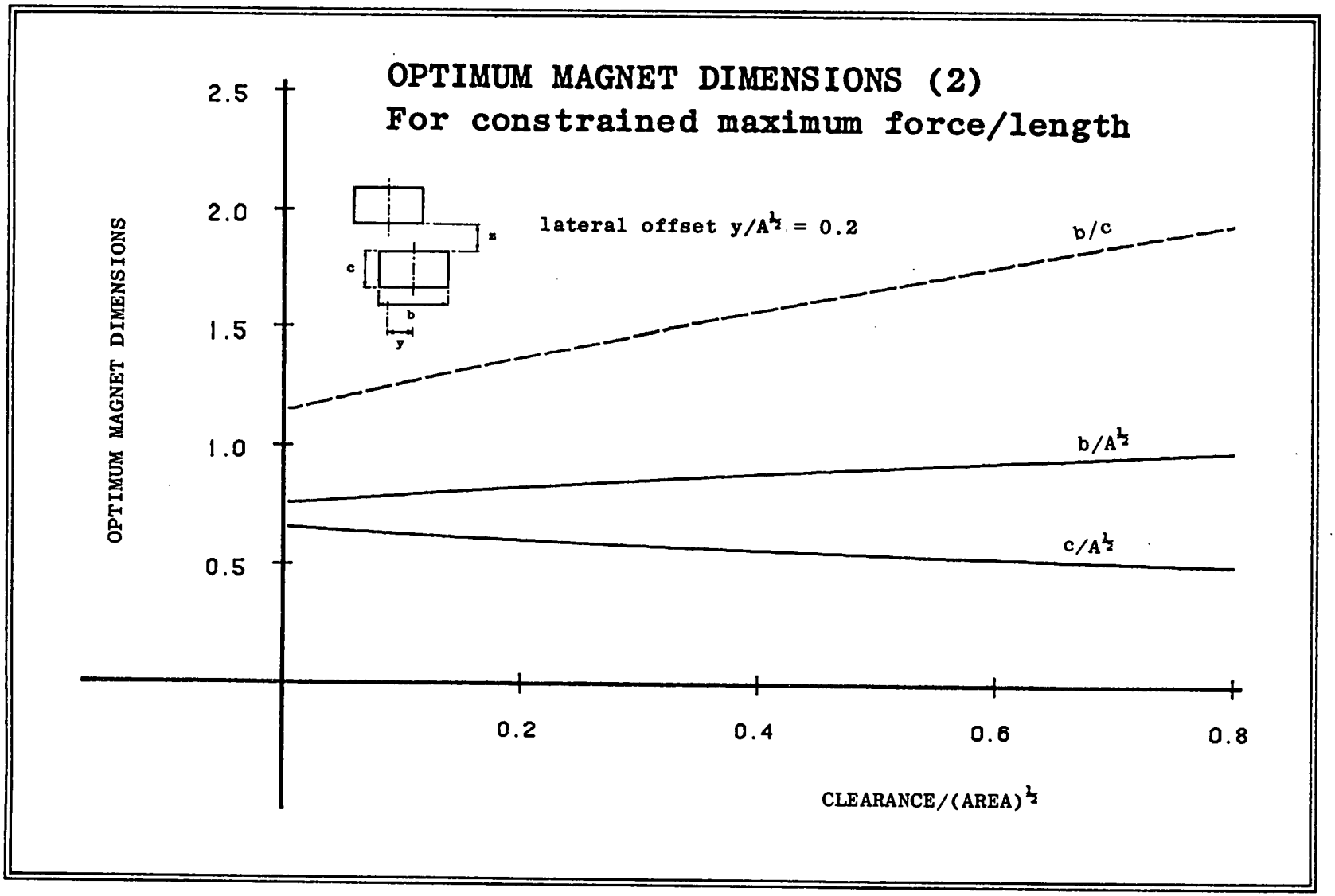
OPTIMUM MAGNET DIMENSIONS (2)
For constrained maximum force/length
OPTIMUM MAGNET DIMENSIONS
2.5
2.0
1.5
1.0
0.5
lateral offset y/A^½ = 0.2
z
c
b
y
b/c
b/A^½
c/A^½
0.2
0.4
0.6
0.8
CLEARANCE/(AREA)^½

FIGURE 8.6

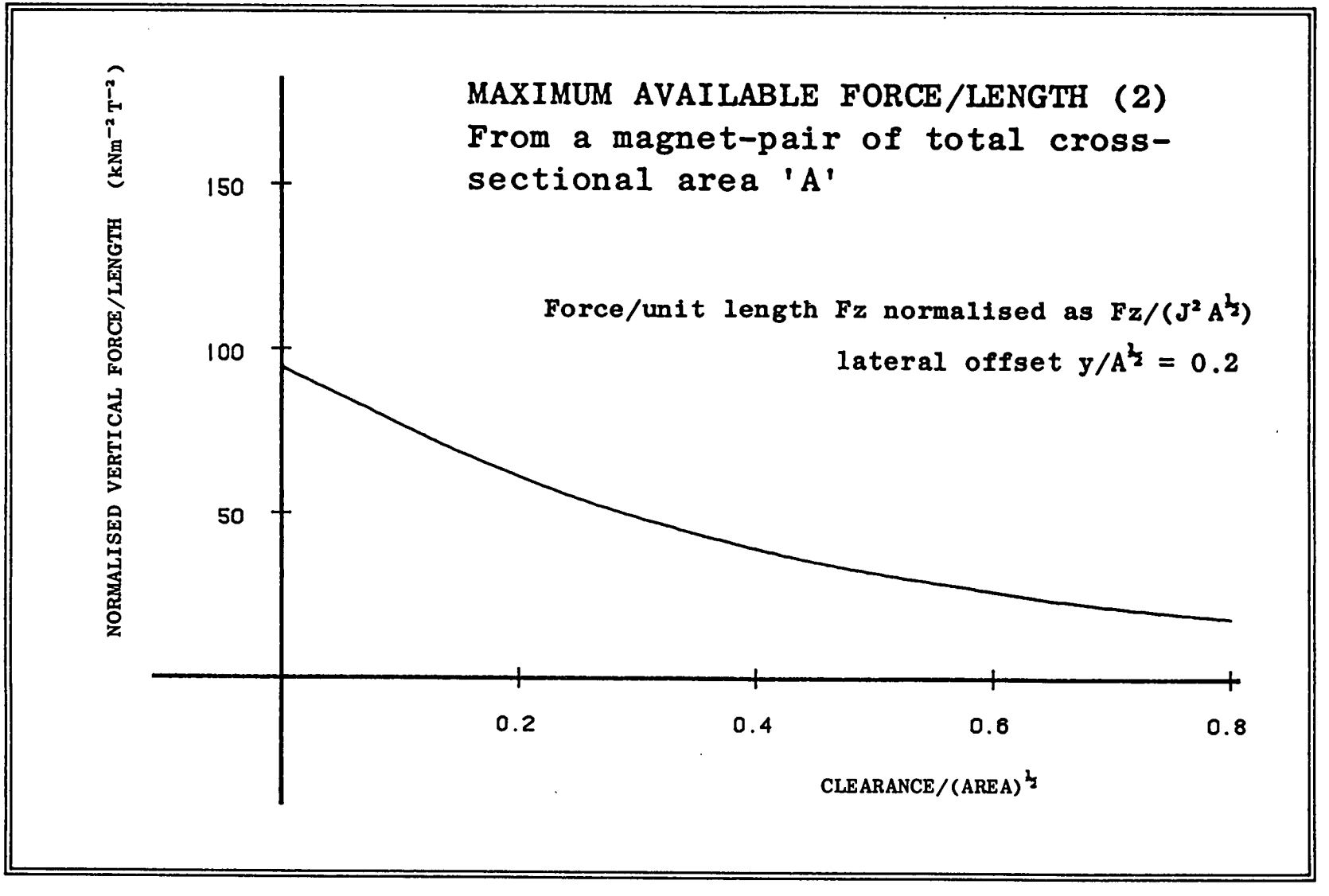
MAXIMUM AVAILABLE FORCE/LENGTH (2)
From a magnet-pair of total cross-sectional area 'A'
Force/unit length Fz normalised as Fz/(J² A½)
lateral offset y/A½ = 0.2
NORMALISED VERTICAL FORCE/LENGTH (kNm⁻² T⁻²)
150
100
50
0.2
0.4
0.6
0.8
CLEARANCE/(AREA)½

FIGURE 8.7

8.6 Geometry Optimisation (2): Constrained Stiffness/Length

With a constant area constraint again imposed, the above analysis is repeated almost exactly, only this time the geometry is optimised for maximum vertical stiffness/unit length K_z. The full expression for K_z is given in equation 8.7. In a two dimensional geometry, stiffness/unit length is independent of scale, and hence the optimum values of K_z will automatically be scale-independent, requiring for normalisation only to be divided by the magnetisation product J^2. The condition for a constant-area constrained maximum of stiffness/unit length is given by:

$$dK_z/db = 0 \qquad (8.16)$$

and hence by analogy with equations 8.10 - 8.12, the equation which must be solved for each combination of clearance and offset is given by:

$$\partial K_z/\partial b - c/b\,(\partial K_z/\partial c) = 0 \qquad (8.17)$$

Because of the similarity of this to the previous analysis, solutions of equation 8.17 are achieved in practice by using the same computational procedure described in section 8.5, replacing the partial derivatives of F_z with those of K_z; analytic expressions can again be used. Some typical results for the constrained stiffness/unit length optimisation are shown in figures 8.8 - 8.11. Figure 8.8 shows the optimum dimensions at increasing pole-clearances in the zero-offset case, with corresponding maximum-available stiffness/length given in figure 8.9. Points to note include:

(1) The optimum aspect ratio increases with increasing clearance, similar to the case for optimum force (see section 8.5).

(2) continued on p.127

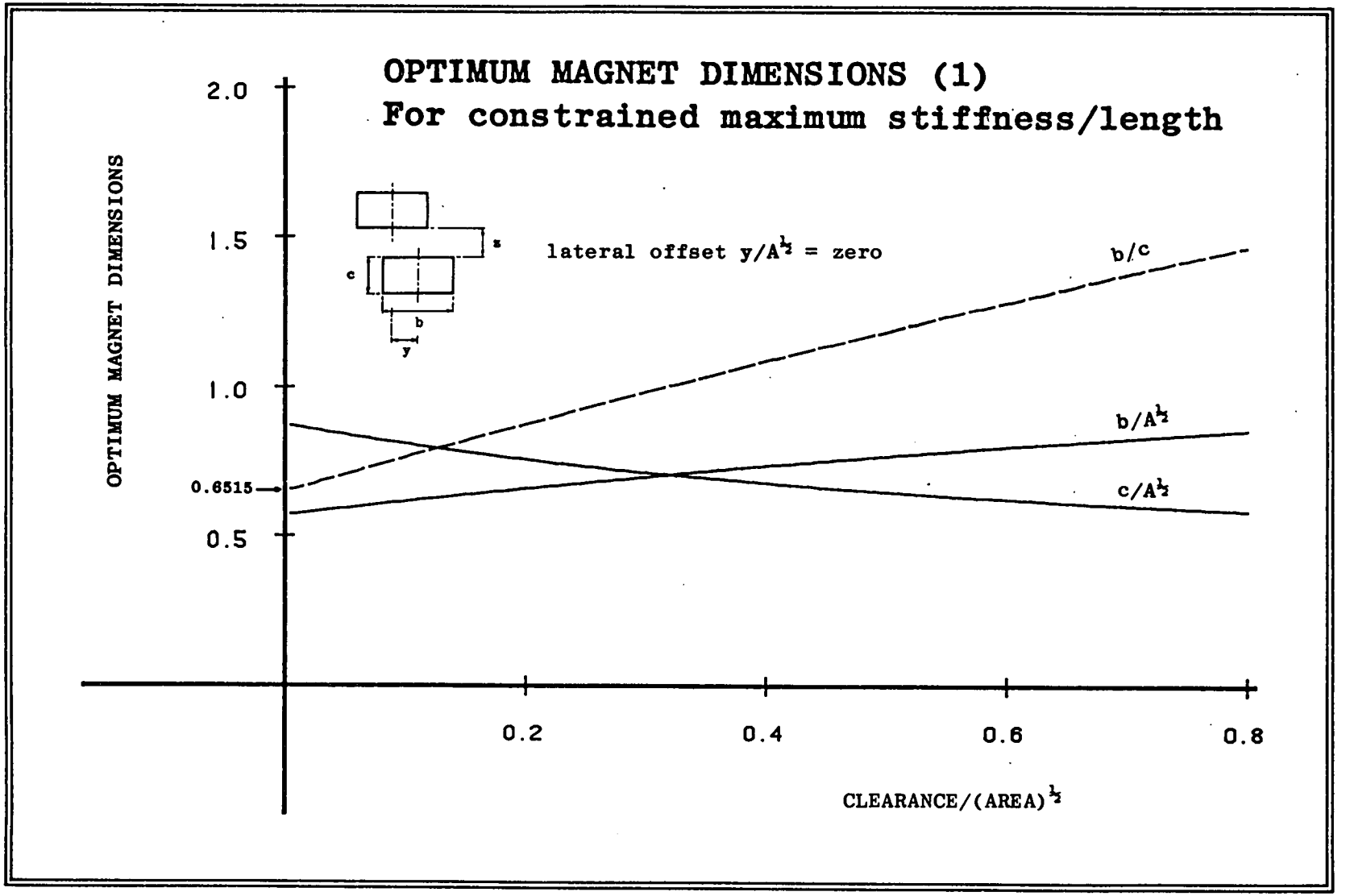
OPTIMUM MAGNET DIMENSIONS (1)
For constrained maximum stiffness/length
OPTIMUM MAGNET DIMENSIONS
2.0
1.5
1.0
0.6515
0.5
lateral offset y/A^½ = zero
z
c
b
y
b/c
b/A^½
c/A^½
0.2
0.4
0.6
0.8
CLEARANCE/(AREA)^½

FIGURE 8.8

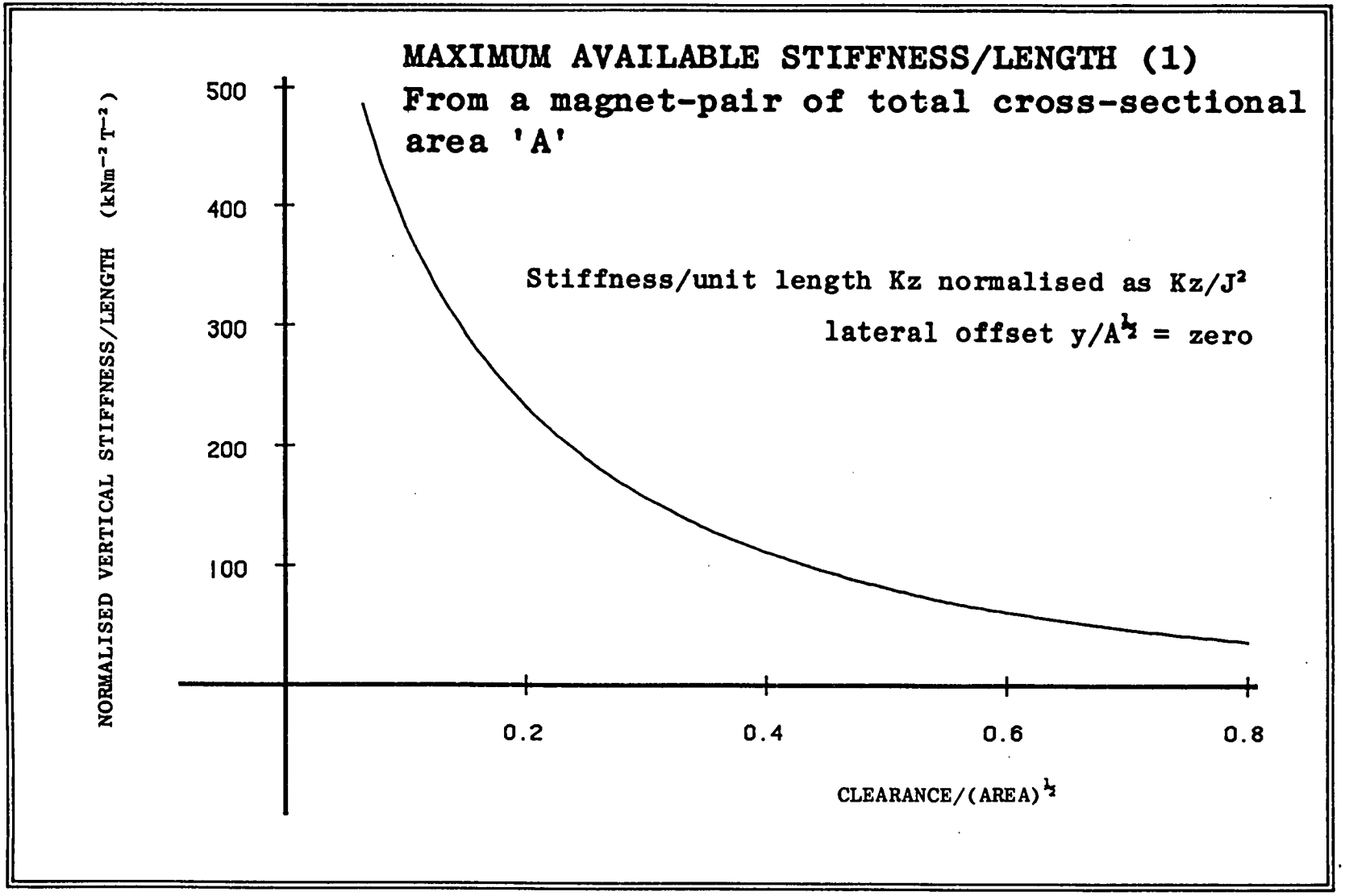
MAXIMUM AVAILABLE STIFFNESS/LENGTH (1)
From a magnet-pair of total cross-sectional area 'A'
Stiffness/unit length Kz normalised as Kz/J²
lateral offset y/A^½ = zero
NORMALISED VERTICAL STIFFNESS/LENGTH (kNm⁻² T⁻²)
500
400
300
200
100
0.2
0.4
0.6
0.8
CLEARANCE/(AREA)^½

FIGURE 8.9

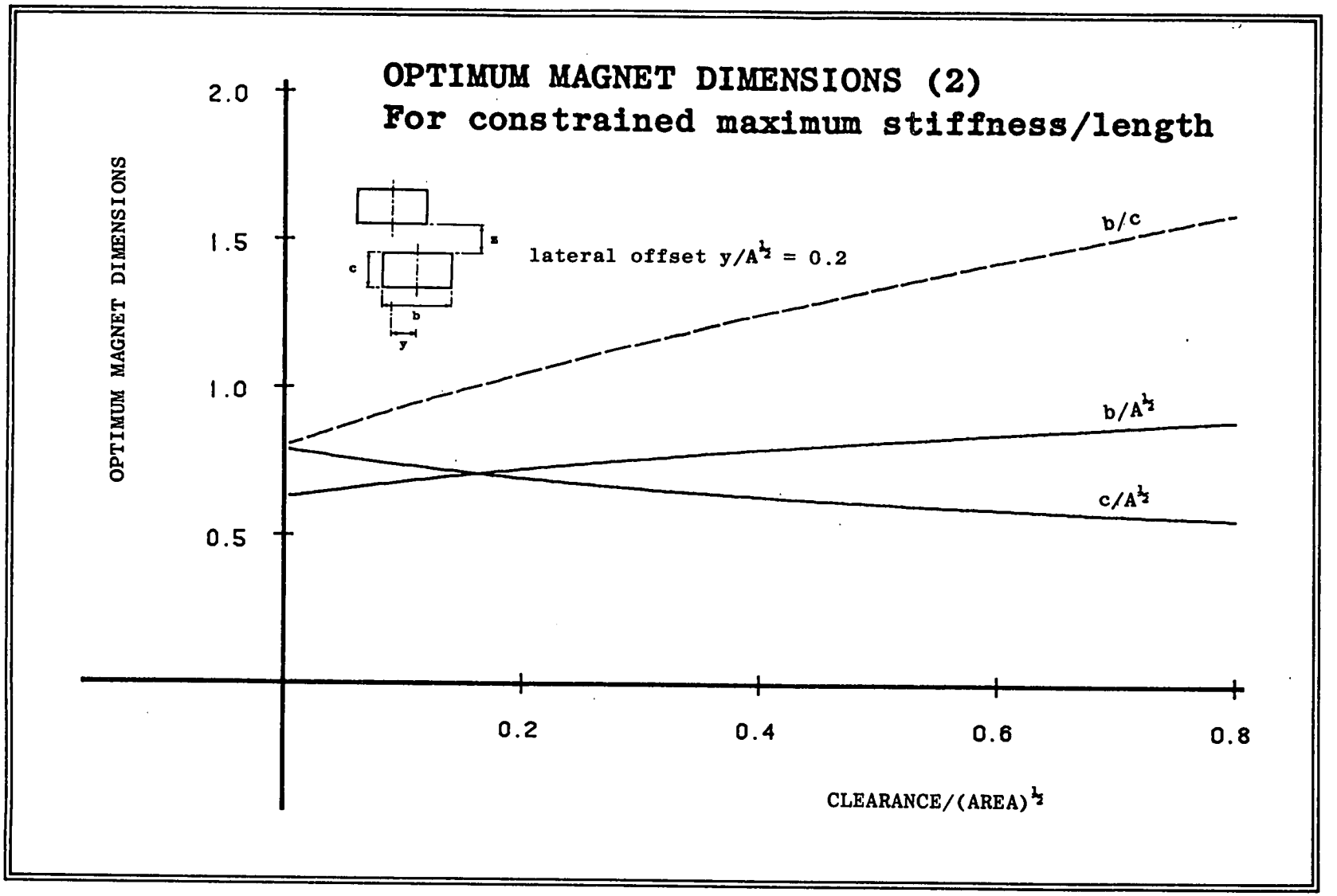
OPTIMUM MAGNET DIMENSIONS (2)
For constrained maximum stiffness/length
OPTIMUM MAGNET DIMENSIONS
2.0
1.5
1.0
0.5
lateral offset y/A½ = 0.2
z
c
b
y
b/c
b/A½
c/A½
0.2
0.4
0.6
0.8
CLEARANCE/(AREA)½

FIGURE 8.10

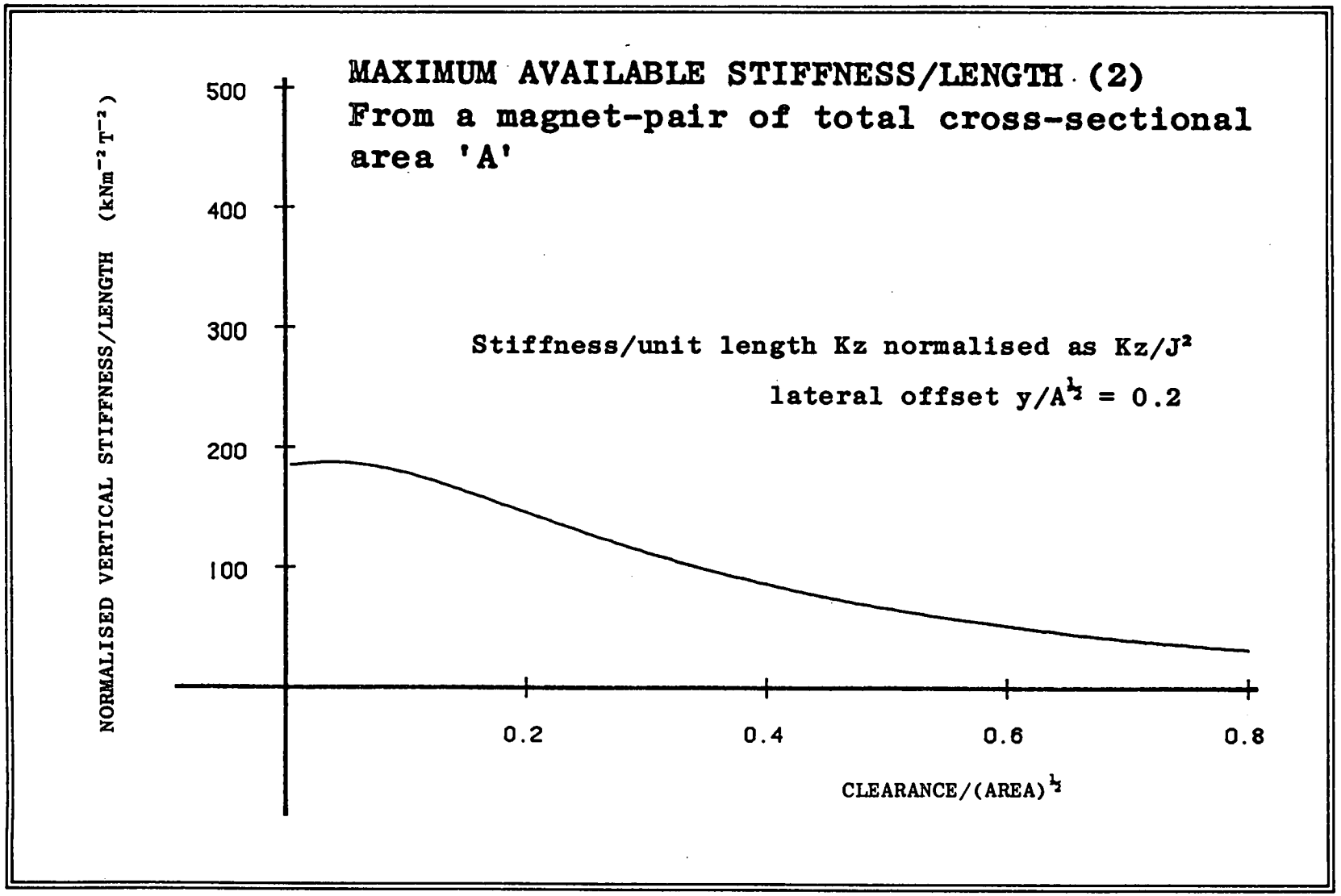
MAXIMUM AVAILABLE STIFFNESS/LENGTH (2)
From a magnet-pair of total cross-sectional area 'A'
Stiffness/unit length Kz normalised as Kz/J²
lateral offset y/A½ = 0.2
NORMALISED VERTICAL STIFFNESS/LENGTH (kNm⁻²T⁻²)
500
400
300
200
100
0.2
0.4
0.6
0.8
CLEARANCE/(AREA)½

FIGURE 8.11

(2) Although maximum-available stiffness tends to infinity as clearance tends to zero, the optimum aspect ratio at pole contact remains well-defined, with:

$$b/c_{opt} = 0.6515 \qquad (8.18)$$

(3) Magnet geometries optimised for stiffness have different dimensions to those optimised for force: compare solutions 8.18 and 8.13, where both represent optimum pole-contact geometries.

The optimum geometry given by equation 8.18 is an approximation: for this special case, it can be rigorously shown that:

$$b/c_{opt} = \sqrt{\frac{8}{9 + \sqrt{97}}} \qquad (8.19)$$

Figures 8.10 and 8.11 illustrate the results of a similar analysis, in which a non-zero lateral offset is specified. In this case, the maximum-available stiffness tends to a finite limit as the pole-clearance approaches zero.

8.7 Optimisation: Applying the Results

To illustrate how the above constrained-optimisation schemes are used in the context of the duck bearing, consider the following example. Suppose that, on stipulating a certain axial magnet pitch, the bearing pressure specification translates into the following requirement: at the minimum allowed pole separation, a single magnet pair must provide a repulsion force of 1000 N per metre circumferential length, but comprise no more than 20 kg/metre of magnet material; strontium ferrite magnets are to be used.

The desired parameters are the maximum pole-clearance possible within the above constraints, and the optimum magnet dimensions which allow it.

Taking the density of strontium ferrite as 4800 kg/m^3, the weight constraint corresponds to a maximum magnet volume of 4.167×10^{-3} m^3 per metre of magnet length, and hence a total cross sectional area A of 4.167×10^{-3} m^2. The force/length requirement is 1000 N/m: to express this in normalised units, divide by $J^2A^{\frac{1}{2}}$, where J is typically 0.32 tesla; the resulting normalised force/length F_z equals 151.3 $kNm^{-2}T^{-2}$. Using the curve in figure 8.5 (or, better, a computer-generated look-up table) the dimensionless clearance corresponding to F_z(normalised) is given by $z/A^{\frac{1}{2}} = 0.0146$, which represents a true clearance of 0.94 mm. From figure 8.4 the optimum magnet aspect ratio is read off against dimensionless clearance, hence $b/c_{opt} = 1.01$.

The resulting optimised system dimensions would thus be:

$$\begin{aligned} \text{cross sectional area A/2, single magnet} &= 2084 \text{ mm}^2 \\ \text{optimum magnet aspect ratio b/c} &= 1.01 \\ \text{hence magnet-width b} &= 45.8 \text{ mm} \\ \text{height c} &= 45.5 \text{ mm} \\ \text{maximum pole-separation z} &= 0.94 \text{ mm} \end{aligned} \qquad (8.20)$$

The results of the stiffness optimisation scheme of section 8.6 would be applied in exactly the same way as above, had the initial specification been expressed in terms of required stiffness rather than force per unit length.

In general terms, what the results of the two preceding analyses allow is stipulation of any two parameters from a choice of force (or stiffness), magnet-weight, and pole clearance, with the optimum value of the third then returned, together with the appropriate magnet dimensions.

8.8 Geometry Optimisation (3): Unconstrained Force/Unit Volume

In this, and the subsequent, optimisation procedure, no constraint is placed on magnet cross-sectional area, and for any given combination of clearance and offset, the maximum value of force or stiffness per unit volume is found by seeking the global-optimum magnet dimensions.

The analytical geometry is again that shown in figure 7.2. In the first case optimisation is for maximum vertical force/unit volume F_V, where for symmetric magnets:

$$F_V = F_Z/2bc \tag{8.21}$$

where F_Z is given by equation 8.1. Imposing no constraint on area, the magnets' width and height are independent variables, and a global maximum of F_V is found from:

$$\partial F_V/\partial b = \partial F_V/\partial c = 0 \tag{8.22}$$

which, from equation 8.21, then represents the simultaneous requirements:

$$\partial F_Z/\partial b - F_Z/b = 0 \tag{8.23}$$

$$\partial F_Z/\partial c - F_Z/c = 0 \tag{8.24}$$

The partial derivatives are the same as previously used in the constrained optimisation procedure. In this case however, a more sophisticated optimisation algorithm is necessary: there are now two conditions to be simultaneously satisfied, where before, a function of only one variable was involved. The algorithm used in the present study was the 'method of steepest ascent', an optimisation technique suggested by Box et al (1969) which is applicable to nonlinear functions of many variables, and in which an iterative search is used to find simultaneously the values of all the variables corresponding to a maximum of

the objective function (in this case F_V), with a solution returned when all the partial derivatives equal zero. The routine was again implemented on a microcomputer.

For a given combination of pole-clearance and offset, the solution to equations 8.23 and 8.24 consists of the maximum available force/unit volume $F_V(opt)$, and the corresponding values of magnet dimensions b and c. Once the optimum solution is known for a given ratio y/z, the solutions for this ratio at any scale are automatically known, using the laws given in section 8.4. Consequently, the results of the present optimisation scheme, expressed in normalised units of $F_V(opt)$, form a single curve, plotted against the dimensionless ratio y/z. This curve is shown in figure 8.12, while figure 8.13 gives the corresponding optimum magnet dimensions.

The values of $F_V(opt)$ are normalised according to section 8.4(b): the use of pole clearance as the normalising cross-sectional dimension allows the curves to be interpreted as results predicted for increasing offset at constant clearance. It is then seen that maximum available force/unit volume decreases with offset, while increasingly large magnets are required to achieve optimum material efficiency (as demonstrated by an increase in both width and height, ie. b/z and c/z respectively). However, the optimum aspect ratio b/c remains roughly the same over the range y/z = 0 to 2. For the case of fully aligned magnets (y/z = 0), the results are directly comparable with those of Minnich (1971) and Coffey et al (1972), in whose analyses force maxima were estimated graphically. In both cases the optimum dimensional ratios were estimated as b/z = 2.0 and c/z = 1.5, compared with the present results:

$$b/z_{opt} = 2.005 \qquad (8.25)$$

$$c/z_{opt} = 1.372 \qquad (8.26)$$

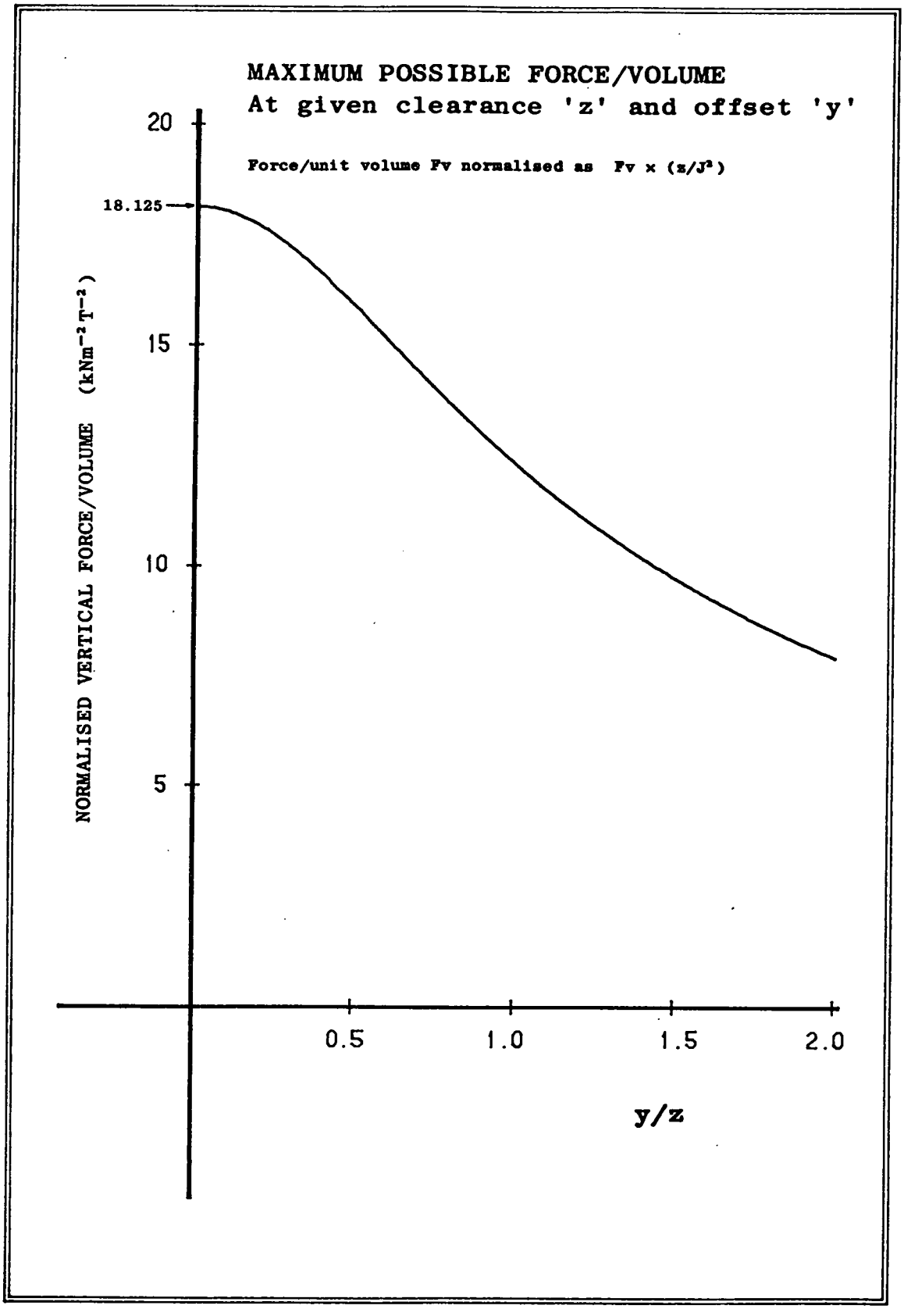
MAXIMUM POSSIBLE FORCE/VOLUME
At given clearance 'z' and offset 'y'
Force/unit volume Fv normalised as Fv x (z/J²)
NORMALISED VERTICAL FORCE/VOLUME (kNm⁻²T⁻²)
20
18.125
15
10
5
0.5
1.0
1.5
2.0
y/z

FIGURE 8.12

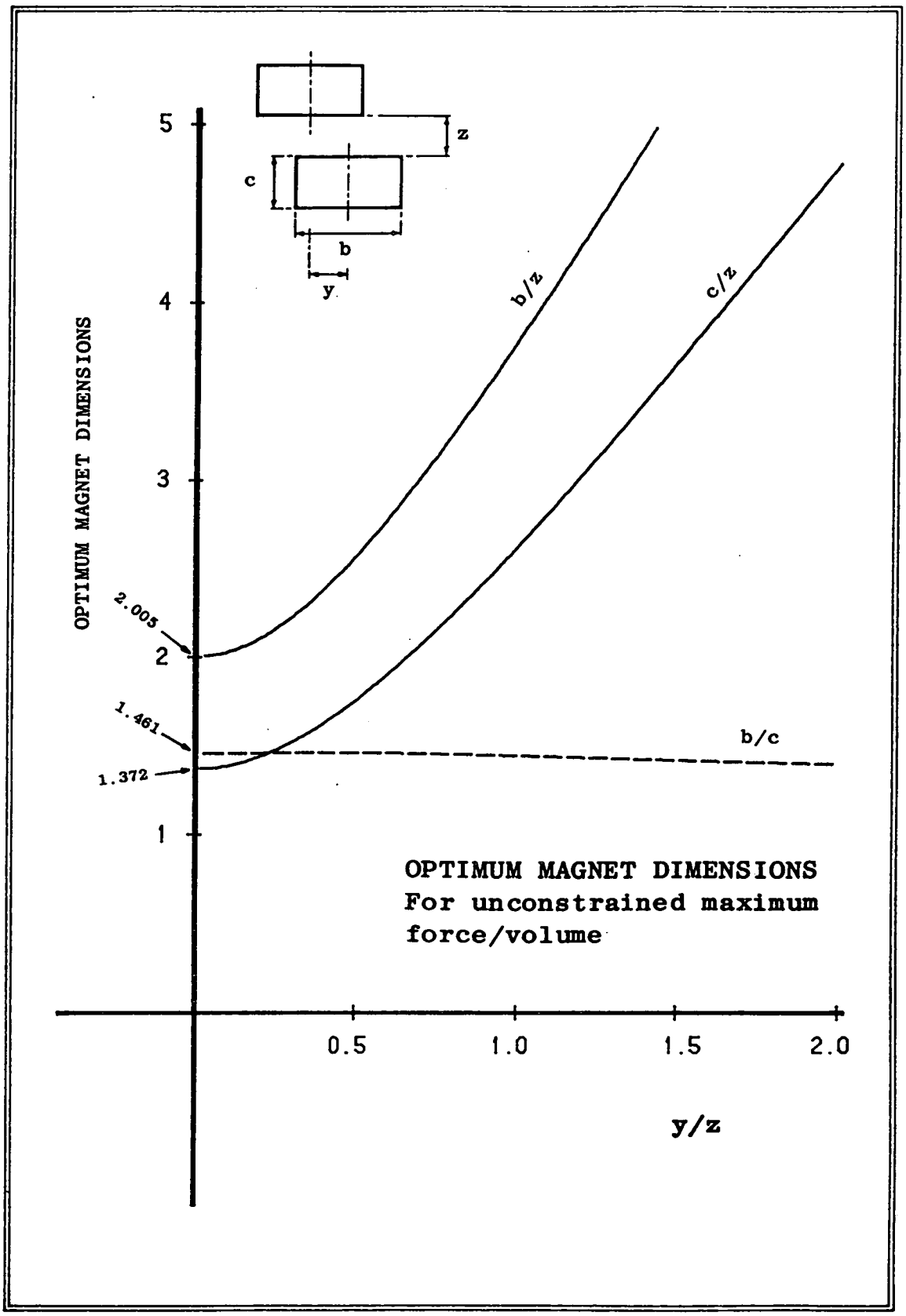
OPTIMUM MAGNET DIMENSIONS
5
4
3
2
1
z
c
b
y
b/z
c/z
b/c
2.003
1.461
1.372
OPTIMUM MAGNET DIMENSIONS
For unconstrained maximum
force/volume
0.5
1.0
1.5
2.0
y/z

FIGURE 8.13

The maximum-possible force/unit volume is given, from the present analysis, by:

$$F_V(\text{opt}) = 18.12\ J^2/z \quad kN/m^3 \qquad (8.27)$$

with the force/unit length of the optimum geometry found from:

$$F_Z(\text{opt}) = 99.74\ J^2 z \quad kN/m \qquad (8.28)$$

Although the present results predict a magnet height c/z_{opt} some 8.5% smaller than the previous estimates, the above value of maximum force/unit volume is only 0.2% higher than that calculated on the basis of the previous graphically-found dimensions, indicating that $F_V(\text{opt})$ is relatively insensitive to magnet-height in the region of the optimum geometry. This highlights a strength of the present analysis, showing the numerical method to be more suited to pinpointing a relatively 'flat' maximum. However, it is noteworthy that in terms of material efficiency there is little to choose between the optimum magnet dimensions predicted here, and those previously published.

8.9 Geometry Optimisation (4): Unconstrained Stiffness/Volume

The procedure in this case is exactly equivalent to that in section 8.8, though with the objective function now stiffness/unit volume K_V rather than force/unit volume F_V. Hence, by analogy with equations 8.23 and 8.24, the simultaneous requirements for a global maximum of K_V are given by:

$$\partial K_Z/\partial b - K_Z/b = 0 \qquad (8.29)$$

$$\partial K_Z/\partial c - K_Z/c = 0 \qquad (8.30)$$

where the partial derivatives are evaluated, as before, from equation 8.7. Solutions to equations 8.29 and 8.30 are found using the gradient-search technique described in section 8.8.

Normalisation of $K_v(opt)$ is achieved by multiplying by z^2/J^2 (see section 8.4): choice of the clearance z as the normalising dimension is explained in section 8.8.

The results of the analysis are presented in figures 8.14 and 8.15. Figure 8.14 shows that $K_v(opt)$ decreases very sharply (note the log scale) with offset. For the case of zero lateral offset the maximum stiffness/volume is given by:

$$K_v(opt) = 23.45\ J^2/z^2 \quad \text{kN/m per cubic metre} \qquad (8.31)$$

The optimum magnet dimensions corresponding to this case are:

$$\begin{aligned} b/z_{opt} &= 1.018 \\ c/z_{opt} &= 0.6697 \\ b/c_{opt} &= 1.519 \end{aligned} \qquad (8.32)$$

The special case of fully-centred magnets was previously considered by Yonnet (1980) who, from graphical solutions, found the value of c/z_{opt} to lie between 0.5 and 1.0, with corresponding b/z_{opt} of approximately 1; his figure for $K_v(opt)$ was 23 J^2/z^2 kN/m/m^3, a value very close to that of the present numerical analysis. In a similar manner to the dependence of maximum force/unit volume on magnet height, discussed in section 8.8, the above figure for $K_v(opt)$ is relatively insensitive to the same parameter: this is demonstrated in the high accuracy of Yonnet's maximum stiffness estimate, calculated on the basis of approximate optimum magnet dimensions.

For increasing lateral offset (as the ratio y/z), the maximum available stiffness/unit volume decreases in a similar manner to that observed with force/unit volume, with larger magnets again required to achieve optimum material efficiency. It is important to remember that any two-dimensional magnet system

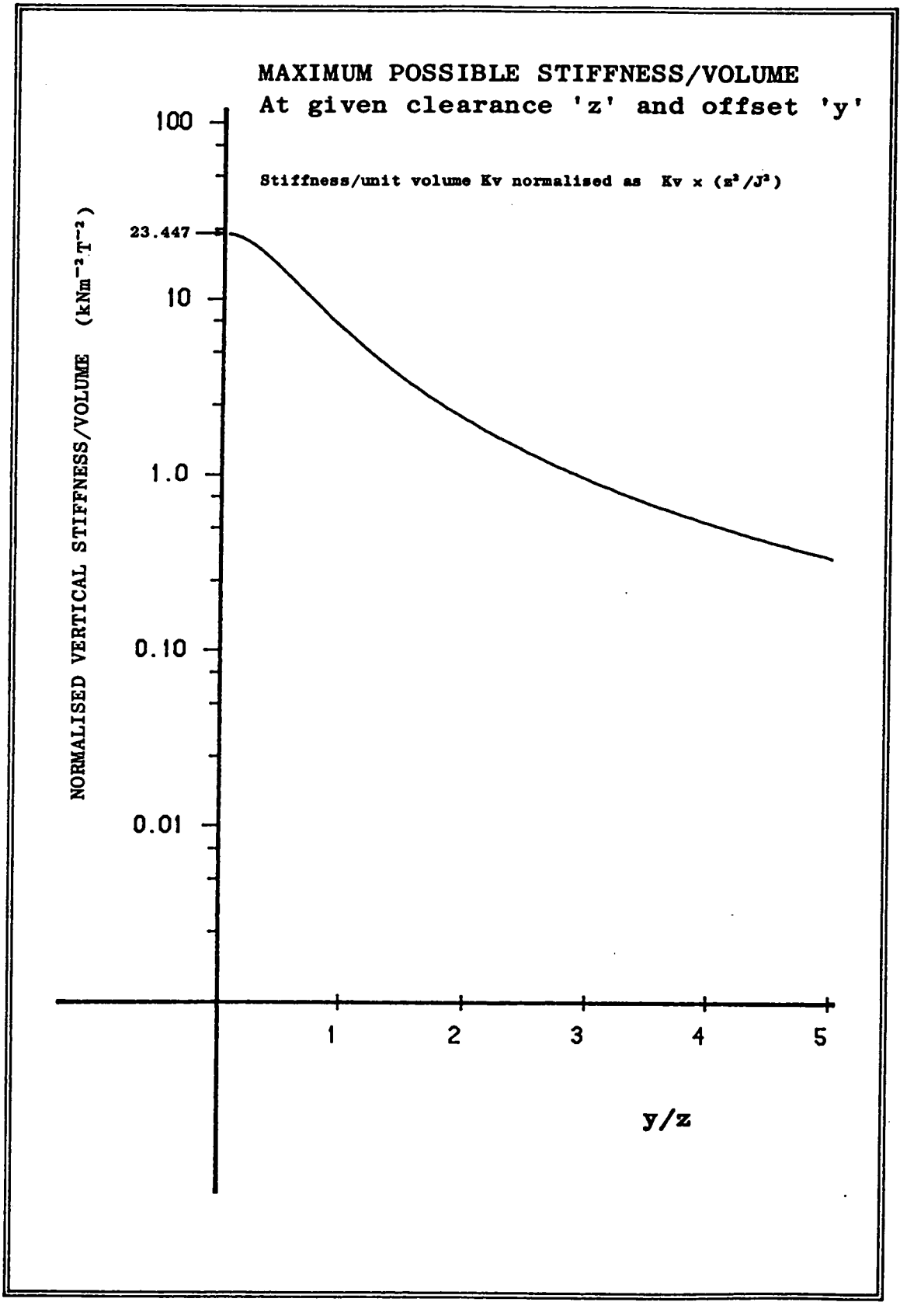
MAXIMUM POSSIBLE STIFFNESS/VOLUME
At given clearance 'z' and offset 'y'
Stiffness/unit volume Kv normalised as Kv x (z²/J²)
NORMALISED VERTICAL STIFFNESS/VOLUME (kNm⁻²T⁻²)
100
23.447
10
1.0
0.10
0.01
1
2
3
4
5
y/z

FIGURE 8.14

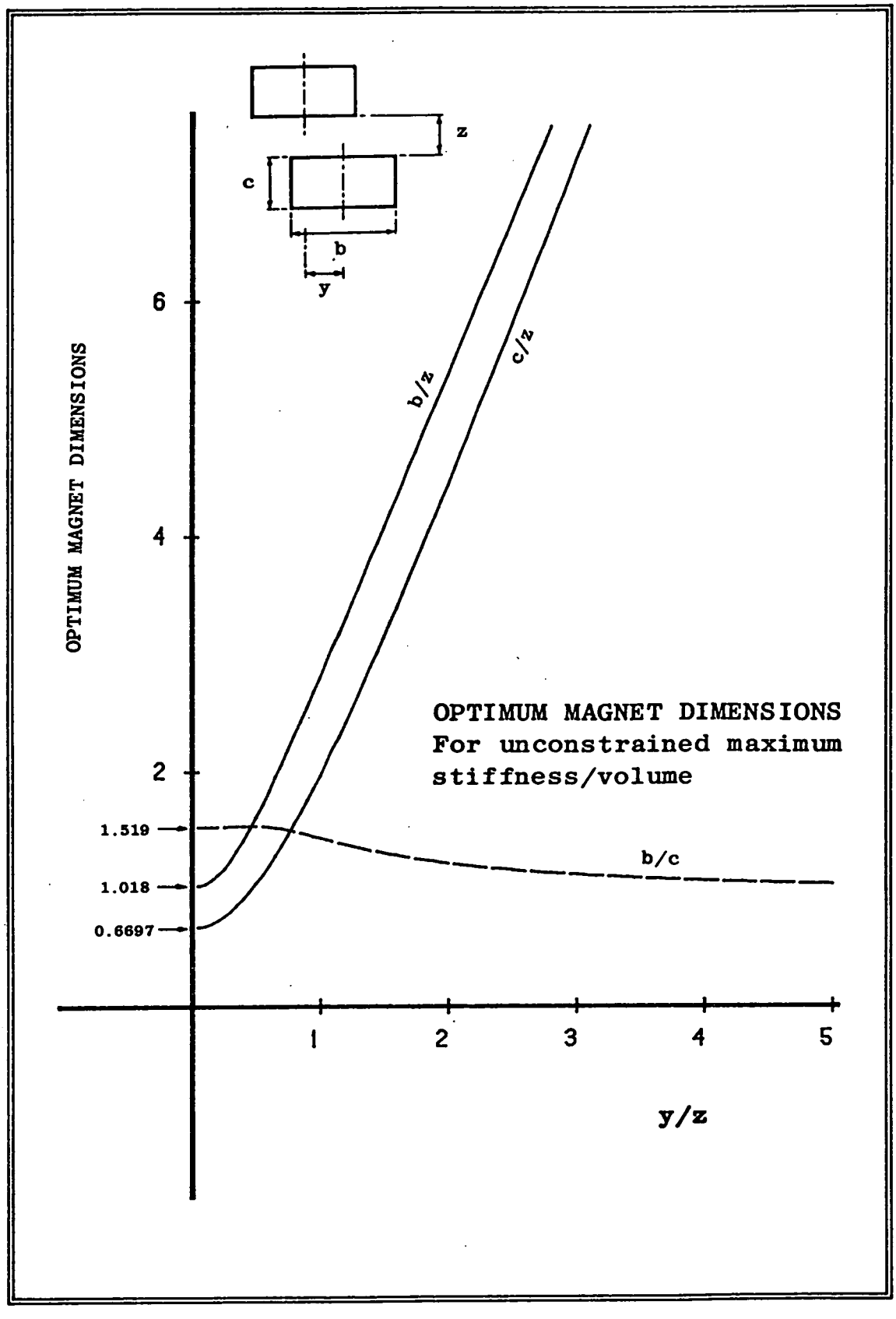
z
c
b
y
6
4
2
OPTIMUM MAGNET DIMENSIONS
b/z
c/z
OPTIMUM MAGNET DIMENSIONS
For unconstrained maximum
stiffness/volume
1.519
1.018
0.6697
b/c
1
2
3
4
5
y/z

FIGURE 8.15

optimised for maximum vertical stiffness is automatically optimised for maximum horizontal (negative) stiffness as well, and hence for maximum lateral instability: this is a consequence of Earnshaw's theorem (see section 8.3).

It can be seen that an unconstrained geometry optimisation is unsuitable in the case of the duck bearing. Assuming an equilibrium pole clearance of 3 mm, and optimising firstly for maximum force/unit volume, the appropriate pole-width b is found from equation 8.25 to be approximately 6 mm. Optimising instead for stiffness/unit volume, equation 8.32 gives the required pole-width as approximately 3 mm. In either case, the magnet dimensions are of the same order as the lateral offsets likely in normal operation, and would result in a system liable to complete collapse (or reversal - see section 8.10) of repulsion force.

8.10 Multiple-Pair Magnet Arrangements

The above optimisation procedures are all based on a single magnet-pair interaction. In practice, each magnet on one side of the proposed bearing clearance (see figure 3.4) experiences a force of interaction with every magnet on the other side. Although the axial pitch of the bearing magnets will probably be too great to make this a significant effect, it will nonetheless enhance the repulsion pressure to some extent. In economic terms, optimum geometries based on the preceding results will thus be conservative; the appropriate method for calculating the true characteristics of a given arrangement is described below.

The total vertical force exerted in a multiple-row system is calculated by superposition of single-pair interactions. In a system of n parallel rows, the total repulsion force comprises n^2 components, where each corresponds to a single-pair interaction: these can be calculated from equation 8.1. For systems of identical opposing-magnet geometry and uniform lateral pitch, it is, however, unnecessary to perform n^2

calculations to find the resultant force. Because of inherent symmetry, many of the individual-pair interactions are duplicated (at least in magnitude, if not direction) and it can be shown that the maximum number of calculations necessary in an arrangement of the present kind is only 2n-1.

Previous analyses of two-dimensional multiple-pair configurations have reduced the number of calculations still further. Both Minnich (1971) and Henning (1973) introduced a lateral 'zone of influence' to either side of a given magnet, with only those interactions lying within the zone counting towards the total force, the others being sufficiently weak to neglect. This not only greatly reduced the number of calculations necessary, but dispensed with the need to calculate very small forces as the difference between large ones, which situation arises with widely-separated magnets.

To demonstrate the increase in repulsion arising from cross-interactions, the results shown in figures 8.16 - 8.18 were calculated for a 9-row system, with opposing magnet-pairs of the same dimensions as those considered in sections 8.2 and 8.3 (see figures 8.2 and 8.3), and a lateral pitch of 60 mm. Note that adjacent rows present alternating polarity, in the so-called 'heteropolar' configuration: perhaps contrary to intuition, this arrangement is necessary if the first (and strongest) cross-interaction is to be a repulsion, rather than an attraction. The overall repulsion in a 'homopolar' configuration is by the same token weaker than the sum of its component interactions (see Baran, 1971).

In figure 8.16, the benefit accruing from a close-pitched heteropolar layout is seen: overall repulsion is compared with that calculated as nine times the single-pair interaction force. The corresponding increase in stiffness is shown in figure 8.17.

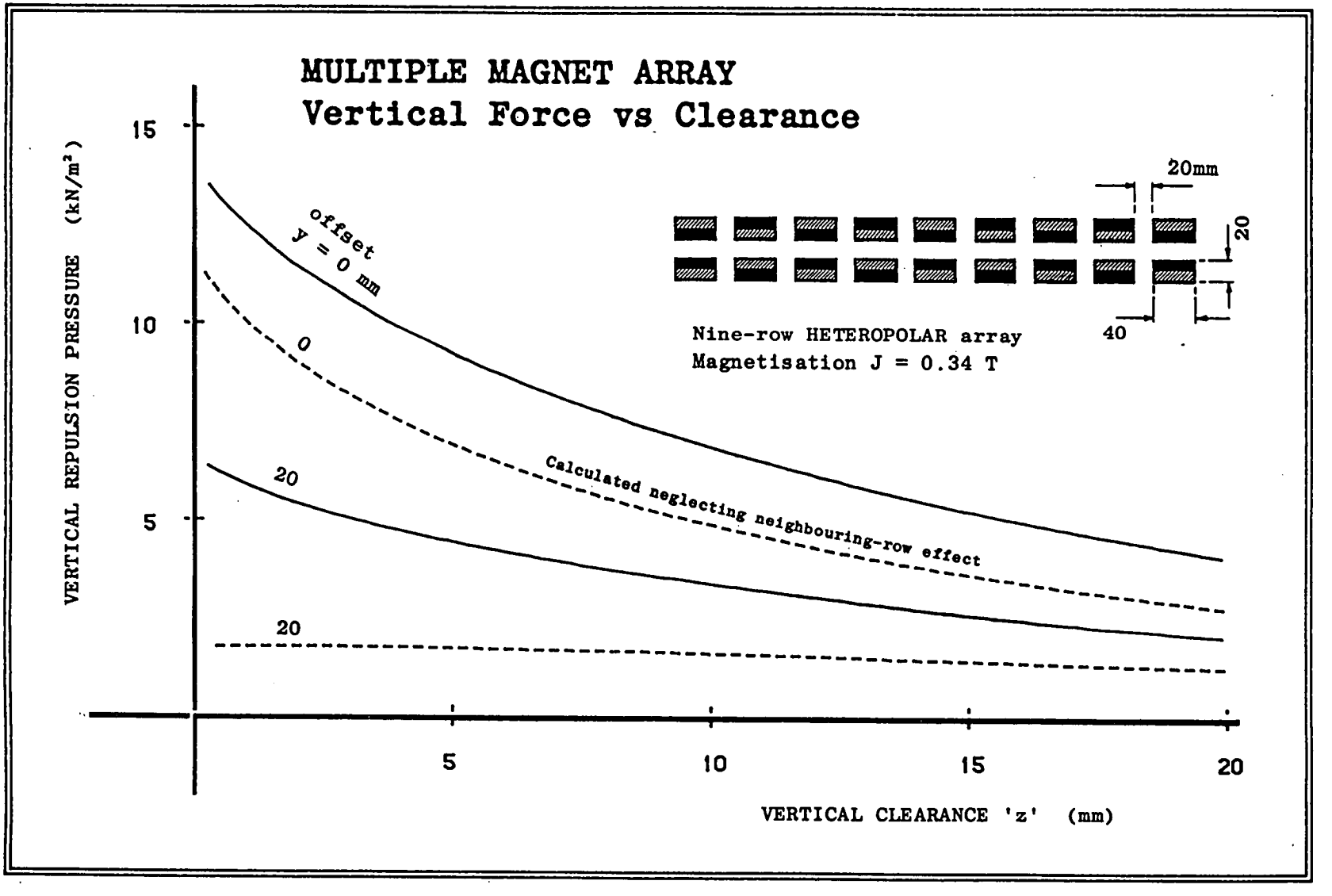
MULTIPLE MAGNET ARRAY
Vertical Force vs Clearance
VERTICAL REPULSION PRESSURE (kN/m²)
15
10
5
offset
y = 0 mm
0
20
20
Calculated neglecting neighbouring-row effect
20mm
20
40
Nine-row HETEROPOLAR array
Magnetisation J = 0.34 T
5
10
15
20
VERTICAL CLEARANCE 'z' (mm)

FIGURE 8.16

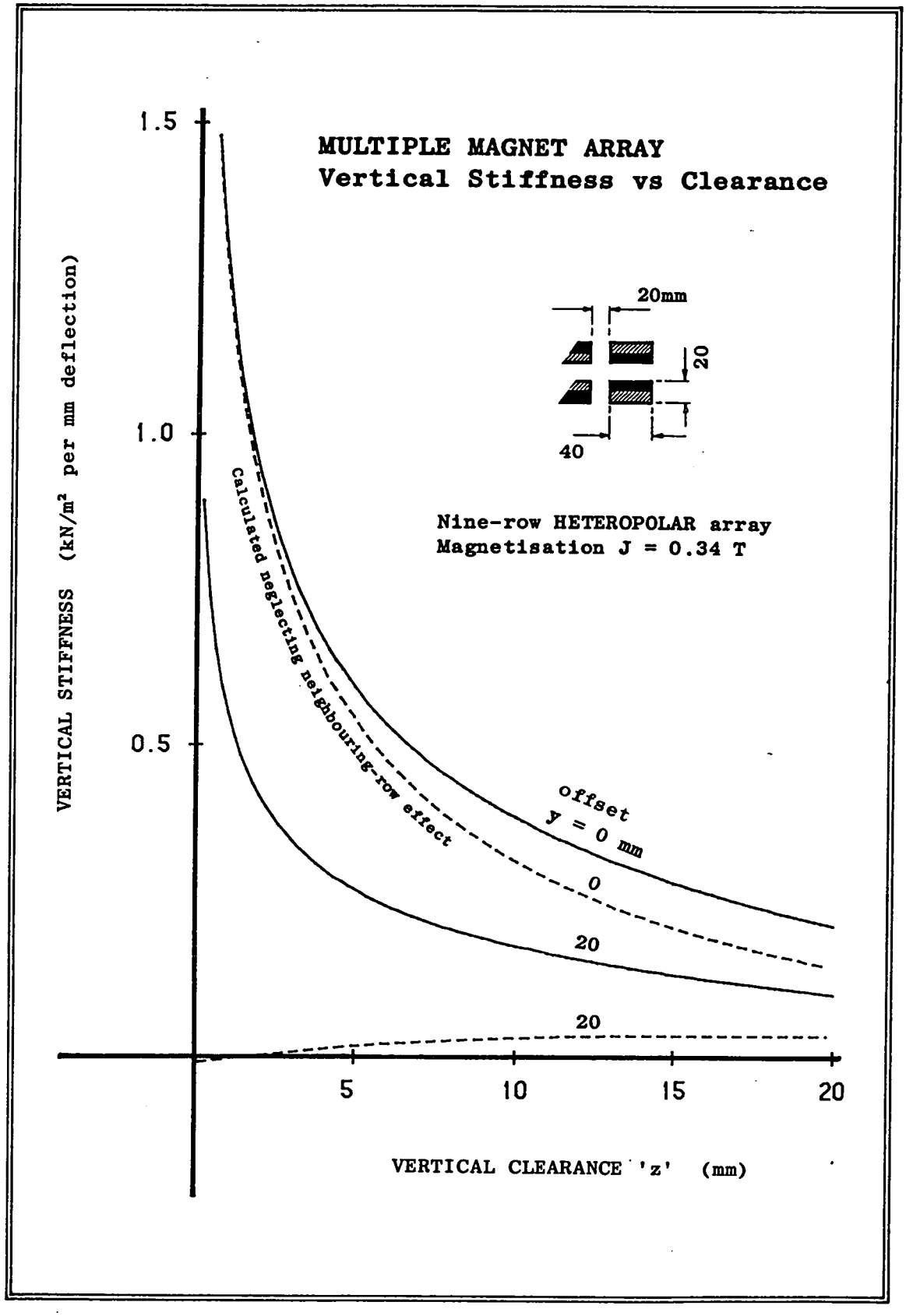
MULTIPLE MAGNET ARRAY
Vertical Stiffness vs Clearance
20mm
20
40
Nine-row HETEROPOLAR array
Magnetisation J = 0.34 T
VERTICAL STIFFNESS (kN/m² per mm deflection)
1.5
1.0
0.5
Calculated neglecting neighbouring-row effect
offset
y = 0 mm
0
20
20
5
10
15
20
VERTICAL CLEARANCE 'z' (mm)

FIGURE 8.17

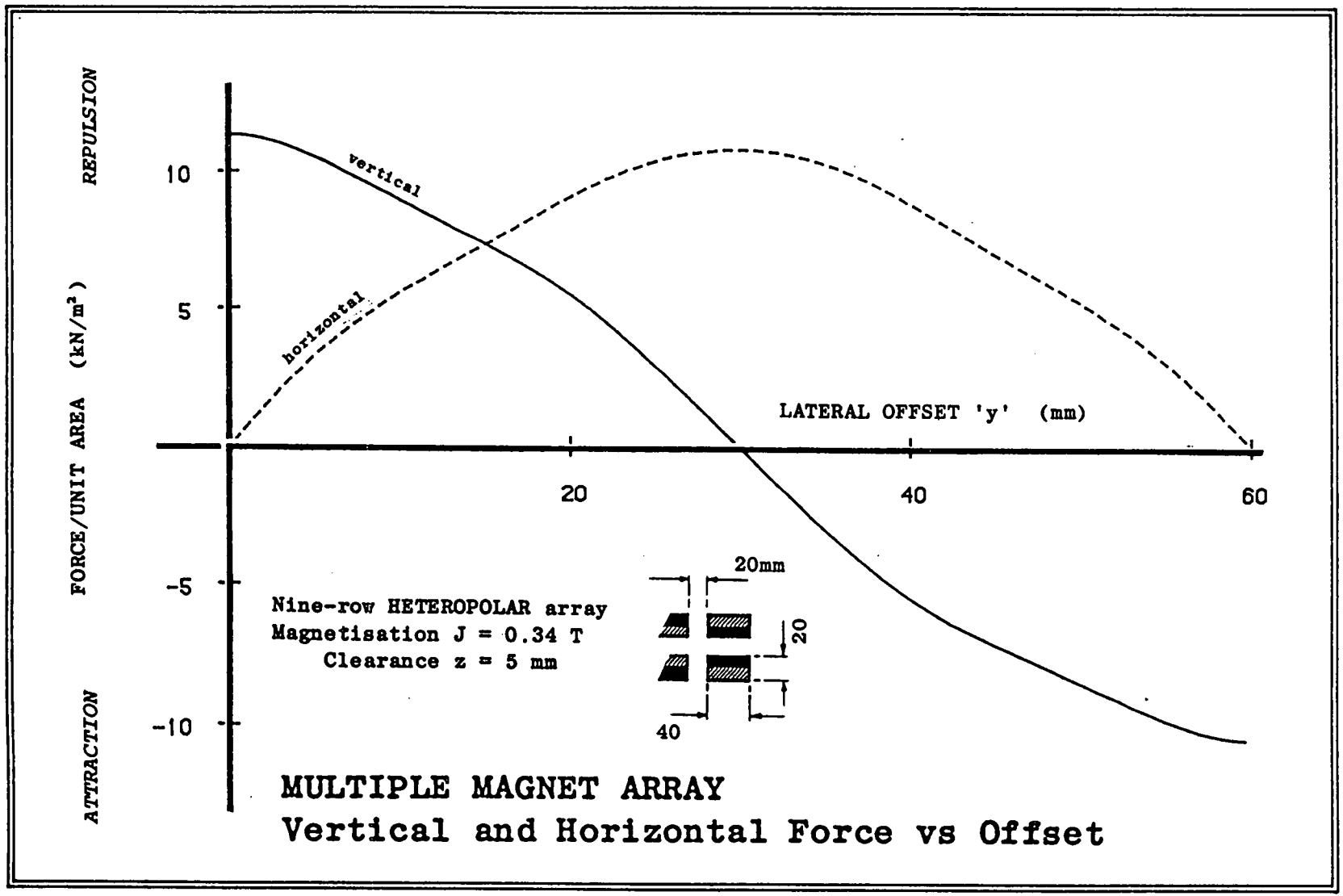
REPULSION
FORCE/UNIT AREA (kN/m²)
ATTRACTION
10
5
-5
-10
vertical
horizontal
LATERAL OFFSET 'y' (mm)
20
40
60
Nine-row HETEROPOLAR array
Magnetisation J = 0.34 T
Clearance z = 5 mm
20mm
20
40
MULTIPLE MAGNET ARRAY
Vertical and Horizontal Force vs Offset

FIGURE 8.18

Figure 8.18 shows the less favourable aspect of the neighbouring-row effect, namely an increase in lateral instability. This is seen as an increase of horizontal force with offset, corresponding to negative lateral stiffness. With a lateral offset of three-quarters the pole-width, vertical repulsion has collapsed. At an offset equal to the lateral pitch (60 mm), the heteropolar system goes into full attraction.

8.11 Three-Dimensional Magnet Optimisation (1): Constrained

This analysis is included for academic interest: the result represents the maximum force which can ever be exerted between two rectangular permanent magnets. The analytic geometry is that shown in figure 8.19. No lateral offsets are considered, and only symmetric magnet geometries are examined in which, furthermore, length L and width W are equal, ie. the magnets are square in plan. These preconditions are all, for reasons of symmetry, necessary for a geometry to provide maximum force/unit volume (see Coffey et al, 1972).

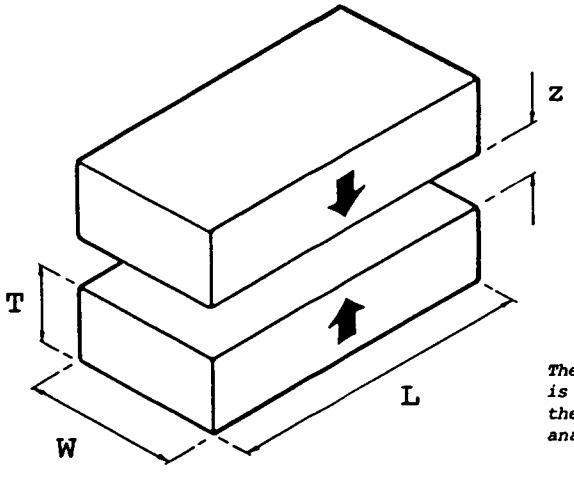

volume V = 2LWT

The dimensional notation used is that of Coffey et al (1972); these authors quote the full analytic expression for force.

FIGURE 8.19: Analytic Geometry for a Symmetric, Three-dimensional Magnet Pair

The three-dimensional magnet geometry is analysed to find the following two quantities:

(a) The maximum vertical repulsion force F available from a fixed total volume V.

(b) The maximum-available vertical force/unit volume F/V at any clearance z (see section 8.12).

The first of these requires a constrained optimisation with fixed total volume V where, for the given geometry:

$$V = 2W^2T \tag{8.33}$$

From which:

$$W = (V/2T)^{\frac{1}{2}} \tag{8.34}$$

Imposing a constant-volume constraint reduces the repulsion force F to a function of only one variable: thickness T is arbitrarily chosen. Maximum force occurs at pole-contact, and hence the required condition for a maximum is given by:

$$dF/dT_{z=0} = 0 \tag{8.35}$$

From equation 8.33, the expression for a constant-volume constrained maximum is then:

$$\partial F/\partial T + (\partial F/\partial W)\, dW/dT = 0 \tag{8.36}$$

and hence, from 8.34 and 8.36, the required condition for a constrained maximum is:

$$\partial F/\partial T - W/2T\,(\partial F/\partial W) = 0 \tag{8.37}$$

An expression for repulsion force F for the geometry in figure 8.19 is presented by Coffey et al (1972); for the optimum solution, this reduces to the case where L = W (see above). The appropriate partial derivatives are calculable in fully analytic form, from which the solution to equation 8.37 may be found using the Newton-Raphson root-seeking algorithm previously employed in two-dimensional constrained optimisations (see eg. section 8.5). The resulting optimum dimensions are:

$$\begin{aligned} \text{width } W_{opt} &= 1.072\ V^{1/3} \\ \text{thickness } T_{opt} &= 0.4548\ V^{1/3} \\ W/T_{opt} &= 2.466 \end{aligned} \qquad (8.38)$$

The corresponding maximum-available force is given by:

$$F_{opt} = 237.9\ J^2 V^{2/3}\ \text{kN} \qquad (8.39)$$

This last figure represents the maximum force which can ever be exerted by two rectangular bar magnets.

8.12 Three-Dimensional Magnet Optimisation (2): Unconstrained

Finally, the maximum-possible force/unit volume is found for a three-dimensional magnet-pair. The analytic geometry is the same as in section 8.11, ie. symmetric, square magnets. This time, however, there is no constant-volume constraint, and simultaneous solutions are required to the following two equations:

$$\partial/\partial T\ (F/V) = 0 \qquad (8.40)$$

$$\partial/\partial W\ (F/V) = 0 \qquad (8.41)$$

Using the relationship given by equation 8.33, the above requirements are expressed as:

$$(\partial F/\partial T - F/T) = 0 \qquad (8.42)$$

$$(\partial F/\partial W - 2F/W) = 0 \qquad (8.43)$$

To obtain simultaneous solutions to equations 8.42 and 8.43, the method of steepest-ascent (described in section 8.8) is used. In the present case the objective function is F/V, and the two independent variables are the magnet dimensions W and T; clearance z is constant. The analysis yields the following results:

$$W/z_{opt} = 3.079$$

$$T/z_{opt} = 1.357 \qquad (8.44)$$

$$W/T_{opt} = 2.269$$

with the corresponding maximum-available force/unit volume given as:

$$F/V_{opt} = 20.40\ J^2/z \quad kN/m^3 \qquad (8.45)$$

The above value of F/V_{opt} can be directly compared with that for a two-dimensional magnet-pair, given in equation 8.27. The optimised three-dimensional magnets are then seen to represent 12.5% more efficient use of magnetic material.

In their analysis of this geometry, Coffey et al (1972) found the optimum magnet dimensions graphically, with resulting values for W/z_{opt} and T/z_{opt} of 3.0 and 1.5, repectively, and corresponding F/V_{opt} of 20,300 J^2/z N/m^3. As in the two-dimensional case, a relatively wide latitude is seen to exist in the magnet dimensions capable of delivering

near-optimum efficiency. These authors' results indicate a value of maximum force/unit volume only 0.5% less than that of the present analysis, although using magnets with a total volume some 8% greater.

8.13 Conclusions

The geometry optimisation schemes described in this chapter make possible the following procedures, referring to a two-dimensional magnet pair:

(1) By specifying any two parameters from a choice of force/unit length, magnet-weight, and pole-clearance, the optimum value of the third can be automatically found. This includes cases where a horizontal pole-offset is assumed.

(2) As in (1) above, replacing force/unit length with stiffness/unit length.

(3) By specifying pole clearance alone, the maximum force/unit volume or stiffness/unit volume can be found. Again, lateral offsets may be stipulated.

The way in which an optimum magnet geometry might be selected in practice has been demonstrated in a worked example. Several of the results of both the two-dimensional and the three-dimensional geometry optimisation analyses represent special cases, in which the material efficiency represents the maximum which can be achieved using hard magnets. These results are summarised in table 8.1. In some instances previous estimates exist for optimum dimensions (see table 8.1), and the results of the present study are found to differ from these by up to about 9%. The new estimates should be the more accurate, on account of the computer numerical methods used to estimate function maxima. The optimisation results are highly general, and apply to any system for which ideal-magnet assumptions can be made.

TABLE 8.1

Summary of 'special case' optimum rectangular magnet geometries. Those marked with an asterisk (*) have previously been estimated by semi-graphical techniques. For details of the analyses, refer to the sections noted in each case.

	TWO-DIMENSIONAL	THREE-DIMENSIONAL
	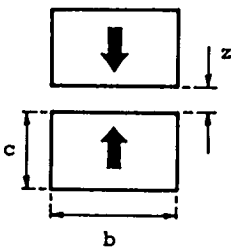 *magnet width : b* *height : c* *pole separation : z* *magnetisation : J* *NOTE: area* A = 2bc	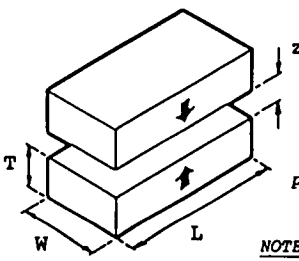 *magnet width : W* *length : L* *height : T* *pole separation : z* *magnetisation : J* *NOTE: volume* V = 2LWT
Maximum vertical repulsion force available from a rectangular magnet pair of combined volume V (three-dimensional case) or cross sectional area A (two-dimensional case). Pole contact (z = 0) is assumed.	Force/unit length $F_z = 167.2\ J^2A^{\frac{1}{2}}$ kN/m Optimum aspect ratio b/c = 0.9914 *(see section 8.5)*	Force $F = 237.9\ J^2V^{2/3}$ kN Optimum dimensional ratios: W/T = 2.466 L/T = " *(see section 8.11)*
Maximum force/unit volume available from a rectangular magnet pair at a given pole clearance z.	* Force/unit volume $F_V = 18.12\ J^2/z$ kN/m^3 Optimum dimensions: b = 2.005 z c = 1.372 z *(see section 8.8)*	* Force/unit volume F/V = 20.40 J^2/z kN/m^3 Optimum dimensions: W = 3.079 z L = " T = 1.357 z *(see section 8.12)*
Maximum vertical stiffness available from a rectangular magnet pair of combined volume V (three-dimensional case) or cross sectional area A (two dimensional case). Pole contact (z = 0) is assumed.	Stiffness/unit length K_z is theoretically infinite. Optimum aspect ratio b/c = 0.6515 *(see section 8.6)*	N/A
Maximum stiffness/unit volume available from a rectangular magnet pair at a given pole clearance z.	* Stiffness/unit volume $K_V = 23.45\ J^2/z^2$ kN/m^4 Optimum dimensions: b = 1.018 z c = 0.6697 z *(see section 8.9)*	N/A

In terms of the present application, the increase in repulsion which can be gained by using a close-pitched heteropolar magnet array has been demonstrated. So too has the danger of axial misalignment of opposing magnets in the bearing. As a rough guide, the maximum lateral offset of opposing pole faces should not exceed about 20% of their width. This highlights the relationship which exists between axial alignment and bearing cost: the better the alignment possible, the smaller the magnets which can be used.

CHAPTER 9
PERMANENT MAGNET ANALYSIS - EXPERIMENTAL RESULTS

9.1 Chapter Summary

The experiments described in this chapter were designed to verify the results of the optimisation procedures contained in chapter 8. After a list of the specific experimental objectives, there follows a description of the 'levitation bed' used to collect magnetic force/clearance data. The experimental magnets themselves are then described, together with the means by which single blocks of three different geometries were used to provide six experimental magnet pairs. The ability of the levitation bed to simulate two-dimensional magnet geometries is demonstrated. Some typical results are presented in the form of force/clearance and stiffness/clearance curves.

Non-ideal magnetisation is discussed, and experimentally demonstrated. Finally, the experimental results are compared with those of theoretical geometry optimisation schemes. In this procedure, the correct methods of comparing results are emphasised, and important use of the scaling laws is repeatedly seen.

9.2 Experimental Objectives

The specific experimental objectives were to verify the results of the four optimisation procedures dealing with two-dimensional magnet pairs, ie.:

(1) constrained force/unit length

(2) constrained stiffness/unit length

(3) unconstrained force/unit volume

(4) unconstrained stiffness/unit volume

Only isolated magnet pairs were examined, in all cases using symmetric opposing blocks. No multiple-row configurations were

tested. An overall objective was to ascertain with how much confidence large-scale bearing characteristics could be predicted on the basis of ideal-magnet theory.

9.3 Experimental Apparatus (1): The Magnet Levitation-Bed

Force measurements were made using a magnetic 'levitation-bed', of the design shown in figure 9.1. The bed consisted of two plywood boards connected together at one end by a 'frictionless' hinge, with the magnets fixed at the other end, oriented in mutual vertical repulsion. The magnet blocks were held against end-stops by clamps, to keep their long axes parallel and give them a horizontal position reference.

Over the range of experimental levitation heights used, the arc in which the upper magnet was constrained to move approximated well to pure vertical translation. The maximum rotation of the upper magnet was less than 2°, and the horizontal misalignment thus introduced never exceeded 4% of the pole-clearance. To allow variation of the magnets' lateral offset, the lower board was connected to the hinge via a third board, forming an extension-arm: this is illustrated in figure 9.2. The arm could be rigidly clamped in any position between two end-stops, and by this means the required amount of offset was preselected.

To load the magnet-pair, a weight-pan was suspended from the upper board, at a known distance from the hinge-axis (see figure 9.2). A set of calibrated weights was used to load the pan, with repulsion force measured by taking moments about the axis. The vertical force acting on the upper magnet was found from:

$$F = M/L_c \qquad (9.1)$$

where:

M = total weight-moment

L_c = distance from hinge axis to magnet centroid

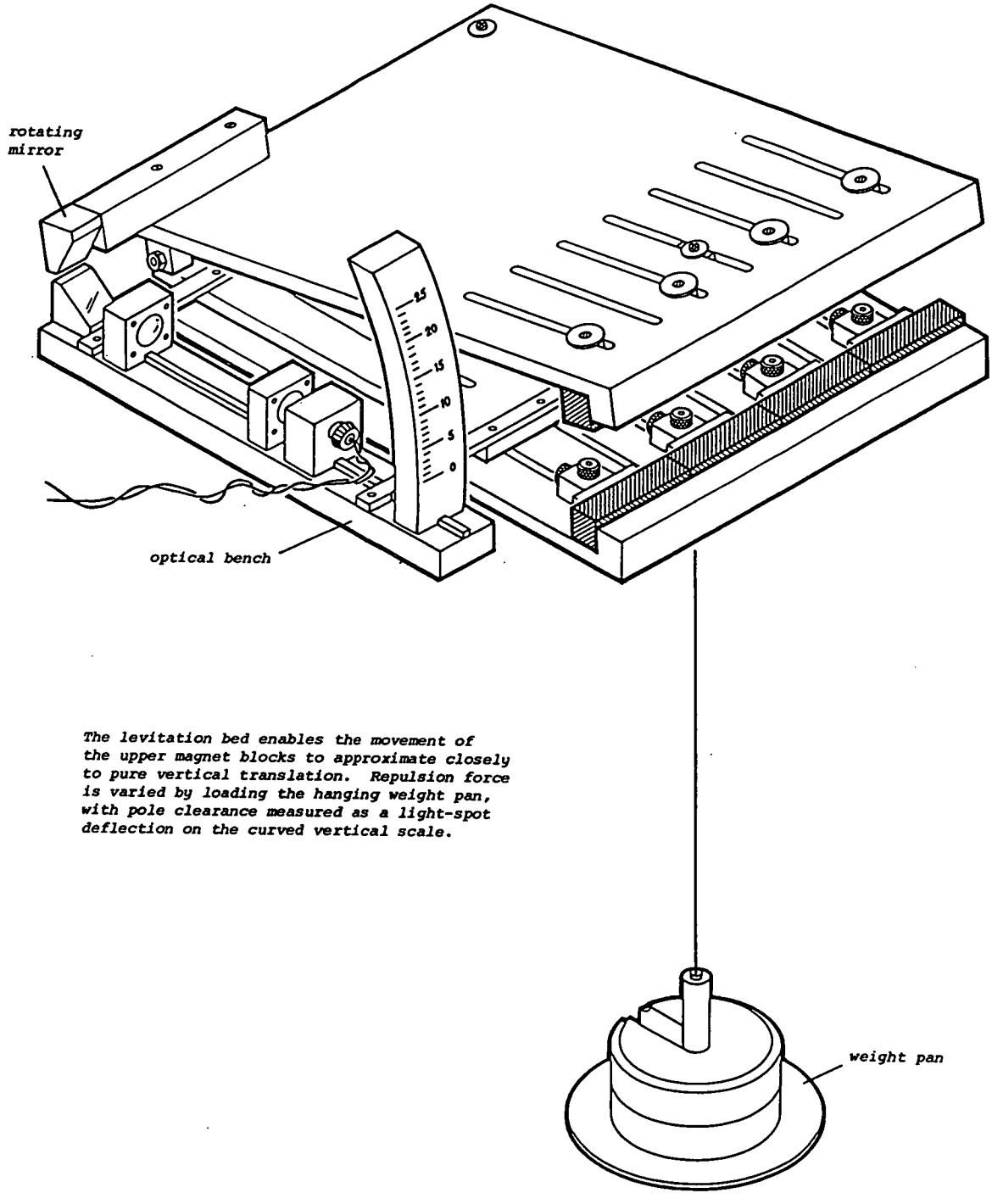

The levitation bed enables the movement of the upper magnet blocks to approximate closely to pure vertical translation. Repulsion force is varied by loading the hanging weight pan, with pole clearance measured as a light-spot deflection on the curved vertical scale.

FIGURE 9.1
The Permanent Magnet 'Levitation Bed'

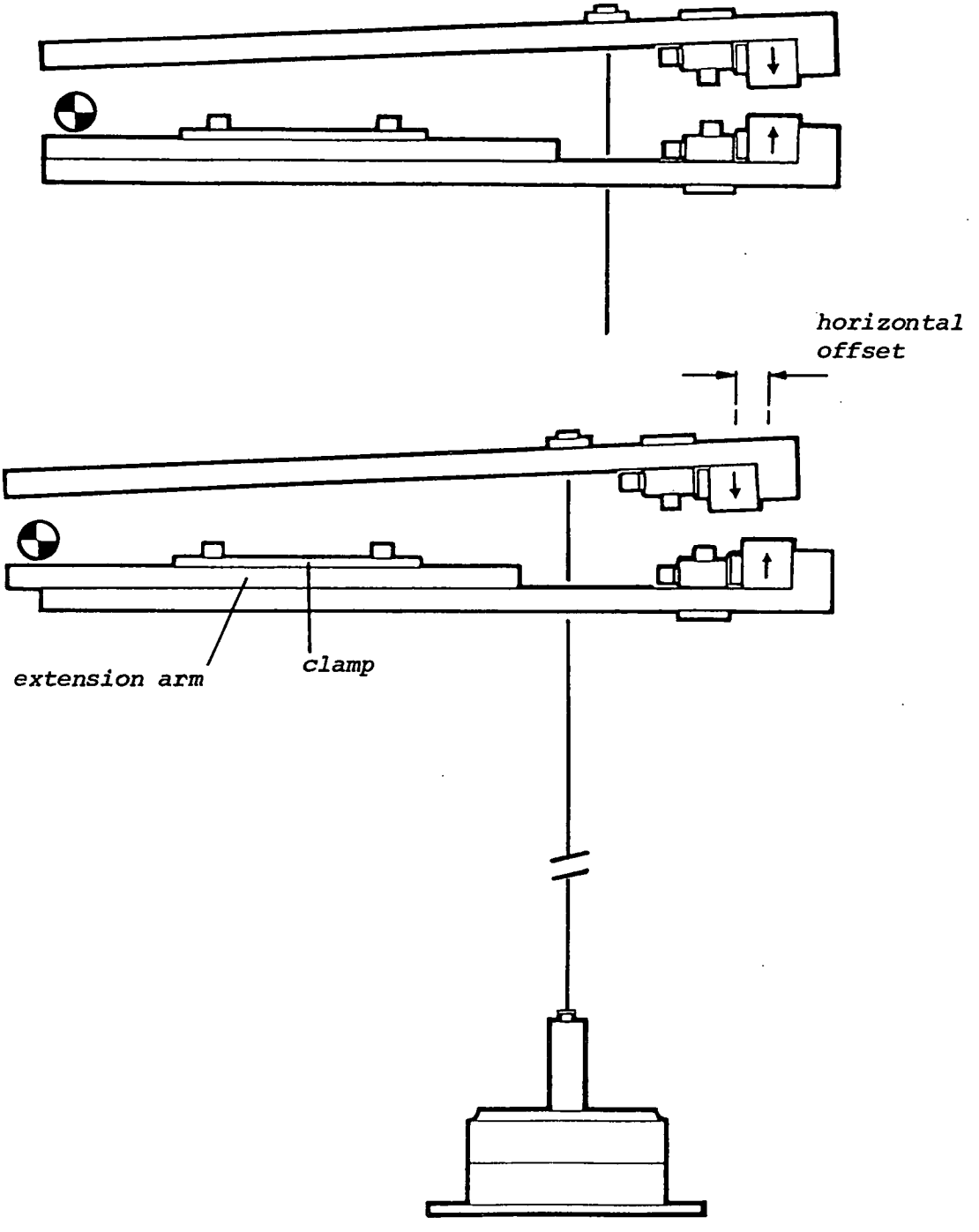

FIGURE 9.2
Arrangement for Varying Magnets' Horizontal Offset

Because the upper magnet moved in a slight arc, experimental values of F given by equation 9.1 were subject to error in cases where non-zero lateral offset was selected. This occured because the line of action of the vertical repulsion force acting on the upper magnet was no longer that of its weight, in addition to which there now existed a horizontal repulsion force on it, whose line of action did not pass through the hinge axis.

Both effects were judged to give rise to small moments acting on the upper board, in addition to that given by FL_c. A worst estimate of the error incurred was made by considering a magnet-pair offset by half a pole-width, with the two pole-faces in contact. From an examination of the approximate force-distribution in the equivalent air-cored solenoids, it was shown that the two effects noted above tended to oppose each other, lowering the overall error, and that the percentage error resulting from use of equation 9.1, for a magnet-pair of pole-width b and height c, with true values of resultant vertical and horizontal repulsion force F_z and F_y, respectively, would not exceed the following figure:

$$\text{maximum error (\%)} = 100/(2L_c) \times (cF_z/F_y - b) \qquad (9.2)$$

The average error for the experimental magnet pairs under worst-case conditions was found to be less than 3%. The error decreased rapidly and nonlinearly to zero at zero offset (neglecting the rotation-induced offset noted above).

Using the levitation bed, pole-clearance was measured optically: the apparatus can be seen in figure 9.1. An optical bench, comprising light source, collimating lens, objective lens, and angled mirror, was attached to the lower board. This generated a light-beam, which was reflected via a second mirror mounted on the upper board, to produce a spot on a translucent vertical scale. Rotation of the upper board gave near-linear spot deflection. The system was calibrated for pole-clearance using

a vernier height gauge, and the calibration curve stored in computer memory as an array, to allow both interpolated use, and correction for magnet pole-width. Zeroing was achieved by forcing the magnets into pole-contact, and adjusting the mounting angle of the upper mirror to bring the pointer to scale zero; maximum systematic error was estimated as 0.5 mm. The optical method was sensitive, as the spot deflected through twice the angle of the board's rotation, giving a scale magnification factor of two.

In addition to that noted above, the sources of uncertainty in force/clearance measurement were:

(a) scale-reading error

(b) force error due to non-parallellism of magnets

The first of these was small, with half the smallest scale division corresponding to approximately 0.25 mm. The second again arose because movement of the magnets was rotational rather than translational (see figure 9.2): because magnetic stiffness is nonlinear, a discrepancy was thus introduced in the measured force. With constant stiffness, no error would have existed. It was estimated, however, that the fractional error in force was an order of magnitude lower than the ratio dz/z, where z is pole clearance, and dz its variation introduced by the rotation. The worst-case force error (3%) was therefore adhered to.

The magnets' lateral offset was measured off a horizontal scale on the lower board, zeroed by lining up the two end-stops on a square reference-edge. Maximum error was estimated at approximately 0.3 mm.

To avoid corrupting experimental measurements, most components of the levitation bed were constructed from non-magnetic materials. Wood was extensively used, and metal parts were

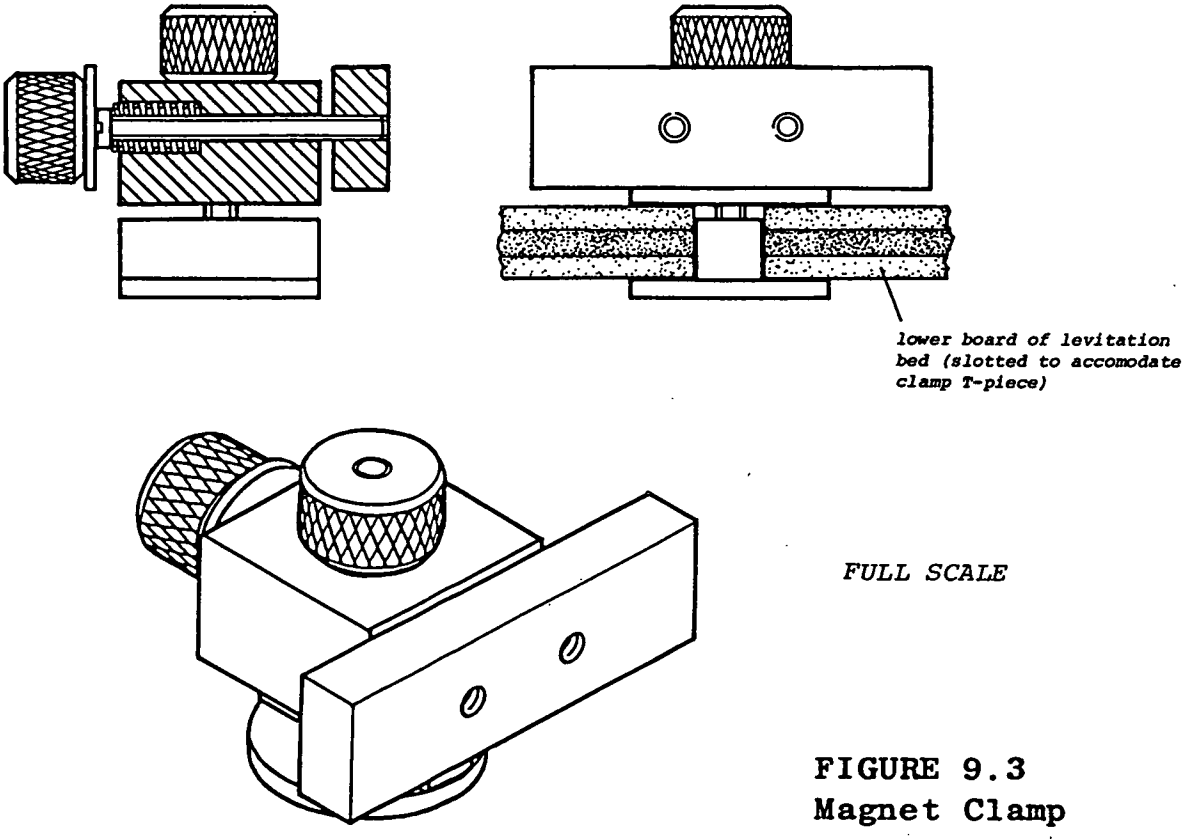

FIGURE 9.3
Magnet Clamp

machined from aluminium alloy. In a few instances it was found necessary to use magnetic-steel components, but the presence of these was found to exert negligible effect. This was checked by observing the change in magnet pole-clearance when such a component was introduced into the magnets' vicinity. In no case was any change discernible. Although the weights used to load the bed were of magnetisable material, they were kept well out of the region of magnetic influence, by hanging them from a suitably long tie-line. The clamps used to secure the magnets were of the design illustrated in figure 9.3. These exerted a purely horizontal force, and allowed easy positioning of the magnets, with no tendency to damage their surfaces.

9.4 Experimental Apparatus (2): The Magnets

The experimental magnets were manufactured by the Stackpole Corporation of Kane, Pennsylvania, and supplied by Ampohm Ltd. Thirty rectangular blocks of anisotropic strontium ferrite were supplied pre-magnetised. The blocks were all of the same nominal length, but came with three different cross-sectional dimensions. The nominal specification for the blocks is given in table 9.1, with the nominal dimensions shown in figure 9.4.

Table 9.1 Nominal Specification of Experimental Magnets

(Physical characteristics measured at 25°C)

material	:	anisotropic strontium ferrite, premagnetised
remanent magnetisation J	:	0.34 tesla
temperature coefficient of J	:	-0.2%/C°
intrinsic coercive force H_{ci}	:	318 kA/m
density	:	4700 - 5100 kg/m^3
dimensions	:	see figure 9.4

The smallest magnets (type A), had been ground on all surfaces; the other blocks (types B and C) were more roughly finished, with some surfaces exhibiting the marks of saw-cutting, and others still bearing impressions of the shuttering used in manufacture. In all cases, dimensional tolerances of better than 0.8% applied. Densities were below the nominal minimum by up to 4.5% (types B and C). Measurement of intrinsic magnetisation J was not attempted: the nominal remanent magnetisation of 0.34 T was initially used for theoretical comparisons; the appropriateness of this assumption is discussed in greater detail later.

MAGNET GEOMETRY	DIMENSIONAL TOLERANCE (mm)	DENSITY (kgm^{-3})
A	0.10	4640
B	0.15	4490
C	0.20	4490

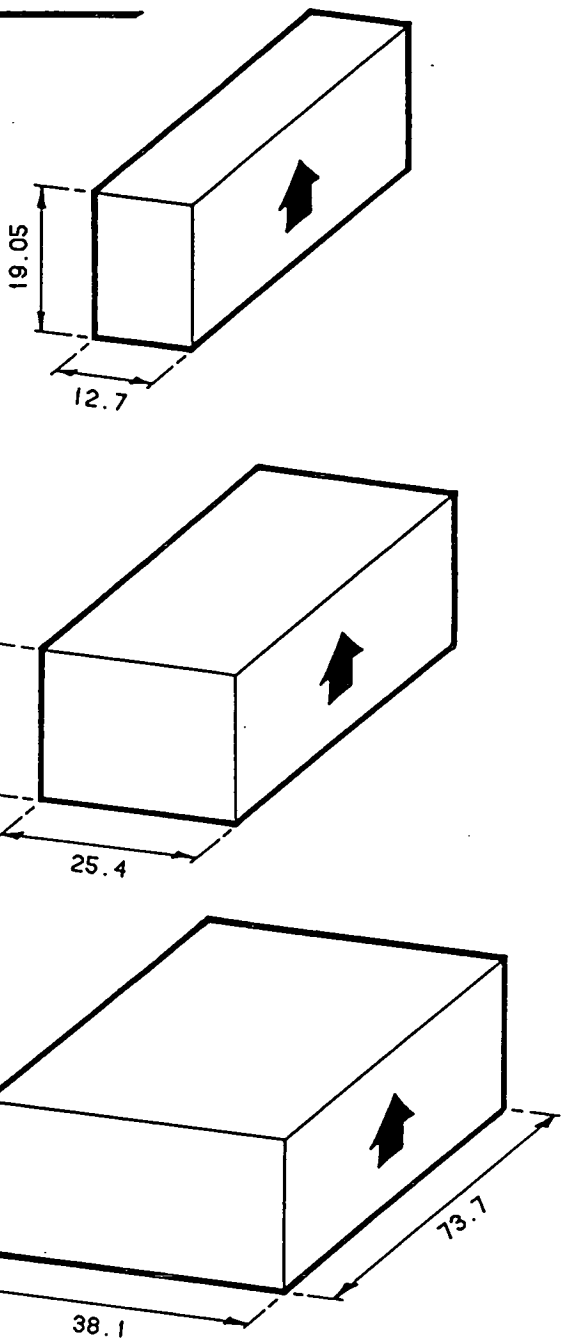

FIGURE 9.4
The Experimental Magnet Set

Although only three different block cross-sections were available, several others were created by clamping together two or more blocks to form larger magnets. This technique relied on the following assumptions:

(1) A number of magnets clamped together with their magnetic axes oriented in parallel will exhibit the same characteristics as a single magnet of the same overall size.

(2) A two-dimensional magnet-pair with opposing, ie. antiparallel, magnetic axes, is exactly equivalent in terms of force and stiffness as a pair with coparallel, ie., 'side-by-side' magnetic axes, as shown in figure 9.5.

The first assumption is verifiable by calculating firstly the field external to two magnetic blocks placed very close together, and then that for a single block of the same overall

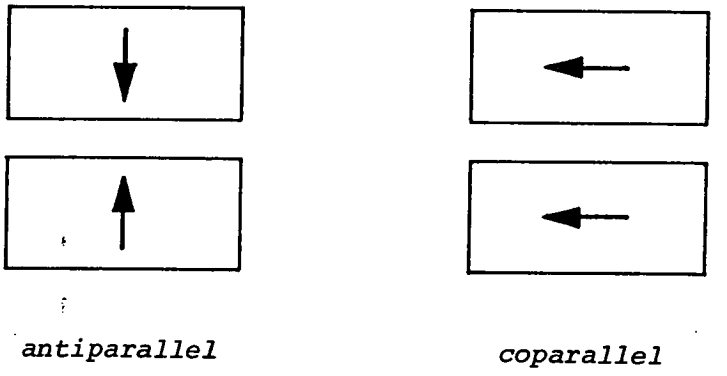

With a two-dimensional magnet pair of any geometry, repulsion force and stiffness remain unchanged if the magnetic vectors of the opposing blocks are counter-rotated through the same angle. Hence the two magnet pairs above will theoretically exhibit the same characteristics. For an explanation of this phenomenon, see Yonnet (1978) or Rowlands (1980).

FIGURE 9.5
Equivalent Configurations for Two-dimensional Magnets

dimensions. The effect of a small air-gap is found negligible. The second (perhaps surprising) assumption is based on theoretical analyses performed by Yonnet (1978) and Rowlands (1980), and can be easily verified by calculation.

Six cross-sectional geometries were examined. These were constructed from blocks A, B, and C, as shown in figure 9.6 (note that in geometry no.1 the two component blocks exert mutual repulsion forces, requiring to be firmly clamped together, while geometry no.5 effectively holds itself together). In all experiments, the opposing magnet-pair consisted of a single upper block (comprising up to three components) in levitation above four identical blocks clamped end-to-end, as shown in figure 9.7. This approximates to a true two-dimensional case, the characteristics of which are best understood by considering the equivalent rectangular solenoids, as shown.

9.5 Verifying the Two-Dimensional Geometry

To determine whether the experimental magnet arrangement of 'one vs four' (see figure 9.7) was effectively equivalent to a two-dimensional geometry, the following test was performed. Four sets of measurements were made of vertical repulsion force vs pole clearance, using a single levitated magnet above a line comprised in turn of one, two, three, and four lower magnets. The results can be seen in figure 9.8, in a comparison of the four force/clearance curves. The three measured using two, three, and four lower blocks are almost perfectly superimposed, and show poorer repulsion characteristics than the one-vs-one interaction. The shortfall is explained in terms of solenoid theory by the decreased repulsion contribution of the end current windings. In this case, convergence to two-dimensional character was apparently accomplished using only two magnets in the lower row. Despite this, a one-vs-four configuration was adhered to in all quantitative experiments, to ensure confidence in the two-dimensional approximation.

MAGNET PAIR No.	sub-blocks		b (mm)	c (mm)	aspect ratio b/c
1	A+A	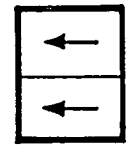	19.05	25.4	0.75
2	B	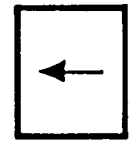	20.3	25.4	0.80
3	B	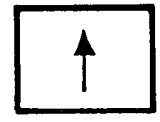	25.4	20.3	1.25
4	2A+B	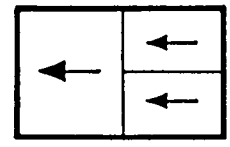	39.4	25.4	1.55
5	B+B	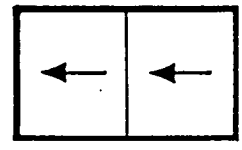	40.6	25.4	1.60
6	C	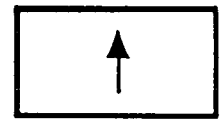	38.1	20.3	1.875

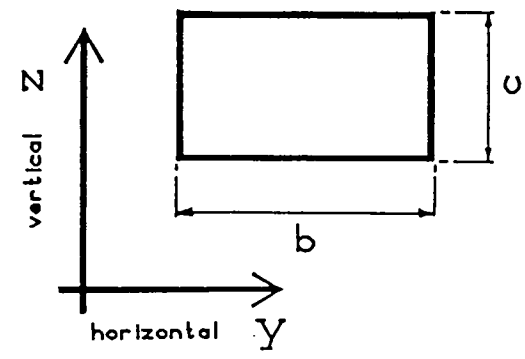

FIGURE 9.6
Experimental Magnet Pair Geometries

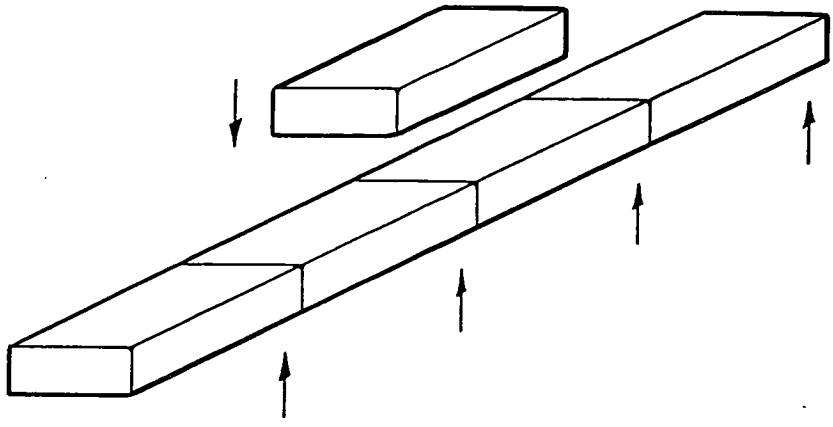

The 'one vs four' experimental configuration is used to approximate a two-dimensional magnet pair interaction. A single upper block is levitated above the mid-point of a line of four similar blocks.

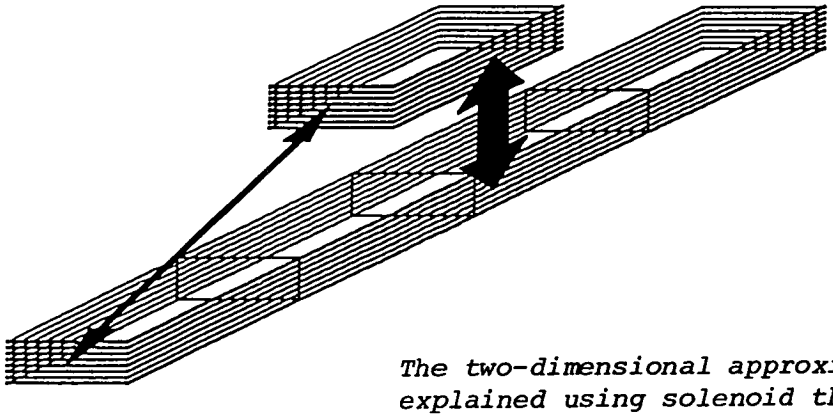

The two-dimensional approximation may be explained using solenoid theory. Forces exist only between parallel current-carrying wires; in the above configuration the end interactions are thus relatively weak. Note too the cancelling of internal currents.

FIGURE 9.7
Explanation of Two-dimensional Magnet Approximation

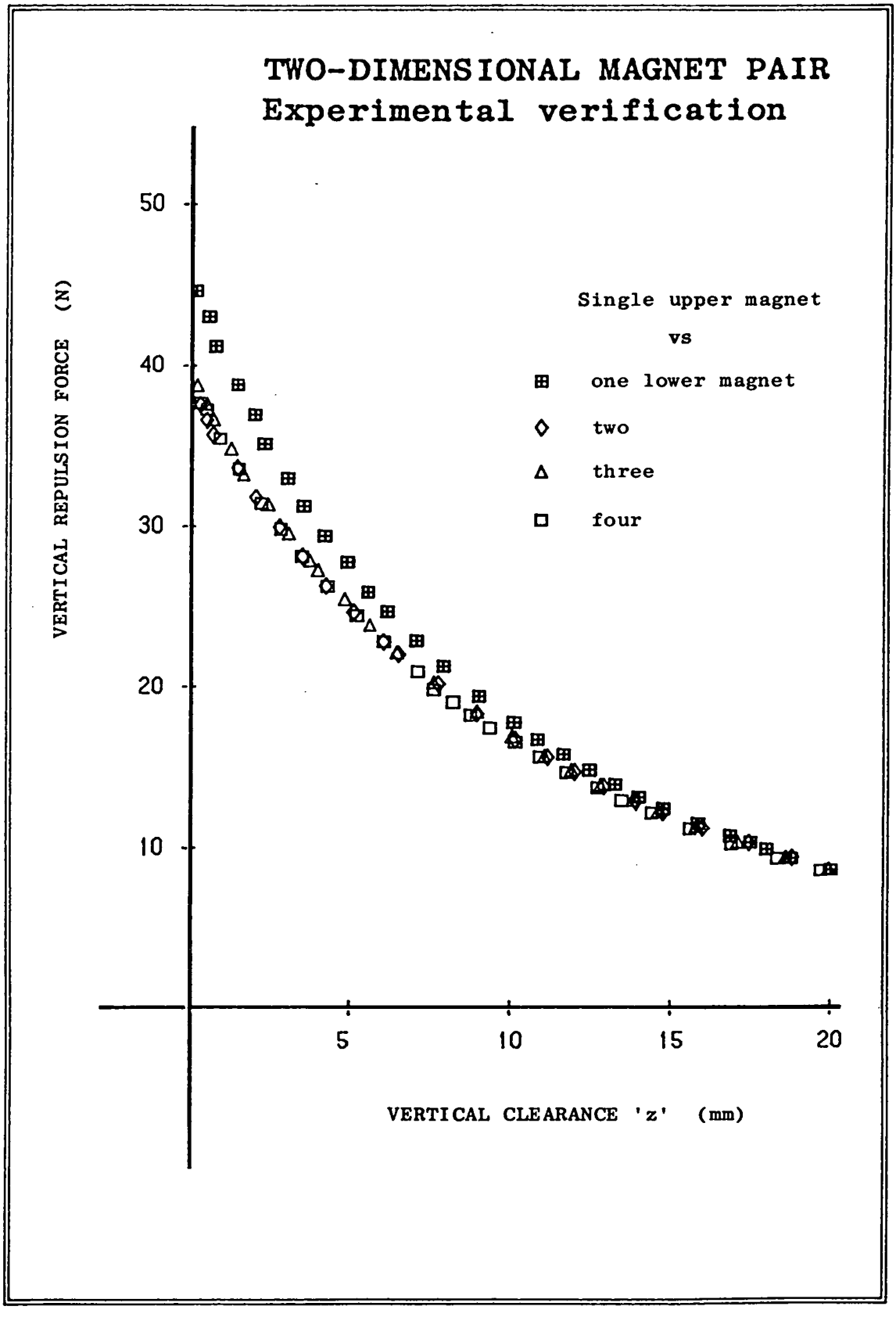
TWO-DIMENSIONAL MAGNET PAIR
Experimental verification
VERTICAL REPULSION FORCE (N)
50
40
30
20
10
5
10
15
20
VERTICAL CLEARANCE 'z' (mm)
Single upper magnet
vs
one lower magnet
two
three
four

FIGURE 9.8

9.6 Force Measurements

Most of the data necessary for verifying optimum-geometry predictions were extracted from force/clearance curves measured for each of the six experimental geometries shown above. For each geometry, curves were recorded corresponding to several fixed values of lateral offset, starting with the fully aligned case for which y = 0. The amount by which offset was incremented was related to the cross-sectional area of the pair under test (see section 9.9). No measurements were taken at zero clearance, due to the difficulty in loading the magnets to pole-contact without incurring a physical reaction force.

Typical experimental force/clearance curves can be seen in figures 9.9 and 9.10; the theoretical curves are calculated on the basis of nominal magnetisation J = 0.34 T. For the first geometry (no.4), the agreement is very good: figure 9.10 shows poorer correlation (pair no.5). Discrepancies of the kind seen in the second case are attributed to non-ideal magnetisation, rather than any systematic error in the measurements. For instance, a clearance error of about 3 mm, compared with the predicted maximum of 0.5 mm, would have to be contemplated to account for the observed results. Similarly, negligible errors in force measurement occur at small offset and clearance, where the experimental discrepancy is greatest.

Repulsion force is proportional to magnetisation squared, so only small deviations from nominal magnetisation need be invoked to explain the observed results. Therefore, for each of the six magnet-pairs, best-fit theoretical curves were calculated and a value of 'apparent magnetisation' assigned. Figure 9.11 shows the curve-fits for the magnets with the lowest, and highest apparent-J values. The average for the six pairs was 98.5% nominal, and the spread 9%. In all cases the experimental points lay close to theoretical curve fits based on apparent magnetisation, with the only signs of deviation being at small pole-clearance: this strongly suggests non-ideal magnetisation.

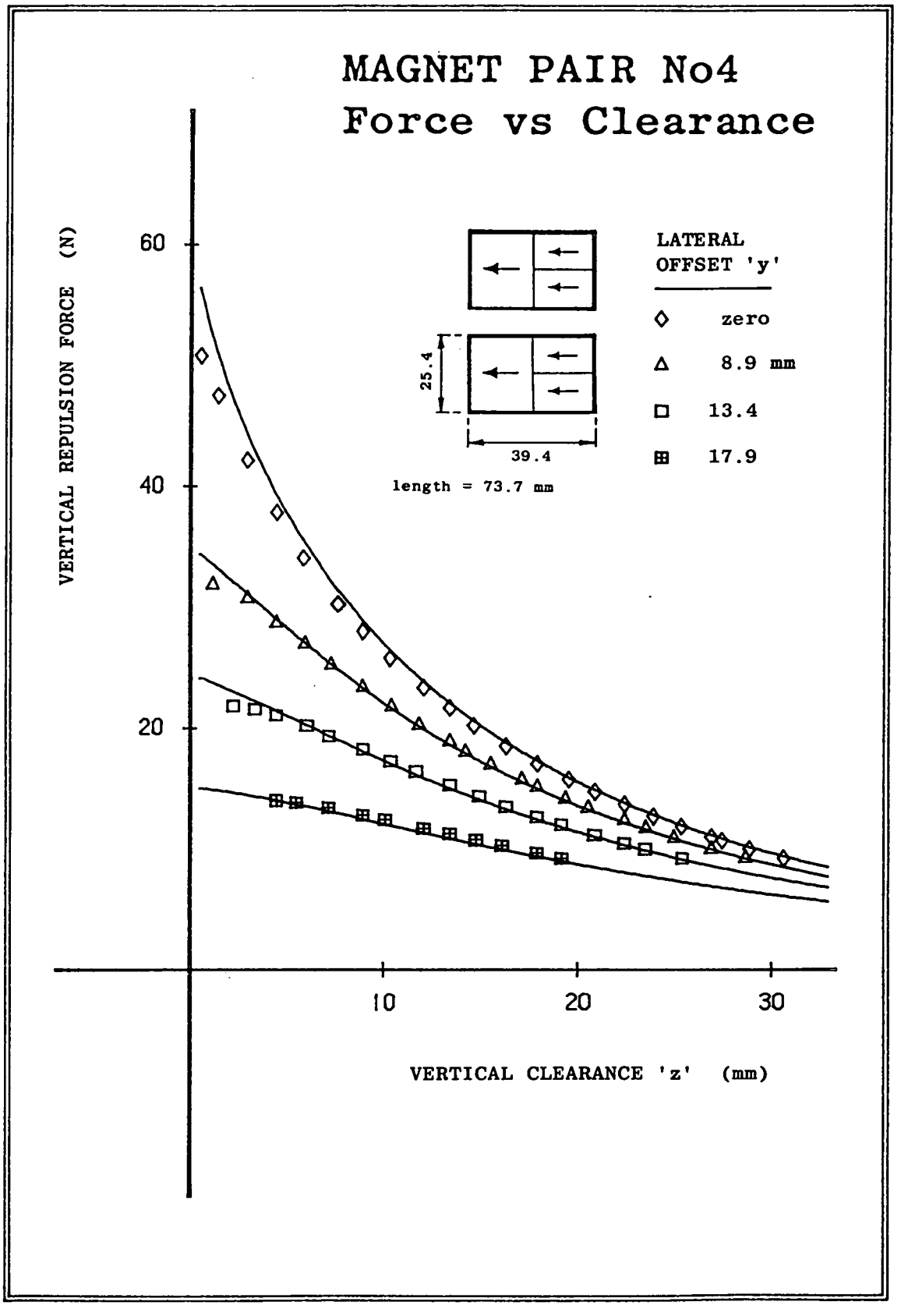
MAGNET PAIR No4
Force vs Clearance
VERTICAL REPULSION FORCE (N)
60
40
20
10
20
30
VERTICAL CLEARANCE 'z' (mm)
LATERAL
OFFSET 'y'
zero
8.9 mm
13.4
17.9
25.4
39.4
length = 73.7 mm

FIGURE 9.9

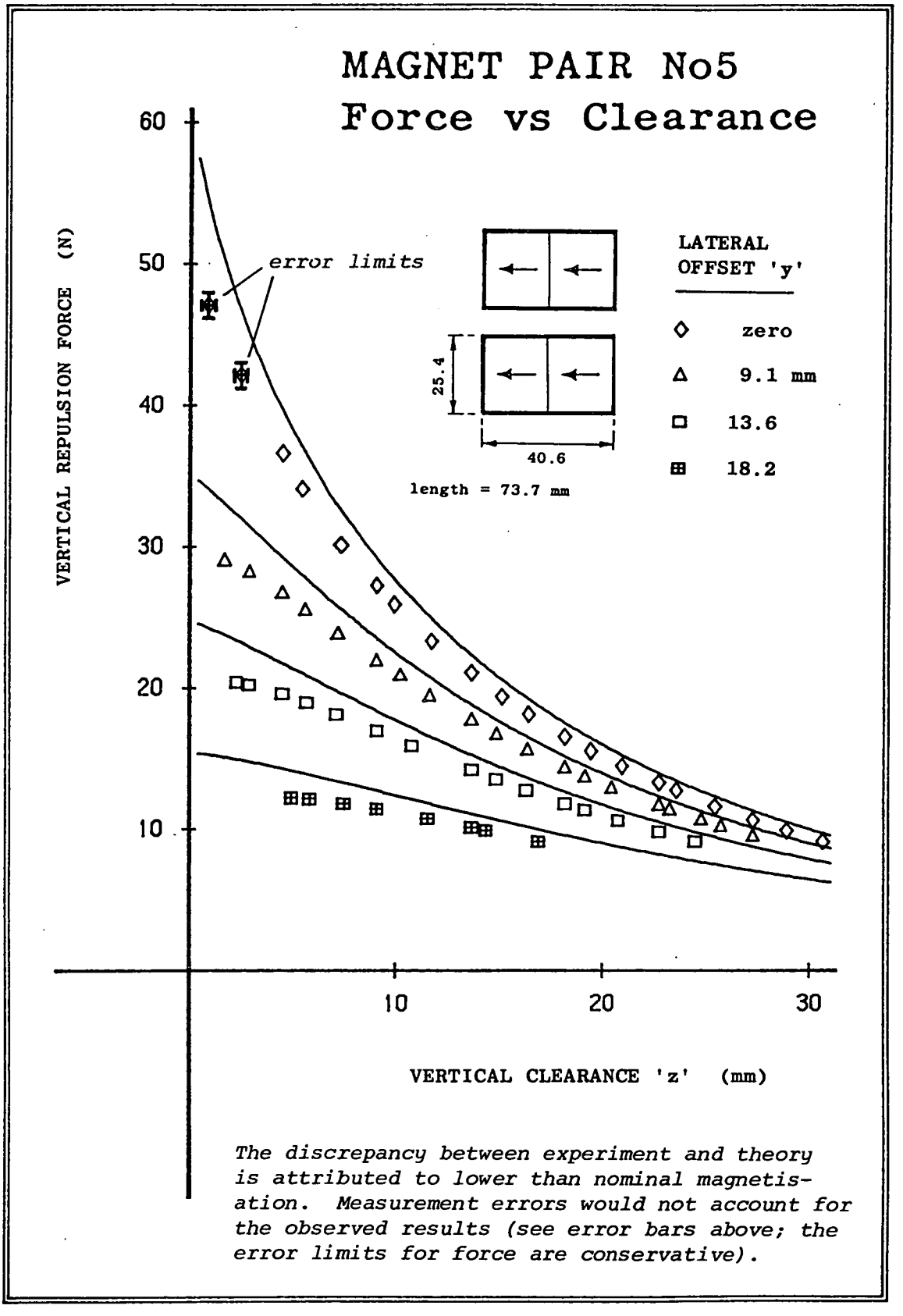
MAGNET PAIR No5
Force vs Clearance
VERTICAL REPULSION FORCE (N)
60
50
40
30
20
10
error limits
25.4
40.6
length = 73.7 mm
LATERAL
OFFSET 'y'
zero
9.1 mm
13.6
18.2
10
20
30
VERTICAL CLEARANCE 'z' (mm)
The discrepancy between experiment and theory is attributed to lower than nominal magnetisation. Measurement errors would not account for the observed results (see error bars above; the error limits for force are conservative).

FIGURE 9.10

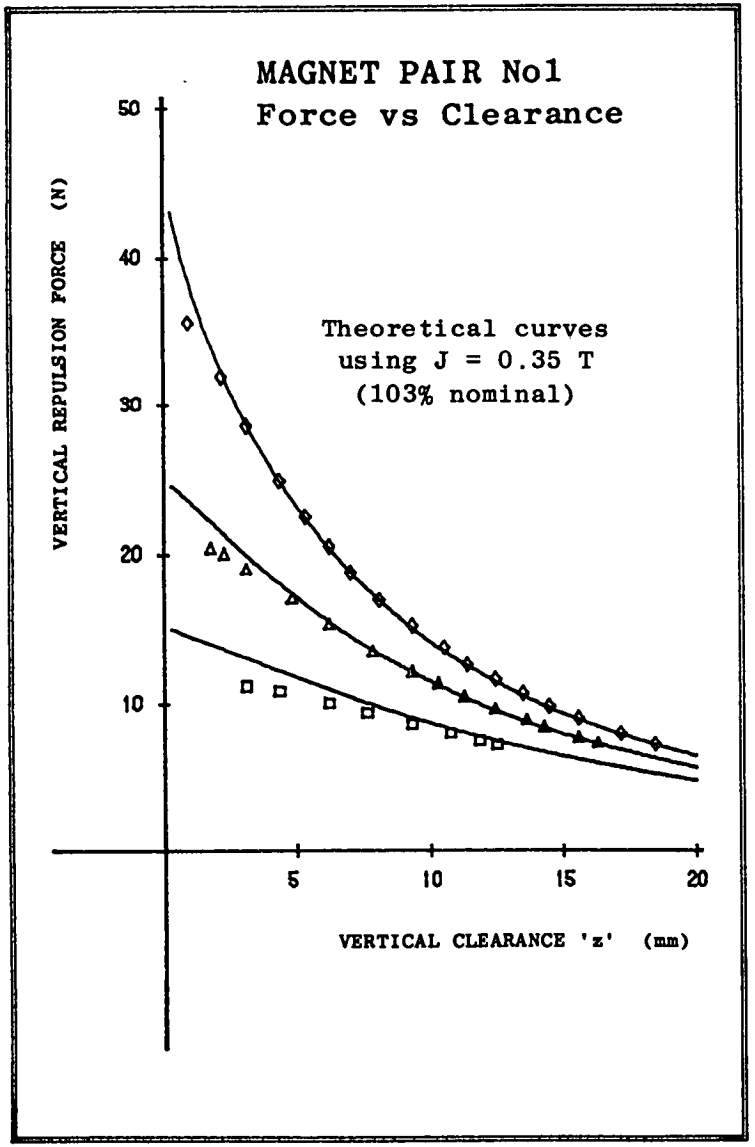
MAGNET PAIR No1
Force vs Clearance
VERTICAL REPULSION FORCE (N)
50
40
30
20
10
Theoretical curves
using J = 0.35 T
(103% nominal)
5
10
15
20
VERTICAL CLEARANCE 'z' (mm)

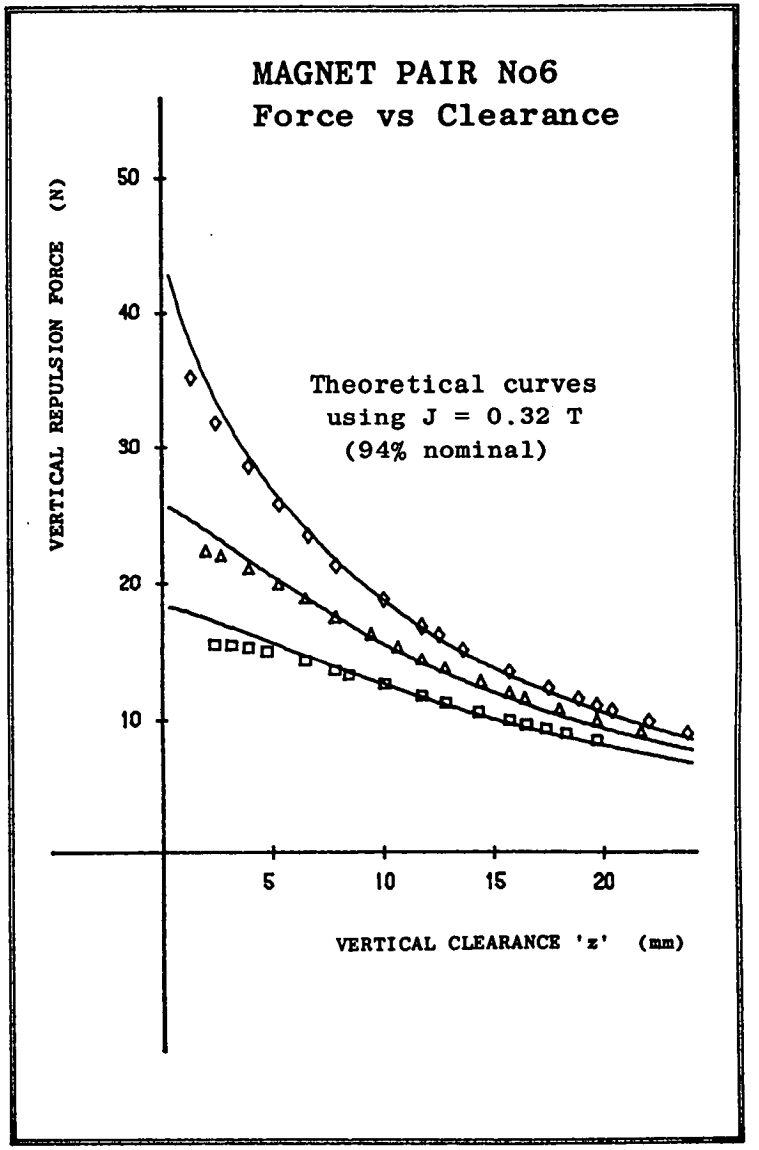
MAGNET PAIR No6
Force vs Clearance
VERTICAL REPULSION FORCE (N)
50
40
30
20
10
Theoretical curves
using J = 0.32 T
(94% nominal)
5
10
15
20
VERTICAL CLEARANCE 'z' (mm)

FIGURE 9.11

Assigning apparent-magnetisation values is a useful practical expedient for estimating repulsion force: once the apparent-J of a particular block is known, its geometric force characteristics otherwise accord well with theory. Measurement of a magnet's force/clearance curves provides the easiest way of determining its effective magnetisation (estimates based on external field strength are difficult to make). The necessary assumption in this procedure is that magnetisation is uniform throughout the material. This certainly seems to have been true for the magnets used in the present investigation.

9.7 Magnetic Stiffness

Vertical magnetic stiffness was found by numerical differentiation, using force curve data of the kind graphed in figures 9.9 - 9.11. For example, the resulting stiffness/clearance curves for magnet pair no.4 can be seen in figure 9.12. Stiffness curves for each of the six experimental magnet pairs were compared with theoretical calculations, based in all cases on apparent magnetisation values (see above). The curves were smoothed to overcome 'noise', using three point least-squares smoothing. All experimental curves showed the same very strong characteristic, visible in figure 9.12, that although at large clearances the correspondence between experiment and theory is quite good, it becomes progressively worse as clearance tends to zero, with experimental values falling well short of theory. The nonideality is provisionally attributed to reversible demagnetisation and/or non-uniform magnetisation.

Both effects would be most evident at pole-contact, when the highest adverse field strengths are experienced. Whatever the cause of the discrepancy, it is to be expected from the nature of the calculated stiffnesses. With zero lateral offset, stiffness theoretically tends to infinity as pole clearance tends to zero: real magnets must inevitably exhibit a shortfall under these conditions. For non-zero offset, with only partial

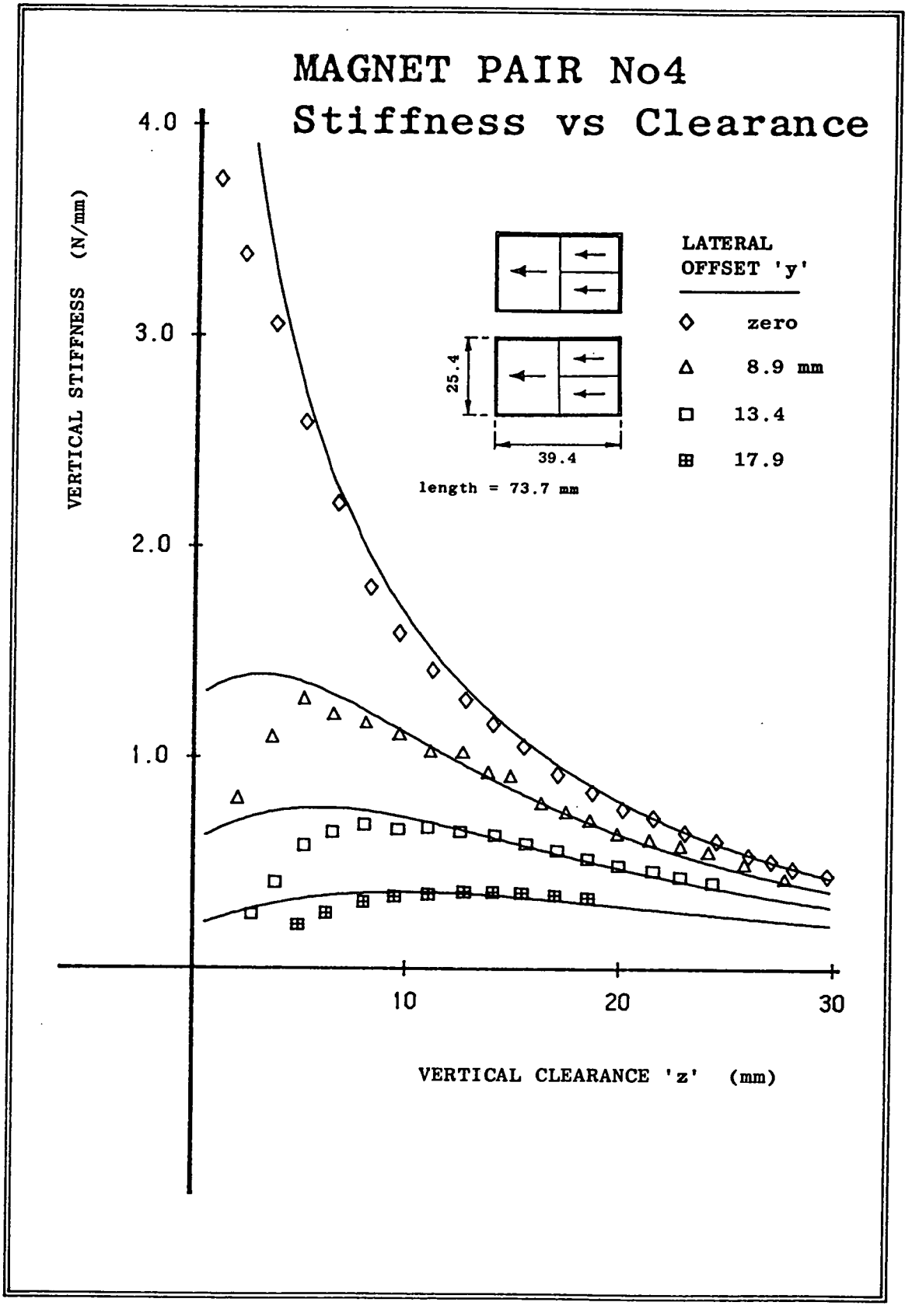
MAGNET PAIR No4
Stiffness vs Clearance
VERTICAL STIFFNESS (N/mm)
4.0
3.0
2.0
1.0
10
20
30
VERTICAL CLEARANCE 'z' (mm)
LATERAL
OFFSET 'y'
zero
8.9 mm
13.4
17.9
25.4
39.4
length = 73.7 mm

FIGURE 9.12

pole-overlap, the theoretical curves tend to finite limits (see figure 8.3): in such cases, it could then be argued that the magnet-pair represents the superposition of an ideal pair with zero pole-overlap, and a non-ideal pair with full pole-overlap, and the net stiffness falls short due to the contribution of the latter.

9.8 Demonstration of Non-Uniform Magnetisation

Non-uniform magnetisation is difficult to quantify, but can be illustrated by the results of the following experiment. A two-dimensional magnet pair comprising high-grade barium ferrite blocks was set up on the levitation-bed. The magnets were offcuts from the outer edges of much wider blocks, where a low magnetising field strength might have been expected during manufacture, resulting in locally non-uniform magnetisation.

Two sets of measurements were taken. In the first, vertical repulsion force was measured at a constant clearance, over a range of lateral offset values. The procedure was then repeated exactly, though after first rotating the upper magnet through 180° about its vertical axis. Its magnetic orientation was unchanged, and the overall configuration was to all intents the same as before. The two resulting curves of vertical force vs lateral offset appear together in figure 9.13(a). Each curve is symmetrical about its centreline, and the overall form of the two is identical. However, one of the curves has suffered an apparent lateral shift of about 4 mm. Figure (b) shows the effect of translating it 4.19 mm to the right: the resulting fit is excellent.

To account for the difference between the results, it is suggested that both magnets were non-uniformly magnetised, in such a way that each contained a 'dead-zone' of low magnetic

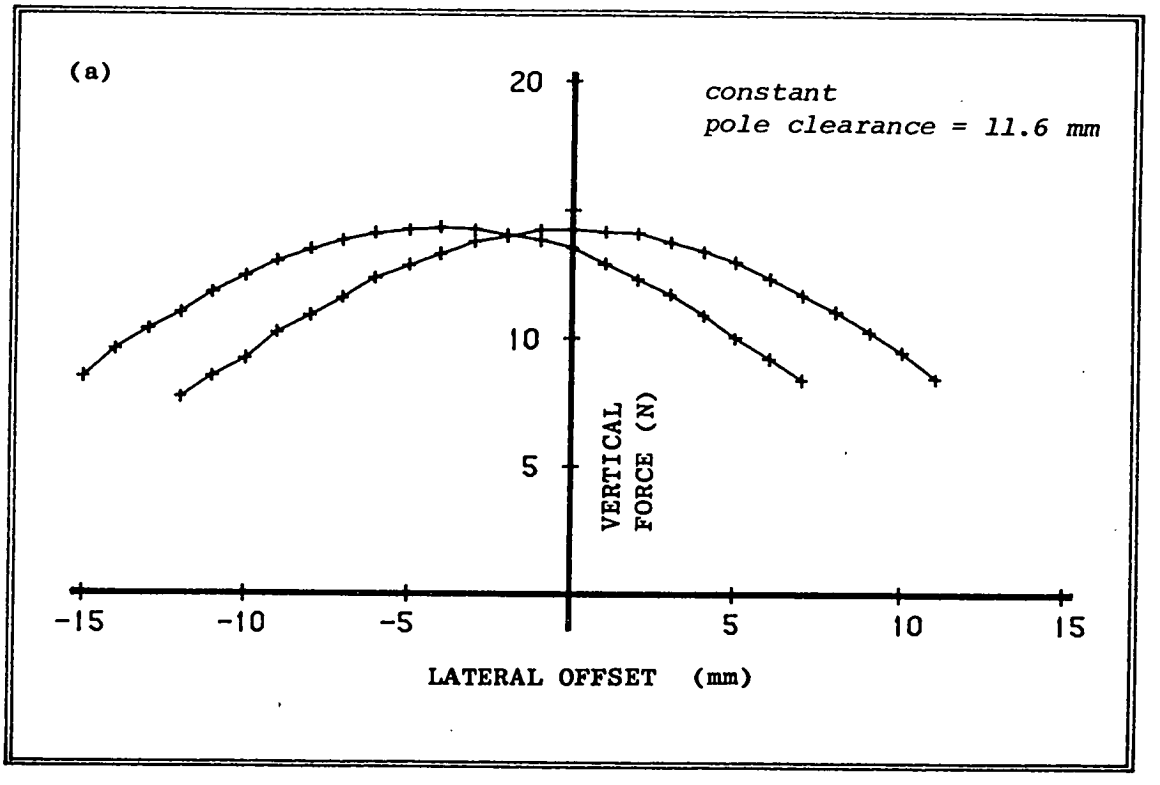

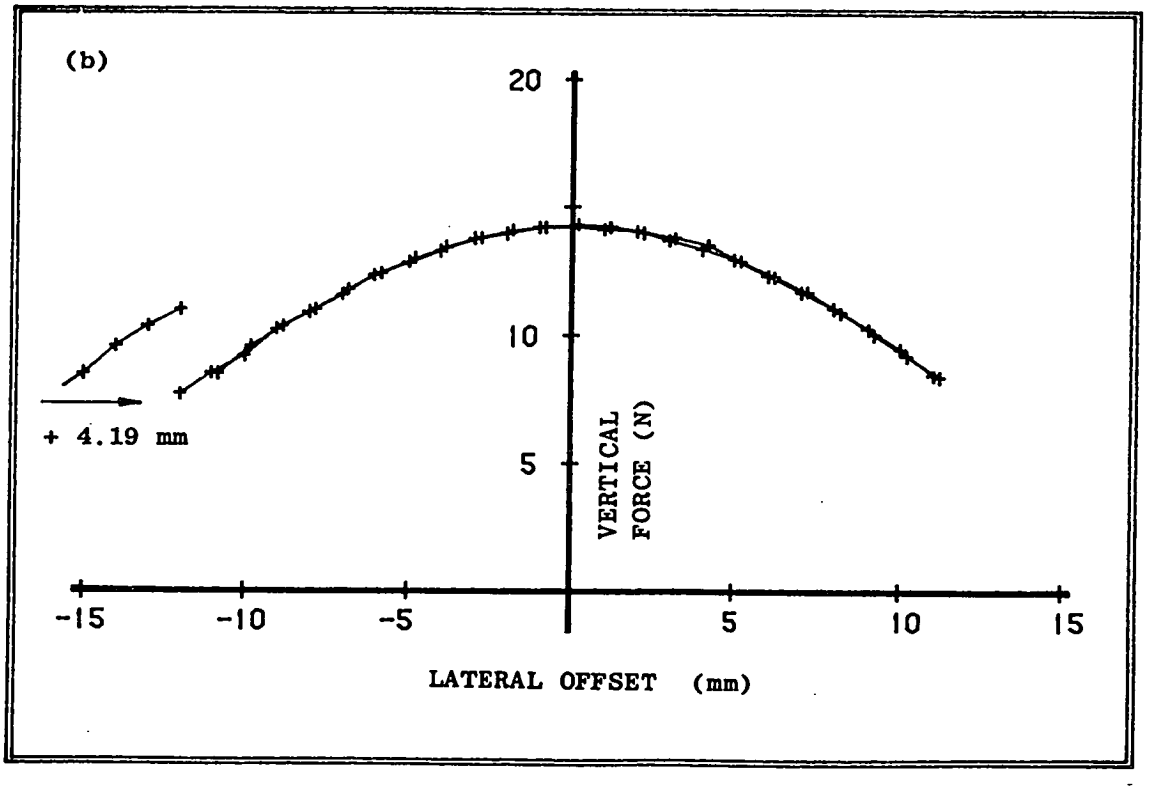

FIGURE 9.13
Demonstration of Non-uniform Magnetisation.
See section 9.8, also figure 9.14.

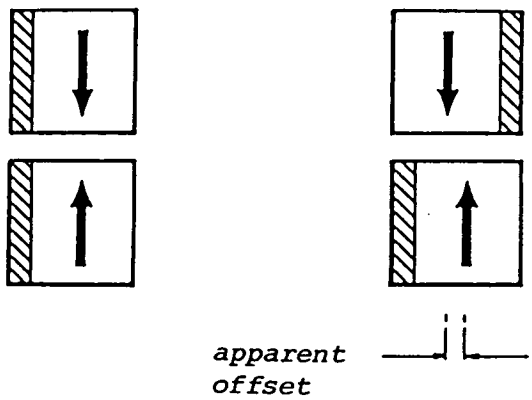

In both configurations, the magnet pair is in nominally perfect lateral alignment. However, the existence of non-magnetised 'dead zones' in the two blocks causes the right hand arrangement to behave as though a finite lateral offset existed. Maximum vertical repulsion is then only observed once a real offset, equivalent to the width of the dead zones, has been set (see figure 9.13).

FIGURE 9.14
Non-uniform Magnetisation

strength, as shown in figure 9.14. In the first experiment, the two dead-zones lined up, and the position of maximum vertical repulsion corresponded to that of zero nominal offset. In the second case, rotation of the upper block introduced a 'built-in' offset, and maximum repulsion was then only observed after the equivalent real offset.

The results of previous experiments using rare-earth cobalt magnets (Tsui et al, 1972, Craik and Harrison, 1974, and Yonnet, 1980) have shown better agreement with theory than those of the present work: the small size of the magnets used in these cases may well have allowed for a more uniform magnetising field during manufacture. However, in the design of a large-scale magnetic bearing such as that in the present case, allowance

must be made for the possibility of non-ideal magnetisation. The results of this study suggest that although ideal magnet assumptions allow repulsion forces to be predicted with some degree of confidence, they serve badly when calculating stiffness at small clearances. A future analysis is recommended in which allowances for non-uniform and reversible magnetisation would be included at the the theoretical stage, possibly by superposing ideal and non-ideal magnets, where the non-ideality would be clearance-dependent. For practical purposes, however, an empirical rule for the minimum 'safe' clearance at which theory holds good is noted at the end of section 9.10.

9.9 Optimum Geometries (1): Constrained Force/Length

The first procedure was an attempt to verify the theoretical results described in section 8.5. In this, and the subsequent, examination of constrained geometries, the optimum magnet aspect ratio b/c was sought for a fixed total area A (= 2bc), over a range of values of pole-clearance and offset.

Measured values of force/unit length F_z were normalised in this case by dividing by $A^{\frac{1}{2}}$. This choice of representative linear dimension is important: normalising is equivalent to scaling the representative dimension to unity (see section 8.4), and the results were thus scaled to represent those for magnet-pairs all of the same cross-sectional area, allowing direct comparison of the dependence on aspect ratio. In setting up each measurement, care was taken to observe geometric similarity of both pole clearance and offset: for example, in figures 9.9 - 9.11 it can be seen that offset y was incremented in amounts corresponding to 0.1 x $A^{\frac{1}{2}}$. Normalisation also included dividing by the magnetisation product J^2, where apparent magnetisation values (see above) were used throughout. The normalised results for this first comparison are presented in figures 9.15 and 9.16, as four curve 'families'.

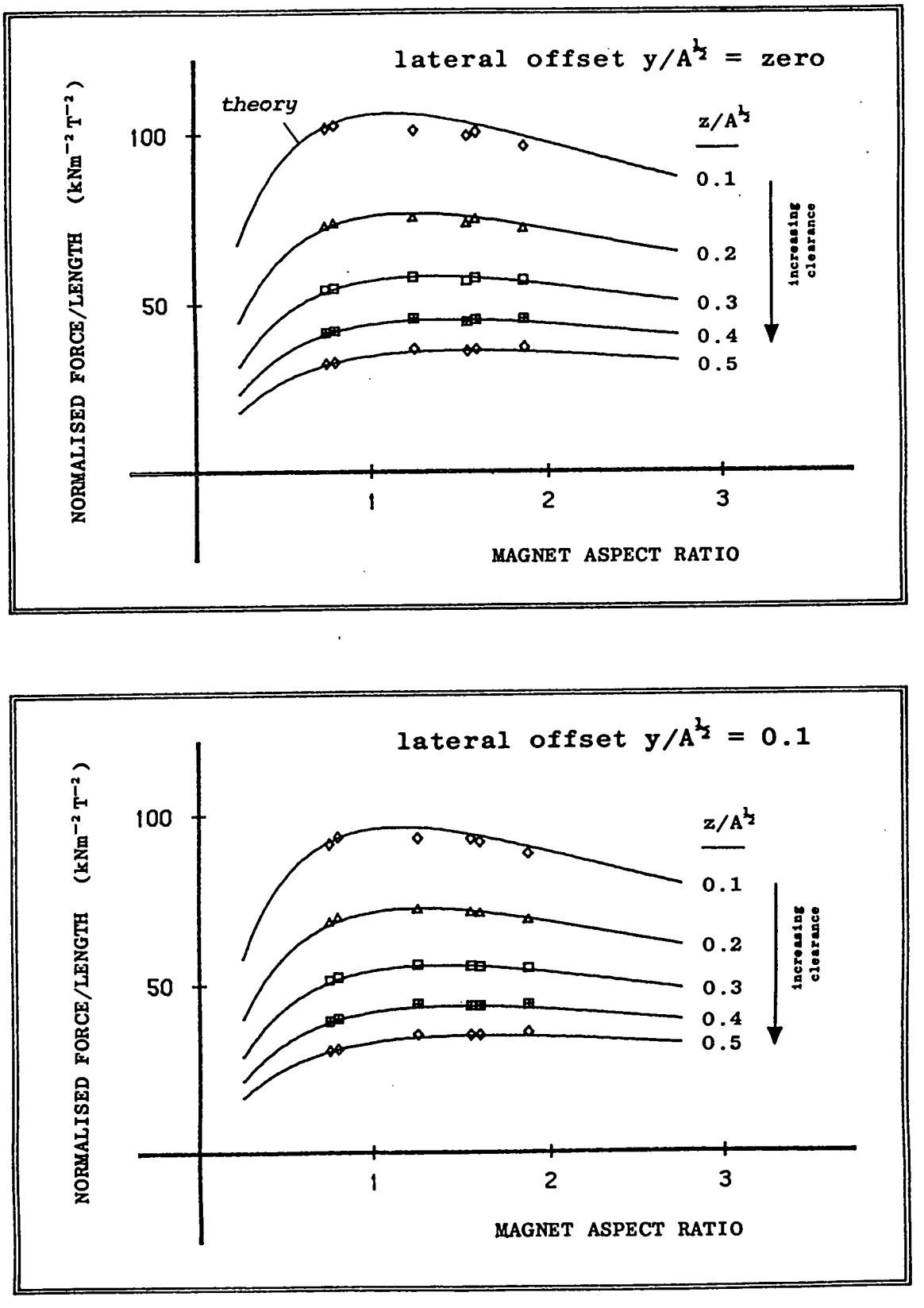

FIGURE 9.15
Experimental Results for Constrained Optimum Force/Unit Length (1). Each curve shows force/unit length as a function of magnet aspect ratio, for fixed cross sectional area, and constant pole-clearance and lateral offset. Theoretical comparisons are based on apparent-magnetisation. See also figure 9.16.

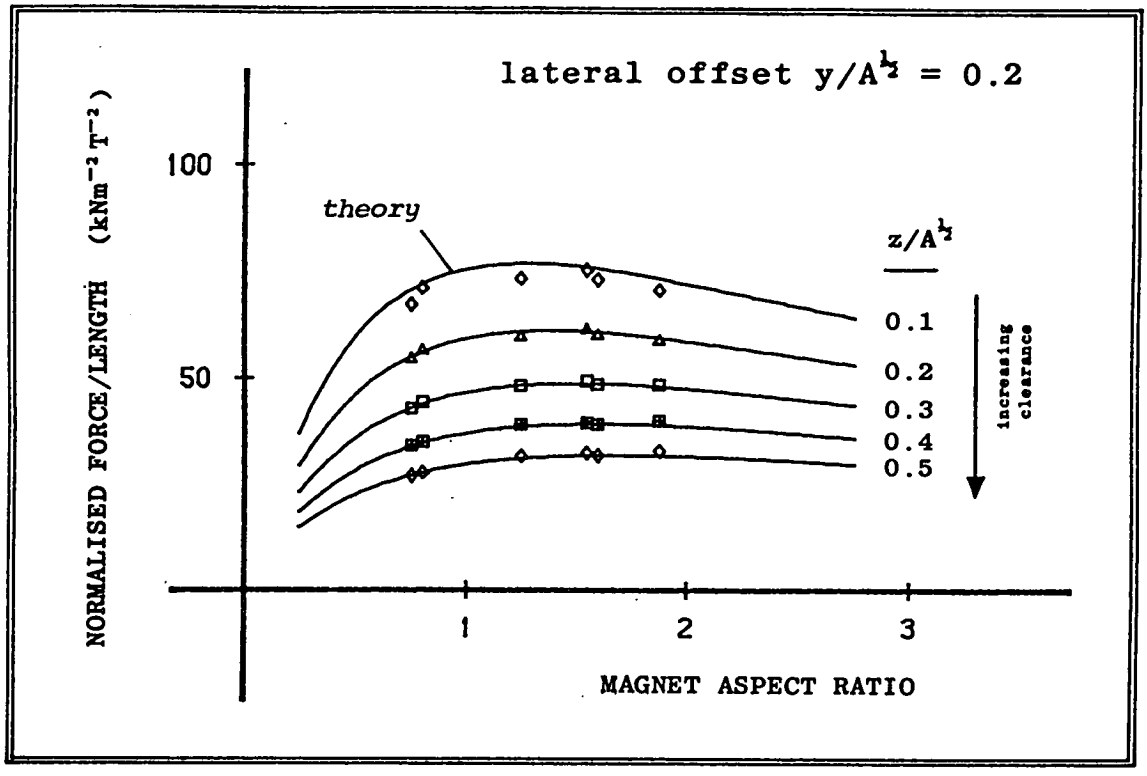

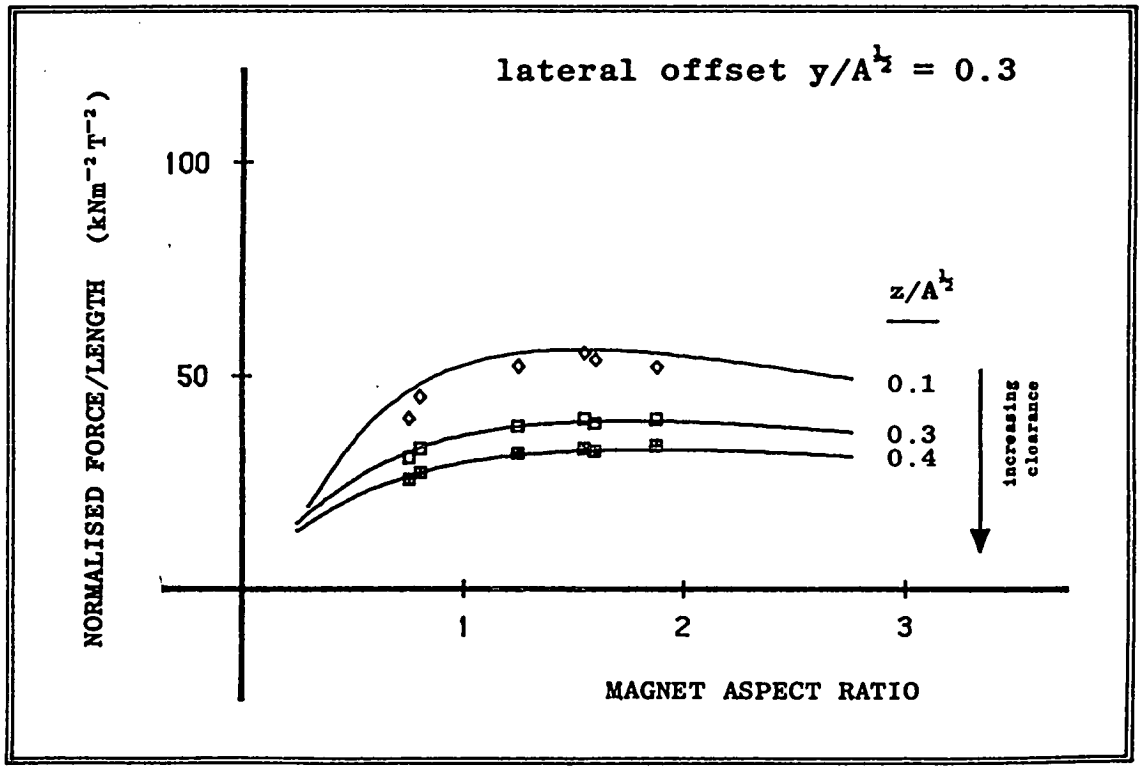

FIGURE 9.16
Experimental Results for Constrained Optimum Force/Unit Length (2).
See caption under figure 9.15.

Each individual curve in figures 9.15 and 9.16 shows available force/unit length F_z plotted against aspect ratio, for constant pole-clearance and offset. Each family comprises curves for several values of clearance (increasing downwards) at fixed offset, and the four families correspond to four offsets, including zero. The correlation between experiment and theory is in general good, and the following trends can be seen:

(1) With increasing lateral offset, maximum repulsion is obtained using higher aspect ratios.

(2) Although the optimum aspect ratio increases with increasing clearance, the curves flatten off, exhibiting less well-defined maxima.

The first observation is predicted from a comparison of figures 8.4 and 8.6, and can be interpreted as the need for a certain amount of pole-overlap to be retained as the magnets become offset. The flattening of the curves observed at increasing clearance is attributable to the nature of magnetic forces, which decrease with distance: whatever inverse-power law is obeyed, as pole separation increases, the magnitude of the incremental forces within a magnet will become more uniform, and exhibit less dependence on the block geometry. Hence a wider latitude is seen in the range of geometries able to provide near-optimum force.

9.10 Optimum Geometries (2): Constrained Stiffness/Length

The experimental comparisons in this case are analogous to those immediately above. For stiffness/unit length, however, no dimensional normalisation is required, as K_z is already scale-independent (see section 8.4). The experimental results are shown in figures 9.17 and 9.18.

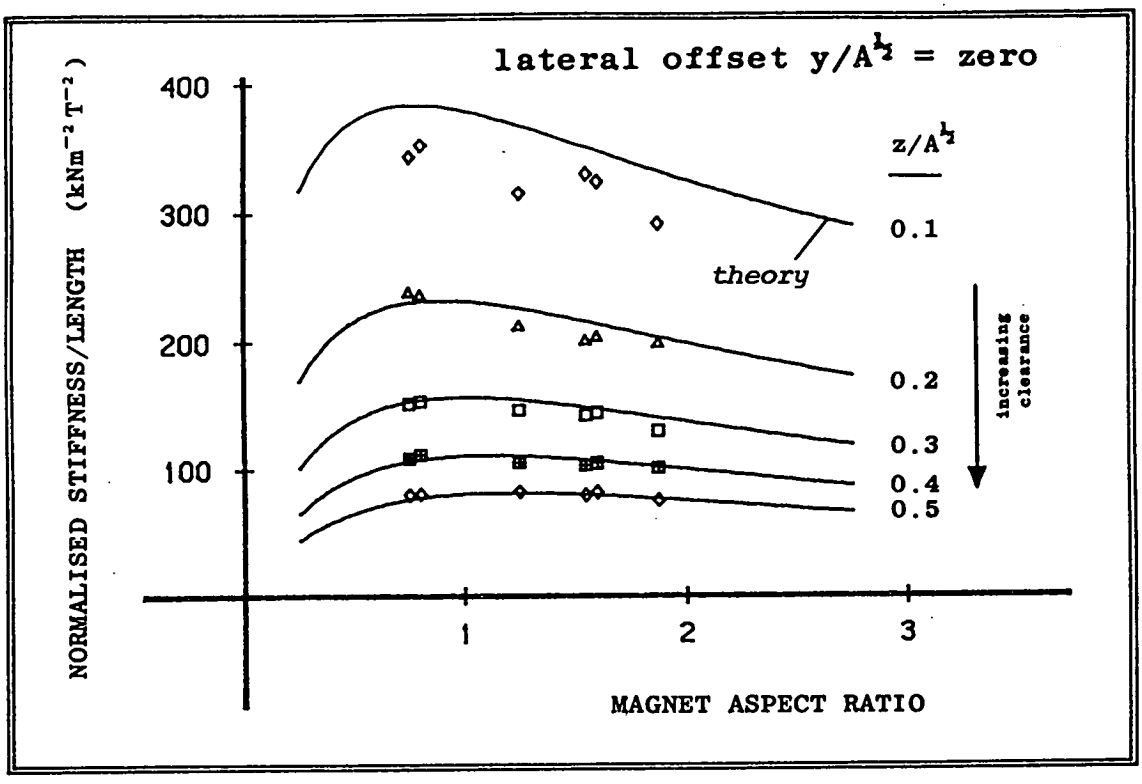

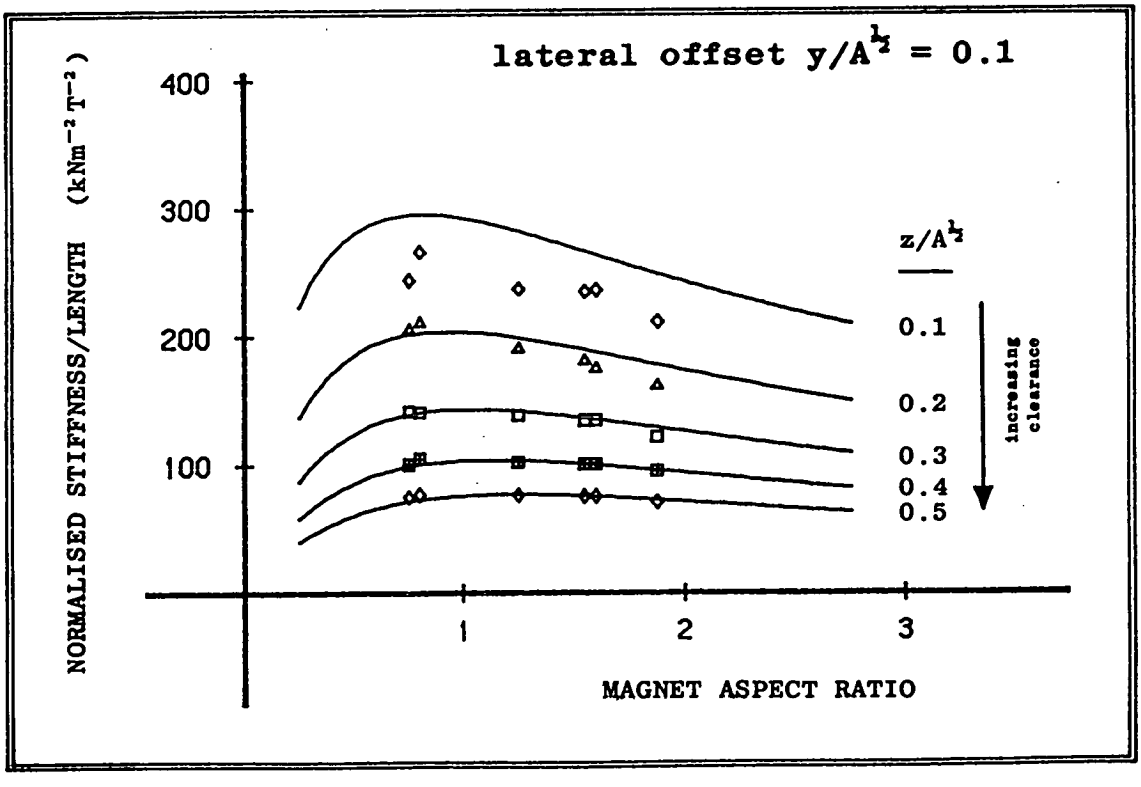

FIGURE 9.17
Experimental Results for Constrained Optimum Stiffness/Unit Length (1). Each curve shows stiffness/unit length plotted as a function of magnet aspect ratio, with total cross-sectional area, pole-clearance, and lateral offset all constant. Theoretical comparisons are based on apparent magnetisation. See also figure 9.18.

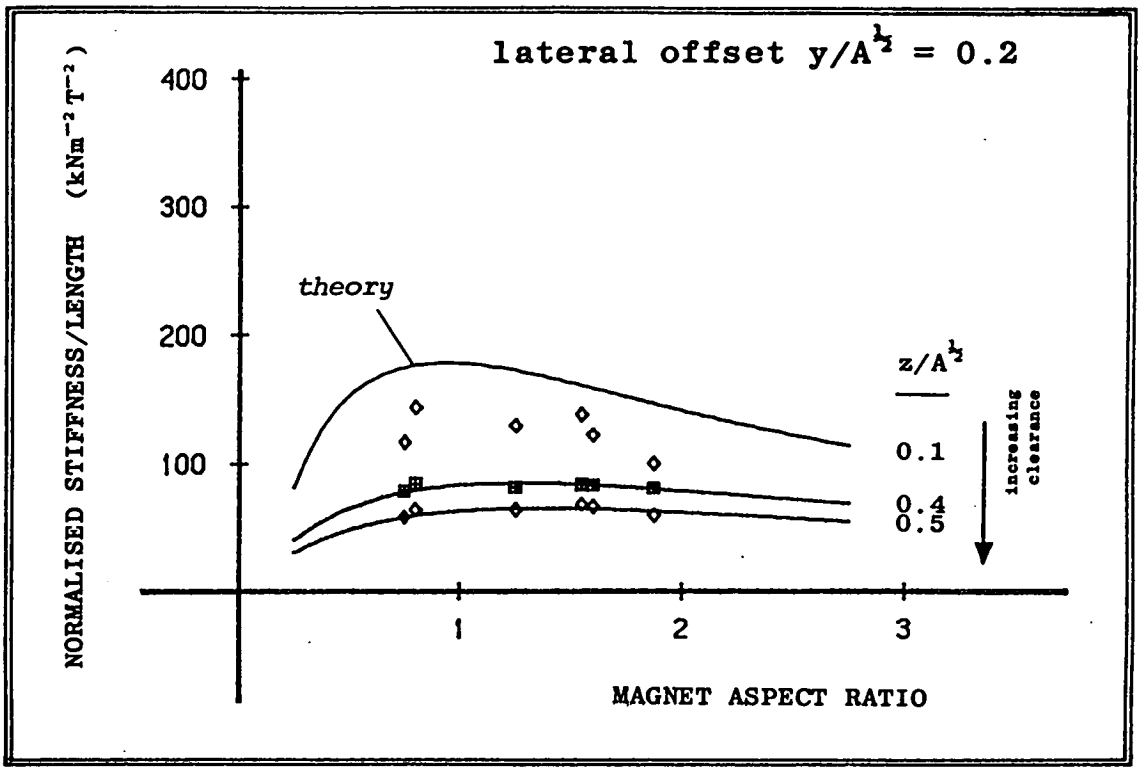

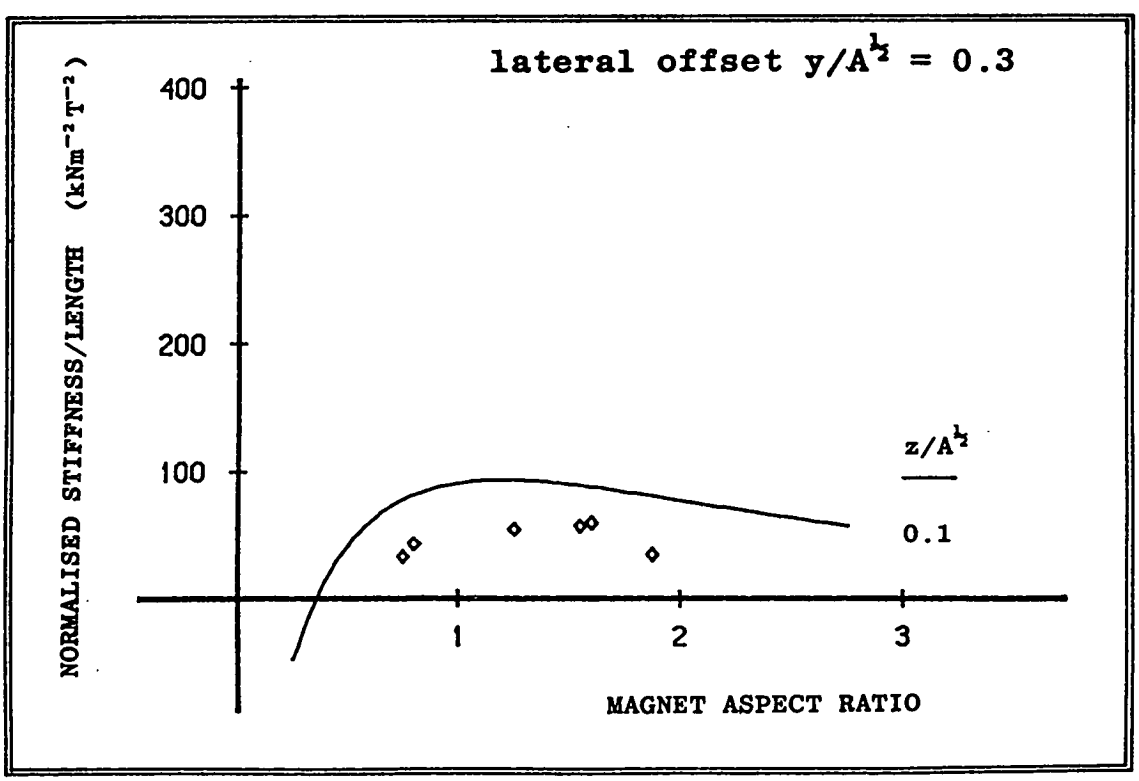

FIGURE 9.18
Experimental Results for Constrained Optimum Stiffness/Unit Length (2).
See caption under figure 9.17.

From figures 9.17 and 9.18 it is seen that:

(1) The same trends apply to stiffness/unit length as noted for force/unit length (see section 9.9).

(2) The shortfall in stiffness at small clearances is strongly in evidence.

In all cases, correlation with theory becomes good at a value of $z/A^{\frac{1}{2}}$ greater than about 0.3: this is therefore suggested as a criterion for confidence in theoretical stiffness calculations.

9.11 Optimum Geometries (3): Unconstrained Force/Volume

The results in this section correspond to the theoretical optimisation procedure of section 8.8. To verify unconstrained optimisation results, force/unit volume F_V requires to be investigated in terms not only of magnet shape, but also of size: this reflects the presence of two independent variables in the unconstrained geometry analyses. Clearly, without a vast selection of experimental magnets, magnet width and height can not be independently varied in practice. To circumvent this problem, the experimental procedure invoked a change of variables, from pole width b and height c, to aspect ratio b/c, and cross-sectional area 2bc.

Aspect ratio was varied, as before, by choosing from the six magnet geometries. Cross-sectional area was necessarily constant for each magnet-pair, and the method of 'effectively' varying it made use of the scaling laws. By using the clearance as representative linear dimension, measured values of F_V were normalised to represent measurements made at constant clearance, but with magnets of varying cross-sectional area. Normalisation involved multiplying measured F_V by z (see section 8.4). This scaling technique is explained graphically in figure 9.19, and the experimental results are shown in figures 9.20 - 9.22.

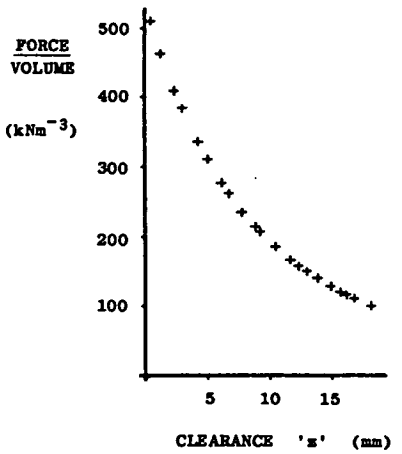

ORIGINAL DATA is force/unit volume for a magnet pair of constant size and increasing pole clearance.

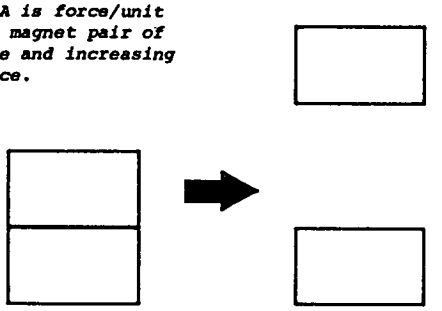

In the initial experiment, the force vs clearance curve is recorded for a fully aligned, symmetric, magnet pair. Because the magnets' volume is necessarily constant, the resulting curve can be plotted as above, as force/unit volume vs clearance. The diagram on the right shows the variation in pole clearance during the experiment.

In order to leave the above results independent of scale, and also effect a tranform of variables, the results are now normalised. Each value of force/unit volume is multiplied by the clearance at which it was measured, while the clearance itself is replaced by the dimensionless ratio of the square root of magnet cross-sectional area to clearance, ie. √(area)/z. The resulting normalised curve is shown below.

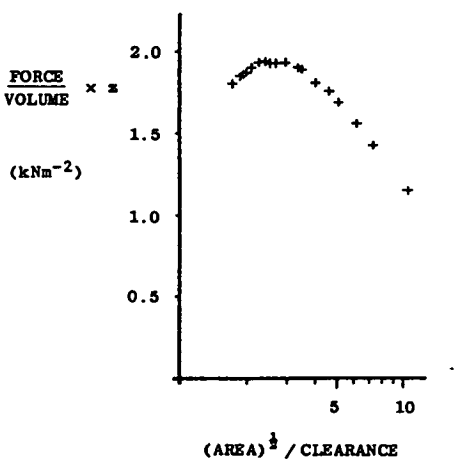

NORMALISED DATA is force/unit volume at a constant clearance, using a magnet pair of increasing size.

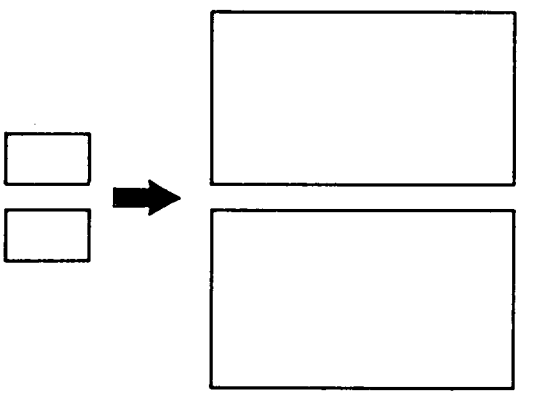

Normalising the results is equivalent to scaling them to represent those which would have accrued had the normalising linear dimension been unity (see section 8.4). In the present case the representative dimension is the clearance, and hence the original data can be replotted as force/unit volume measured at constant clearance, for a magnet pair of increasing size (above, right).

The normalised curve exhibits a well-defined maximum, which corresponds to the optimum ratio of magnet size to pole clearance to yield maximum force/unit volume using magnets of this particular aspect ratio. To investigate the dependence on aspect ratio, it is then necessary to repeat the experiment with magnets of several different cross-sectional geometries. The results of such experiments are shown in figures 9.20 - 9.22.

FIGURE 9.19
Results Normalisation. How the scaling laws are used to effect a change of variables.

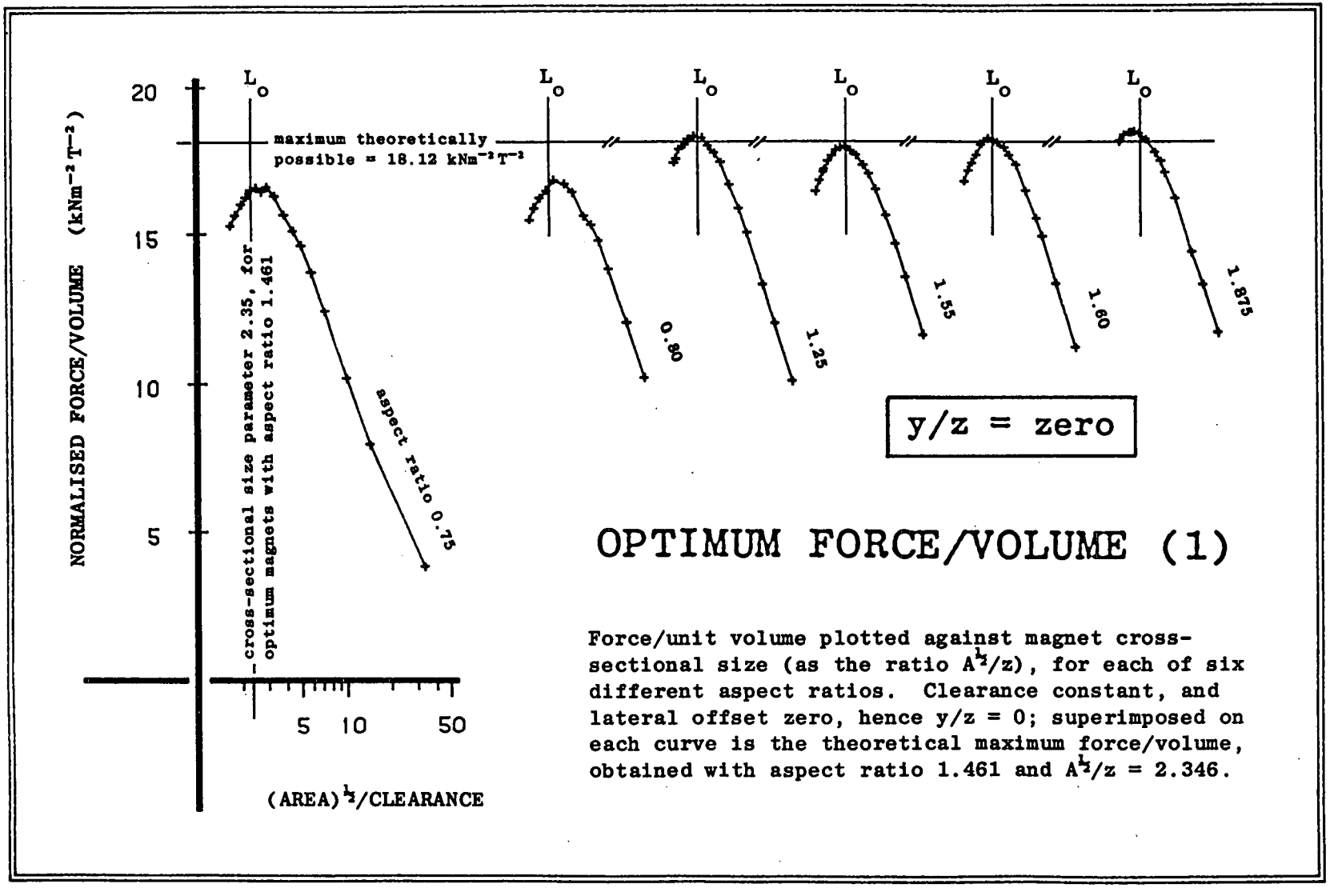

OPTIMUM FORCE/VOLUME (1)

Force/unit volume plotted against magnet cross-sectional size (as the ratio $A^{\frac{1}{2}}/z$), for each of six different aspect ratios. Clearance constant, and lateral offset zero, hence y/z = 0; superimposed on each curve is the theoretical maximum force/volume, obtained with aspect ratio 1.461 and $A^{\frac{1}{2}}/z = 2.346$.

FIGURE 9.20

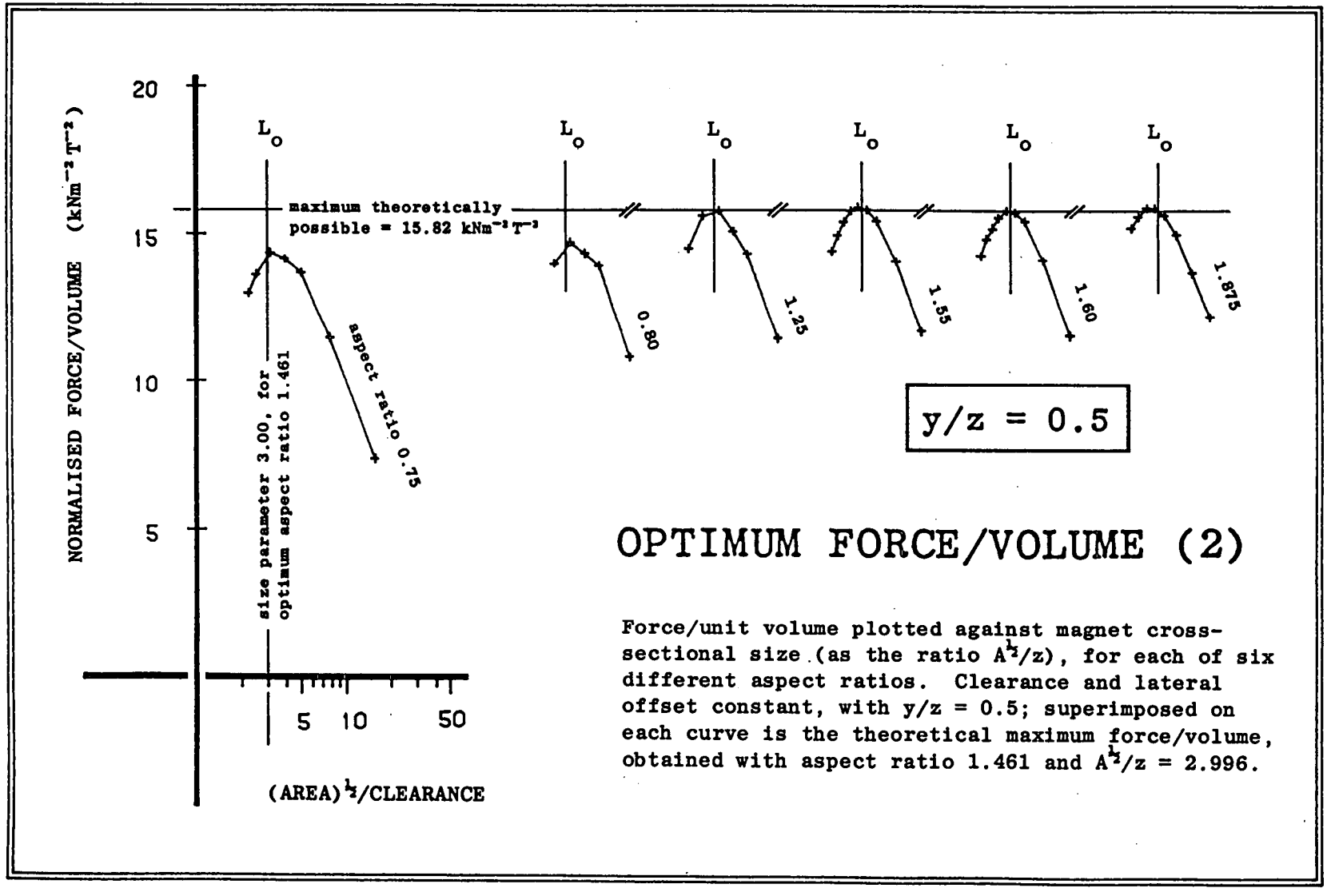

OPTIMUM FORCE/VOLUME (2)

Force/unit volume plotted against magnet cross-sectional size (as the ratio $A^{\frac{1}{2}}/z$), for each of six different aspect ratios. Clearance and lateral offset constant, with y/z = 0.5; superimposed on each curve is the theoretical maximum force/volume, obtained with aspect ratio 1.461 and $A^{\frac{1}{2}}/z = 2.996$.

FIGURE 9.21

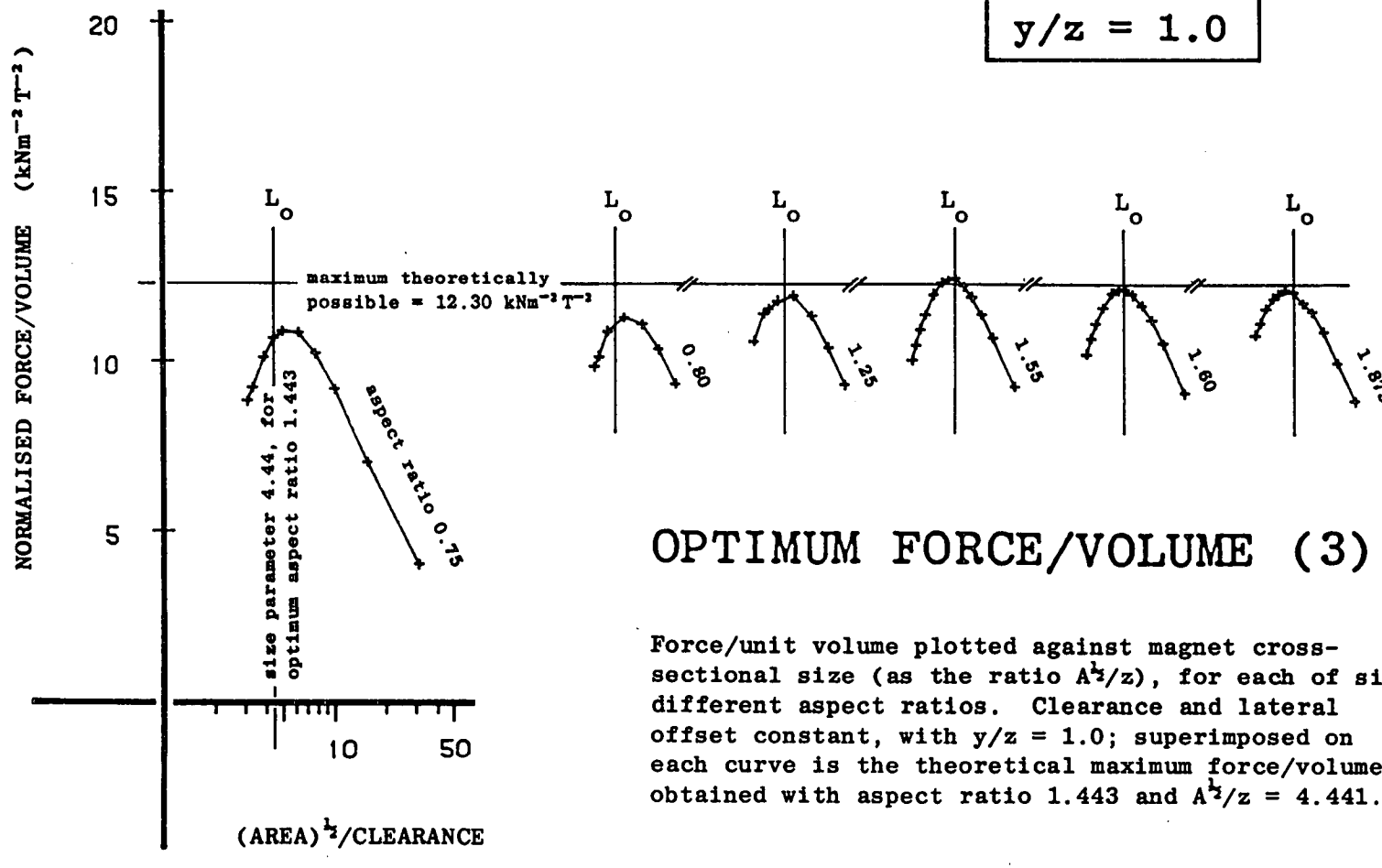

OPTIMUM FORCE/VOLUME (3)

Force/unit volume plotted against magnet cross-sectional size (as the ratio $A^{\frac{1}{2}}/z$), for each of six different aspect ratios. Clearance and lateral offset constant, with y/z = 1.0; superimposed on each curve is the theoretical maximum force/volume, obtained with aspect ratio 1.443 and $A^{\frac{1}{2}}/z = 4.441$.

FIGURE 9.22

Each of figures 9.20 - 9.22 shows six curves, plotted against the same axis set, which is repeated across the page: this is to allow comparison of curve maxima. Note that the curves are formed by joining experimental points, and are not theoretical fits. All six curves in a given figure correspond to measurements at a single value of the ratio y/z. Figure 9.20 shows the results for centred magnets, where y/z equals zero. Each individual curve shows F_V plotted against cross-sectional size (increasing from left to right) for a given aspect ratio. The relative efficiency of different aspect ratios is seen by comparing curves. The theoretical overall-maximum force/unit volume F_V for each value of y/z is marked against each curve, with the axis L_O giving the corresponding optimum size ratio. The results show that:

(1) There is little to choose between aspect ratios in the range 1.25 to 1.875, which straddle the theoretical optimum in all three cases.

(2) Prediction of the optimum magnet size is very good indeed, as demonstrated by the proximity of the curve maxima to the axis L_O, for aspect ratios close to the theoretical optima.

(3) There is practically no shift in the optimum aspect ratio over a range of y/z values 0 - 1.0.

The uniformly high efficiency noted in (1) above is in keeping with the theoretically predicted insensitivity of force/unit volume to aspect ratio (when near the optimum), as discussed in section 8.8. The negligible shift in optimum aspect ratio b/c in the range y/z = 0 - 1.0 is as predicted by the flatness of the appropriate curve in figure 8.13. It may be noted that the entire contents of figures 9.20 - 9.22 represent experimental verification of only three points on the theoretical curve in figure 8.12.

9.12 Optimum Geometries (4): Unconstrained Stiffness/Volume

The results in the final case correspond to the analysis in section 8.9. The same use was made of the scaling laws as above (see figure 9.19), except normalisation was this time achieved by multiplying by clearance squared, according to the rules noted in section 8.4. Only the case of fully-aligned magnets ($y/z = 0$) was considered. The results are shown in figure 9.23, where the format is that used previously in figures 9.20 - 9.22 (see section 9.11). The important features are:

(1) None of the curves is sufficiently complete to show a maximum, with all displaying a marked one-sidedness. The results are less conclusive than those for maximum force/volume.

(2) Notwithstanding (1) above, trends are observable in the results which suggest that the theoretical optimum aspect ratio and cross-sectional size are correct.

The one-sided appearance of the experimental curves is due to an experimental limitation: the leftmost point on each curve represents the maximum clearance at which a measurement could be made. Beyond this (leftwards) the supported magnet-weight alone outstripped available vertical repulsion force. Significantly, the magnet-pair with aspect ratio 0.75, which yielded the most complete curve, was the smallest of the six experimental pairs (see figure 9.6). Because of this, it was able to exert higher absolute values of force/unit volume than the other pairs, at equivalent relative values of clearance (ie. in proportion to cross-sectional size). Expressed differently, if the experiments were to be repeated with magnets half the size of those actually used, well-defined maxima would probably be seen for all six curves. This graphically illustrates the way in which material efficiency improves as magnet size decreases. Although the lack of maxima leaves (2) above open to question, the theoretical curves corresponding to figure 9.23 are shown in figure 9.24, and these tend to support the suggested trends.

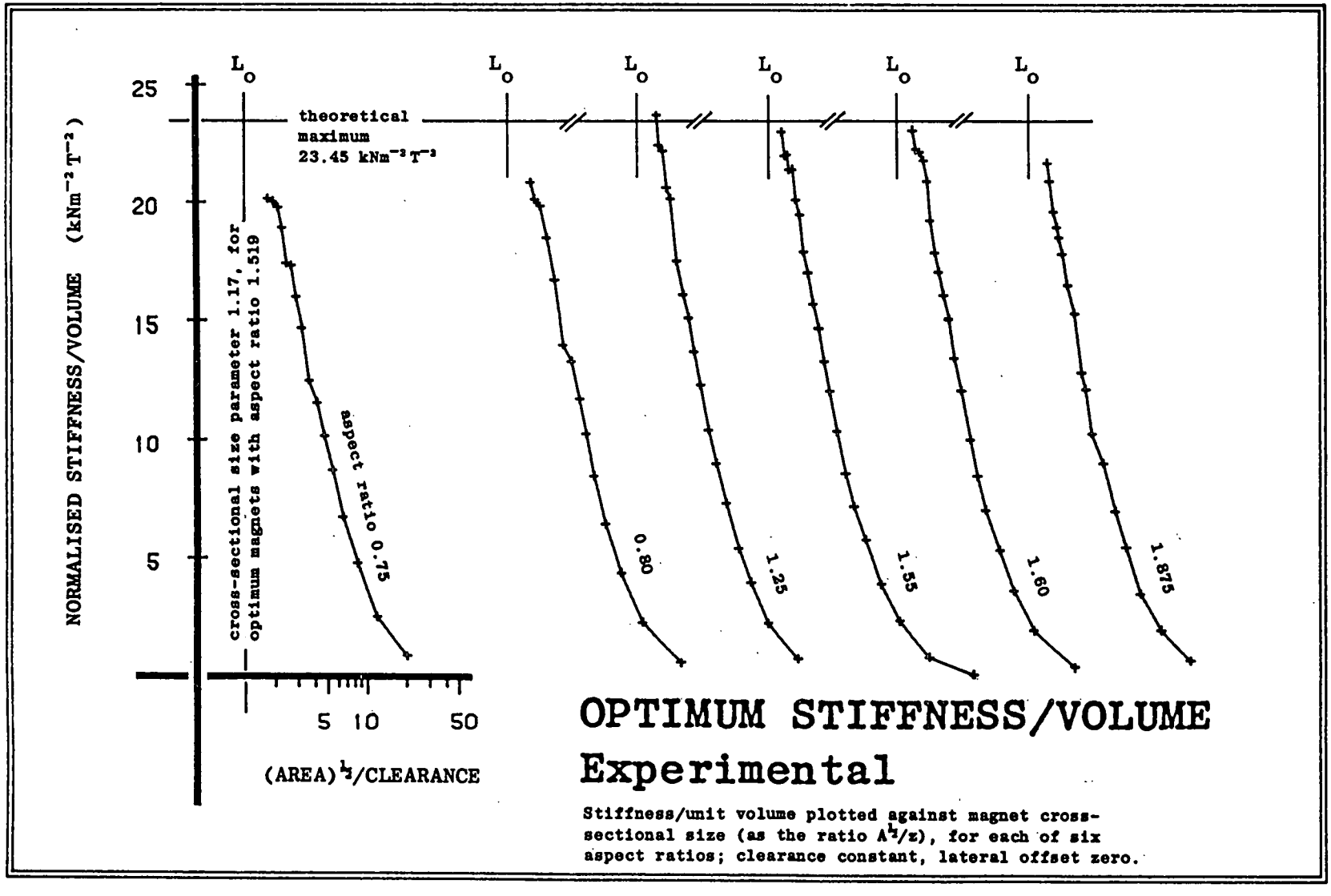

Stiffness/unit volume plotted against magnet cross-sectional size (as the ratio $A^{\frac{1}{2}}/z$), for each of six aspect ratios; clearance constant, lateral offset zero.

FIGURE 9.23

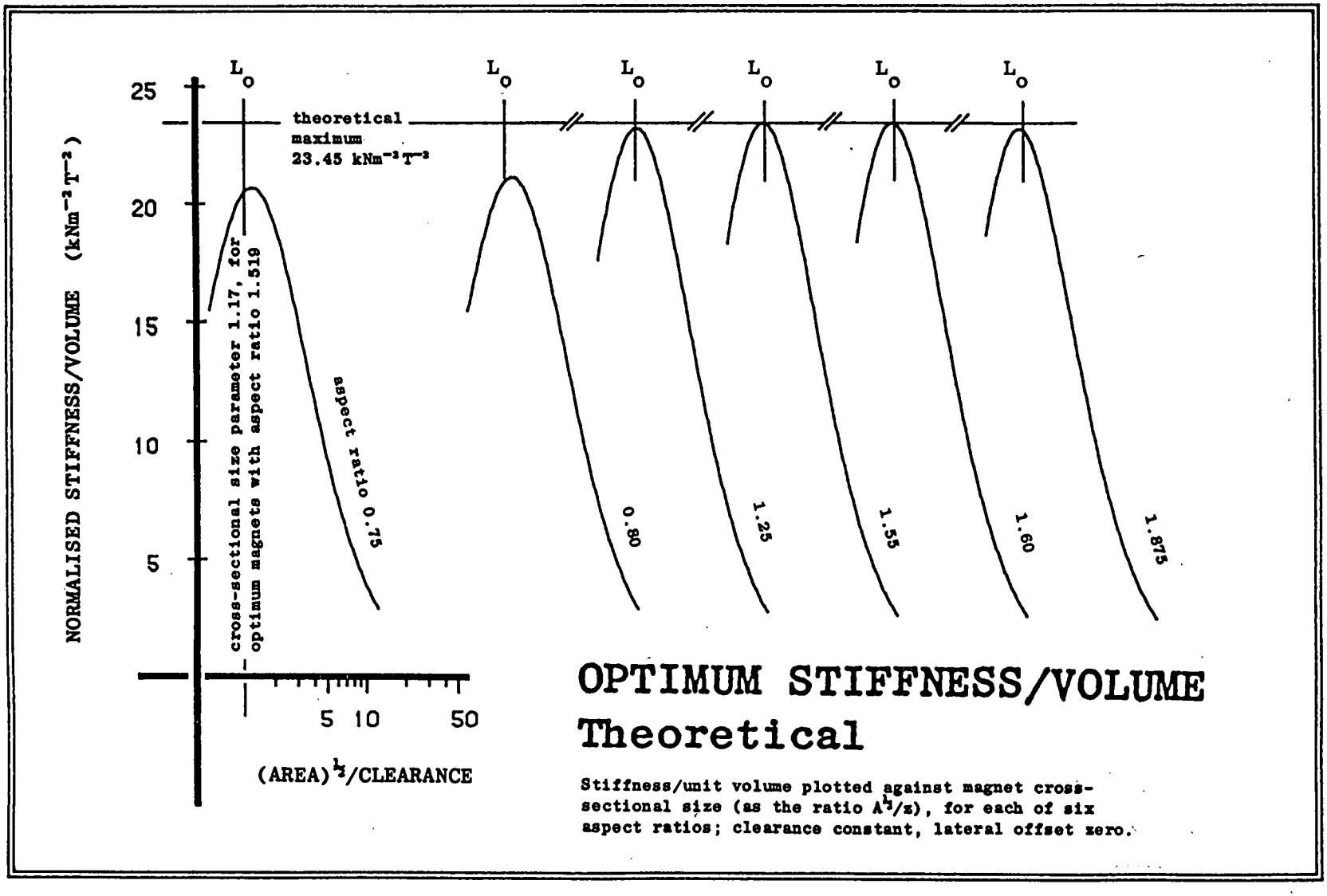
NORMALISED STIFFNESS/VOLUME (kNm⁻³T⁻²)
25
20
15
10
5
L_o
theoretical maximum 23.45 kNm⁻³T⁻²
cross-sectional size parameter 1.17, for optimum magnets with aspect ratio 1.519
aspect ratio 0.75
0.80
1.25
1.55
1.60
1.875
5 10 50
(AREA)^½/CLEARANCE
OPTIMUM STIFFNESS/VOLUME
Theoretical
Stiffness/unit volume plotted against magnet cross-sectional size (as the ratio A^½/z), for each of six aspect ratios; clearance constant, lateral offset zero.

FIGURE 9.24

9.13 Conclusions

The experimental evidence presented in this chapter suggests that the ideal-magnet assumptions of constant and uniform magnetisation make possible useful calculations of magnetic force and stiffness, and prediction of optimum geometries, provided that the following precautions are noted:

(1) Non-ideal magnetisation must be allowed for under certain circumstances. However, magnets of the type used in this study can be successfully 'calibrated' and a value of apparent magnetisation assigned, which replaces the nominal value.

(2) Using apparent magnetisation values, the repulsion force for a given magnet geometry can be estimated from theory with a fair degree of accuracy, typically better than 5%, except near pole contact, where a figure of 10-15% would apply.

(3) The above rule does not apply to theoretical calculations of stiffness. These are more liable to underpredict the effects of non-ideal magnetisation, especially near pole contact. An empirical rule, based on the results of the present study, is that confidence in theoretical stiffness will be as good as in force (assuming calibrated magnetisation in both cases) only when the magnets' pole clearance exceeds about 0.3 times the square root of their combined cross-sectional area.

Despite the phenomenon of non-ideal magnetisation, the experimental results tend to reaffirm the theoretical optimum geometries predicted in chapter 8, for the four analyses dealing with an isolated two-dimensional magnet pair. However, it should be noted that real magnet pairs optimised for maximum stiffness might, if non-ideal magnetisation were taken into account in the optimisation scheme, require different dimensions from those predicted in this study.

On a practical note, the technique of transforming experimental variables, by appropriate use of the scaling laws for magnetic force, proved highly successful.

CHAPTER 10
SUMMARY AND CONCLUSIONS

10.1 Performance Characteristics of the Proposed Bearing

The design of a novel bearing for use in the Salter 'duck' wave energy converter has been described, and a preliminary analysis made of its operating characteristics. The bearing works by combining the principles of self-pressurising fluid lubrication, using seawater as the lubricant, and passive permanent magnet repulsion. Although this combination of features is unusual, each represents a well-tried bearing mechanism, and the proposed design brings the two together in an attempt to meet a unique specification, calling for continuous operation for 25 years in a marine environment. The intended characteristics of the bearing include very low friction, evenly distributed loading with low fluid pressures, compliance, and the ability to withstand low non-reversing loads indefinitely, and much larger cyclic loads for periods greatly in excess of their maximum reversal time.

The lubrication-theory analysis in chapter 4 suggests that the proposed bearing can comfortably achieve these characteristics, provided that the appropriate constructional details, which at this stage are assumed, can be economically realised. Furthermore, in a reassessment of the bearing's performance (chapter 5) taking into account effects neglected by lubrication theory, load enhancement is predicted due to both turbulence and fluid inertia; even assuming turbulent lubrication, however, the maximum frictional power loss is estimated as less than 0.1% of the duck's rated output. One particular aspect of fluid inertia, the so-called 'indirect' effect, is highly significant, potentially offering a large increase in load capacity, as well as an asymmetric bearing response to cyclic loads. Asymmetric response is necessary to avoid large bearing offsets due to the non-reversing component of wave loads.

The indirect effect of fluid inertia takes the form of a static pressure imbalance occuring across the compliant sheet which bounds the compressible bearing lining (attached to the inner surface of the duck). As a result of the imbalance, the lubricating film thickness is controlled not only by stiffness, but by the dynamics of the fluid flowing between the lining and the film. To investigate the magnitude of the effect, a simplified flow model is proposed, in the form of axisymmetric radial flow between two parallel discs, either diverging from, or converging towards, a central orifice. Experimental results, described in chapter 6, suggest that the minimum dimensionless pressure drop across such a discharging orifice is a linear function of reduced Reynolds number, with the constant of proportionality in fair agreement with previous estimates. The results also demonstrate the asymmetry of the effect (no equivalent pressure drop occurs across a recharging orifice), and the additional head losses which can arise with sharp angled inlet profiles. This last feature is attributed to flow separation.

10.2 The Magnetic Repulsion System

Although the use of permanent magnetic repulsion to enhance a compliant hydrostatic bearing is unorthodox, the combination is, at least technically, ideal in the present application. Apart from the necessary axial alignment system, the mechanism can be entirely non-contacting, and thus not susceptible to wear. It is the scale of the required bearing which makes the solution attractive, with the lubricating film thickness dictated by magnetic repulsion to be proportionally the same as in a small-scale squeeze film bearing, but with a load capacity proportionally very much greater. However, it is also the scale which raises the strongest question regarding the viability of the bearing. A single duck/spine module might require between twenty and sixty tonnes of permanent magnets, and it remains to be proved whether mass production of fairly crude magnets in the required numbers would be an economic proposition.

The magnet optimisation analyses in chapter 8 are all based on the assumption of ideal 'hard' magnet characteristics, and yield results applicable to passive permanent magnet bearings on any scale, not solely that of the duck bearing. A summary of the more important solutions appears in table 8.1 (p. 147). The results are intended to allow selection of optimum magnet size and shape for any given requirement in which an isolated magnet pair interaction can be assumed. Several of the results are updates of previous estimates, on which they improve through the use of computer numerical optimisation techniques. The experimental observations described in chapter 9 tend to confirm the theoretical optimum geometries, but also highlight the deviations from ideality which may occur with real magnets. A method of 'calibrating' permanent magnets is suggested.

10.3 Bearing Feasibility

The conclusion of this study is that the proposed duck bearing would be capable of meeting the specification given in chapter 3, provided that certain objectives, which have not yet been examined, can be met. Of these, perhaps the most important is to demonstrate that the cost of the permanent magnet repulsion system, including its axial alignment mechanism, will be realistic. It has been shown in chapters 7 and 8 that the better the axial alignment which can be achieved with the magnets, the smaller they can be. A system in which a lateral offset of 3 mm could occur might require a total magnet weight an order of magnitude greater than a (hypothetical) system in which perfect alignment could be guaranteed (see section 8.13). It would therefore be wise to invest considerable effort in perfecting the design of the alignment mechanism.

Other factors must be considered, not least the many construction details, and the choice of suitable materials (briefly considered in chapter 3). Although the advantages of ferrite magnets were propounded in chapter 7, the effects of a

25 year immersion in chlorinated seawater on the strengths and stiffnesses of suitable materials for the compliant bearing lining remain to be assessed. Methods of attaching the permanent magnets to the semi-rigid sheet, and to the spine surface, must also be investigated, and detailed designs forwarded for the magnet sheet itself, the compressible foam cells, the axial leakage impedances at the ends of the bearing, etc. Overall bearing assembly and disassembly, on station if necessary, has to be carefully planned.

10.4 Suggestions for Further Work

In section 5.9 there was described an analysis, based on the work of previous authors, which might yield more accurately the lubrication characteristics of the proposed bearing. The main advantage of the technique is to allow for a more realistic model of the orifice discharge flows into the lubricating film, including the pressure depressions which occur as a result. However, although this analysis is strongly recommended, it would be unable to account for the possibilities of turbulent lubrication, which is very likely to occur, and variation in the lubricating film thickness, which is essential for exploitation of the 'indirect' effect of fluid inertia. A mathematical model which takes account of the latter would be very useful indeed, as the influence of fluid inertia was seen in chapter 5 to offer a potentially large decrease in the amount of magnetic material required.

Another possibility which should perhaps be considered is a bearing with no magnets at all, in which the low non-reversing loads were supported by rolling elements of some form, but with the cyclic loading supported in exactly the same way as in the current design. The changeover from one load supporting mechanism to the other could be based on the roller cage proposal illustrated in figure 3.2 (chapter 3), although it is to be emphasised that this new design would support the high reversing loads entirely by fluid lubrication. Some degree of

wear would inevitably occur on the rolling elements, but only under conditions of light loading; the advantages would include no need for magnets or an axial alignment system, and hence much lower cost. Alternatively, a study should be carried out to find a method of producing ferrite magnet blocks in much higher numbers, but to much lower tolerances (eg. without surface grinding) than at present. The raw material costs of magnets do not dominate, and the aim would be to emulate the production of bricks.

Finally, the need for a representative experimental model is clear. This would not initially be required to simulate the conditions of the full bearing specification, but simply to demonstrate the enhancement of a self-pressurised hydrostatic bearing by permanent magnet repulsion. Happily, this objective is now being actively pursued.

REFERENCES

Archibald, F. R. (1956): "Load Capacity and Time Relations for Squeeze Films", Trans. ASME, vol. 78, p. 29-35, Jan. 1956.

Baran, W. (1962): "Die Berechnung von Anziehungs- und Haftkraften für magnetisierte Korper quaderförmiger Gestalt", Zeits. für Angewandte Phys., vol. 14, p. 272, 1962.

Baran, W. (1964): "Zur Bestimmung der Kräfte bei Magneten mit starrer Magnetisierung", Zeits. für Angewandte Phys., vol. 17, p. 194-6, 1964.

Baran, W. (1971): "Optiemierung eines permanentmagnetischen Abstützungssystems für spurgebundene Schnellverkehrsmittel", Zeits. für Angewandte Phys., vol. 32, p. 216-8, 1971.

Baran, W. (1972): "Der Augenblickliche Stand und die Weitere Entwicklung auf dem Gebiet der Permanentmagnetischen Abstützungssyteme für Spurgebundene Schnellverkehrsmittel", Int. J. Magnetism, vol. 3, p. 103-11, 1972.

Barwell, F. T. (1979): Bearing Systems, Principles and Practice, Oxford Univ. Press, Oxford, 1979.

Borcherts, R. H. (1971): "Mathematical Analysis of 'Permanent' Magnet Suspension Systems", J. Appl. Phys., vol. 42, no. 4, p. 1528-9, 1971.

Box, M. H., Davies, D., and Swann, H. (1969): Nonlinear Optimisation Techniques, ICI Monograph no. 5, Oliver & Boyd, Edinburgh, 1969.

Castelli, V., Rightmire, G. K., and Fuller, D. D. (1967): "On the Analytical and Experimental Investigation of a Hydrostatic, Axisymmetric Compliant-Surface Thrust Bearing", J. Lub. Tech., vol. 89, p. 510-20, 1967.

Castelli, V., Rightmire, G. K., Benjamin, M. K., and Fuller, D.D. (1969): Design Guide for Hydrostatic Axisymmetric Compliant Surface Thrust Bearings, Technical Rept. No. 16, Lubrication Research Lab., Columbia University, New York, 1969.

Chen, C. P., and Peube, J. (1964): "Sur l'écoulement Radial Divergent d'un Fluide Visqueux Incompressible entre Deux Plans Paralleles", Comptes Rend. Acad. Sci. (Paris), vol. t258, no. 22, p. 5353-55, 1964.

Coffey, H. T., Chilton, F., and Hoppie, L. O. (1972): The Feasibility of Magnetically Levitating High Speed Ground Vehicles, US Federal Railroad Admin. Rept. No. FRA-RT-72-39, Stanford Res. Inst., Menlo Pk., Calif., 1972.

Constantinescu, V. K. (1962): "Analysis of Bearings Operating in a Turbulent Regime", J. Basic Eng., vol. 84, p. 139-51, 1962.

Cooper, R. K., Neil, V. K., and Woodruff, W. R. (1973): "Optimum Permanent Magnet Dimensions for Repulsion Applications", IEEE Trans. Mag., vol. MAG-9, no. 2, p. 125-7, June, 1973.

Craik, D. J. (1966): "Magnetic Fields from Subdivided Surfaces", British J. Appl. Phys., vol. 17, p. 873-8, 1966.

Craik, D. J. (1967): "Demagnetising Fields in Uniformly Magnetised Rectangular Prismatic Crystals", British J. Appl. Phys., vol. 18, p. 1355-6, 1967.

Craik, D. J., and Harrison, A. J. (1974): "Magnetic Field, Potential, Force and Energy Calculations for Permanent Magnets", Procs. 3rd European Conference on Hard Magnetic Materials, p. 33-6, Amsterdam, 1974.

Davies, S. J., and White, C. M. (1928): Proc. Roy. Soc. London, vol. 119A, p. 92, 1928.

Dowson, D. (1967): "Modes of Lubrication in Human Joints", Procs. Symposium on Lubrication and Wear in Living and Artificial Human Joints, London, April, 1967, paper no. 12, pub. Inst. Mech. Engnrs., London, 1967.

Dowson, D., and Taylor, C. M. (1967): "Elastohydrostatic Lubrication of Circular Plate Thrust Bearings", J. Lub. Tech., vol. 89, p. 237-44, July, 1967.

Earnshaw, S. (1839): "On the Nature of the Molecular Forces which Regulate the Constitution of the Luminiferous Ether", Trans. Cambridge Phil. Soc., vol. 7, part 1, p. 97-112, 1839.

ETSU (1985a): Wave Energy - The Department of Energy's R & D Programme 1974-1983, ETSU R26, AERE Harwell, pub. HMSO, March 1985.

ETSU (1985b): Prospects for the Exploitation of the Renewable Energy Technologies in the United Kingdom, ETSU R30, AERE Harwell, pub. HMSO, May 1985.

Henning, G. (1973): "Optiemierung einer gleichgepolten Magnetanordnung als Abstützungssystem für eine Magnetschwebebahn", Technische Mitteilungen Krupp, vol. 31, p. 1-10, 1973.

Hudson, J. A., Phillips, D. C., Wilkins, N. J. M., Davidson, R., and Scott, P. M. (1982): Materials Aspects of Wave Energy Converters, Rept. WESC (82) SP151, AERE Harwell, 1982.

Ishizawa, S. (1965): "The Axisymmetric Laminar Flow in an Arbitrarily Shaped Narrow Gap (1st Report, Theoretical Analysis for the Inlet Region)", Bull. JSME, vol. 8, no. 31, p. 353-67, 1965.

Ishizawa, S. (1966): "The Axisymmetric Laminar Flow in an Arbitrarily Shaped Narrow Gap (2nd Report, Theoretical Analysis of the Downstream Region)", Bull. JSME, vol. 9, no. 33, p. 86-103, 1966.

Jackson, J. D., and Symmons, G. R. (1965a): "The Pressure Distribution in a Hydrostatic Thrust Bearing", Int. J. Mech. Sci., vol. 7, p. 239-42, 1965.

Jackson, J. D., and Symmons, G. R. (1965b): "An Investigation of Radial Laminar Flow Between Two Parallel Discs", Applied Scientific Research (section A), vol. 15, p. 59-75, 1965.

Jeffrey, D. C., Keller, G. J., Mollison, D., Richmond, D. J. E., Salter, S. H., Taylor, J. R. M., and Young, I. (1978): "Study of Mechanisms for Extracting Power from Sea Waves", Edinburgh University Wave Power Project 4th Year Report, July 1978.

Kawashima, G. (1976): "An Experimental Study on Flat Disk Valves", Bull. JSME, vol. 19, no. 130, p. 420-5, April, 1976.

Kawashima, G. (1978): "An Experimental Study on Flat Disk Valves (2nd Report: the Case of a Rounded Inlet Corner of Clearance)", Bull. JSME, vol. 21, no. 160, p. 1500-6, October, 1978.

Kip, A. F. (1969): Fundamentals of Electricity and Magnetism, 2nd edn., McGraw-Hill Kogakusha, Tokyo, 1969.

Kreith, F. (1965): "Reverse Transition in Radial Source Flow Between Two Parallel Plates", The Physics of Fluids, vol. 8, no. 6, p. 1189-90, June, 1965.

Kreysig, E. (1983): Advanced Engineering Mathematics, 5th edn., Wiley and Sons, New York, 1983.

Kuzma, D. C. (1970): "Determination of the Integration Constant for Squeeze Films in Infinitely Long Journal Bearings", J. Lub. Tech., vol. 92, p. 179-80, January, 1970.

Lee, A. J., and Ramster, J. W., editors (1981): Atlas of the Seas around the British Isles, 1st edn., Ministry of Agriculture, Fisheries & Food, pub. HMSO, 1981.

Levy, S. B., and Coogan, C. H., Jr. (1968): "Flexible Membrane Hydrostatic Air Bearing", J. Lub. Tech., vol. 90, p. 184-90, January, 1968.

Livesey, J. L. (1959): "Inertia Effects in Viscous Flows", Int. J. Mech. Sci., vol. 1, p. 84-88, 1959.

Massey, B. S. (1979): Mechanics of Fluids, 4th edn., Van Nostrand Reinhold (UK) Ltd., Berkshire, 1979.

Maxwell, J. C. (1873): Electricity and Magnetism, 3rd edn., vol. 2, Clarendon Press, Oxford, 1873.

McCaig, M. (1961): "Permanent Magnets for Repulsion Systems", Electrical Review, vol. 15, p. 425-8, September, 1961.

McCaig, M. (1968): "Present and Future Technological Applications of Permanent Magnets", IEEE Trans. Mag., vol. MAG-4, no. 3, p. 221-8, September, 1968.

McCaig, M. (1977): Permanent Magnets in Theory and Practice, Pentech Press, London, 1977.

McCutchen, C. W., and Lewis, P. R. (1959): "Mechanism of Animal Joints" (two papers), Nature, vol. 184, p. 1284-5, October 24th, 1959.

McCutchen, C. W. (1967): "Physiological Lubrication", Procs. Symposium on Lubrication and Wear in Living and Artificial Human Joints, London, April, 1967, paper no. 1, pub. Inst. Mech. Engnrs., London, 1967.

McGinn, J. H. (1955): "Observations on the Radial Flow of Water Between Fixed Parallel Plates", Applied Scientific Research (section A), vol. 5, p. 255-64, 1955.

Milne, A. A. (1965): "Inertia Effects in Self Acting Bearing Lubrication", Procs. Int. Symp. on Lubrication and Wear, Houston, Texas, June, 1963, p.423-527, pub. McCutchen, Berkeley, Calif., 1965.

Minnich, S. H. (1971): Vehicle Levitation by Rare Earth Permanent Magnets, General Electric Co. Rept. No. 71-C-104, Schenechtady, New York, March, 1971.

Moller, P. S. (1963): "Radial Flow Without Swirl Between Parallel Plates", Aeronautical Quarterly, vol. 14, p. 163-86, May, 1963.

Mori, H., and Yabe, H. (1966): "Analysis of an Externally Pressurised Thrust Collar Gas Bearing with Multiple Supply Holes", Bull. JSME, vol. 9, no. 35, p. 592-9, 1966.

Mori, H., and Yabe, H. (1967): "Design Equations and Charts of Externally Pressurised Thrust Gas Bearings", Procs. Gas Bearing Symp., University of Southampton, April, 1967, paper no. 8.

Ng, C., and Pan, C. H. T. (1965): "A Linearised Turbulent Lubrication Theory", J. Basic Eng., vol. 87, p. 675-88, 1965.

Orcutt, F. K. (1965): "Investigation of a Partial Arc Pad Bearing in the Superlaminar Flow Regime", J. Basic Eng., vol. 87, p. 145-52, 1965.

Patrat, J. (1975): "Contribution à l'étude des Pressions dans un Ecoulement Radial Divergent", Journal de Mécanique, vol. 14, no. 3, p. 505-22, 1975.

Peube, J. (1963): "Sur l'écoulement Radial Permanent d'un Fluide Visqueux Incompressible entre Deux Plans Parallèles Fixes", Journal de Mécanique, vol. 2, no. 4, p. 377-95, 1963.

Picken, M. J., and Fitzgerald, G. M. F. (1981): Report on the Environmental Factors Relating to the Bristol Cylinder Wave Energy Device, prep. for Sir Robert McAlpine & Sons Ltd. under Dept. of Energy contract, Scottish Marine Biological Assoc., Dunstaffnage, Oban, September, 1981.

Raal, J. D. (1978): "Radial Source Flow Between Parallel Disks", J. Fluid Mech., vol. 85, part 3, p. 401-16, 1978.

Rabinowicz, E. (1968): Standard Handbook of Lubrication Engineering, ASME, ed. O'Connor, J. J., and Boyd, J., chapter 1, McGraw Hill, New York, 1968.

Rayleigh, Lord (1917): "A Simple Problem in Forced lubrication", Engineering, December 14th, 1917, p. 617.

Rowlands, G. (1980): "On the Invariance of the Magnetic Field Strength due to a Uniformly Magnetised Body", IEEE Trans. Mag., vol. MAG-16, no. 2, p. 480-1, March, 1980.

Salter, S. H. (1974): "Wave Power", Nature, vol. 249, no. 5459, p. 720-4, June 21st, 1974.

Salter, S. H. (1978): "The Development of the Duck Concept", Proc. Wave Energy Conf., Heathrow, London, November, 1978, paper no. 2, p. 17-27, pub. HMSO, 1978.

Salter, S. H. (1980): "Recent Progress on Ducks", Proc. IEE, vol. 127, part A, no. 5, p. 308-19, June, 1980.

Salter, S. H. (1981a): "Wave Energy - Problems and Solutions", Journal of the RSA, vol. 129, no. 5301, p. 568-83, August, 1981.

Salter, S. H. (1981b): "Absorbing Wavemakers and Wide Tanks", Procs. Conf. on Directional Wave Spectra Applications, Berkeley, Calif., sponsored by Am. Soc. Civil Engnrs., September, 1981.

Savage, S. B. (1964): "Laminar Radial Flow Between Parallel Plates", Trans. ASME, J. Appl. Mech., vol. 31, p. 594-6, December, 1964.

Schlichting, H. (1979): Boundary Layer Theory, 7th (English) edn., McGraw-Hill, New York, 1979, p. 186.

Shaw, R. (1982): Wave Energy - A Design Challenge, Ellis Horwood Ltd. (distrib. Wiley), Chichester, 1982.

Silvester, R. (1974): Coastal Engineering 1 - Generation, Propagation and Influence of Waves (Developments in Geotechnical Engineering, vol. 4A), Elsevier Scientific Pub. Co., Amsterdam, 1974, p. 87.

Smith, M. I., and Fuller, D. D. (1956): "Journal Bearings Operating at Superlaminar Speeds", Trans. ASME, vol. 78, p. 469, 1956.

Stansfield, F. M. (1970): Hydrostatic Bearings for Machine Tools and Other Applications, Machinery Pub. Co. Ltd., Brighton, Sussex, 1970.

Tsui, J. B. Y., Iden, D. J., Strnat, K. J., and Evers, A. J. (1972): "The Effect of Intrinsic Magnetic Properties on Permanent Magnet Repulsion", IEEE Trans. Mag., vol. MAG-8, no. 2, p. 188-94, June, 1972.

Van Dyke, M. (1970): "Entry Flow in a Channel", J. Fluid Mech., vol. 44, part 4, p. 813-23, 1970.

Vohr, J. H. (1969): "A Study of Inherent Restrictor Characteristics for Hydrostatic Gas Bearings", Proc. 4th Biannual Gas Bearing Symp., University of Southampton, April, 1969, vol. 2, paper no. 30.

Ward-Smith, A. J. (1980): Internal Fluid Flow, Clarendon Press, Oxford, 1980.

Wilcock, D. F. (1977): "Design of Efficient Turbulent Thrust Bearings", J. Lub. Tech., vol. 99, p. 113-21, 1977.

Wilson, S. D. R. (1972): "A Note on Laminar Radial Flow Between Parallel Plates", Applied Scientific Research, vol. 25, p. 349-54, February, 1972.

Yonnet, J. P. (1978a): "Passive Magnetic Bearings", Proc. Third International Workshop on Rare Earth Cobalt Magnets and their Applications, University of California, San Diego, 1978, paper IV-7, p. 241-51.

Yonnet, J. P. (1978b): "Passive Magnetic Bearings with Permanent Magnets", IEEE Trans. Mag., vol. MAG-14, no.5, p. 803-5, 1978.

Yonnet, J. P. (1980): "Etude des Paliers Magnetiques Passifs", PhD thesis, l'Université Scientifique et Médicale, l'Institut National Polytechnique, Grenoble, July, 1980.

Yonnet, J. P. (1981a): "Permanent Magnet Bearings and Couplings", IEEE Trans. Mag., vol. MAG-17, no.1, p. 1169-72, January, 1981.

Yonnet, J. P. (1981b): "Analytical Calculations of Magnetic Bearings", Fifth International Workshop on Rare Earth Cobalt Permanent Magnets, Roanoke, Virginia, June, 1981, paper no. V-3, p. 199-216.

ACKNOWLEDGEMENTS

In conclusion, I would like to thank my supervisor, Stephen Salter, for his help and guidance during my term of study. The frequently-sought advice of Dr George Alder and Dr David Boffey has also been much appreciated. For valuable discussion on the subject of magnetic repulsion, the correspondence of Dr Jean-Paul Yonnet of Grenoble, and Dr Werner Baran of Essen, is gratefully acknowledged, and thanks are due to Ken Boyle, Sarah Hemming, and Mrs Sylvia Furness for translation of the German 'maglev' publications. Jamie Taylor took the photograph which appears in plate 6.2, and Sandy Nelson ran the tank tests which yielded the wave traces shown in figure 4.3.

The work was financially supported by the Science and Engineering Research Council, John Laing plc, the Norwegian Institute of Technology at the University of Trondheim, and the Edinburgh University Department of Mechanical Engineering. The UK Department of Energy are to be thanked for the use of their microcomputing facilities, and for tolerating my occasional forays into the wavepower mechanical workshop.

Finally, my sincere thanks go to all the past and present members of the Edinburgh Wave Power Project who placed at my disposal their advice, encouragement, but most of all friendship, over the last four years.

CGA

November 22nd 1985